MULTI-SCALE OPTIMIZATION FRAMEWORKS FOR INTEGRATED PROCESS AND MATERIAL DESIGN AND INTENSIFICATION

A Dissertation

by

SHACHIT SHANKARAN IYER

Submitted to the Office of Graduate and Professional Studies of
Texas A&M University
in partial fulfillment of the requirements for the degree of

DOCTOR OF PHILOSOPHY

Chair of Committee,	M. M. Faruque Hasan
Committee Members,	Efstratios N. Pistikopoulos
	A. Rashid Hasan
	Phanourios Tamamis
Head of Department,	M. Nazmul Karim

May 2019

Major Subject: Chemical Engineering

ABSTRACT

Meeting energy and chemical production demands while reducing costs and emissions is a grand challenge. Intensified processes which merge multiple tasks while maintaining performance can significantly reduce equipment footprint, energy input and costs. Effectively designing such processes requires balancing competing trade-offs on multiple levels.

A multi-scale framework is developed for simultaneous consideration of operational and material decisions by posing the intensified process design problem as an optimization formulation. Models and constraints related to process operations, process performance, product quality and material properties are incorporated into the framework.

The framework is applied to intensify the separation and storage of methane (CH_4) from feedstocks by exploiting the preferential adsorption properties of zeolites. However, meeting constraints on CH_4 loss and purity while maximizing the storage capacity is a challenge requiring consideration of both process and material decisions. The complete dynamic process model and constraints along with adsorption isotherm models are posed as a nonlinear programming (NLP) problem. Adsorption isotherm data on 178 siliceous zeolite frameworks are obtained using Grand Canonical Monte Carlo (GCMC) simulations. An initialization strategy is developed to aid in optimizing the model using which the top candidate zeolites and their corresponding process conditions are determined for different feed compositions. The analysis is extended to obtain target material property maps by extensively sampling the material property space (Henry coefficient, deliverable capacity, isotherm parameters) using a Latin Hypercube based strategy. Data from publicly available zeolite databases are super-imposed onto these maps to identify the top zeolite structures for process performance and feasibility.

Another application studied is the design of a process to integrate CO_2 capture and syngas production using methane feedstocks. The energy intensive periodic pressure changes employed for adsorbent-based CO_2 capture are avoided by using a CH_4 rich purge feed to strip the adsorbed CO_2 which then becomes feed for syngas production. A data-driven constrained optimization algorithm

is applied to identify process conditions which satisfy process specifications and product quality requirements and to determine optimal process decisions for different objectives and feedstocks. The importance of the multi-scale optimization approach in designing novel intensified processes is demonstrated through these applications.

DEDICATION

To my beloved parents who have been constant pillars of support and have made me the individual who I am.

ACKNOWLEDGMENTS

First of all, I would like to express my sincere gratitude to my advisor Dr. M. M. Faruque Hasan for the constant guidance and support provided to me during the course of my research. His door was always open to discuss about research ideas and topics at any time of the day. I greatly appreciate his providing feedback on various drafts and presentations which has made me a better communicator. I would also like to thank him for providing guidance in multiple academic and professional development areas which has helped me a better researcher.

I want to extend my sincere gratitude toward my committee members Prof. Efstratios N. Pistikopoulos, Dr. Phanourios Tamamis and Prof. A. Rashid Hasan for their support and feedback. My sincere thanks to Prof. Pistikopoulos for taking a special interest in my research and providing feedback and directions for improvement. My research has immensely benefited from the courses taught by Prof. Pistikopoulos, Dr. Tamamis and other faculty with great passion and enthusiasm. I would also like to thank Prof. Perla Balbuena for her support.

I would also thank my colleague Ishan Bajaj for providing help and guidance relating to the inner workings of various optimization algorithms. Salih Demirel helped me understand and appreciate the intricacies of the GAMS modeling environment. I appreciate the conversations and cherish the insights obtained discussing different processes and their models with Akhil Arora. I am grateful for having colleagues such as Manali Zantye, Spyridon Tsolas, Jianping Li, Priyadarshini Balasubramanian and others at the Engineering Research Building for always being there for fruitful discussions about research topics and coding practices.

I would like to thank Ms. Ashley Henley, Prof. Naz Karim and Prof. Arul Jayaraman from the Artie McFerrin Department of Chemical Engineering for helping me out with various general concerns during these years. I sincerely appreciate the support and guidance provided by Marinus Pennings and Ping Luo from Texas A&M High Performance Computing.

Last but not the least, I thank my parents for being a constant source of guidance, support and love throughout my life.

CONTRIBUTORS AND FUNDING SOURCES

Contributors

This work was supported by a dissertation committee consisting of Assistant Professor M. M. Faruque Hasan, Professor Efstratios N. Pistikopoulos and Assistant Professor Phanourios Tamamis of the Artie McFerrin Department of Chemical Engineering and Professor A. Rashid Hasan of the Harold Vance Department of Petroleum Engineering.

A part of the Grand Canonical Monte Carlo analyses in Section 3 was conducted by my colleague Salih Emre Demirel. The data-driven grey box optimization algorithm in Section 4 was developed by my colleague Ishan Bajaj. The reactor model for dry reforming was adapted upon and further incorporated in the integrated process model based on the work of former lab member Priyadarshini Balasubramanian.

All other work conducted for the dissertation was completed by the student independently.

Funding Sources

Graduate study was supported by faculty startup grant from Artie McFerrin Department of Chemical Engineering, Texas A&M University, funds from the U.S. National Science Foundation (award number CBET-1606027) and the American Chemical Society Petroleum Research Fund (ACS PRF 58764-DNI9).

TABLE OF CONTENTS

Page

LIST OF FIGURES

FIGURE Page

LIST OF TABLES

TABLE Page

1. INTRODUCTION AND LITERATURE REVIEW*

Energy efficient and cost-effective processes will be necessary to meet the increasing energy needs of the future in a sustainable manner. Technologies for processing gases such as CO_2 and CH_4 are especially important, since CO_2 emissions due to burning of fossil fuels are linked to climate change while CH_4 is the cleanest fossil fuel available in terms of CO_2 emissions. To limit CO_2 emissions, there is a dire need for technologies for CO_2 capture, utilization and sequestration (CCUS) especially from dilute sources of CO_2. For widespread deployment of such technologies alongside existing infrastructure, there needs to be a significant reduction in the energy consumption and cost of the CO_2 capture step, which currently accounts for upto 60-70% of the cost. Natural gas of which CH_4 is a primary component, is an important fuel source with its demand growing in the coming years. To satisfy the future demand, utilization of unconventional feedstocks such as biogas, landfill gas, coal-bed methane will be required. However, even conventional feedstocks of CH_4 such as natural gas, shale gas can have variable impurities content upto 70% [1]. From these feedstocks, impurities such as acid gases, nitrogen, water, oil and condensates etc. also need to be separated in order to obtain fuel grade CH_4. Separation processes alone account for about 45-55% of the total industrial energy consumption and about 10-15% of the total national energy consumption in the U.S [2].

Design of intensified processes which attempt to merge multiple tasks in a smaller equipment footprint can drive reduction in cost and energy input [3]. Intensified processes are also important for utilizing small scale and scatter sources. While conventional separation and pipeline transportation supply chains exist for conventional large-scale sources, establishing such facilities for small and distributed sources can be cost prohibitive. For utilization of such unconventional feedstocks, modular equipment and processes are necessary since economies of scale would not be effective

*Parts of this section reproduced in part with permission from Iyer, S. S., Demirel, S. E. and Hasan, M. M. F., "Combined Natural Gas Separation and Storage Based on in Silico Material Screening and Process Optimization" *Industrial & Engineering Chemistry Research*, 57 (49), 16727-16750. Copyright 2018 American Chemical Society. Available at `https://pubs.acs.org/doi/10.1021/acs.iecr.8b02690`

as compared to facilities which process large volumes of raw material. Instead, economies can be realized through assembly line based mass production of modular equipment which can reduce the cost of individual units.

1.1 Need for Multi-scale Framework for Process Design and Intensification

vanGerven and Stankiewicz [3] discussed fundamental principles to approach process intensification in four domains: spatial, temporal, thermodynamic and functional on scales ranging from molecular to meso to macro-scale. Portha *et al.* [4] highlighted the importance of intensification both at the local scale on the phenomena level and on the global scale on the overall process level considering interactions between different units. Process intensification can be achieved both on the process design and operation scale and on the material design and development scale. For instance, either different materials with single functionalities [5] or multi-functional materials [6] can be employed to intensify processes e.g., sorption enhanced reaction processes [7]. Examples of intensification approaches which include modifications in process operation along with combining different materials are multi-bed and layered pressure swing adsorption processes [8–10], differential material distributions in the bed [11], multi-material simulated moving beds [12]. Multi-scale considerations can enable understanding and quantifying interaction between phenomena at different scales and can provide opportunities to leverage such interactions in a composite integrated design of new technologies. Onel *et al.* [13] demonstrated the importance of using a multi-scale approach in evaluating the applicability of an intensified reactor alternative for small scale gas to liquid process systems. Multi-scale analysis and supply chain optimization were performed by Hasan *et al.* [14] to CO_2 capture, utilization and sequestrations considering various feed sources, process technologies, materials and resource locations.

1.1.1 Importance of Optimization for Systematic Process Design and Intensification

There is abundant literature [15–18] on using optimization techniques to improve process operating conditions for furthering performance objectives. For instance, Nilchan *et al.* [19] applied a rigorous mathematical programming strategy to optimize the fully discretized dynamic adsorption

model for describing pressure swing adsorption (PSA) systems and bed interactions. Aboosadi *et al.* [20] optimized a tri-reforming reactor for methanol synthesis using a differential evolution algorithm. Bildia *et al.* [21] optimized the design of intensified processes for dimethyl ether (DME) synthesis and compared it with traditional reactor-separator-recycle processes. Biegler [15] describe advanced optimization strategies for batch systems to integrate both the scheduling and unit interactions.

Systematic frameworks incorporating optimization-based approaches have been developed to systematically identify, design and evaluate novel process configurations. These involve simultaneous optimization of both the process configurations and process operations [22]. Ismail *et al.* [23] presented a systematic approach for synthesis of combined reactor-separator systems using a multi-functional process module representation. Recker *et al.* [24] developed a systematic framework for performing optimization-based design of integrated reaction separation processes. Nikolic et al. [25] developed an optimization framework for analyzing pressure swing adsorption cycles involving multi-bed and multi-layered configurations. A superstructure based optimization framework was used by Agarwal *et al.* [26, 27] to obtain optimal cycle configurations using a fully discretized model for pre and post combustion PSA systems. Henao and Maravelias [22] developed a superstructure optimization framework using surrogate-models instead of complex non-linear process models to reduce the complexity of optimization.

Optimization techniques have also been utilized to obtain performance limits and feasibility maps and indices for process designs. Swaney and Grossman [28] developed a general framework for quantifying flexibility in process design and operation through the use of a flexibility index. Pistikopoulos and Mazzuchi [29] presented a flexibility analysis approach for processes with stochastic parameters. Desmet *et al.* [30] employed a global optimization based approach to determine performance limits on productivity of isothermal packed bed reactors subject to allowable ranges of inlet pressures and catalyst layer thickness and pore volumes. Dua and Pistikopoulos [31] applied multi-parametric mixed integer optimization approaches for material design and process synthesis under uncertainty. Cruz and Manousiouthakis [32] synthesized and identified the perfor-

mance limits for reaction separation networks through formulation of an infinite linear program. Carrasco and Lima [33] have recently developed a framework to calculate input spaces for feasible operation for process design and intensification of natural gas utilization systems. Optimization techniques thus provide a way to analyze and evaluate the performance of process designs in order to form a strong case for industrial adoption and deployment.

The preponderance of works on process optimization consider the possibilities in the process decision variable space for a fixed or limited set of materials. This can be a very useful tool for improving the operation and performance for well studied processes for which the best materials are identified. However, for the design of novel intensified processes, especially for which the appropriate candidate materials are not yet identified or well studied, it will be important to evaluate the new process designs for a range of candidate materials.

1.1.2 Materials Screening and Design for Improved Process Performance

Nanoporous materials such as zeolites, metal-organic frameworks posses preferential gas adsorption properties due to large gravimetric and volumetric internal surface areas, unique pore structures and large accessible volume making them candidate materials for gas separation and storage applications. Due to the different topology and type of atoms which can constitute a nanoporous material structure and hence influence its pore characterization metrics such as density, porosity, accessible surface area and volume, a large number of experimental and theoretical structures are possible. Over 200 pure silica zeolitic frameworks have been experimentally identified with over 2 million hypothetical zeolites computationally identified through different combinations of bonding with silicon and oxygen [34,35]. Over 3,000,000 different nanoporous materials which include zeolites, metal-organic frameworks (MOFs), zeolitic imidiazolate frameworks (ZIFs) and porous polymer networks (PPNs) have been generated *in silico* by different research groups along with about 5000 experimentally synthesized MOFs [36].

This has led to abundant research in effectively screening materials from a large number of potential candidates for different process applications. For example, Kim *et al.* [37,38] performed large scale computational screening of zeolites for ethane/ethene separation and for CO_2 separa-

tions using membranes respectively, while Lin *et al.* [39] screen zeolites and zeolitic imidazolate framework structures for carbon capture. Similarly, there are many works on high throughput computational screening of metal organic frameworks (MOFs) for different separation applications like carbon capture, methane storage, CH_4/H_2 separation [40–44]. Wu *et al.* [5] screened faujasite zeolite structures with different Si/Al ratios for temperature swing adsorption systems and concluded that high Al content is favorable at equilibrium conditions. While material screening studies are useful in obtaining the list of top materials and key properties for a particular application, they usually compare material properties at fixed set of process conditions.

A combination of theoretical and data-driven insights have also been applied to determine optimal properties and link structural descriptors to properties for nanoporous adsorbents. Gomez-Gualdron *et al.* [45] identified optimal heat of adsorption for nanoporous materials which maximizes the deliverable capacity for isothermal and non-isothermal methane storage and delivery applications. Simon *et al.* [46] investigated the existing and hypothetical zeolite database using a combination of theoretical models and data and provided a range for the optimal heat of adsorption for methane storage and delivery and demonstrated its dependence on the structure of the material. Recently, machine learning based approaches [47–51] have been used to identify structure property relationships from datasets collected through computationally expensive simulations and provide ranges of values of structural descriptors for various applications. For instance, Ohno and Mukae [48] used a machine learning approach using Guassian process regression to identify ranges of methane uptake for different values of pore descriptors such as surface areas, void fractions and maximum pore diameters. Fernandez *et al.* [52] used decison tree models to provide rules on densities and void fractions for optimal MOFs for methane storage applications. They also developed classifiers to screen material databases for candidate MOFs with desired CO_2 adsorption capacities for carbon capture applications [49].

1.1.3 Toward Consideration of Both Process Operation and Materials for Novel Designs

Design of novel intensified processes is more comprehensive when decisions at both process and material scales are considered at the outset. Compared to works employing process model-

ing and optimization, there are fewer works that consider both materials and process development simultaneously especially for adsorbent based processes. Some examples of simultaneous consideration of process and material decisions in the design stage do exist in literature for simultaneous process and solvent design applications through computer aided molecule design [53–56] where possible structural and functional groups describing novel solvents were proposed using group contribution theory [53, 57] which involves predicting the properties of solvents, polymers based on the additivity principle of individual contributions to physical properties due to the different functional groups present. The contributions of the number and type of functional groups constituting the molecular structure of the solvent is related with its properties such as heat capacity, density, viscosity. Suitable constraints such as octet rule are imposed to ensure structural feasibility of the designed group. Hamad and El-Halwagi [58] applied such an optimization based procedure to simultaneously synthesize mass separating agents e.g. solvents and mass-exchange networks incorporating process objectives and metrics for solvent design. Pistikopoulos and Stefanis [57] applied a systematic procedure to identify optimal solvents which satisfy plant-wide operational and environmental constraints. Papadopoulos and Linke applied a molecular clustering based approach to group together similar solvents for integrated process and solvent design while incorporating solvent design information into process synthesis problem. Recently, the group contribution method has also been applied for prediction of adsorbent activity coefficients for removal of naturally occurring radioactive material from liquid adsorbates such as waste water [59].

For adsorbent based processes, Wiersum *et al.* [60] developed tailored adsorbent performance indicators based on conventional material screening metrics such as working capacities, heat of adsorption and binary selectivities for CO_2/CH_4 separation. For the optimization of a VSA system for post combustion carbon capture, Rajagopalan *et al.* [61] observed that most commonly used metrics such as working capacities, selectivities and other figures of merit are not able to accurately rank materials when the complete process is evaluated. Ga *et al.* [62] obtained additional material performance indicators analytically based on an idealized PSA process model to enable comparison between the performance of different materials without the need for dynamic process

simulations. Guo *et al.* [63] perform iterative process optimization using fully discretized models and experimentation to finally obtain both accurate isotherm parameters and optimal conditions for their material and process respectively. Belmabkhout *et al.* [64] studied multiple adsorbents and identified key adsorbent properties such as pore volumes and strength of interactions which influence CO_2 capture costs at different pressures and feed compositions and proposed metal-organic frameworks as demonstrating great potential due to their tunability. Similarly, Berger and Bhown [65, 66] screened adsorbents using a simplified equilibrium model to identify optimum heat of adsorption which minimizes the energy penalty for carbon capture for varying pressures and feed compositions.

Floudas and coworkers [1, 67, 68] performed both *in-silico* material screening and process optimization of pressure swing adsorption systems for CO_2 capture, natural gas separation and hydrogen sulfide removal applications respectively. Their analysis spans atomistic and mesoscopic scales for performing the materials screening and the macroscopic scale for performing the process optimization. Similar analysis was extended to a process case study involving simulated moving bed chromatography by Hasan *et al.* [12].

Transitioning from sequential design of materials followed by tuning process performance to an optimization based inverse design framework can help in identifying directions of improvement in material properties for satisfying or improving process constraints and objectives. This is important to ensure that a novel process configuration is not rejected because it is not evaluated at the material property range which is best suited for the process application. Moreover, this approach will be valuable for identifying optimal material properties for design of novel processes and for guiding experimental efforts in tuning material properties.

1.1.4 Challenges

The recent studies in literature which incorporate both process and material considerations together primarily focus on well studied existing process systems. However, while evaluating novel and intensified process designs, it is important to consider both the range of possible process operation and the range of available material property space to provide a much more holistic picture.

However, there are challenges which plague such multi-scale considerations both from the material and process point of view. Multi-scale optimization is challenging since it often requires solving high-fidelity models at the molecular and process scales [13, 69]. For example, there are different length and time scales involved in material property prediction right from highly computationally expensive ab-initio quantum mechanical modeling approaches such as Density Functional Theory (DFT), to a lesser but still considerably computationally expensive molecular simulation approaches such as Molecular Dynamics (MD) and Grand Canonical Monte Carlo (GCMC) simulations which utilize knowledge of parameters such as partial charges on the atoms from quantum mechanical calculations [40]. Due to the time consuming nature of simulations at molecular scales, lumped parameters and properties obtained from such high fidelity analyses are used in macro and process scale approaches. This necessitates the sequential use of models at different aggregation levels to pass parameters from a lower level to use in a model at a next level up. While doing so, Vlachos highlighted [70] that a considerable amount of data produced by high fidelity simulations at lower (finer) scale is compressed into a few parameters as it is passed to a higher (coarser) scale [70]. Biegler [69] discussed the importance and demonstrated the use of reduced order models in place of original detailed models for multi-scale applications. Recently, some of these approaches have been attempted with regards to multi-scale modeling and optimization of gas separations [1, 67, 71] and pharmaceutical [72] processes.

The availability, costs and characteristics of materials currently limit the process performance for different applications in gas separation, storage and conversion. There are a lot of experimental studies on improving the properties of existing synthesized materials by modifying/doping them with other materials, employing novel synthesis techniques etc. However, experiments are expensive and time consuming. Moreover, the huge number of possible structures and properties and the large computation times required for rigorous molecular and process simulations leads to a need for identifying target material ranges rather than a brute force approach screening every material. It is important to have a systematic optimization based framework for identifying feasible and optimal material property ranges for process applications. This can greatly help in reducing

the material property search space while offering insights into identifying possible directions for material property tuning. Though there are experimental techniques to synthesize and tune individual nanoporous materials [73–75], there is a paucity of general closed form analytical relations relating experimental modifications to observed properties.

The design of intensified processes which attempt to merge multiple phenomena can lead to multiple tradeoffs between competing process metrics. Moreover, constraints on loss of feed and unreacted streams through the process vents and outlets have to be limited while maximizing process objectives such as performance and cost-effectiveness. This can lead to difficulties in even identifying the values of process decision variables which can lead to a feasible process operation meeting the imposed constraints. Thakur *et al.* [76] mentioned the need to perform trial and error simulations to obtain a operating point which gives a desired product purity for comparing their modified process design for pressure swing adsorption. A rigorous process modeling and optimization framework thus becomes necessary to identify feasible points of operation and further optimize the process objectives. If no feasible point of operation is found, then appropriate modification of designs and formulation of constraints can be performed for arriving at a feasible operating regimes with respect to process and product specifications and emission limits.

Additionally, particular applications also pose additional challenges for intensification of tasks. For example, the separation of CO_2, CH_4 from sources of medium or lower concentration with a variety of impurities such as water, hydrogen sulfide, mercaptans, nitrogen can prove to be expensive. Presence of both strongly and weakly adsorbing impurities especially pose challenges for modular and intensified designs with limited no of pressure/temperature excursions. Similarly, integration of tasks in a single unit which require individually opposing optimal conditions e.g. endothermic reactions which require high temperature and adsorption onto zeolites which is favored at low temperatures can be challenging. CO_2 being a thermodynamically stable molecule, its conversion to other chemicals can be very energy-intensive.

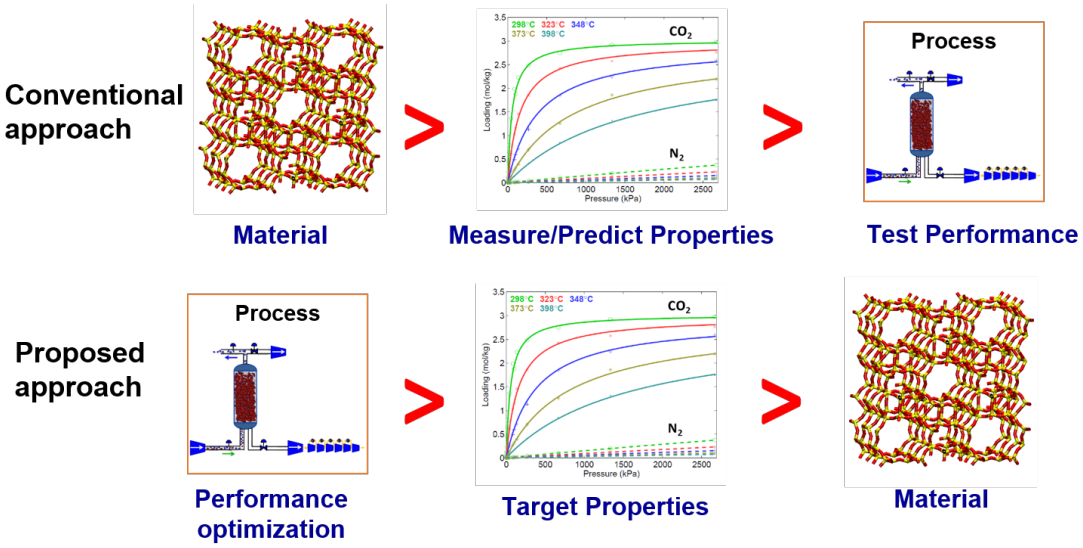

Figure 1.1: Proposed approach of inverse material design using a multi-scale optimization framework. While conventional approach based on existing and synthesized materials attempts to test and tune process performance based on the properties of the material selected, the proposed paradigm attempts to estimate target material properties and design materials which optimize specific process objectives.

1.2 Research Goals and Objectives

The overarching goal is to transition to a design paradigm (Fig. 1.1) which is instrumental in identifying properties and designing materials which optimize process performance while meeting technology specific requirements. In this work, progress is made toward this goal by outlining the following research objectives:

- Develop a multi-scale process and materials intensifications framework for design and evaluation of novel adsorbent based processes for unconventional gaseous feedstocks. The framework is to be posed as an optimization formulation which optimizes a process objective such as performance or cost while incorporating the process and material models and models connecting both scales, constraints on process operation and metrics. This also involves developing appropriate process models to characterize dynamic adsorption of gases in a column filled with nanoporous adsorbents such as zeolites. The process models being dynamic in nature, incorporate partial differential equations which need to be converted to algebraic

formulations for use with existing optimization solvers. In addition to process models, the goal is to obtain data for different zeolite adsorbents to enable uniform comparison using the framework by applying molecular simulation approaches and develop analytical models such as isotherm models to incorporate the material data into the framework. Developing and incorporating initialization strategies to effectively solve the highly nonlinear process models incorporated is also required for solving the problems for a variety of cases.

- Apply the framework to identify conditions for an intensified process design which attempts to exploit the multi-functional gas separation and storage properties of zeolites to combine the process operation in a single column module. For instance, this can be a process to enable combined separation and storage [77] of CH_4 in a single module from a feed containing CH_4/N_2 for application in adsorbent natural gas (ANG) systems. The goal is then to design a process for the combined separation and storage of CH_4 and compare the performance of a set of candidate materials at the corresponding conditions which are optimum for the individual material. This also involves appropriately formulating constraints which maintain product purity and limit losses of reactants while maximizing a process objective such as CH_4 storage. Such process optimization driven material screening can then be used to determine the relative ranking of the materials for different feed conditions and identify material candidates which satisfy the constraints imposed on the process operation.

- Provide feasibility maps of material properties, e.g., equilibrium adsorption loading, Henry coefficients for feasible process operation subject to process constraints imposed. Beyond identifying feasibility, maps of constraint violations can be useful in identifying the effect of material properties on the deviation from feasibility. The goal is to relate ranges of the continuous material property space to the values of total and individual constraint violation obtained and identify where currently available existing and hypothetically designed materials lie in the feasibility space.

- Apply the framework for identifying an initial feasible point of operation and further op-

timize process objectives while integrating the process operation of CO_2 capture from flue gas and its subsequent utilization to syngas while monetizing unconventional CH_4 feeds. Since the process objectives have to be maximized subject to constraints on unreacted and vented CO_2 and CH_4, syngas ratio and product purity constraints, identifying even feasible operating points without resorting to an optimization framework can be non intuitive.

1.3 Organization of the Dissertation

The dissertation is organized as follows:

In Section 2, details about the development of the multi-scale design and intensification framework is presented as an optimization formulation along with an elaborate summary of the different components in the process operational and material scales which comprise the framework. A discussion about obtaining analytical algebraic models for the dynamic process constraints and material data is provided. Further initialization and data-driven strategies for solving the overall optimization formulation are also discussed.

In Section 3, the framework is applied in a process design case of utilizing the preferential adsorption capabilities of zeolites to design a process for combined separation and storage of CH_4. Details on the complete algebraic optimization formulation of the process is provided. Adsorption properties for different zeolites are obtained *via* Monte Carlo simulations. The candidate top performing zeolites and their corresponding process operating conditions are obtained for a range of CH_4 and N_2 feeds. The presence of CO_2 in the feed on process performance and the number of zeolites feasible for process operation is also presented. The discussion of the combined separation and storage technology is extended to obtain constraint violation and feasibility maps over the range of material property space. Details about the methodology adopted for mapping the complete material property input space e.g. CH_4 and N_2 space using just three parameters while retaining the characteristics of the overall isotherm space is provided. The material properties along with the intermediate process metrics which play a significant role in the satisfaction or lack thereof of the constraints relating to the process metrics such as loss and purity are identified. The available existing zeolites [78] and the hypothetical generated zeolites [46, 79] are also depicted in

the feasibility and constraint violation maps.

In Section 4, the details about the process design and simulation methodology for integrating carbon capture from flue gas and CO_2 conversion to syngas using methane rich feeds is provided. This is followed by a discussion on the narrow window of process operation which satisfies the imposed constraints and utilization of a data-driven optimization strategy to reduce constraint violation and optimize the process for two case studies involving natural gas and biogas feeds respectively.

In section 5, the overall conclusions drawn from the use of the framework is summarized and some future directions and challenges pertaining to the broader applicability of the framework to other process designs and applications is briefly discussed.

2. A MULTI-SCALE PROCESS AND MATERIALS OPTIMIZATION FRAMEWORK FOR INTENSIFICATION*

For designing and evaluating processes for intensified applications, it is necessary to capture the progress of different phenomena involved over both spatial and temporal domains to predict process performance. Understanding and incorporating the various equilibrium, kinetic and transport effects and leveraging the trade-offs between competing phenomena systematically is critical. For process designs to reflect actual performance, the underlying model needs to capture the above effects appropriately and should incorporate reliable material and physical properties. If there are different choice of materials involved in the decision making, their effects on the overall process performance also needs to be accounted for. Additionally, constraints on process operations and product specifications influence the scope, cost-effectiveness and applicability of different designs. An optimization formulation based approach can be useful in incorporating different models and satisfying the imposed constraints to optimize desired objectives. Such an approach can be versatile enough to evaluate the inherent flexibility and the robustness of the design to handle changes in operational parameters such as feed compositions and effect of different choices of materials. Other factors such as large-scale deployment, geographical proximity to resources, etc. can also affect the feasibility and effectiveness of process designs but in this work, we will limit the scope of our analysis to the process development and material selection scales. An optimization-based multi-scale process and materials intensification framework is developed for designing and evaluating process designs and is described below.

*Parts of this section reproduced in part with permission from Iyer, S. S., Demirel, S. E. and Hasan, M. M. F., "Combined Natural Gas Separation and Storage Based on in Silico Material Screening and Process Optimization" *Industrial & Engineering Chemistry Research*, 57 (49), 16727-16750. Copyright 2018 American Chemical Society. Available at `https://pubs.acs.org/doi/10.1021/acs.iecr.8b02690`

2.1 Framework Description

The generalized optimization formulation of the multi-scale design framework is described below.

$$\min_{\mathbf{X}} \quad Z = F\left(\mathbf{X}, \boldsymbol{\alpha}, \int_z f_z(\mathbf{X}, \boldsymbol{\alpha})\, dz\,, \int_t f_t(\mathbf{X}, \boldsymbol{\alpha})\, dt\right) \qquad \text{(Objective Function)} \tag{2.1a}$$

s.t.

$$h^P(\mathbf{X}, \boldsymbol{\alpha}, \frac{\partial \boldsymbol{\alpha}}{\partial t}, \frac{\partial \boldsymbol{\alpha}}{\partial z}, \frac{\partial^2 \boldsymbol{\alpha}}{\partial z^2}, \boldsymbol{\gamma}) = 0 \qquad \text{(Process Model)} \tag{2.1b}$$

$$G^P\left(\mathbf{X}, \boldsymbol{\alpha}, \int_z g_z(\mathbf{X}, \boldsymbol{\alpha})\, dz\,, \int_t g_t(\mathbf{X}, \boldsymbol{\alpha})\, dt\right) \leq 0 \qquad \text{(Process Performance Constraints)} \tag{2.1c}$$

$$h^{MP}(\boldsymbol{\alpha}, \boldsymbol{\beta}, \boldsymbol{\gamma}) = 0 \qquad \text{(Material-Process Connectivity Model)} \tag{2.1d}$$

$$h^M(\boldsymbol{\delta}, \boldsymbol{\beta}) = 0 \qquad \text{(Material Structure-Property Model)} \tag{2.1e}$$

$$\mathbf{X} \in [\mathbf{X}^L, \mathbf{X}^U] \subseteq \mathbb{R}^d \qquad \text{(Decision Variable Bounds)} \tag{2.1f}$$

In the above formulation, $\boldsymbol{\alpha}$ is the vector of state variables of the process (e.g., pressure, temperature, gaseous phase mole fraction, adsorbent phase gas loadings), $\mathbf{X}$ is the vector of process design variables (e.g., feed pressure and temperature, pressure and temperature at column boundaries, feed velocities, column dimensions, process duration, void fractions), $\boldsymbol{\beta}$ is a vector of material properties (e.g., density, equilibrium adsorption isotherm parameters, specific heat capacity, diffusion co-efficient, heat of adsorption, reaction kinetics parameters), $\boldsymbol{\gamma}$ denotes a vector of material-centric process parameters which includes the values of material properties such as heat of adsorption, adsorbent loadings at the process state variables such as temperature, pressure and

compositions while $\boldsymbol{\delta}$ can include structural, geometric and pore descriptors (e.g. crystal structures, unit cell dimensions, accessible surface area, pore volumes) of material under consideration.

$F\left(\mathbf{X}, \boldsymbol{\alpha}, \int_z f_z(\mathbf{X}, \boldsymbol{\alpha})\, dz\,, \int_t f_t(\mathbf{X}, \boldsymbol{\alpha})\, dt\right)$ is the objective function which can represent process performance and economic metrics such as total gas stored, conversion, productivity, total cost per product. The process model $h^P(\mathbf{X}, \boldsymbol{\alpha}, \frac{\partial \boldsymbol{\alpha}}{\partial t}, \frac{\partial \boldsymbol{\alpha}}{\partial z}, \frac{\partial^2 \boldsymbol{\alpha}}{\partial z^2}, \boldsymbol{\gamma}) = 0$ includes the mass and energy balances, pressure drop correlations, boundary conditions, initial conditions and other auxiliary expressions which completely describe the process. $G^P\left(\mathbf{X}, \boldsymbol{\alpha}, \int_z g_z(\mathbf{X}, \boldsymbol{\alpha})\, dz\,, \int_t g_t(\mathbf{X}, \boldsymbol{\alpha})\, dt\right) \leq 0$ represent set of inequalities which account for the bounds on the process performance metrics, product quality etc. $h^M(\boldsymbol{\delta}, \boldsymbol{\beta})$ denotes the material model which relates structural, chemical and geometric characteristics with the material properties such as adsorption loading isotherm data, heat of adsorption, Henry co-efficient. $h^{MP}(\boldsymbol{\alpha}, \boldsymbol{\beta}, \boldsymbol{\gamma})$ is the material process connectivity model which describes the values of the material-centric properties at the conditions of the process state variables such as pressure, temperature and mole fraction. Examples of such material process connectivity models include rate expressions, extended equilibrium adsorption isotherms, mass transfer driving force equations etc.

2.1.1 Process Models

The process model included in the framework $h^P(\mathbf{X}, \boldsymbol{\alpha}, \frac{\partial \boldsymbol{\alpha}}{\partial t}, \frac{\partial \boldsymbol{\alpha}}{\partial z}, \frac{\partial^2 \boldsymbol{\alpha}}{\partial z^2}, \boldsymbol{\gamma}) = 0$, is used to capture the bulk and interfacial transport phenomena, depletion and generation of different species along with the associated temperature and pressure effects and describe the behavior of various phenomena occurring in a particular application. There are however multiple levels of complexities in process modeling in terms of multiple dimensions, multiple phases, modeling of complex geometries which may be required for predicting process performance for different applications. In this dissertation, the framework is demonstrated with a one dimensional generalized model [80] characterizing packed bed systems with gas adsorption and reaction while accounting for the dynamic effects. Different systems such as reactors, adsorbers, sorption-enhanced reactors, layered bed configurations and different modes of operation such as steady state, unsteady state and cyclic processes can be modeled by neglecting the appropriate terms in the generalized model. An exam-

ple of a partial differential equation which describes the component mole balance of adsorption of gas species in a column filled with adsorbent with varying temperature, pressures is given below:

$$\frac{\partial y_i}{\partial t} = \frac{y_i}{T}\frac{\partial T}{\partial t} - \frac{y_i}{P}\frac{\partial P}{\partial t} + \frac{T}{P}D_L\frac{\partial}{\partial z}\left(\frac{P}{T}\frac{\partial y_i}{\partial z}\right) - \frac{T}{P}\frac{\partial}{\partial z}\left(\frac{y_i P v}{T}\right) - \frac{RT}{P}\frac{(1-\varepsilon)}{\varepsilon}\frac{\partial q_i}{\partial t} \quad \forall i \in I \quad (2.2)$$

The multi-scale optimization framework is however posed as an optimization formulation. Process models containing differential terms need be converted to equivalent or approximate algebraic formulations, to be solved with current state of the art optimization solvers available in literature. For this an appropriate discretization strategy is necessary in both spatial and temporal domains. A variety of discretization strategies such as finite difference, finite volume, finite element and other Taylor series expansion based methods such as collocation methods exist. For integrating along the temporal dimension, implicit and explicit methods are available, where implicit methods are used when there are steep gradients in the profiles of the transient variables.

A discretization strategy involving finite volume in space and implicit Euler method for time integration is described below. The spatial dimension is divided into a number of spatial finite volumes N_J. The average value of a conserved quantity over each finite volume is denoted by subscript $j \in J = \{1, 2, .., N\}$. For instance, $P_j = (\int_{V_j} P(t)dV)/\Delta V$ denotes the average pressure at a time t in a location of the column corresponding to a volume indexed j. To approximate the spatial derivatives, they are integrated over each cell with the values at the finite volume boundaries denoted by indices $j - 0.5$ and $j + 0.5$ respectively and the average value over the finite volume denoted by index j. Different schemes such as Van Leer, Weighted Essentially Non-Oscillatory (WENO) can be used to relate the values of the neighboring finite volumes with each other [81] depending on their applicability for the process model and the accuracy requirements. For instance, the upwind differencing scheme (UDS) is used to relate the value of the finite volume boundary at $j + 0.5$ with the corresponding value upstream at j e.g. $P_{j+0.5} = P_j$. The values at both of the column ends at $j = 0.5$ and $j = N + 0.5$ are given by the respective boundary conditions. The use of the first order accurate UDS scheme avoids non-physical oscillations [82] in the so-

lution however it does introduce some numerical diffusion. The temporal derivatives occurring in the differential equations can be converted to algebraic equations using explicit, implicit and combination of explicit and implicit timestepping schemes. Fully explicit schemes though easier to solve and express as a function of known variables are not unconditionally stable for all choices of the time step length. Fully implicit schemes require solving a set of equations at every time step in the integration but are unconditionally stable for choices of time step length. However, for both schemes the accuracy is improved if the number of time steps chosen are increased which translates to shorter length of time steps. For instance, if the differential equation to be discretized is $\frac{dy}{dt} = F(t, y)$, then the corresponding backward Euler approximation for a time step k will be $\frac{y_k - y_{k-1}}{\Delta t} = F(t_k, y_k)$ where the value of y at $k-1$ th step is known through recursively solving the scheme from the value of y at the initial condition.

An alternate approach to could be building approximate algebraic surrogate models using data obtained from solving the process model for a variety of conditions [83]. Appropriate sampling methods are used to sample the values of the decision variables and obtain the corresponding process outputs [84]. Based on such a dataset, algebraic input-output surrogate models can be constructed to represent the behavior of the process with respect to the chosen inputs and output variables. This can be useful if the process model is highly complex to use a complete discretization formulation as is the case for many cyclic process operations.

Based on the formulation of the process model, the appropriate formulations for the constraints on process performance metrics such as feed loss, unconverted reactants, purity, productivity can be expressed as a function of process decision variables and the process state variables at different locations of space and time.

2.1.2 Material Models

It is difficult to obtain explicit or closed form equations $h^M(\boldsymbol{\delta}, \boldsymbol{\beta})$ to directly relate the material properties $\boldsymbol{\beta}$ (e.g. adsorption isotherm parameters) with structural and geometric properties of materials $\boldsymbol{\delta}$ such as void fraction, density, crystal structure and topography, pore size distribution etc from theoretical insights. These properties are usually obtained through experiments or by

applying rigorous computational methods. However, experiments to synthesize and characterize materials can be expensive and time consuming to evaluate the large number of candidate structures. Also there is abundant experimental data and synthesis methods available for a few widely used materials such as zeolites 13X, 5A, ZSM-5, MOF-5 but there can be a paucity of available data for a large number of material candidates which are not yet close to commercialization for the existing technologies.

2.1.2.1 Obtaining Material Data

In order to be consistent in exploring and obtaining data about the wide range of materials available in the databases, computational methods are valuable. Though compared to experiments, the computational methods are cheaper, rigorous high fidelity molecular simulations especially those involving predicting properties from ab-initio first principles using quantum mechanical models such as Density Functional Theory (DFT) [85] can be computationally expensive. However, there are other computationally lesser expensive molecular simulation methods such as molecular dynamics, Monte Carlo simulations which include some of the values of parameters such as partial atomic charges from ab-initio models and experiments to make the simulations computationally more tractable.

For instance, for obtaining the equilibrium gas adsorption loading for gases such as CO_2, N_2 and CH_4 on pure silica zeolites considered in this work, Grand Canonical Monte Carlo (GCMC) simulations are employed. Openly available molecular simulation packages such as `RASPA` [86] which has been previously employed for a variety of molecular simulation studies can be used to perform the GCMC simulations [87] to determine pure component equilibrium loadings on nanoporous materials. The simulations are performed in a grand canonical ensemble (μVT) where exchange of energy and molecules between a fixed volume V of a system (adsorbent framework) and reservoir (bulk gas) is allowed at constant chemical potential μ and temperature T. From a reservoir containing molecules of gas, insertion and deletion moves of gas molecules into or from the adsorbent framework is performed. Within the adsorbent framework, appropriate translation and rotation moves of the gas molecules are performed. The difference in total energy of the system

after performing these moves is calculated to determine the acceptance probability of the moves. Coulombic and Van der Waals interactions between the adsorbate and the adsorbent molecules are considered to obtain the interaction energies. Equilibrium is assumed to be attained when the gas in the reservoir and the gas in the framework have the same chemical potential. The chemical potential is related to the system pressure using an appropriate equation of state. The number of molecules inside the framework at equilibrium is then used to calculate the equilibrium adsorption loading. Other metrics such as the density of the adsorbent, isoteric heat of adsorption, Henry co-efficients and binary gas selectivities are also obtained using the `RASPA` package.

The GCMC simulation results for CH_4 on two silicalite (MFI) structures from van Koningsveld *et al.* [88] and IZA-SC database [78] are compared with experimental data on silicalite (MFI) from Zhu *et al.* [89]. There is a good agreement with experimental data at pressures less than 1 bar for both the structures, but there is some deviation at higher pressures for both structures which could be due to differences in the void fraction, density and other structural features in the silicalite crystals used. For N_2, the simulation results for the MFI framework atom positions from van Koningsveld *et al.* [88] are in good agreement with the simulation results (for the same atom positions) and the experimental results in Watanabe *et al.* [90] shown in Fig. 2.1. The results for atom positions from the MFI structure in the IZA-SC database used in this work, is also shown in Fig. 2.1 for the sake of completeness.

2.1.2.2 Constructing Models from Material Data

For use of the data on material metrics collected through molecular simulations or through experiments in the optimization formulation of the multi-scale framework, it is important to develop analytical models which represent the data. This is necessary to predict the values of the material properties in the intermediate ranges between sampled data points where original data is not available. Appropriate models with tunable parameters which include insights about the mechanism of the phenomena to which the data pertain to are employed. Some examples of such models such as reaction rate expressions and adsorption isotherms expressions which are used to model gas reaction and gas adsorption data which include functional forms describing the general characteristics

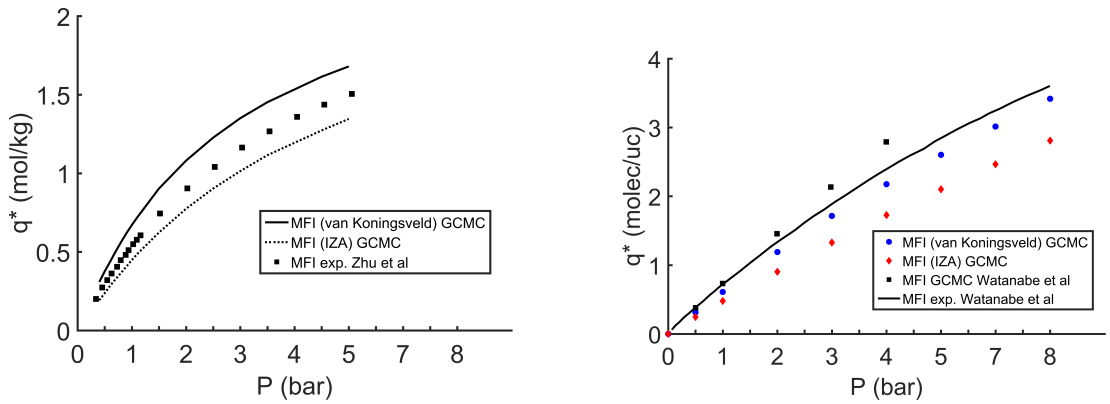

(a) CH_4 (b) N_2

Figure 2.1: Validation of GCMC simulation results with experimental data for CH_4 and N_2 on zeolite MFI (a) Validation of GCMC simulation results obtained for silicalite atom positions from van Koningsveld *et al.* [88] and from the IZA-SC database with experimental data for CH_4 on silicalite (MFI) at 303 K from Zhu *et al.* [89] (b) Validation of GCMC results obtained for two silicalite atom positions from van Koningsveld *et al.* [88] and from the IZA-SC database with experimental data and simulation results (van Koningsveld) for N_2 on silicalite (MFI) at 298 K from Watanabe *et al.* [90] (Iyer *et al.* [77]).

of the reaction and adsorption phenomena for different catalyst and adsorbents. The tunable parameters in the model are obtained by fitting the model to the data obtained for the specific catalyst or adsorbent.

For instance, the methodology for obtaining parameters for the Langmuir adsorption isotherm to describe the data obtained from GCMC simulations is described below. The adsorption isotherm model parameters $q^s_{i,s}$, $b^0_{i,s}$ and $\Delta U_{i,s}$ which comprise the material property vector $\boldsymbol{\beta}$ are obtained by fitting the pure component equilibrium adsorption data obtained from the above molecular simulations to a single component Langmuir adsorption isotherm model. The respective adsorption data for each gas-zeolite pair is fitted to a pure component dual site Langmuir adsorption isotherm model. The appropriate isotherm parameters are obtained by performing minimization of the least square error between the data and the model. The resulting optimization problem described in

eq. 2.3 is solved to global optimality using ANTIGONE [91].

$$
\begin{aligned}
\underset{b^0,\Delta U,q^s}{\text{Min.}} \quad & \sum_k \left(q_{i,n} - \hat{q_{i,n}}\right)^2 && \text{(Objective)} \\
\textit{s.t.} \quad & \hat{q_{i,n}} = \sum_{s \in S} \frac{q^s_{i,s} b^0_{i,s} e^{-\frac{\Delta U_{i,s}}{RT_n}} c_{i,n}}{1 + b^0_{i,s} e^{-\frac{\Delta U_{i,s}}{RT_n}} c_{i,n}} && \text{(Dual site Langmuir Isotherm Model)} \\
& c_{i,n} = \frac{y_i P_n}{RT_n} && \text{(Ideal Gas Assumption)} \\
& \left.\begin{aligned} b^0_{i,s} &\in [b^{0\,L}_{i,s}, b^{0\,U}_{i,s}] \\ q^s_{i,s} &\in [q^{s\,L}_{i,s}, q^{s\,U}_{i,s}] \\ \Delta U_{i,s} &\in [\Delta U^L_{i,s}, \Delta U^U_{i,s}] \end{aligned}\right\} && \text{(Bounds)}
\end{aligned}
\tag{2.4}
$$

where $q_{i,n}$ and $\hat{q_{i,n}}$ are the data and model prediction respectively for data point n, $q^s_{i,s}$ is the saturation capacity parameter in the dual site Langmuir isotherm. The isotherm model along with the corresponding parameters pertaining to the choice of the material is then incorporated in the overall process model. The GCMC simulation data fitted to a dual site Langmuir isotherm for zeolite LTA is shown in Fig. 2.2.

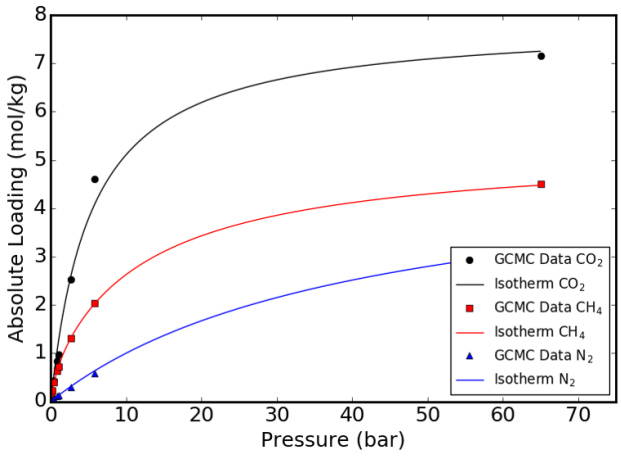

Figure 2.2: Dual-site Langmuir adsorption isotherm model fitted to data from GCMC simulations for zeolite LTA at 298 K (Iyer *et al.* [77]).

2.1.3 Connecting Material Model Parameters with Processes

The material-centric process parameters ($\boldsymbol{\gamma}$) establish the connection between the process state variables $\boldsymbol{\alpha}$ and material property parameters $\boldsymbol{\beta}$ of the optimization formulation. These relations are used to calculate the values of material-centric properties such as equilibrium adsorption loading of individual gases in a mixture, mass transfer coefficients, catalyst effectiveness factor at the values of the pressure, temperatures, compositions, velocities at different locations and time inside the process equipment. Some examples of such relations are provided below. An extended dual site Langmuir isotherm model (eq. 2.5) which has been tested in literature [92] to predict mixture adsorption can be employed to model the equilibrium adsorption loadings q_i^* at different pressures, temperatures and compositions of a multi-component gas mixture based on isotherm parameters fitted to individual pure component gas data. This data can be either obtained from experiments or by performing molecular simulations as discussed before.

$$q_i^* = \sum_{s \in S} \frac{q_{i,s}^s b_{i,s} \frac{y_i P}{RT}}{1 + \sum_{i \in I} b_{i,s} \frac{y_i P}{RT}} \quad \forall i \in I \tag{2.5}$$

where $b_{i,s} = b_{i,s}^0 e^{-\Delta U_{i,s}/RT}$ and I is the set of gases in the mixture. The lumped mass transfer co-efficient k_i describing the rate of adsorption of gas i into the adsorbent is given by eq. 2.6.

$$k_i = \frac{15\,\varepsilon_p D_p c_i}{q_i^* r_p^2} \quad \forall i \in I \tag{2.6}$$

where ε_p is the particle voidage, $D_p \left(= \frac{D_m}{\tau'}\right)$ is the macropore diffusivity, $c_i = \frac{y_i P}{RT}$, D_m is the molecular diffusivity, q_i^* is the equilibrium saturation capacity of gas species i on the adsorbent and r_p and τ' are the particle radius and the tortuosity of the adsorbent respectively.

These relations act as a bridge between the phenomena at the micro and macro scales at the material level which influence the averaged bulk properties and performance metrics at the process level. When applied in an optimization framework such as this one, these are instrumental in determining the target material properties necessary to optimize process objectives.

3. APPLICATION TO COMBINED NATURAL GAS SEPARATION AND STORAGE*

3.1 Key Contributions

Natural gas, the primary component of which is methane (CH_4), is the fastest growing fossil fuel source. It is set to account for almost 25% of the total primary energy consumption by 2035 [93]. To meet future demands, it will be necessary to tap into unconventional methane sources such as coal-bed methane, biogas and landfill gas. However, these sources contain varying levels of impurities which must be separated out in order to obtain fuel and pipeline grade CH_4. Some sources of natural gas are uneconomical to develop due to high impurity content which can be as high as 70% [1]. Moreover, a large number of untapped sources are smaller in capacity and are distributed over a wide area. For utilization of CH_4 from these sources, either access to existing separation infrastructure needs to be provided *via* pipelines or new infrastructure needs to be constructed. After separation, the CH_4 has to be then transported to the consumers through pipelines or LNG tankers. Both laying of pipelines and new infrastructure construction can be capital intensive for small and distributed sources where economies of scale cannot be realized. For such sources, cheaper and modular technologies with smaller footprints can be potential candidates. The cost of such modular units can be reduced by mass production. These can then be deployed to utilize small and remote sources of CH_4. Process intensification [3, 94–96] can enable development of such technologies by merging two or more tasks (eg., separation and storage) in a single unit or module to reduce the cost and/or footprint.

Major impurities which need to be separated from methane sources CO_2, N_2, H_2O, H_2S and mercaptans [68, 97, 98]. For the unconventional sources such as coal-bed methane gas, biogas and landfill gas, the CO_2 percentages can be between 25-60% [1]. About 16% of known gas reserves in the US contain high amounts of N_2 [99, 100]. The potential use of nitrogen as an energizer for

*Parts of this section reproduced in part with permission from Iyer, S. S., Demirel, S. E. and Hasan, M. M. F., "Combined Natural Gas Separation and Storage Based on in Silico Material Screening and Process Optimization" *Industrial & Engineering Chemistry Research*, 57 (49), 16727-16750. Copyright 2018 American Chemical Society. Available at `https://pubs.acs.org/doi/10.1021/acs.iecr.8b02690`

hydraulic fracturing applications would also increase the N_2 content in the natural gas [101]. For the separation of impurities from CH_4 especially from low capacity sources, pressure swing adsorption (PSA) [102, 103] is a promising technology which is based on the preferential adsorption of a gas from a mixture using a nanoporous material (e.g., zeolites, metal-organic frameworks). These materials have preferential gas adsorption and gas storage properties due to their unique pore structure and large internal surface area. There is also abundant literature on the modeling and optimization of PSA processes for applications such as CO_2 capture, CH_4 separation, H_2 purification [9, 26, 44, 104]. These pressure swing adsorption processes involve excursions in pressure in every operating cycle. The cumulative energy consumption from well to wheel adds up due to the operation of compressors and vacuum pumps necessary to effect these periodic pressure changes.

There has also been significant research in methane storage applications using nanoporous materials due to increased interest in adsorbent natural gas (ANG) systems over compressed natural gas systems (CNG) for vehicular applications. ANG systems operate at a lower pressure than CNG thus posing lesser risk, allowing increased cargo space through use of conformable tanks and enabling lower refueling cost [105]. However, the low energy density of natural gas compared to gasoline and the need for on-board storage space may limit the driving range [106]. In order to offset these challenges, the Advanced Research Project Agency-Energy (ARPA-E) set a target of 315 v (STP)/v for CH_4 deliverable capacity in ANG systems based on economic competitiveness with CNG [36]. This target has not yet been achieved but nanoporous materials such as zeolites, metal-organic frameworks (MOFs) and carbon-based materials are promising candidates. High-throughput *in silico* screening methods have been proposed to determine the best materials and performance limits for CH_4 storage [36, 45, 48, 52].

Though there is significant literature on screening and discovery of nanoporous materials for individual CH_4 storage and CH_4 separation [1, 43, 44] applications, intensification of both separation and storage together poses significant challenges. Materials which demonstrate high selectivity for CH_4 may not have a high storage capacity for CH_4. Similarly, materials which have a high storage capacity for CH_4 may not demonstrate high selectivity for CH_4. Thus finding materials which lead

to both high CH_4 purity and high CH_4 storage simultaneously poses a significant challenge [107]. In addition, the process conditions and the feed composition of the gas to be separated can influence process and material performance. For example, the increased presence of more strongly adsorbing gases than CH_4 such as CO_2 in the feed mixture can adversely affect both CH_4 storage and purity.

Since decisions at different scales can affect the overall process performance, consideration of process insights into material screening can be important to effectively screen for the desired materials. For instance, for the intensification of CH_4 separation and storage using micro-porous materials, the variations in the gas selectivity and storage properties among different material choices will affect the corresponding process operating conditions for optimal performance.

The aim of the current work is to intensify CH_4 separation and storage tasks by exploiting both the multifunctional properties of adsorbent materials and operating conditions of the process. Conventional zeolites have low CH_4 deliverable capacities around 100 v/v [106], however, considering their low cost, good thermal stabilities and their widespread use in current industrial applications [108], in this work the focus is on zeolites for intensification of both separation and storage activities. To address the technical challenges described previously, a combined separation and storage process is developed with the following features:

- Separation of CH_4 from impurities from unconventional feedstocks and its storage within a smaller footprint in terms of energy and equipment.
- Simultaneous separation and storage of CH_4 from a CH_4/N_2 feed mixture in a modular column unit.
- Elimination of periodic pressure/temperature changes in process operation.
- Use of top materials based on process optimization.

In section 3.2, a description of the combined separation and storage (CSS) process designed in this work is provided. In section 3.3, a multi-scale optimization formulation describing both material and process scales of the CSS process is described. Further, in that section, the conservation

equations describing the process model and details about Grand Canonical Monte Carlo (GCMC) simulations performed to obtain gas-material properties are described. In Section 3.4, the multi-scale optimization formulation containing derivative and integral terms described in Section 3.3 is converted to an algebraic formulation and posed as a non-linear programming problem. Subsequently, in section 3.5, the NLP optimization problem is solved to determine the maximum CH_4 storage using the CSS process for different binary CH_4/N_2 feed compositions. Top zeolites are ranked based on maximum CH_4 storage capacity (v (STP)/v) obtained for different N_2 contents in the natural gas feed subject to CH_4 purity $\geq 90\%$ and CH_4 loss $\leq 10\%$. In section 3.6, the maps of variation in process feasibility and violation of process constraints with changes in material properties are provided and discussed. The effect of a small amount (3%) of a strongly adsorbing gas like CO_2 in feed is also investigated. Summarizing remarks are presented in section 3.7.

3.2 Combined Separation and Storage (CSS)

For lower capacity stranded methane sources, cryogenic distillation for N_2 separation is not cost-effective [16]. Alternative technologies such as membrane separation and pressure swing adsorption using solid adsorbents are more attractive for such sources. In a typical pressure swing adsorption application, for example, in the case of CH_4/N_2 separation, CH_4 at high pressure is fed to a column filled with an adsorbent kinetically selective towards N_2. This results in separation of N_2 from the mixture and a high pressure CH_4 product is obtained. The adsorbent in the column is then regenerated by de-pressurizing and purging the column to remove N_2 at a lower pressure. The column can then be used again for further separation in the next cycle. Similarly, for the case of CH_4/CO_2 separation which happens in the guard bed, CO_2 gets selectively adsorbed by the adsorbent at high pressure, while an almost CO_2 free feed exits the column. The column saturated with CO_2 is then desorbed at a much lower pressure to regenerate the column. The higher affinity of CO_2 to zeolites requires the use of much lower pressure that that needed for CH_4/N_2 separation. The cumulative energy consumption incurred in a cycle increases due to the periodic need for pressurization and de-pressurization resulting in higher operating cost.

The combined separation and storage process attempts to intensify the separation and storage

operations involved in CH_4 processing by leveraging the multifunctional properties of nanoporous materials such as zeolites. It aims to eliminate the need for periodic swings in pressure to separate and store CH_4 and N_2 by optimal choice of both materials and process conditions to ensure acceptable performance. The proposed overall supply chain of an application for the combined separation and storage process technology is depicted in Fig. 3.1. It involves a processing and filling station where a methane rich feed is separated off CO_2 and then the resultant gas rich in CH_4 and N_2 is simultaneously separated and stored in modular column units/canisters. It is also assumed that H_2O and toxic sulfur containing impurities such as H_2S and mercaptons are separated from the gas mixture upstream before being fed to the CSS process. After the storage of CH_4, the column module is then transported to end users for use in applications such as ANG systems or sent to a central facility for further processing. After the depletion of CH_4 in the column at the end user, it could be transported back to the closest CSS facility to be refilled again. This is most useful for small and distant unconventional feed sources where conventional asset investment such as plant and pipeline infrastructure would be uneconomical due to lower volumes than necessary to reach economies of scale.

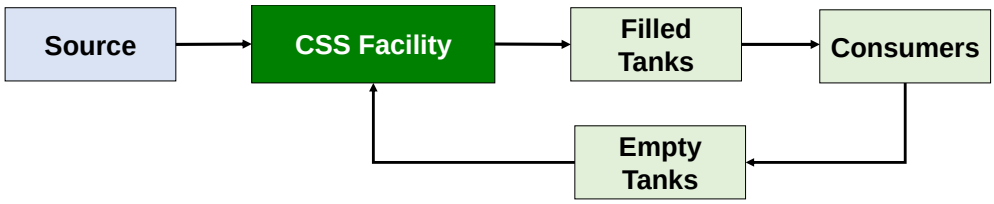

Figure 3.1: Potential supply chain of the combined separation and storage (CSS) process. The modular column units filled with CH_4 separated from stranded and small unconventional feedstocks can be transported to the end user or to a centralized facility for further processing (Iyer *et al.* [77]).

The key equipment employed in the combined separation and storage (CSS) technology consists of modular adsorption columns filled with nanoporous materials such as zeolites. Since CO_2 has a stronger affinity to most zeolites, compared to CH_4 and N_2, it must be separated in advance

to enable simultaneous separation and storage of CH_4 from the resulting CH_4/N_2 mixture. For this purpose, the feed is first introduced through a guard bed (Fig. 3.2) containing a CO_2 selective zeolite to separate CO_2 using a conventional PSA process. This results in a binary feed mixture primarily comprising of CH_4 and N_2.

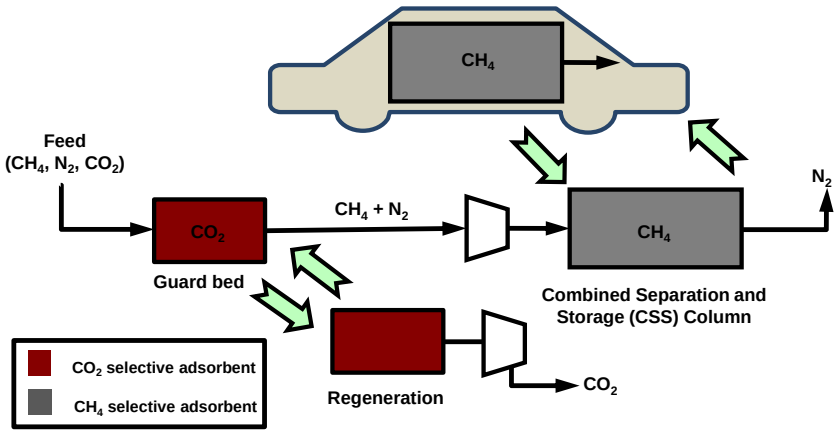

Figure 3.2: Equipment needed for the combined separation and storage (CSS) of CH_4. These include a guard bed with a CO_2 selective adsorbent to remove most of the CO_2 and a CSS column filled with a CH_4 selective adsorbent to enable combined separation and storage of CH_4 and N_2 (Iyer *et al.* [77]).

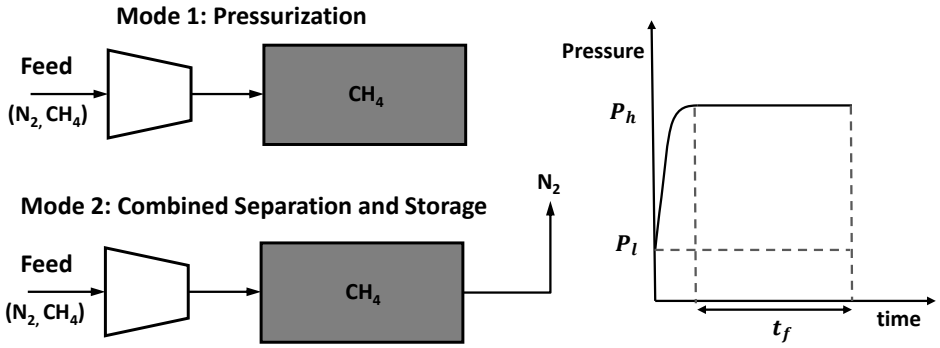

Figure 3.3: Schematic of the combined separation and storage (CSS) process. (a) Pressurization mode is used to raise the pressure of the column to the desired filling pressure. (b) Combined separation and storage (CSS) mode of the process involves simultaneous storage of CH_4 and separation of N_2 through the exit of the column (Iyer *et al.* [77]).

This outlet gas from the guard bed becomes the feed for the combined separation and storage (CSS) process which employs a column filled with a CH_4 selective adsorbent. The column used in this case is one that has returned to the facility for refueling after being depleted of CH_4. The process operates in two modes as shown in Fig. 3.3. In the pressurization mode, the depleted column is first pressurized with a feed gas (CH_4 and N_2) to a certain optimum filling pressure while keeping the other end of the column closed. After this, the equipment is switched to a combined separation and storage (CSS) mode where the same feed gas is fed to the column at the filling pressure with the other end of the column kept open. The gas exiting the column from this end can contain both the impurity N_2 and the desired gas CH_4. This mode is continued till either the column is saturated with CH_4 or the amount of CH_4 exiting the column reaches a certain limit. The goal of the process design is to choose an appropriate CH_4 selective material and determine the process operating conditions which maximize the total CH_4 stored from the gas mixture while ensuring that the purity of stored CH_4 and the losses of CH_4 through the outlet are within acceptable limits. Switching the equipment configuration between pressurization and CSS modes does not have to happen for every column processed. Rather the equipment operation could be switched to one mode or the other for processing a number of columns at once. While a pressure swing adsorption cycle is needed for CO_2 separation using the guard bed, the CSS process avoids the need for periodic swings in pressure to separate and store CH_4 leading to energy savings (Fig. 3.4). Note that the additional energy cost incurred in the transportation of the columns by the end user to and from the facility is not considered in this work.

3.3 Multiscale Optimization for CSS

To design the combined separation and storage (CSS) process, *i.e.* selecting process conditions and materials such that the amount of CH_4 stored in the column is maximized while meeting limits on maximum acceptable CH_4 loss and minimum acceptable CH_4 purity, it is necessary to formulate an appropriate optimization problem. Such a formulation will also enable evaluating the feasibility and effectiveness of the process for changes in feed and process conditions. The nonlinear algebraic partial differential equation (NAPDE) process and materials optimization formulation for the

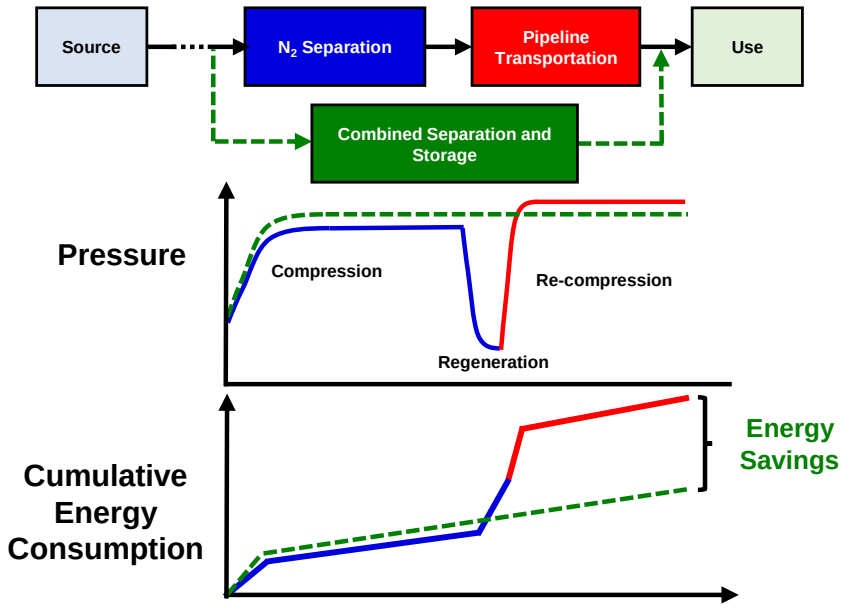

Figure 3.4: Key process intensification idea behind the CSS process. The process attempts to intensify the separation and storage aspects of the conventional supply chain for N_2 separation from CH_4 and adapt them for the utilization of unconventional methane feedstocks. The operation of the CSS process eliminates energy intensive recurrent pressure changes involved in conventional pressure swing processes (Iyer *et al.* [77]).

CSS process based on the general formulation in eq. 2.1 is shown in eq. 3.1.

$$\min_{\mathbf{X}} \quad \int_z f(\mathbf{X}, \boldsymbol{\alpha}|_{t=t_f})\, dz \qquad \text{(Objective Function)} \qquad (3.1a)$$

s.t.

$$\left.\begin{aligned} & h^{CE}(\mathbf{X}, \boldsymbol{\alpha}, \tfrac{\partial \boldsymbol{\alpha}}{\partial t}, \tfrac{\partial \boldsymbol{\alpha}}{\partial z}, \tfrac{\partial^2 \boldsymbol{\alpha}}{\partial z^2}, \boldsymbol{\gamma}) = 0 \\ & h^{BC}(\mathbf{X}, \boldsymbol{\alpha}, \tfrac{\partial \boldsymbol{\alpha}}{\partial z}\big|_{z=0}, \tfrac{\partial \boldsymbol{\alpha}}{\partial z}\big|_{z=L}) = 0 \\ & h^{IC}\big(\mathbf{X}, \boldsymbol{\alpha}|_{t=0}\big) = 0 \end{aligned}\right\} \qquad \text{(Process Model)} \qquad (3.1b)$$

$$\left.\begin{aligned} & \textstyle\int_z g(\mathbf{X}, \boldsymbol{\alpha}|_{t=0}, \boldsymbol{\alpha}|_{t=t_f})\, dz \le 0 \\ & \textstyle\int_t g(\mathbf{X}, \boldsymbol{\alpha}|_{z=0}, \boldsymbol{\alpha}|_{z=L})\, dt \le 0 \end{aligned}\right\} \qquad \text{(Process Performance Constraints)} \qquad (3.1c)$$

$$h^{MP}(\boldsymbol{\alpha}, \boldsymbol{\beta}, \boldsymbol{\gamma}) = 0 \qquad \text{(Material-Process Connectivity Model)} \qquad (3.1d)$$

$$h^M(\boldsymbol{\delta}, \boldsymbol{\beta}) = 0 \qquad \text{(Material Structure-Property Model)} \qquad (3.1e)$$

$$\mathbf{X} \in [\mathbf{X}^L, \mathbf{X}^U] \subseteq \mathbb{R}^d \qquad \text{(Decision Variable Bounds)} \qquad (3.1f)$$

In the optimization formulation of Eq. 3.1, $\boldsymbol{\alpha}$ is vector of process state variables such as gas (y_i) and adsorbent (q_i) phase composition of each gas species i, pressure (P), gas temperature (T) and the column wall temperature (T_w) at each spatial (axial) (z) and temporal (t) co-ordinate. $\boldsymbol{\beta}$ includes material properties such as adsorption isotherm parameters for each gas species, $\boldsymbol{\gamma}$ denotes a vector of material-centric process parameters used in this work such as heat of adsorption (ΔH_i) for a gas species at a given temperature, equilibrium adsorption loading (q_i^*) at different pressures, temperatures and compositions, lumped mass transfer co-efficient (k_i) for each gas species i while $\mathbf{X}$ is the d-dimensional vector of d CSS process design variables considered (filling pressure P_h, duration of operation of CSS mode t_f, feed velocity v_f). $\mathbf{X}^L$ and $\mathbf{X}^U$ are the lower and upper bounds on the process decision variables respectively. $\int_z f(\mathbf{X}, \boldsymbol{\alpha}|_{t=t_f})\, dz$ is the objective function to be optimized which in the case of the CSS process is the amount of CH_4 stored in the column at the end of process operation. $h^{CE}(\mathbf{X}, \boldsymbol{\alpha}, \frac{\partial \boldsymbol{\alpha}}{\partial t}, \frac{\partial \boldsymbol{\alpha}}{\partial z}, \frac{\partial^2 \boldsymbol{\alpha}}{\partial z^2}, \boldsymbol{\gamma}) = 0$ describes the relations involving spatial and temporal derivatives pertaining to the mass, energy and momentum conservation terms along with the auxiliary equations regarding the parameters involved in them. $h^{BC}(\mathbf{X}, \boldsymbol{\alpha}, \frac{\partial \boldsymbol{\alpha}}{\partial z}\big|_{z=0}, \frac{\partial \boldsymbol{\alpha}}{\partial z}\big|_{z=L}) = 0$ and $h^{IC}\big(\mathbf{X}, \boldsymbol{\alpha}|_{t=0}\big) = 0$ describe the boundary conditions at the ends of the column and the initial column conditions at the start of the process respectively. $\int_z g(\mathbf{X}, \boldsymbol{\alpha}|_{t=0}, \boldsymbol{\alpha}|_{t=t_f})\, dz \leq 0$ and $\int_t g(\mathbf{X}, \boldsymbol{\alpha}|_{z=0}, \boldsymbol{\alpha}|_{z=L})\, dt \leq 0$ represent the CSS process performance constraints, namely, purity of CH_4 stored in the column at the end of the process and the percentage of the CH_4 lost through the column outlet over the course of the process, respectively. $h^{MP}(\boldsymbol{\alpha}, \boldsymbol{\beta}, \boldsymbol{\gamma})$ includes equations connecting material properties such as adsorption isotherm parameters with the process state variables to obtain the equilibrium adsorption loadings, heat of adsorption values and lumped mass transfer co-efficients corresponding to different state variables. $h^M(\boldsymbol{\delta}, \boldsymbol{\beta})$ relates the structural characteristics $\boldsymbol{\delta}$ of the material such as density, void fraction, pore size distribution and crystal structure etc. with the material properties (e.g. adsorption isotherm

parameters).

3.3.1 Objective Function

The objective function $\int_z f(\mathbf{X}, \boldsymbol{\alpha}|_{t=t_f})\, dz$ in the above multi-scale modeling and optimization problem is set as the amount of CH_4 stored in the column at the end of the process. This is calculated by integrating the values of the state variables ($\boldsymbol{\alpha}$) at the end of the process ($t = t_f$) over the length (z) of the column. The total number of moles of gas stored n_{i,t_f} in the column at the end of the CSS time is calculated as shown in eq. 3.2, where y_i, P, T and q_i are the gas phase mole fraction, column pressure and temperature and the adsorption loading respectively, R is the universal gas constant, ρ_s is the density of the adsorbent, A is the column cross-sectional area, L is the length of the column and ε is the void fraction of the column. The total moles of gas stored n_{i,t_f} includes both the species i present in the gaseous phase and adsorbed phase inside the column at the end of the process. It is important to note values of the state variables (y_i, P, T and q_i) at the end of the process *i.e.* $t = t_f$ can only be calculated after solving the complete model of the process.

$$n_{t_f,i} = \int_0^L f(\mathbf{X}, \boldsymbol{\alpha}|_{t=t_f})\, dz = \int_0^L \left(\frac{\varepsilon A y_i(t) P(t)}{RT(t)} + (1-\varepsilon) A \rho_s q_i(t) \right) dz \quad i = CH_4,\, t = t_f \tag{3.2}$$

Thus the objective function $\int_0^L f(\mathbf{X}, \boldsymbol{\alpha}|_{t=t_f})\, dz$, depends on the process design variables $\boldsymbol{X} = \{P_h, v_f, t_f\}$ and the process state variable $\boldsymbol{\alpha} = \{y_i, q_i, P, T, T_w\}$ values at the end of the process.

3.3.2 Process Model

As discussed in Section 3.2, the process operates in two modes: (a) pressurization and (b) combined separation and storage (CSS) mode. During the pressurization mode, there is no gas exiting the column. The pressure increase is achieved by feeding gas to the column, the other end of which is shut. Next step after this is operation under the combined separation and storage (CSS) mode. There can however be a delay between when a column undergoes the pressurization and the CSS step. Hence, it would be a reasonable assumption that the gas in the column before the start of the

CSS mode is assumed to be in equilibrium with the adsorbent. An equilibrium-based model can be used to calculate the conditions in the column at this juncture.

For operation under the subsequent combined separation and storage (CSS) mode, the other end of the column is now opened to allow the impurity (N_2) to exit the column. However, it is possible that along with N_2, some CH_4 also exits the column. Hence, the CH_4 losses through the column outlet need to be tracked, requiring the extension of a simple equilibrium based model into a rigorous dynamic model.

The comparison between use of a simple equilibrium based dynamic model and a rigorous dynamic model incorporating mass transfer, convection and dispersion effects along the column is shown in Fig. 3.5. The simpler equilibrium based model considers the column as a lumped system with the solid adsorbent attaining instantaneous equilibrium on contact with gas. On introduction of feed gas to a column which is saturated with an initial composition of gas, the redistribution of gas between the gas and the adsorbed phase takes place due to a mass transfer driving force. If mass transfer limitations are not considered, as in the equilibrium model, the adsorbent can be assumed to reach instantaneous equilibrium with the incoming feed gas. The part of the column which has not yet come in contact with the incoming feed gas, however, is still at equilibrium at the initial composition. The equilibrium model thus predicts a sharp transition between two zones of the column, one with adsorbent in equilibrium with the feed composition and another zone in equilibrium with the initial composition. This subsequently results in a sharp transition in the outlet gas composition profile of the column obtained from the equilibrium-based model at $t = 34.58$ s for the case shown in Fig. 3.5. When mass transfer limitations are considered along the bed, there is a transition zone called mass transfer zone (MTZ) between the above two equilibrium zones where the gas compositions vary from the feed to the initial composition. This is also reflected as a smoother transition in the outlet composition profile for the rigorous model in Fig. 3.5. The details regarding the calculation of the outlet composition profile using the equilibrium model is provided in Appendix A. As observed from Fig. 3.5, though the equilibrium based model can approximate the profile, there can be considerable overestimation or underestimation in the calculation of the

moles of gas exiting the column outlet based on the profile. The rigorous dynamic model is thus required to calculate the exact loss of CH_4 through the outlet of the column with time, so that the operation could be halted before the loss reaches the specified limit.

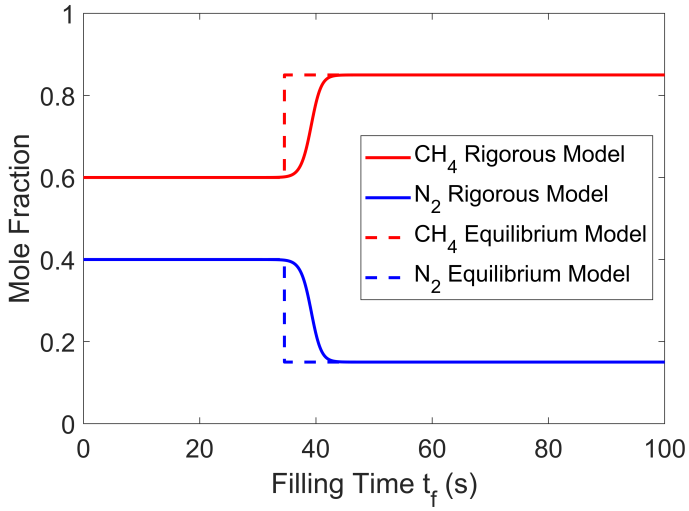

Figure 3.5: Comparison of the mole fraction profiles with time for the gas exiting the column module during operation under CSS mode obtained using an equilibrium-based dynamic model with a rigorous dynamic model. It can be observed that there is a deviation in the profiles in the region between $t_f = 30$ s to $t_f = 45$ s, which leads to an appreciable difference in the calculation of the number moles of gas exiting the column. The transition in the compositions using the equilibrium-based model occurs at 34.58 s. Profiles are obtained for gas of feed composition 85% CH_4/15% N_2 fed to a column with adsorbent (AFY) initially in equilibrium with gas of composition 60% CH_4/40% N_2. Column Presssure $P_h = 65$ bar, feed velocity $v_f = 0.1$ m/s (Iyer *et al.* [77]).

For the calculation of the desired objective and process performance metrics such as CH_4 storage, purity and loss, the values of the state variables $\boldsymbol{\alpha}$ along both spatial (axial) and temporal co-ordinates are required. Hence a one-dimensional dynamic model is needed to model the adsorption of gas into the adsorbent in the column during the CSS mode of the process.

3.3.2.1 Conservation Equations: $h^{CE}(\mathbf{X}, \boldsymbol{\alpha}, \frac{\partial \boldsymbol{\alpha}}{\partial t}, \frac{\partial \boldsymbol{\alpha}}{\partial z}, \frac{\partial^2 \boldsymbol{\alpha}}{\partial z^2}, \boldsymbol{\gamma}) = 0$

The major assumptions made in the dynamic model [80, 81, 109, 110] are ideal gas behavior, absence of gradients in the radial direction, axial dispersion, instant establishment of equilibrium

between the gas and the solid adsorbent and absence of any chemical reaction between gas species. Details about validation of the dynamic model with adsorption and reaction systems can be found in Arora *et al.* [80]. Mass transfer into the adsorbent is assumed to be controlled by molecular diffusion into the macropores and is represented by a lumped linear driving force (LDF) formulation which is found to work well in practice [111]. Extended Langmuir model [92] which has been tested in literature to model the equilibrium adsorption of the gas mixture based on single-component adsorption isotherms is employed. Based on the above assumptions, the equations which describe the mass and energy balances, pressure drop effects, mass transfer driving force relation, and other auxiliary relations used to model the CSS process are given below.

Component Mass Balance:

$$\frac{\partial y_i}{\partial t} = \frac{y_i}{T}\frac{\partial T}{\partial t} - \frac{y_i}{P}\frac{\partial P}{\partial t} + \frac{T}{P}D_L\frac{\partial}{\partial z}\left(\frac{P}{T}\frac{\partial y_i}{\partial z}\right) - \frac{T}{P}\frac{\partial}{\partial z}\left(\frac{y_i P v}{T}\right) - \frac{RT}{P}\frac{(1-\varepsilon)}{\varepsilon}\frac{\partial q_i}{\partial t} \qquad \forall i \in I \quad (3.3)$$

Overall Mass Balance:

$$\frac{\partial P}{\partial t} = \frac{P}{T}\frac{\partial T}{\partial t} - T\frac{\partial}{\partial z}\Big(\frac{Pv}{T}\Big) - RT\frac{(1-\varepsilon)}{\varepsilon}\sum_{i\in I}\frac{\partial q_i}{\partial t} \quad (3.4)$$

Energy Balance inside the Column:

$$\begin{aligned}(1-\varepsilon)\left(\rho_s C_{p,s} + C_{p,a}\sum_{i\in I} q_i\right)\frac{\partial T}{\partial t} = K_z\frac{\partial^2 T}{\partial z^2} - \frac{2\,h_i}{r_i}(T - T_w) \quad (3.5)\\ + (1-\varepsilon)\sum_{i\in I}(-\Delta H_i)\,\frac{\partial q_i}{\partial t} - \frac{\varepsilon C_{p,g}}{R}\frac{\partial P}{\partial t} - \frac{\varepsilon C_{p,g}}{R}\frac{\partial (Pv)}{\partial z}\\ - (1-\varepsilon)C_{p,a}T\sum_{i\in I}\frac{\partial q_i}{\partial t}\end{aligned}$$

Energy balance across the column wall:

$$\rho_w C_{p,w}\frac{\partial T_w}{\partial t} = K_w\frac{\partial^2 T_w}{\partial z^2} + \frac{2\,r_i h_i}{(r_o^2 - r_i^2)}\,(T - T_w) - \frac{2\,r_o h_o}{(r_o^2 - r_i^2)}\,(T_w - T_a) \quad (3.6)$$

Momentum Balance (Darcy's Law) :

$$\frac{\partial P}{\partial z} = -\frac{150\,\mu v}{4\,r_p^2}\left(\frac{1-\varepsilon}{\varepsilon}\right)^2 \tag{3.7}$$

Linear Driving Force Model:

$$\frac{\partial q_i}{\partial t} = k_i(q_i^* - q_i) \quad \forall i \in I \tag{3.8}$$

Axial Dispersion Co-efficient:

$$D_L = 0.7\,D_m + v_f r_p \tag{3.9}$$

3.3.2.2 Boundary Conditions: $h^{BC}(\mathbf{X}, \boldsymbol{\alpha}, \frac{\partial \boldsymbol{\alpha}}{\partial z}\big|_{z=0}, \frac{\partial \boldsymbol{\alpha}}{\partial z}\big|_{z=L}) = 0$

For describing different modes of column operation, appropriate boundary conditions need to be specified. For the pressurization mode of the process, a simplified equilibrium model is used as discussed before and no boundary conditions are required. To describe the column behavior in CSS mode, the one-dimensional dynamic model described above is employed along with the Danckwerts boundary conditions [112] for open-open operation as shown in eq. 3.10–3.17. This is because, during the CSS mode, both ends of the column are kept open and feed is fed through one end of the column and the impurities are vented out through the other end.

At column inlet $z = 0$:

$$-D_L\frac{\partial y_i}{\partial z}\bigg|_{z=0} = v|_{z=0}\,(y_{f,i} - y_i|_{z=0}) \qquad \forall i \in I \setminus \{N_I\} \tag{3.10}$$

$$-K_z\frac{\partial T}{\partial z}\bigg|_{z=0} = v|_{z=0}\varepsilon\rho_g Cp_{p,g}\,(T_f - T|_{z=0}) \tag{3.11}$$

$$v|_{z=0} = v_f \tag{3.12}$$

$$T_w|_{z=0} = T_a \tag{3.13}$$

At column inlet $z = L$:

$$\frac{\partial y_i}{\partial z}\bigg|_{z=0} = 0 \qquad \forall i \in I \setminus \{N_I\} \tag{3.14}$$

$$\left.\frac{\partial T}{\partial z}\right|_{z=0} = 0 \tag{3.15}$$

$$P|_{z=L} = P_h \tag{3.16}$$

$$T_w|_{z=0} = T_a \tag{3.17}$$

3.3.2.3 Initial Conditions: $h^{IC}\left(\mathbf{X}, \boldsymbol{\alpha}|_{t=0}\right) = 0$

To capture the effect of initial state of the column on the dynamic response of its state variables, suitable initial conditions need to be specified. The initial conditions at the start of the pressurization mode of the process are the conditions in the column after its depletion at the consumer. The initial conditions for the subsequent combined separation and storage (CSS) mode of the process will be the equilibrium conditions attained long time after the pressurization mode. The calculation of the initial conditions for these modes, is discussed in detail in eq. A.66–A.77 along with the complete optimization model formulation in Appendix A.2.

3.3.3 Process Performance Constraints

The process performance constraints ($\int_z g(\mathbf{X}, \boldsymbol{\alpha}|_{t=0}, \boldsymbol{\alpha}|_{t=t_f})\, dz \leq 0$, $\int_t g(\mathbf{X}, \boldsymbol{\alpha}|_{z=0}, \boldsymbol{\alpha}|_{z=L})\, dt \leq 0$) include the constraints imposed on process performance such as purity of stored CH_4, losses of gases through the vent, etc. to ensure feasibility and effectiveness of the designed process. These can be calculated as described below.

3.3.3.1 CH_4 Purity

The purity of the CH_4 stored in the column at the end of the process can be calculated by taking a ratio of the moles of CH_4 stored in the column over the total moles of all the gas species (eq. 3.18).

$$pur_{CH_4} = \frac{n_{t_f,CH_4}}{\sum_{i\in I} n_{t_f,i}} = \int_0^L \frac{\dfrac{\varepsilon A y_{CH_4}(t) P(t)}{RT(t)} + (1-\varepsilon) A \rho_s q_{CH_4}(t)}{\sum_{i\in I}\left(\dfrac{\varepsilon A y_i(t) P(t)}{RT(t)} + (1-\varepsilon) A \rho_s q_i(t)\right)} dz \qquad t = t_f \tag{3.18}$$

3.3.3.2 CH_4 Loss

This is the ratio of the total amount of CH_4 exiting the column (n_i^{out}) during the process to the total amount of CH_4 fed to the column during the pressurization $n_i^{in,\,press}$ and the combined separation and storage modes $n_i^{in,\,css}$. The calculation of n_i^{out} will require solving the process model for obtaining the values of the state variables (y_i, P, T and q_i) at $z = L$ with time. The calculation of $n_i^{in,\,press}$ based on the equilibrium model assumption (eq. A.69) is discussed in the complete algebraic model formulation in Appendix A.2.

$$l_i = \frac{n_i^{out}}{n_i^{in,\,css} + n_i^{in,\,press}} \quad i = CH_4 \tag{3.19}$$

$$n_i^{out} = \int_0^{t_f} \Big(\frac{\varepsilon Av(t,L)\; y_i(t,L))P(t,L)}{RT(t,L)} \Big) dt \quad i = CH_4 \tag{3.20}$$

$$n_i^{in,\,css} = \int_0^{t_f} \Big(\frac{\varepsilon Av(t,0)\; y_i(t,0))P(t,0)}{RT(t,0)} \Big) dt \quad i = CH_4 \tag{3.21}$$

3.3.4 Material-Process Connectivity Model: $h^{MP}(\boldsymbol{\alpha}, \boldsymbol{\beta}, \boldsymbol{\gamma})$

The process model described in Section 3.3.2 requires material-centric process parameters (γ) such as mass transfer co-efficient for the linear driving force model describing the kinetics of gas adsorption, adsorption equilibrium loading at different pressures and temperatures, heat of adsorption of a gas on an adsorbent. The relations describing the lumped mass transfer co-efficient k_i used in the linear driving force mass transfer relation and those to to predict mixture adsorption at different pressures, temperatures and compositions of a multi-component gas mixture are described in eq. 3.8 and eq. 2.5 respectively. The isosteric heat of adsorption ($q_{st\,i}$) for gas i on adsorbent is obtained by applying the Clausius-Clapeyron equation [113, 114] to the pure component dual site adsorption isotherm. The enthalpy of adsorption is the negative of the isoteric heat of adsorption and is given in eq. 3.22.

$$\Delta H_i = -q_{st\,i} = \frac{q_{i,1}^s b_{i,1}(RT' + b_{i,2}P')^2 \Delta U_{i,1}' + q_{i,2}^s b_{i,2}(RT' + b_{i,1}P')^2 \Delta U_{i,2}'}{q_{i,1}^s b_{i,1}(RT' + b_{i,2}P')^2 + q_{i,2}^s b_{i,2}(RT' + b_{i,1}P')^2} \tag{3.22}$$

where ΔH_i is the adsorption enthalpy of species i on the adsorbent, $P^{'}$ and $T^{'}$ are taken to be 1000 Pa and 298 K respectively, $b_{i,s} = b^0_{i,s} e^{-\frac{\Delta U_{i,s}}{RT^{'}}}$ and $\Delta U^{'}_{i,s} = \Delta U_{i,s} - RT^{'}$.

3.3.5 Material Structure-Property Models for CSS: $h^M(\boldsymbol{\delta}, \boldsymbol{\beta}) = 0$

To perform screening over a number of materials (zeolites), the individual gas-zeolite properties required in this work, namely the pure component adsorption isotherm parameters are obtained through the following molecular simulation and subsequent parameter estimation strategy described below.

3.3.5.1 GCMC Simulation Details

Though there is abundant experimental data for zeolites with different Si/Al ratios and cations for a variety of gases and conditions available in the NIST/ARPA-E Database of Novel and Emerging Adsorbent Materials [115], it was difficult in our experience to find data for all three gases (CO_2, N_2, CH_4) on pure silica frameworks in the IZA-SC database of zeolite structures [78] for a uniform set of conditions. Hence, the equilibrium gas adsorption data is obtained using Grand Canonical Monte Carlo (GCMC) simulations. The simulations are performed to obtain pure component gas-adsorbent equilibrium loading data for gases CO_2, N_2 and CH_4 on zeolites.

The different Leonard-Jones interaction parameters to describe the Van der Waals interactions considered in the simulations are obtained from the Garcia-Perez forcefield [116] for silica zeolites and are listed in Table 3.1 and 3.2. For statistical significance of the results, we use 50000 equilibration and 50000 production cycles [117] for obtaining the properties of interest. Equal probabilities of the individual GCMC moves, namely, translation 20%, rotation 20%, reinsertion 20%, swap *i.e.* insertion and deletion 40% are used [117]. Rotation move is not included for CH_4 due to the use of a united-atom model, while it is considered for CO_2 and N_2 [118] . The void fraction and pore characterization data is obtained from ZEOmics database [119]. We do not consider any blocking of inaccessible pores. A $3 \times 3 \times 3$ unit cell is chosen for the simulations and periodic boundary conditions are employed. For zeolites, with an inappropriate number of unit cells warning, a maximum of $4 \times 4 \times 4$ unit cells is employed. The charges on all Si ($+2.05$)

and O (-1.025) atoms in the zeolite framework is kept constant for all gases and materials and is obtained from the Garcia-Perez forcefield [116].

Table 3.1: Pair-wise Lennard Jones interaction parameters for adsorbate-adsorbate and adsorbate-adsorbent interactions. Lorentz-Berthelot mixing rules are used for other unspecified cross-terms (Iyer *et al.* [77]).

Atom Pair	σ (Å)	ε/k_B (K)	Atom Pair	σ (Å)	ε/k_B (K)
C_{CH_4}-C_{CH_4}	3.72	158.5	C_{CH_4}-O_{zeo}	3.47	115.00
C_{CO_2}-O_{zeo}	2.7815	50.2	O_{CO_2}-O_{zeo}	2.9195	84.93
C_{CO_2}-C_{CO_2}	2.76	28.129	O_{CO_2}-O_{CO_2}	3.033	80.507
C_{CO_2}-O_{CO_2}	2.89	47.59	O_{zeo}-O_{zeo}	2.806	89.6
N_{N_2}-N_{N_2}	3.306	38.30	N_{N_2}–O_{zeo}	3.06	58.25

Table 3.2: Partial charges on the pseudo-atoms of the adsorbate models and the zeolite framework. `com` represents a massless point charge placed at the centre of mass of the molecule (Iyer *et al.* [77]).

Atom	Charge [e^-]	Atom	[e^-]
O_{zeo}	-1.025	Si_{zeo}	+2.05
N_{N_2}	-0.4048	N_{com}	+0.8096
C_{CO_2}	+0.6512	O_{CO_2}	-0.3256

3.4 A Discretization-based NLP Formulation

The aforementioned optimization formulation with terms containing integrals and partial derivatives, has to be converted into a completely algebraic form, in order for it to be solved by invoking existing nonlinear programming (NLP) solvers. This can be achieved by discretizing the partial differential equations in the model describing the CSS process in Section 3.3.2, over both space and time by choosing adequate number of divisions in both domains. This can lead to an approximated but completely algebraic formulation of the optimization model discussed in the previous

section. A finite volume framework [81] is employed to perform the spatial discretization. N_J spatial finite volumes are used along the column and the upwind differencing scheme (UDS) is used to relate the value of the finite volume boundary at $j + 0.5$ with the corresponding value upstream at j e.g. $P_{j+0.5} = P_j$. For calculating the volumes at both the ends of the column, boundary conditions are used. To convert the partial derivatives in time to algebraic equations, an implicit scheme such as a backward Euler scheme is employed. The overall temporal domain is split into $N_K - 1$ time steps, with $k \in K = \{1, 2, .., N_K\}$, where $k = 1$ and $k = N_K$ denotes the initial and final times respectively. It is an unconditionally stable scheme necessary to prevent unrealistically unbounded numerical solutions for stiff systems which involve steep concentration gradients such as those encountered in adsorption applications.

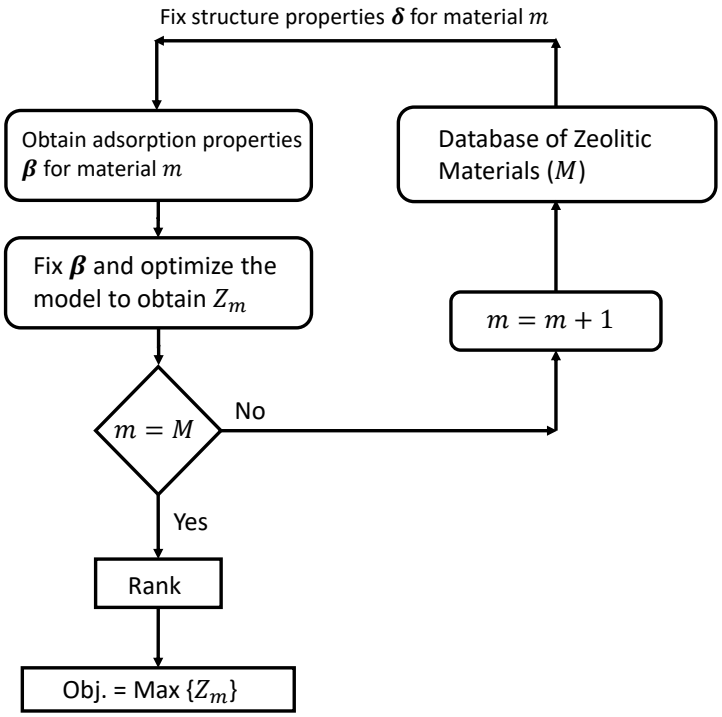

Figure 3.6: Flow chart of the overall optimization strategy used in this work where the properties corresponding to a material $\boldsymbol{\beta}$ are fixed and the resultant model is optimized. This is carried out for every material in the database. The materials in the database are then ranked based on their optimal objective values Z_m obtained from each optimization (Iyer *et al.* [77]).

Applying the above discretization to the optimization formulation in eq. 3.1, leads to the following completely algebraic formulation as described in eq. 3.23. The $h^M(\boldsymbol{\delta}, \boldsymbol{\beta}) = 0$ is treated as a black-box function and is not included in this formulation, since an external package (RASPA) is used to calculate the material parameters $\boldsymbol{\beta}$ based on the material structural properties $\boldsymbol{\delta}$. The overall process and materials optimization strategy employed in this work is shown in Figure 3.6. First, for a chosen material m from the database and its adsorption properties $\boldsymbol{\beta}$ for different gases are calculated using Grand Canonical Monte Carlo (GCMC) simulations. Fixing the adsorption properties and thereby the material, the resultant process model is optimized to obtain an objective Z_m. This is repeated till Z_m for all the materials in the candidate pool are evaluated. After this, the desired materials are ranked based on their objective function values (Z_m) obtained.

$$\min_{\mathbf{X}} \quad Z_m = \sum_{j \in J} \tilde{f}(\mathbf{X}, \tilde{\boldsymbol{\alpha}}|_{k=N_k})\, \Delta z \qquad \text{(Objective Function)}$$

(3.23a)

s.t.

$$\left.\begin{aligned} &\tilde{h}^{CE}(\mathbf{X}, \tilde{\boldsymbol{\alpha}}, \tfrac{\Delta\tilde{\boldsymbol{\alpha}}}{\Delta t}, \tfrac{\Delta\tilde{\boldsymbol{\alpha}}}{\Delta z}, \tfrac{\Delta(\frac{\Delta\tilde{\boldsymbol{\alpha}}}{\Delta z})}{\Delta z}, \tilde{\boldsymbol{\gamma}}) = 0 \\ &\tilde{h}^{BC}(\mathbf{X}, \tilde{\boldsymbol{\alpha}}, \tfrac{\Delta\tilde{\boldsymbol{\alpha}}}{\Delta z}\big|_{j=0.5}, \tfrac{\Delta\tilde{\boldsymbol{\alpha}}}{\partial z}\big|_{j=N_J+0.5}) = 0 \\ &\tilde{h}^{IC}\big(\mathbf{X}, \tilde{\boldsymbol{\alpha}}|_{k=1}\big) = 0 \end{aligned}\right\} \qquad \text{(Process Model)}$$

(3.23b)

$$\left.\begin{aligned} &\textstyle\sum_{j \in J} \tilde{g}(\mathbf{X}, \tilde{\boldsymbol{\alpha}}|_{k=1}, \tilde{\boldsymbol{\alpha}}|_{k=N_K})\, \Delta z \le 0 \\ &\textstyle\sum_{k \in K} \tilde{g}(\mathbf{X}, \tilde{\boldsymbol{\alpha}}|_{j=0.5}, \tilde{\boldsymbol{\alpha}}|_{j=N_J+0.5})\, \Delta t \le 0 \end{aligned}\right\} \qquad \text{(Process Performance Constraints)}$$

(3.23c)

$$\tilde{h}^{MP}(\tilde{\boldsymbol{\alpha}}, \boldsymbol{\beta}, \tilde{\boldsymbol{\gamma}}) = 0 \qquad \text{(Material-Process Connectivity Model)}$$

(3.23d)

$$\mathbf{X} \in [\mathbf{X}^L, \mathbf{X}^U] \subseteq \mathbb{R}^d \qquad \text{(Decision Variable Bounds)} \tag{3.23e}$$

The corresponding equations and details comprising the complete algebraic optimization model formulation for the combined separation and storage process in eq. 3.23 are described in the Appendix A.2.

3.4.1 Solution Strategy

The accuracy of the discretized algebraic model described in the previous section increases with the number of spatial volumes and temporal time-steps used. However, consequently the size of the model i.e. number of equations and variables increases. For instance, for a 2 component system employing 10 discretization in the spatial and temporal dimensions, the number of state variables is 600. Solving the NLP model for even a single material presents challenges especially due to the dimensionality of the completely discretized model. A good initial guess needs to be provided for the convergence of such a model.

For this, an initialization strategy is employed wherein the solution profile obtained from simulation at a fixed set of conditions is provided as initial guess to the optimization problem. The initial guess value from the simulation is provided not just for the state variables, but for all the intermediate variables encountered in the model. For performing the simulations, the NAPDE model equations along with the boundary conditions are spatially discretized into an ordinary differential equation initial-value problem (ODE-IVP) and then solved in `MATLAB`® environment using the built-in `ode23s` time-stepper for a chosen material and a set of feed and initial conditions. The solution of ODE-IVP provides the values of the state variables (x_i, y_i, P, T, T_w) at different times and locations in the column. Based on the solution profiles obtained, the initial guess value for every variable in the discretized optimization model is provided. This considerably aids the NLP solver `GAMS/CONOPT` [120] to find an initial feasible solution quickly and converge to an optimum. The schematic of the solution strategy employed is shown in Figure 3.7. The exact sequence of steps and the model equations used in the solution strategy are described as follows:

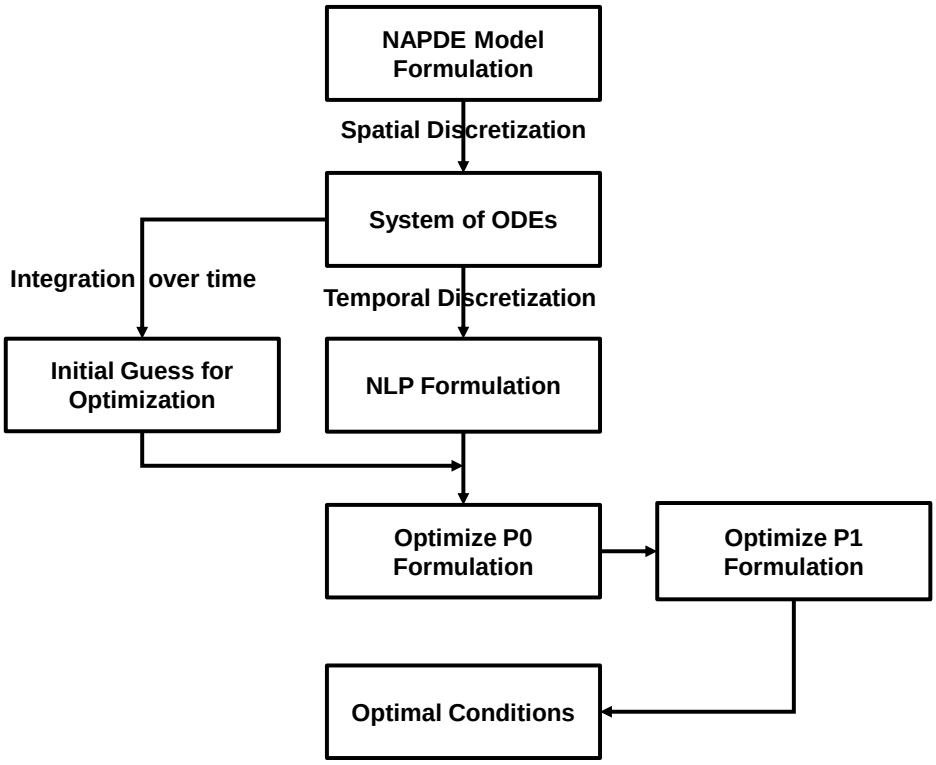

Figure 3.7: Flow chart of the discretization and initialization strategy for the fully discretized process model used for obtaining optimal operating conditions. Initial guess from simulation is provided to the optimization models to aid convergence (Iyer *et al.* [77]).

3.4.1.1 Initialization

Firstly, the set of equations describing the equilibrium conditions after pressurization mode (eq. A.66–A.77) are solved using `GAMS/CONOPT` for a fixed value of P_h. Using the equilibrium compositions thus obtained as the initial conditions for the CSS process mode, an ordinary differential equation initial-value problem (ODE-IVP) problem comprising the spatially discretized process model equations is integrated over time for the same value of P_h used and fixed value of the other decision variables (v_f and t_f).

Using the solution profiles obtained from `MATLAB`®, the value of each of the variables involved in the discretized optimization model formulation can be calculated. Since adaptive time steps for integration are used in `ode23s`, so obtaining the values corresponding to the exact time step used in the fully discretized model is not possible. However, the values of variables at these time steps

can be suitably interpolated using the solution profiles. The decision variables are fixed at the respective values of the simulation conditions leading to a optimization sub-problem formulation $P0$. Initial guess values for other variables in the model are provided from the simulation solution profiles as described above. The equations concerning the process metrics eq. A.83–A.95 are not included in this model.

$$
\begin{aligned}
P0: \max. \quad & Z_{obj} && \text{(Objective)} \\
\text{subject to} \quad & Z_{obj} = 0 && \text{(Dummy objective)} \\
& \text{eq. A.11–A.82} && \text{(Discretized process model)} \\
& \text{eq. A.96–A.103} && \text{(Bounds on state variables)} \\
& \left.\begin{aligned} P_h &= P_{h\,sim} \\ v_f &= v_{f\,sim} \\ t_f &= t_{f\,sim} \end{aligned}\right\} && \text{(Fixed decision variables)}
\end{aligned}
$$

The sub-problem $P0$ is then solved using GAMS/CONOPT. In our experience, we are able to converge to a feasible and subsequently to an optimal solution faster on applying the above initialization strategy rather than just initializing a few key variables, which in many cases did not yield even a feasible solution. Optimizing highly nonlinear NLP models such as this one requires good starting solutions, scaling and bound specifications.

3.4.1.2 Maximization of CH_4 Storage

After solving the $P0$ sub-problem, the complete optimization model $P1$ with relaxed decision variable values and incorporating the equations pertaining to the process metrics (eq. A.83–A.95) is optimized to maximize the process objective, *i.e.* CH_4 storage at the end of the process for a given material. The initial values of the variables common to the models $P0$ and $P1$ is explicitly assigned from the optimal solution of $P0$ in addition to the values such as Jacobians, sensitivities

which may be retained in memory by GAMS.

$P1$: max.	Z_{obj}	(Objective)
subject to	$Z_{obj} = n_{CH_4,N_K}$	(Objective: CH_4 stored at final time)
	eq. A.11–A.82	(Discretized process model)
	eq. A.83–A.95	(Process metrics and constraints)
	eq. A.96–A.103	(Bounds on state variables)
	eq. A.104–A.106	(Bounds on decision variables)

3.5 Results and Discussion

Solving the $P1$ optimization problem above provides the value of the maximum CH_4 stored per unit volume of a given adsorbent at the end of the process and the corresponding optimal values of outlet pressure set, duration of process operation and the feed velocity for the CSS mode. In order to rank different materials according to their CH_4 storage capacities, the strategy described above is implemented for every material candidate to obtain the optimal objective values. Based on the objective function values, the top materials and their corresponding process decision variables i.e. operation pressure, duration of operation, feed velocity can be ranked.

Multiple cases with varying feed compositions are investigated which demonstrate the performance of the combined separation and storage technology for CH_4 storage from feed mixtures containing N_2. These cases help in elucidating the relative difficulty of the intensified multifunctional combined separation and storage of CH_4 for different feed conditions. The values of the parameters used in the NLP model are provided in Table 3.3. For all the cases investigated, the initial condition of the column, *i.e.* the pressure and the composition of the depleted column returned to the facility, is set as P^{init} = 5.8 bar, $y_{N_2}^{init}$=0.05 and $y_{CH_4}^{init}$=0.95. The initial temperature T^{init} is set to be the ambient temperature of 298 K. The column is assumed to operate at a single

Table 3.3: Parameters used for CSS process optimization (Iyer *et al.* [77]).

Parameter	Unit	Value
Feed temperature, T_f	K	298.15
Ambient temperature, T_a	K	298.15
Column length, L	m	1
Column inner radius, r_i	m	0.10
Column outer radius, r_o	m	0.125
Column void fraction, ε	–	0.37
Particle porosity, ε_p	–	0.35
Gas phase viscosity, μ	Pa s	1.72×10^{-5}
Molecular diffusivity D_L	$m^2\ s^{-1}$	1.6×10^{-5}
Axial gas thermal conductivity, K_z	J $m^{-1}K^{-1}\ s^{-1}$	0.09
Gas phase specific heat capacity, C_{pg}	J $mol^{-1}K^{-1}$	34.7
Adsorbed phase specific heat capacity, C_{pa}	J $mol^{-1}K^{-1}$	34.7
Adsorbent specific heat capacity, C_{ps}	J $kg^{-1}K^{-1}$	1070
Inside heat transfer coefficient, h_i	W $m^{-2}K^{-1}$	8.6
Outside heat transfer coefficient, h_o	W $m^{-2}K^{-1}$	2.5
Particle radius, r_p	m	1×10^{-3}
Column wall thermal conductivity, K_w	J $m^{-1}K^{-1}\ s^{-1}$	16
Column wall density, ρ_w	kg m^{-3}	7800
Column wall specific heat capacity, C_{pw}	J $kg^{-1}K^{-1}$	502
Scaling parameters		
T_0	K	298.15
q_0^s	mol kg^{-1}	15

pressure for the combined separation and storage (CSS) mode of the process. The minimum limit on purity of CH_4 stored at the final time is set at 90% ($pur_{CH_4} = 0.9$) and the maximum limit on loss percentage of CH_4 is set to be 10% ($l_{CH_4} = 0.1$) of CH_4 fed. 10 finite volumes ($N_J = 10$) in space and 50 time steps ($N_K = 51$) are used for obtaining the fully discretized model incorporated in the NLP formulation for the following case studies. The fixed decision variables for solving all the $P0$ sub-problem are $P_{h\ sim}$ = 0.99*35 bar [1], $t_{f\ sim}$ = 150 s and $v_{f\ sim}$ = 1 m/s. The bounds on the decision variables $\mathbf{X}$ for the $P1$ problem are given in Table 3.4 while the values of the bounds on the state variables in Table A.1.

[1]Since the initial guess values for $P0$ problem are obtained at 35 bar, setting $P_{h\ sim}$ exactly at 35 bar poses numerical difficulties.

Table 3.4: Decision variable bounds for CSS process optimization (Iyer *et al.* [77]).

Parameter	Unit	Lower bound	Upper bound
CSS mode filling pressure, P_h	Pa	5.8×10^5	65×10^5
Duration of operation, t	s	10	250
Feed interstitial velocity, v_f	m s^{-1}	0.05	1.5

3.5.1 Optimal CSS for N_2-contaminated Feed

In this section, changing the relative composition of CH_4 and N_2 in the feed mixture and its influence on the optimal performance of the CSS process is investigated. Four cases of feed compositions are considered below where the percentage of N_2 in the feed mixture varies from 15% to 30%. The ranking of materials with the highest CH_4 storage achieved for all the cases along with the corresponding optimal process conditions is listed in Table 3.5.

3.5.1.1 85% CH_4 and 15% N_2

For this feed composition, zeolite SBN give rise to the highest moles of CH_4 stored (239.99 mol) in the column at the end of the CSS process. This translates to an adsorbed phase volumetric storage capacity $n_{CH_4,ads}$ of 240.95 v(STP)/v adsorbent. The corresponding optimal process conditions are P_h = 64.82 bar, t_f = 10 s, v_f= 0.05 m/s. The optimal zeolites for this feed composition ranked in order of decreasing CH_4 storage are SBN, AFY, RHO, APD, DFT, EMT and STW respectively and their corresponding optimal values are listed in Table 3.5. 30 zeolites are found to be feasible for process operation under this feed condition. Other than SBN and EMT for which the optimal pressure is the upper bound (65 bar), the optimal pressures for the other zeolites for maximum storage are not necessarily at the upper bound of the filling pressure. However, for all the zeolites, the duration of operation of CSS mode and the feed velocity are at or close to the lower bound (10 s and 0.05 m/s respectively). This is in order to minimize CH_4 losses through the

[2] 30 zeolites are found to be feasible.
[3] 27 zeolites are found to be feasible.
[4] 9 zeolites are found to be feasible.
[5] 5 zeolites are found to be feasible.

Table 3.5: Top zeolites feasible for operation ranked in order of decreasing CH_4 storage from a feed containing only CH_4 and N_2 (Iyer *et al.* [77])

Zeolites	Objective	Ads. vol. capacity	Process Decision Variables		
	n_{CH_4,N_K} (mol)	$n_{CH_4,ads}$ (v(STP)/v)	P_h (bar)	t (s)	v_f (m/s)
Feed: 85% CH_4 and 15% N_2 [2]					
SBN	239.99	240.95	64.82	10	0.05
AFY	167.46	169.41	50.20	10	0.076
RHO	156.51	153.47	54.33	10	0.05
APD	144.49	148.58	37.33	10	0.05
DFT	139.58	144.36	33.14	10	0.05
EMT	134.60	128.74	65	14.60	0.05
STW	130.91	134.08	30.38	10	0.05
Feed: 80% CH_4 and 20% N_2 [3]					
Zeolite	n_{CH_4,N_K} (mol)	$n_{CH_4,ads}$ (v(STP)/v)	P_h (bar)	t (s)	v_f (m/s)
SBN	179.47	193.21	23.91	19.38	0.05
APD	141.52	145.91	38.84	10	0.05
DFT	135.89	141.11	33.38	10	0.05
EMT	126.82	122.55	65	16.82	0.05
STW	125.13	129.72	26.99	10	0.05
Feed: 75% CH_4 and 25% N_2 [4]					
Zeolite	n_{CH_4,N_K} (mol)	$n_{CH_4,ads}$ (v(STP)/v)	P_h (bar)	t (s)	v_f (m/s)
SBN	150.55	164.21	16.01	10	0.097
APD	137.08	142.19	38.50	10	0.051
DFT	131.51	137.30	32.73	10	0.05
STW	106.59	113.74	16.36	10	0.05
EMT	101.08	101.19	46.96	10	0.10
Feed: 70% CH_4 and 30% N_2 [5]					
Zeolite	n_{CH_4,N_K} (mol)	$n_{CH_4,ads}$ (v(STP)/v)	P_h (bar)	t (s)	v_f (m/s)
SBN	135.51	148.48	13.10	10	0.05
APD	120.37	128.46	24.26	10	0.055
DFT	117.10	125.14	21.67	10	0.052
STW	96.95	104.48	12.79	10	0.05
EMT	68.63	71.48	24.99	10	0.079

outlet of the column.

3.5.1.2 80% CH_4 and 20% N_2

For this feed composition, the highest CH_4 storage obtained is again for zeolite SBN with 179.47 moles of CH_4 stored in the column at the end of the process. The decrease in CH_4 storage compared to the previous feed composition is due to the increase in impurity N_2/decrease in CH_4.

The corresponding optimal process conditions for SBN are P_h = 23.91 bar, t = 19.38 s, v_f= 0.05 m/s. 27 zeolites are found to be optimal for this case and the top optimal zeolites among them are SBN, APD, DFT, EMT and STW in the order of decreasing CH_4 storage capacity. Other than for zeolite EMT, the optimal pressure obtained is not at the upper bound on the filling pressure as seen from Table 3.5.

3.5.1.3 75% CH_4 and 25% N_2

For this feed composition, the highest CH_4 storage obtained is lesser than both the above cases with 150.55 moles of CH_4 stored for zeolite SBN. The corresponding optimal process conditions for SBN are P_h = 16.01 bar, t = 10 s, v_f= 0.097 m/s. 9 zeolites are optimal for this case, with the top five zeolites for CH_4 storage being the same as the previous case. It is also observed from Table 3.5 that the optimal pressures for the top five zeolites in this case are far from the upper bound on the filling pressure (65 bar).

3.5.1.4 70% CH_4 and 30% N_2

For this feed composition, the highest CH_4 storage is again obtained for zeolite SBN with 135.51 moles stored in the column. The corresponding optimal process conditions for SBN are P_h = 13.10 bar, t = 10 s, v_f= 0.05 m/s. The top 5 zeolites obtained for the previous two cases are the only zeolites feasible for CSS process operation under this feed condition.

It is observed that some of the zeolites such as SBN, APD and DFT are among the best for more than one feed conditions. It is also observed that with decrease in CH_4 in the feed composition, the maximum CH_4 storage achieved with the optimal zeolite has also decreased. For example, the maximum moles of CH_4 stored in the column using SBN for 85% CH_4 and 15% N_2 feed is 239.98 moles while for 70% CH_4 and 30% N_2 feed, it decreases to 135.51 moles. The number of zeolites which are feasible with respect to the process constraints of purity and loss decrease with the decreasing percentage of CH_4% in the feed. For example, for 85% CH_4 and 15% N_2 feed, 30 zeolites are feasible, while for 70% CH_4 and 30% N_2 feed, only five zeolites are feasible. From Table 3.5, it is evident that for the top zeolites, optimal operating conditions of filling pressure P_h

can range anywhere between 12-65 bar, while the CSS mode duration and feed velocity are very close to the lower bounds 10 s and 0.05 m/s respectively. This is to prevent loss of CH_4 through the outlet of the column and retain the purity of CH_4 stored in the column. Although, the highest pressure operation is preferred for CH_4 storage into a column from a pure CH_4 feed, the highest storage pressure (65 bar in this case) is not always the optimal pressure for the combined separation and storage (CSS) process. This is because the feed mixture contains N_2 in addition to CH_4 which needs to be separated, hence the loss of CH_4 through the column outlet and the purity of stored CH_4 both have to be balanced.

3.5.2 Effect of CO_2 in Feed

Though almost all of the CO_2 is considered to be separated out before the CSS process by employing a CO_2 selective guard bed, the effect of 3% of N_2 impurity being substituted by CO_2 is examined to account for any variability in operation of guard bed. The four corresponding feed compositions tested are described as follows and the corresponding optimal process conditions are listed in Table 3.6.

3.5.2.1 85% CH_4, 12% N_2 and 3% CO_2

Only four zeolites meet the constraints and are feasible for this case, compared to 30 for the case with 85% CH_4/15% N_2. These four zeolites are SBN, EMT, LTA and STF out of which the highest CH_4 storage of 198.11 moles is achieved for SBN at P_h = 29.94 bar, t = 10 s, v_f= 0.05 m/s. The maximum CH_4 storage capacity was much higher at 239.99 moles for the case of just N_2 being present as impurity in the 85% CH_4/15% N_2 feed. The presence of CO_2, which has a stronger adsorption affinity than CH_4 and N_2, in the feed gas mixture reduces both the maximum moles of CH_4 stored for the top zeolite SBN while also reducing the number of zeolites which meet the feasibility requirements of the process.

3.5.2.2 80% CH_4, 17% N_2 and 3% CO_2

Just three zeolites, SBN, EMT and LTA are feasible for this case, with the maximum storage of 149.02 moles achieved for SBN at P_h = 14.27 bar, t = 19.29 s, v_f= 0.05 m/s. For the case of

Table 3.6: Zeolites feasible for operation ranked in order of decreasing CH_4 storage from feed containing CH_4, N_2 and 3% CO_2 (Iyer *et al.* [77]).

Zeolites	Objective	Ads. vol. capacity	Process Decision Variables		
	n_{CH_4,N_K} (mol)	$n_{CH_4,ads}$ (v(STP)/v)	P_h (bar)	t (s)	v_f (m/s)
Feed: 85% CH_4, 12% N_2 and 3% CO_2					
Zeolite	n_{CH_4,N_K} (mol)	$n_{CH_4,ads}$ (v(STP)/v)	P_h (bar)	t (s)	v_f (m/s)
SBN	198.11	210.46	29.94	10	0.05
EMT	135.05	129.20	65	13.94	0.05
LTA	115.22	115.62	35.12	10	0.05
STF	79.41	82.07	18.27	10	0.051
Feed: 80% CH_4, 17% N_2 and 3% CO_2					
Zeolite	n_{CH_4,N_K} (mol)	$n_{CH_4,ads}$ (v(STP)/v)	P_h (bar)	t (s)	v_f (m/s)
SBN	149.02	162.63	14.27	19.29	0.05
EMT	127.26	123.02	65	16.11	0.05
LTA	97.23	100.58	23.71	10	0.054
Feed: 75% CH_4, 22% N_2 and 3% CO_2					
Zeolite	n_{CH_4,N_K} (mol)	$n_{CH_4,ads}$ (v(STP)/v)	P_h (bar)	t (s)	v_f (m/s)
SBN	131.23	143.96	11.11	10	0.05
EMT	90.79	92.19	37.70	10	0.10
Feed: 70% CH_4, 27% N_2 and 3% CO_2					
Zeolite	n_{CH_4,N_K} (mol)	$n_{CH_4,ads}$ (v(STP)/v)	P_h (bar)	t (s)	v_f (m/s)
SBN	122.36	134.51	9.79	10	0.05
EMT	66.00	68.97	22.43	10	0.073

80% CH_4/20% N_2, the maximum CH_4 storage achieved was 179.47 moles for SBN which is much higher than the present case involving 3% CO_2. Also, 24 additional zeolites can meet the process feasibility criteria when no N_2 is present in the feed.

3.5.2.3 75% CH_4, 22% N_2 and 3% CO_2

For this case, just two zeolites SBN and EMT are feasible, with 131.23 moles of CH_4 stored using SBN. As observed previously, the corresponding maximum CH_4 storage for the corresponding feed without any CO_2 is higher at 150.55 moles.

3.5.2.4 70% CH_4, 27% N_2 and 3% CO_2

Again for this case, just two zeolites SBN and EMT are feasible, with the highest CH_4 storage of 122.36 moles of obtained using SBN. This is lower than CH_4 storage of 135.51 moles achieved

with zeolite SBN for the case of 70% CH_4/30% N_2. However, the storage capacity of EMT for the present case is only slightly lower (66 moles) than that of the corresponding case with no CO_2 (68.63 moles).

Comparing Tables 3.5 and 3.6, it is evident that on substituting some of the N_2 (3%) with CO_2, the number of zeolites feasible for process operation has decreased over all cases. It is also observed that the introduction of CO_2 results in lower CH_4 storage compared to when only N_2 is present, for even the zeolites which are feasible for both cases. As mentioned previously, this is due to the stronger adsorption affinity of CO_2 to zeolites, compared to CH_4 and N_2. This can be more clearly observed from Figure 3.8 which shows the variation of optimal CH_4 storage with different feed compositions for top zeolites SBN and EMT.

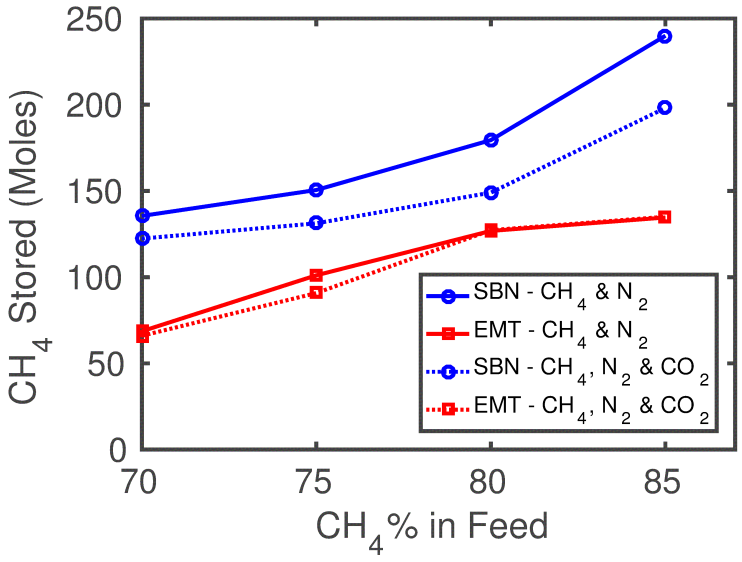

Figure 3.8: The effect of maximum CH_4 storage obtained for top zeolites SBN and EMT with change in percentage CH_4 in feed. The effect of substituting some of the N_2 in CH_4/N_2 feed with 3% CO_2 is also depicted in the graph (Iyer *et al.* [77]).

The CH_4 deliverable capacity $\Delta n^{CH_4}_{P_h,5.8}$, which is the difference between the CH_4 stored n_{CH_4,N_K} at optimal pressure P_h and the initial moles of CH_4 stored in the column at 5.8 bar [36, 45, 48, 52] is also optimized for the above cases and listed in the last column of Tables 3.7 and 3.8. Since the

initial column conditions such as pressure, temperature and gas phase compositions are set to be the same for for all the above cases, the initial moles of CH_4 stored is also fixed for a given material. Hence, optimizing the deliverable capacity yields the same optimal conditions or very similar ones to those obtained for total CH_4 storage capacity. Though the relative ranking of the zeolites change considerably, the zeolites which are feasible for all the above feed conditions is the same regardless of whether the CH_4 deliverable capacity or the CH_4 storage capacity is optimized.

Table 3.7: Top zeolites ranked in order of decreasing CH_4 delivery capacity between optimal pressure P_h and initial pressure 5.8 bar for a feed containing only CH_4 and N_2 (Iyer *et al.* [77]).

Zeolites	Objective	Process Decision Variables		
	$\Delta n^{CH_4}_{P_h,5.8}$ (mol)	P_h (bar)	t (s)	v_f (m/s)
Feed: 85% CH_4 and 15% N_2 [6]				
SBN	136.88	64.82	10	0.05
AFY	114.16	50.20	10	0.076
RHO	93.72	54.33	10	0.05
EMT	89.70	65	14.60	0.05
AFR	84.24	56.25	10	0.05
OBW	82.88	55.46	10	0.05
Feed: 80% CH_4 and 20% N_2 [7]				
Zeolite	$\Delta n^{CH_4}_{P_h,5.8}$ (mol)	P_h(bar)	t (s)	v_f(m/s)
EMT	81.92	65	16.82	0.05
SBN	76.36	23.91	19.39	0.05
APD	52.99	38.84	10	0.05
STW	49.66	2 26.99	10	0.05
DFT	48.35	33.38	10	0.05
RHO	45.87	21.07	10	0.069
Feed: 75% CH_4 and 25% N_2 [8]				
Zeolite	$\Delta n^{CH_4}_{P_h,5.8}$ (mol)	P_h(bar)	t (s)	v_f (m/s)
EMT	56.18	46.96	10	0.10
APD	48.55	38.50	10	0.05
SBN	47.45	16.01	10	0.097
DFT	43.96	32.73	10	0.05
STW	31.12	16.36	10	0.05
Feed: 70% CH_4 and 30% N_2 [9]				
Zeolite	$\Delta n^{CH_4}_{P_h,5.8}$ (mol)	P_h(bar)	t (s)	v_f(m/s)
SBN	32.40	13.10	10	0.05
APD	31.84	24.26	10	0.055
DFT	29.55	21.67	10	0.052
EMT	23.73	24.99	10	0 0.079
STW	21.48	12.79	10	0.05

To further illustrate the process operation, the process flow sheet is updated with the optimal so-

[6] 30 zeolites are found to be feasible.

[7] 27 zeolites are found to be feasible.

[8] 9 zeolites are found to be feasible.

[9] 5 zeolites are found to be feasible.

Table 3.8: Top zeolites ranked in order of decreasing CH_4 delivery capacity between optimal pressure P_h and initial pressure 5.8 bar for feed containing CH_4, N_2 and 3% CO_2 (Iyer *et al.* [77]).

Feed: 85% CH_4, 12% N_2 and 3% CO_2				
Zeolite	$\Delta n^{CH_4}_{P_h,5.8}$ (mol)	P_h(bar)	t (s)	v_f (m/s)
SBN	95.00	29.94	10	0.05
EMT	90.16	65	13.94	0.05
LTA	57.84	35.12	10	0.05
STF	29.81	18.27	10	0.05
Feed: 80% CH_4, 17% N_2 and 3% CO_2				
Zeolite	$\Delta n^{CH_4}_{P_h,5.8}$ (mol)	P_h(bar)	t (s)	v_f (m/s)
EMT	82.36	65	16.11	0.05
SBN	45.92	14.27	19.29	0.05
LTA	39.85	23.71	10	0.054
Feed: 75% CH_4, 22% N_2 and 3% CO_2				
Zeolite	$\Delta n^{CH_4}_{P_h,5.8}$ (mol)	P_h(bar)	t (s)	v_f (m/s)
EMT	45.89	37.70	10	0.10
SBN	28.13	11.11	10	0.05
Feed: 70% CH_4, 27% N_2 and 3% CO_2				
Zeolite	$\Delta n^{CH_4}_{P_h,5.8}$ (mol)	P_h(bar)	t (s)	v_f (m/s)
EMT	21.11	22.43	10	0.073
SBN	19.26	9.79	10	0.05

lution obtained for two feed compositions, *i.e.* 80% CH_4/20% N_2 and 85% CH_4/15% N_2. Fig. 3.9a shows the amount of CH_4 sent to the column, stored in the column and lost in the outlet for the optimum result of zeolite SBN for feed of 80% CH_4/20% N_2. Starting with an initial CH_4 storage of 103.10 moles at 5.8 bar, which is the case for the column depleted at the end user, in the pressurization step, 76.16 more moles of CH_4 are fed to the column which increase the the CH_4 storage to 179.26 moles with a purity of 89.87%. The combined separation and storage (CSS) mode is just run for 19.94 s due to the CH_4 loss reaching the set limit of 10%. During this period, the storage capacity and the CH_4 purity slightly increases to 179.47 moles and 90%, respectively, due to some separation of N_2 through the outlet. For the case of 85% CH_4/15% N_2 as shown in Fig. 3.9b, it is again observed that most of the increase in CH_4 storage occurs during the pressurization step. In fact, it is observed that the operation of the CSS mode in this case, results in a slight decrease in CH_4 storage and purity. This is because some of the already stored CH_4 exits the column once the other end of the column is opened for the CSS operation, while some of the N_2 from the feed fed to

the column get stored in the column at these conditions. Due to the dynamic nature of the process, it is difficult to predict such behavior before solving the model for cases such as this one. Based on the optimal solutions of above cases, it is observed that the CSS process is reduced largely to a CH_4 storage process with CH_4/N_2 separation affected by the need to limit the loss of CH_4 fed or already present in the column.

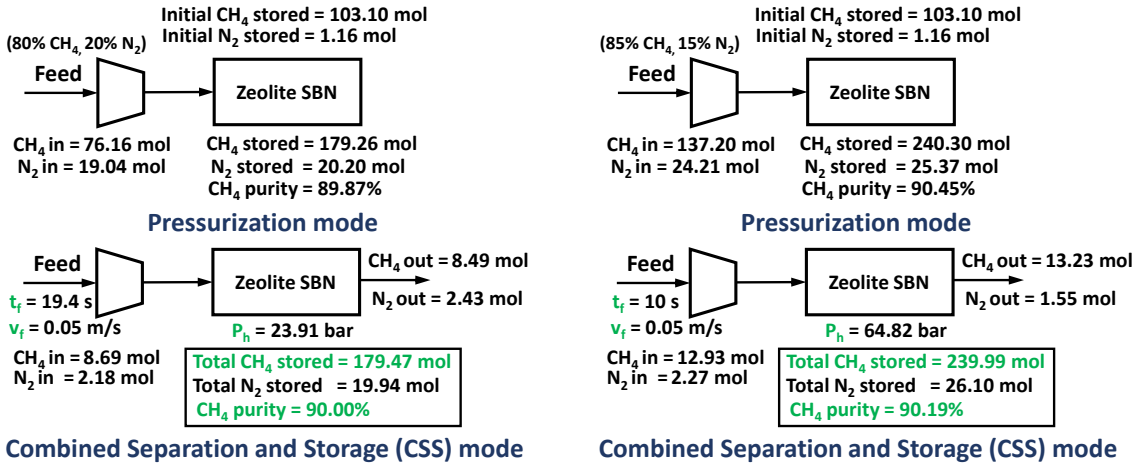

(a) 80% CH_4, 20% N_2

(b) 85% CH_4, 15% N_2

Figure 3.9: CH_4 mole balance over the column at optimum conditions. (a) For feed of 80% CH_4/20% N_2 at the optimum results obtained, it is observed that most of the storage of CH_4 occurs in the initial pressurization mode, where there is no separation. During the combined separation and storage (CSS) mode, a slight improvement in CH_4 storage and purity achieved, before the loss of CH_4 through the open end exceeds the limit of 10%. (b) For feed of 85% CH_4/15% N_2, it is again observed that most of the gain in CH_4 storage happens in the pressurization mode. In fact, during the CSS mode, the loss of CH_4 through the outlet exceeds the CH_4 fed leading to a slight decrease in CH_4 storage and purity (Iyer *et al.* [77]).

3.5.3 Top Zeolites for CSS

Figure 3.10 depicts the CH_4 and N_2 pure component equilibrium adsorption isotherms at 298 K for all the pure silica zeolites considered in this work. Among them, the isotherms for the zeolites such as SBN, AFY, RHO, APD, DFT, EMT and STW which demonstrate high CH_4 storage for the CSS process are shown in bold.

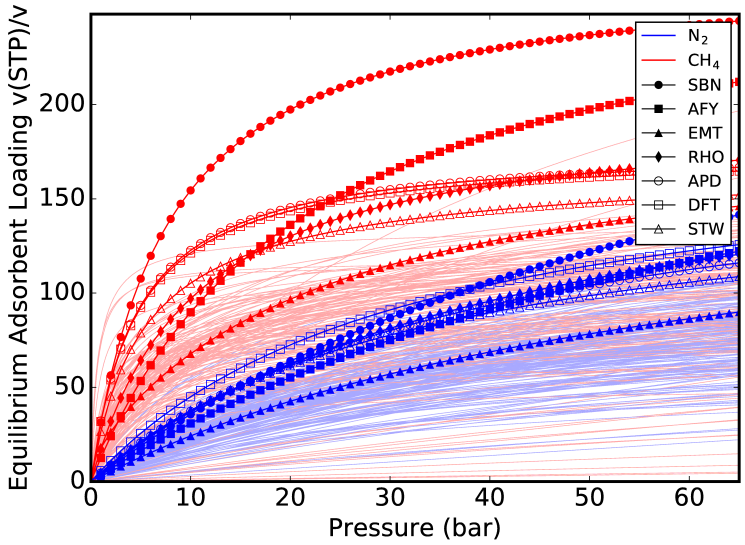

Figure 3.10: The CH_4 and N_2 isotherms at 298 K of the zeolites feasible for the CSS process superimposed (darker shades) over the corresponding isotherms of all other zeolites (lighter shades). It is observed that the zeolites which maximize the moles of CH_4 stored at the end of the process have both the CH_4 and N_2 equilibrium storage capacities toward the higher end of the spectrum (Iyer *et al.* [77]).

From the figure, it can be observed that with the exemption of EMT, the other top zeolites, namely, SBN, AFY, RHO, APD, DFT and STW are on the higher end of the spectrum of equilibrium CH_4 storage capacities at higher pressures. It is also observed that their corresponding N_2 isotherms are also toward the higher end of the spectrum of N_2 isotherms of all zeolites. However, this is not always the case as zeolite ACO which has the third highest volumetric equilibrium loading at a pressure of around 60 bar for pure methane feed as seen from Figure 3.10 is ranked 27^{th} among the top zeolites for CSS operation for both CH_4/N_2: 85%/15% feed and CH_4/N_2: 80%/20% feeds respectively. It is also not feasible for CSS operation for other feed conditions investigated. A screening metric based on only pure component CH_4 equilibrium storage capacity at high pressures thus would not be suitable for such an analysis. A similar case is observed with the CH_4/N_2 binary selectivity metric. The ratio of Henry co-efficients of CH_4 and N_2 on zeolites (calculated using RASPA) gives the binary selectivity toward CH_4 (S_{CH_4/N_2}) for separation. It is observed that the top ten zeolites with the highest values of binary selectivity (S_{CH_4/N_2}) such as MTN, DOH,

MEP, SOD, MAR, FAR and others (Table 3.9) are not feasible for the CSS process for the feed compositions investigated. This is because the storage aspect of the CSS process largely dominates compared to the separation.

Table 3.9: Zeolites with the highest Henry co-efficient based binary adsorption selectivity toward CH_4 at 298 K for CH_4/N_2 binary mixture (Iyer *et al.* [77]).

Zeolite	S_{CH_4/N_2}
MTN	20.24
DOH	17.94
MEP	16.93
SOD	14.43
MAR	13.97
FAR	13.64
CGF	12.22
ZON	12.18
GIU	12.16
RUT	11.85

Fig. 3.11 maps the zeolites with respect to both pure component volumetric storage capacity at 65 bar and the CH_4/N_2 binary selectivity (S_{CH_4/N_2}). The zeolites which are feasible with respect to the loss and purity constraints for the case of combined separation and storage of CH_4 from a CH_4/N_2: 85%/15% feed are depicted using green markers, while the rest of the zeolites which are infeasible with respect to the imposed constraints are depicted using hollow red markers. For the zeolites feasible for CSS operation, the relative rankings of the zeolites based on the maximum volumetric storage of CH_4 obtained at optimum conditions is also shown. The top ranked zeolites have high CH_4 pure component volumetric storage capacity at 65 bar which is a consequence of our objective of maximizing the volumetric storage capacity of CH_4 in the column. However, since the loss and purity constraints dictate the feasible operation of the process, the extent to which the storage of CH_4 from a CH_4/N_2: 85%/15% feed is possible is limited by the zeolite selectivity and the pressure of the operation. From Fig. 3.11, it is observed that, though increase in selectivity

improves the ranking, pressure of CSS operation at optimum also influences the maximum volumetric storage capacity of CH_4 in the column thereby affecting the rankings. For example, though AFR and OSO have close values of CH_4/N_2 binary selectivity (3.97 and 3.95 respectively) and CH_4 pure component volumetric storage capacity at 65 bar (150 and 138 v(STP)/v respectively), the pressure of operation which optimizes the storage while maintaining feasibility with respect to process constraints such as loss and purity is different for AFR and OSO with 56.24 bar and 28.93 bar respectively. This leads to a storage capacity of 119.34 and 93.94 v(STP)/v respectively. The consideration of both process operation and material screening in design can thus enable determining materials which are the best candidates while satisfying imposed process constraints. The pore structural features of the zeolites such as accessible volume, channels and cage diameters which contribute in part to the high equilibrium CH_4 capacity at higher pressures also increase the equilibrium N_2 storage capacities for these zeolites. From the pore structure visualizations for these zeolites (Fig. 3.12) obtained from the ZEOMICS web-tool [119, 121] it is clear that both N_2 and CH_4 with kinetic diameters of 3.6 Å and 3.8 Å respectively are able to access the channels and cages of these zeolites. For the case of SBN, which performs very well in all of the above cases, Kim *et al.* [107] observe that the available binding sites in SBN are spaced close to the 4.15 Å distance [46] that maximizes CH_4-CH_4 interactions making it most suitable for concentrating feeds with medium concentrations of CH_4. Although there are other zeolites with higher CH_4 storage capacities as observed from the pure component isotherms in Figure 3.10, higher CH_4 storage is achieved using EMT for the cases considered. Similarly, zeolites AFY and RHO with high pure component CH_4 storage capacities and ranked within the top three for the case of 85% CH_4/15% N_2 feed are not within the top 5 zeolites for the subsequent cases with increase in N_2%. Moreover, even for the same zeolite, the optimal process conditions such as the filling pressure P_h can be significantly different over the various feed compositions as seen for zeolite EMT in Table 3.5.

To summarize, it is important to note that the material screening performed is tailored for the conditions and constraints of the application being studied i.e. the feed composition of the source

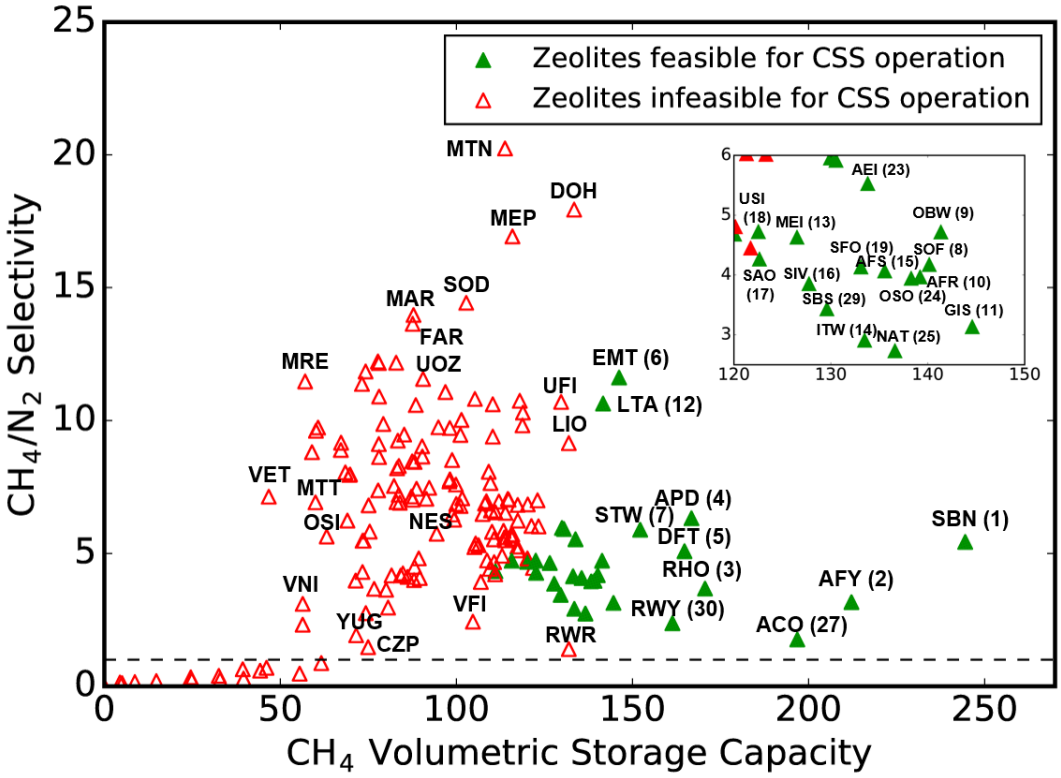

Figure 3.11: Pure silica zeolites considered plotted against CH_4 volumetric storage capacity at 65 bar from a pure CH_4 feed and CH_4/N_2 binary selectivity in the Henry region. The dotted line represents CH_4/N_2 binary selectivity of 1. Zeolites feasible for CSS operation with respect to the loss and purity constraints for a feed of CH_4/N_2: 85%/15% are shown using green filled triangles along with their relative rankings (based on the optimal volumetric storage of CH_4), while the zeolites which are infeasible are depicted using hollow red markers. All the top ranked zeolites have high CH_4 volumetric storage capacity, with the relative ranking influenced by both CH_4/N_2 binary selectivity and pressure used in CSS operation (Iyer *et al.* [77]).

gas, initial composition of the column, purity and loss limits. For a different feed composition, the top materials and the corresponding process decision variables obtained by performing screening can be different. Without the rigorous dynamic model, it will be difficult to quantify the loss of CH_4 over time during the CSS step when both column ends are open. The multiscale approach thus affords us an advantage compared to approaches which screen materials based only on material metrics such as highest loading, selectivity etc. in ensuring that only the materials which satisfy the imposed process constraints are considered for ranking.

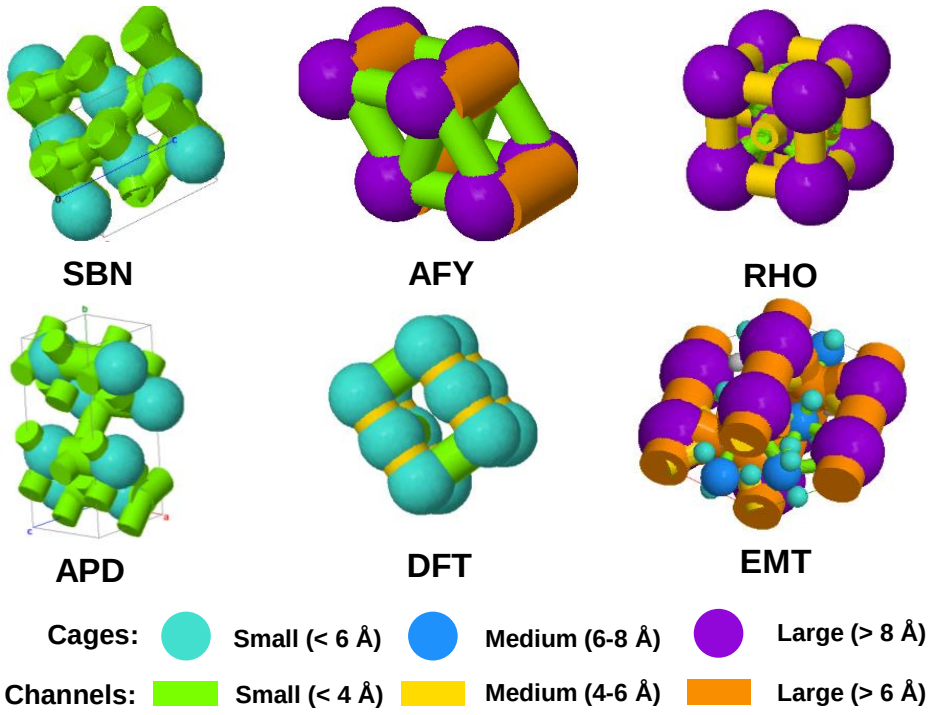

Figure 3.12: The pore structures of the top pure silica zeolites from the IZA-SC database which maximize CH_4 storage while meeting the combined separation and storage (CSS) process constraints. Zeolites AFY, RHO and EMT possess medium to large channels feeding the large cages, while zeolites SBN, APD and DFT have smaller cages and channels. Both N_2 and CH_4 with their kinetic diameter being 3.6 Å and 3.8 Å respectively are able to access the channels and cages of the above zeolites (The pore structure visualizations are taken from the pore characterization web-tool ZEOMICS.) (Iyer *et al.* [77]).

This signifies the importance of simultaneous consideration of process optimization and material screening especially in the context of designing and evaluating new process designs. For example, if the evaluation of novel intensified processes such as the CSS process was based solely on the result of a single chosen material or feed condition, then there is a chance of missing conditions and materials for which the design could be applicable and effective.

3.6 From Existing Materials to Mapping the Feasibility of Process Operation over Material Property Space

In the previous subsections, the top materials (zeolites) which maximize the moles of CH_4 stored in the column, at the end of the combined separation and storage process is identified using

process optimization-based material screening. The zeolites considered are then plotted with respect to CH_4 storage capacity at 65 bar and the selectivity based on CH_4 and N_2 Henry co-efficients as observed in Fig. 3.11. However, it can also be observed that, though, the existing pure silica zeolites considered are depicted in Fig. 3.11, they do not fully and adequately span the range of Henry selectivity and storage capacities. Though it is evident from the figure, that the CH_4 volumetric storage capacities at the lowest and highest end of the range result in infeasibility and feasibility with respect to the process performance constraints, for the values with moderate CH_4 volumetric storage capacities (125 v(STP)/v) there is an overlap between the feasible and the infeasible region. Moreover, the lack of data points and the resulting sparse distribution in certain ranges is not adequate to map the material property space for feasibility with respect to the constraints imposed. Hence an analysis such as the one described below, where the material property space is uniformly mapped can result in identifying regions in the material property space which meet the process performance constraints imposed.

3.6.1 Constructing the Material Space

To construct a map of material properties, the choice of material properties which determine the space are paramount. The material-centric parameters used in the previous section is quite rigorous with 12 parameters for the dual-site isotherm, 3 parameters for each gas and each site considered along with the density of the zeolite. Though all these parameters affect the overall values of the loss and purity, mapping the feasibility in a 13 parameter space and drawing conclusions from it can be cumbersome. To span the space comprising the ranges of different adsorption loading capacity at different pressures, a simpler single site isotherm model can be used.

$$q_i^* = \frac{q_i^s b_i \frac{y_i P}{RT}}{1 + \sum_{i \in I} b_i \frac{y_i P}{RT}} \qquad \forall i \in I \tag{3.24}$$

where $b_i = b_i^0 e^{-\Delta U_i / RT}$

Simplifying the isotherm model to this single site model (eq. 3.24) still gives rise to 3 parameters (q^s, ΔU and b^0) for each gas leading to a total of 6 parameters for the CH_4/N_2 binary system.

Out of these, q^s is representative of the saturation capacity of the gas at infinite pressures while both q^s and $b_i = b_i^0 e^{-\Delta U_i/RT}$ dictate the initial slope of the isotherm at low pressures, the Henry co-efficient. Since b_i in the isotherm model is determined by both b^0 and ΔU_i, to further reduce the number of parameters, the value of ΔU_i is fixed and calculated based on the mean value of the isoteric heat of adsorption for each gas on the existing zeolites. b^0 is however varied to span the range of b_i for a fixed ΔU_i. Also since at very high pressures, the saturation loading is proportional to the accessible volume in the material, it can be assumed q^s is same for both CH_4 and N_2 neglecting differences in the accessible volume due to different kinetic diameters of the two gases. The density of the material is fixed to 1690 kg/m^3 which is the mean of the densities of the pure silica zeolites considered in the previous section. This simplified the isotherm model to three parameters, namely, the total saturation capacity at infinite pressures q^s, the parameters $b_{N_2}^0$ and $b_{CH_4}^0$ influencing the initial slope of the isotherms for the two gases. These three parameters are adequate to define the general shape of CH_4 and N_2 isotherms and are varied to span the whole isotherm space. The upper and lower bound of the ranges for q^s, $b_{N_2}^0$ and $b_{CH_4}^0$ are given in Table 3.10. A Latin Hypercube based sampling strategy is used to sample the property space randomly and uniformly. Due to the large differences between the order of magnitude of the upper and lower bound of the range for $b_{N_2}^0$ and $b_{CH_4}^0$, half of the samples (1000) are obtained considering the logarithm of the upper and lower bounds of the range and the other half (1000) of the samples are obtained based on the actual values of the upper and lower bounds of the range. In our experience, this ensures that the sample points are well distributed within the range of consideration for $b_{N_2}^0$ and $b_{CH_4}^0$. Since the CH_4 isotherms of many of the existing materials considered have higher storage capacity than N_2 isotherms over the range of pressures, the values of $b_{N_2}^0$ and $b_{CH_4}^0$ are swapped in case of $b_{N_2}^0 e^{-\Delta U_{N_2}/RT} \geq b_{CH_4}^0 e^{-\Delta U_{CH_4}/RT}$.

For each of the sample, an optimization problem *P2* similar to the *P1* problem in the previous subsection is solved with the following modifications. The same initialization strategy used for *P1* is also used for the *P2* problem. The objective is modified to the sum of the extent of violations of the constraint on CH_4 purity and CH_4 loss expressed in percentages. The relevant constraints

Table 3.10: Upper and lower bounds for the ranges of isotherm parameters for mapping the material property space.

Parameter	Lower bound	Upper bound
q_{st}	0.05	10
$b^0_{N_2}$	1×10^{-10}	1×10^{-4}
$b^0_{CH_4}$	1×10^{-9}	0.01

eq. A.87 and eq. A.95 are modified with positive slack variables s_p and s_l added which account for the magnitude of constraint violation. In this analysis, as in the previous section, the value of pur_{lim} is set to 0.90 and the value of l_{max} is set to 0.10. However, the initial mole fraction of CH_4 in the gas phase before start of the process $y^{init}_{CH_4}$ in this analysis is set to the pur_{lim} value of 0.90 instead of the value of 0.95 used in the previous section for simplicity in drawing conclusions from the feasibility maps. The feed composition of the incoming gas is 85% CH_4 and 15% N_2.

$$pur_{i,k} \geq pur_{lim} - s_p \qquad i = CH_4, k = N_K \quad (3.25)$$

$$l_i \leq l_{max} + s_l \qquad i = CH_4 \quad (3.26)$$

$$s_p \geq 0 \quad (3.27)$$

$$s_l \geq 0 \quad (3.28)$$

$P2$: min. Z_{obj} (Objective)

subject to $Z_{obj} = 100\ (s_p + s_l)$ (Objective: Total Constraint violation)

eq. A.11–A.82 (Discretized process model)

eq. A.83–A.86, eq.A.88–A.94, eq. 3.25–3.28 (Process metrics and constraints)

eq. A.96–A.103 (Bounds on state variables)

eq. A.104–A.106 (Bounds on decision variables)

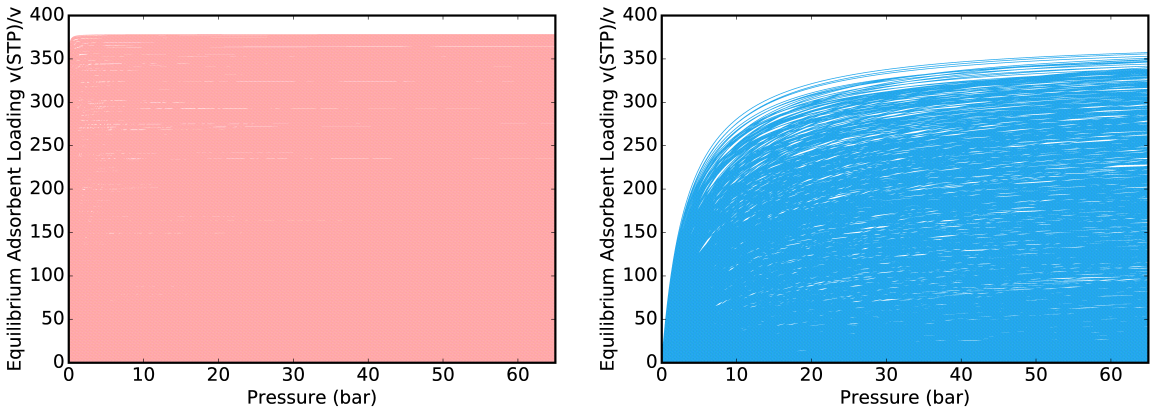

(a) CH_4 isotherms (b) N_2 isotherms

Figure 3.13: CH_4 and N_2 adsorption isotherm space considered at 298 K.

Applying the sampling strategy, the CH_4 and N_2 isotherm space at 298 K is mapped out pertaining to the samples chosen by the sampling strategy. At each of these samples, optimizations to minimize the sum of the total constraint violation (Z_{obj}) is solved. For cases with very low values of b^0 and q_{st} where the solver fails due to numerical issues are neglected. The resulting isotherms pertaining to samples which result in successful convergence of the isotherm to an optimal solution are shown in Fig. 3.13. It can be observed that these samples adequately span the isotherm space of CH_4 and N_2.

3.6.2 Feasibility Map of Material Property Space

Similar to Fig. 3.11, the feasible and infeasible data points obtained from minimizing the constraint violation are plotted with respect to the Henry selectivity *i.e.* ratio of the Henry co-efficients of CH_4 and N_2 are shown in Fig. 3.14. Though similar to Fig. 3.11, it is observed that at low values of CH_4 storage capacity at 65 bar, feasibility with respect to the constraints imposed is not

achieved, the demarcation between points which lead to feasible and infeasible values of the constraints is not clear for moderate to higher values of CH_4 storage capacity at 65 bar. The variation with respect to the CH_4/N_2 Henry selectivity ratio is also unclear in both Fig. 3.11 and 3.14. How-

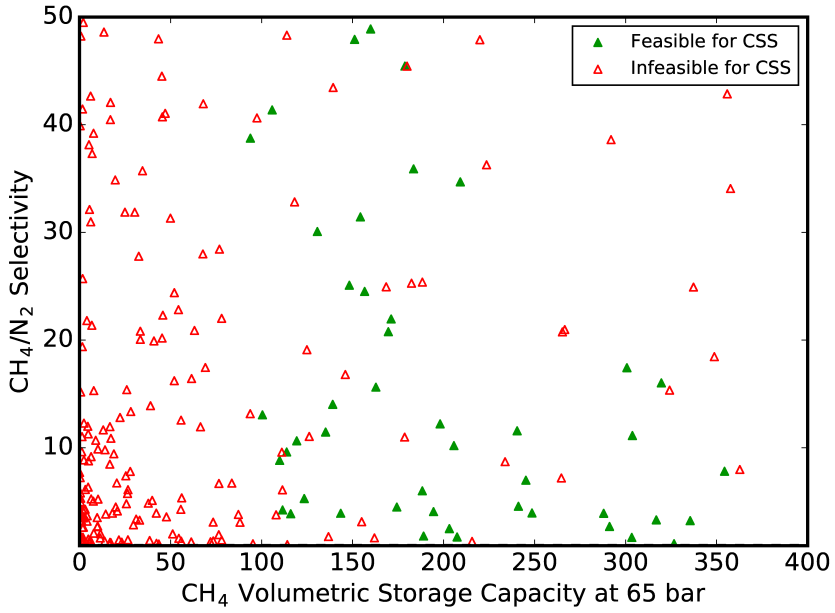

Figure 3.14: Feasibility map corresponding to the material property space spanned by CH_4/N_2 Henry selectivity ratio and CH_4 volumetric storage capacity at 65 bar for feed of 85% CH_4 and 15% N_2. Red triangles denote the points which are infeasible and the green triangles denote the points which are feasible with respect to the process constraints.

ever, if instead of the CH_4/N_2 Henry selectivity ratio, if the CH_4 Henry coefficient is chosen as the y axis, a demarcation between feasible and infeasible region is observed. In Fig. 3.15, the feasible region with respect to CH_4 Henry coefficient and metrics such as CH_4 storage capacity at 65 bar and the CH_4 capacity difference between the optimal pressure P_h chosen and the initial pressure P_l = 5.8 bar is depicted.

3.6.3 Feasibility Map of the Input Isotherm Space

This analysis can also be used to obtain a feasibility map which corresponds to the input space of adsorption parameters (q^s, $b^0_{N_2}$ and $b^0_{CH_4}$) as seen from Fig. 3.16. It is observed that there is a

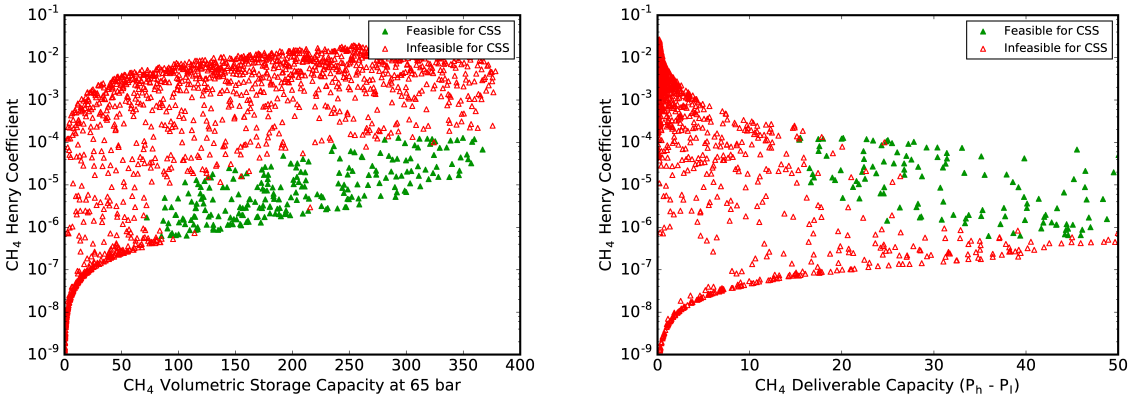

(a) CH_4 Henry coefficient vs CH_4 storage capacity at 65 bar

(b) CH_4 Henry coefficient vs CH_4 deliverable capacity

Figure 3.15: Feasibility map corresponding to CH_4 Henry coefficient and metrics such as CH_4 storage capacity at 65 bar and the CH_4 capacity difference between the optimal pressure P_h chosen and the initial pressure P_l = 5.8 bar. Red triangles denote the points which are infeasible and the green triangles denote the points which are feasible with respect to the process constraints.

certain minimum value of CH_4 maximum saturation storage capacity q^s below which feasibility with respect to the process constraints is not achieved. Similarly, very high and low values of $b^0_{CH_4}$ are also not feasible, resulting a range in the input parameter space which widens as q^s increases. Based on these characteristics observed in the feasibility map of the isotherm space, an isotherm space spanning the range of isotherms which correspond to these parameters can be obtained. A moderate range of $b^0_{CH_4}$ required for feasible process operation, precludes highly flat and highly steep isotherms in the initial low pressure region. Similarly, a certain minimum value of q^s, will result in the set of isotherms which result in process feasibility to have a certain minimum storage capacity at 65 bar. This can be observed in the range of the isotherms of CH_4 and N_2 which result in process feasibility. The shape of the N_2 isotherm space is a direct consequence of the sampling strategy which constraints the initial isotherm slopes of N_2 below that of CH_4 which is the case with a majority of CH_4 selective materials. This is well evident from the extent of the ranges of the isotherm spaces which result in feasible process operation as observed from FIg. 3.17. A salient and important understanding obtained from this map is that isotherms outside

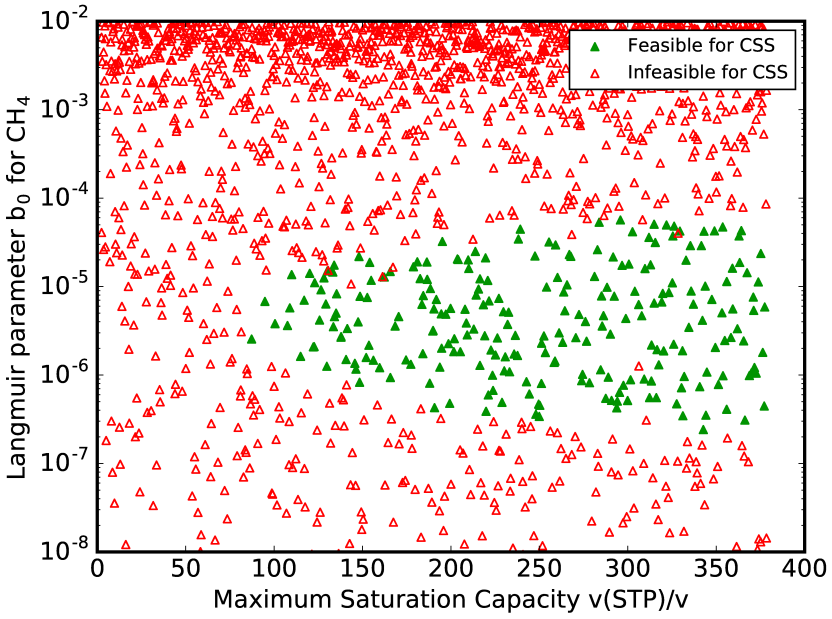

Figure 3.16: Feasibility map corresponding to the input adsorbent parameter space spanned by $b^0_{CH_4}$ and maximum volumetric saturation storage capacity q^s for feed of 85% CH_4 and 15% N_2. Red triangles denote the points which are infeasible and the green triangles denote the points which are feasible with respect to the process constraints.

of these ranges are not favorable to meet the process constraints. Though Fig. 3.15 describes the

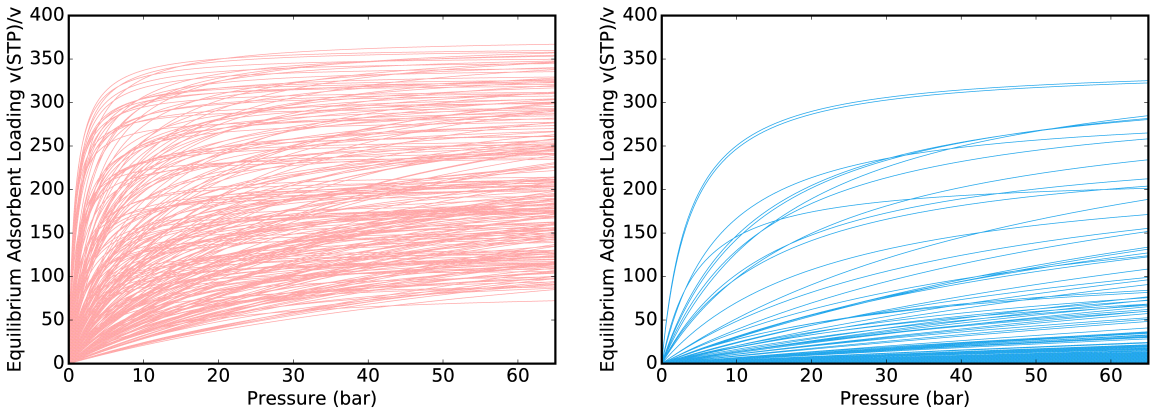

(a) CH_4 isotherms

(b) N_2 isotherms

Figure 3.17: CH_4 and N_2 space of isotherms feasible for process operation at 298 K and feed of 85% CH_4 and 15% N_2.

feasible and infeasible region with respect to the process performance constraints of CH_4 loss and CH_4 purity, the extent of the constraint violation at different values of the material properties are depicted in Fig. 3.18. These express the deviation of the CH_4 loss fraction from l_{max} = 0.10 and the reduction in the purity fraction of stored CH_4 from pur_{lim} = 0.90. The plots in Fig. 3.18 display a gradation in the magnitude of constraint violation with the value of the material metrics. It is observed that in Fig. 3.18a the constraint violation reduces as the process proceeds toward higher value of CH_4 storage capacity at the region where CH_4 storage capacity is very low. Beyond a certain minimum value of CH_4 storage capacity, the Henry co-efficient of CH_4 which influences the initial slope of the isotherm is important for determining the constraint violation. For a given value of CH_4 storage capacity at 65 bar, a lower Henry co-efficient or a less steep isotherm is beneficial in reducing the constraint violation. As the CH_4 storage capacity, increases the minimum CH_4 Henry coefficient necessary to maintain feasibility also increases. In Fig. 3.18b, similarly, a certain minimum difference in the CH_4 adsorbent loading capacity between the initial pressure P_l = 5.8 bar and optimal CSS filling pressure chosen of P_h *i.e.* deliverable capacity. For a given CH_4 loading capacity difference, higher CH_4 Henry coefficient is preferred, as it dictates the magnitude of the loading capacities at P_h and P_l. The overall shape of the plot is constrained by the single-site isotherm equation, as only a certain range of CH_4 Henry coefficients can lead to a certain CH_4 deliverable capacity. These constraint violation maps can be very useful in determining the extent of deviation from feasibility for a particular set of material property metrics for a chosen process configuration. It is important to note that the constraint violation values at each data point in the material property space are obtained as a result of solving a minimization problem which allows for inherent flexibility in the choice of the process decision variables to achieve the minimum.

3.6.4 Identifying Key Constraints and Variables Influencing Process Feasibility

To understand the reason for the nature of the feasibility maps, it is important to understand the individual contribution of both the process constraints namely CH_4 loss and CH_4 purity on the overall feasibility. Constraint violation maps can enable understanding the constraints which govern the process and the range in the material property space where they are active, inactive or

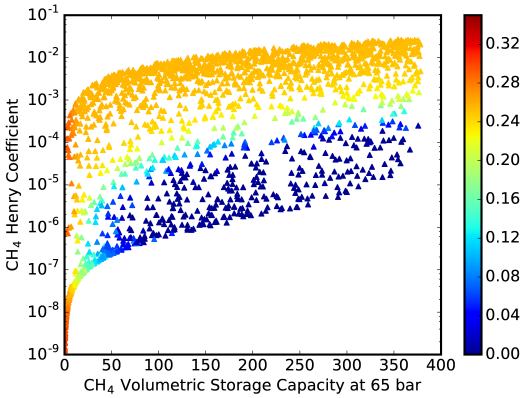

(a) Total Constraint violation: CH_4 Henry coefficient vs CH_4 storage capacity at 65 bar

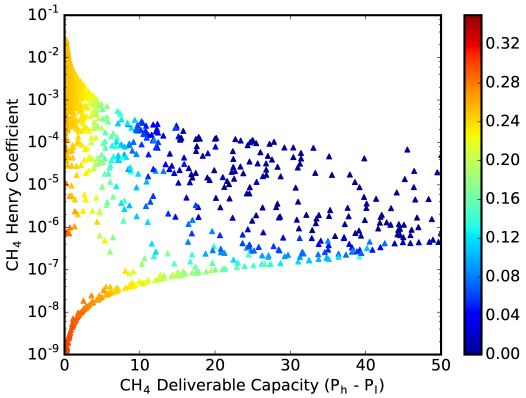

(b) Total Constraint violation: CH_4 Henry coefficient vs CH_4 deliverable capacity

Figure 3.18: Constraint violation map corresponding to CH_4 Henry coefficient and metrics such as CH_4 storage capacity at 65 bar and the CH_4 capacity difference between the optimal pressure P_h chosen and the initial pressure P_l = 5.8 bar

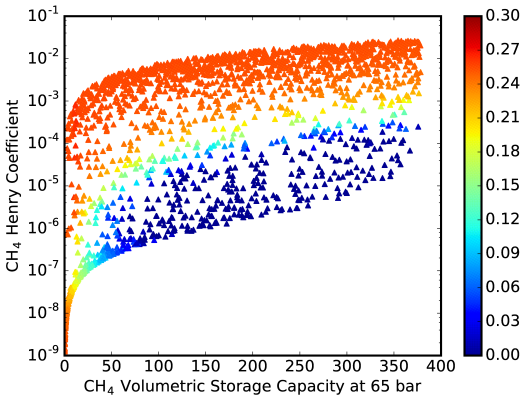

(a) Loss Fraction Constraint Violation

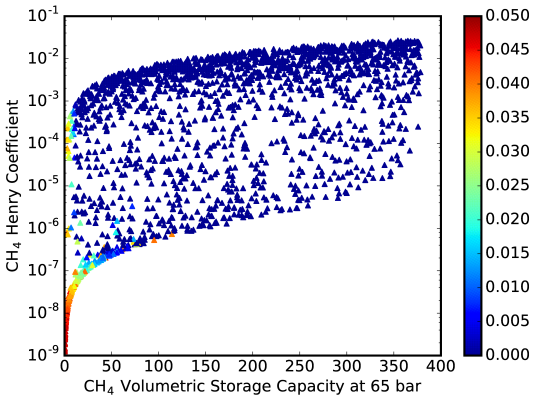

(b) Purity Fraction Constraint Violation

Figure 3.19: Constraint violation map corresponding to CH_4 Henry coefficient and CH_4 storage capacity at 65 bar for CH_4 loss and CH_4 purity constraints

violated. For example, Fig. 3.19a and b shows the constraint violation for the CH_4 loss and CH_4 purity constraint respectively. It can be observed that a smaller subspace of the mapped material property space meets the constraint on CH_4 loss fraction compared to that of the purity fraction of the stored CH_4 in the column. For this feed of 85% CH_4 and 15% N_2, the purity constraint on CH_4

is largely satisfied in the material property range considered due to the high purity of gas stored initially in the column before the pressurization step and the feed having a high CH_4 content at 85%. The loss constraint however is representative of the ratio of moles of CH_4 exiting the column along with N_2 to the moles of CH_4 fed to the process. The mole fraction of CH_4 in the gas phase

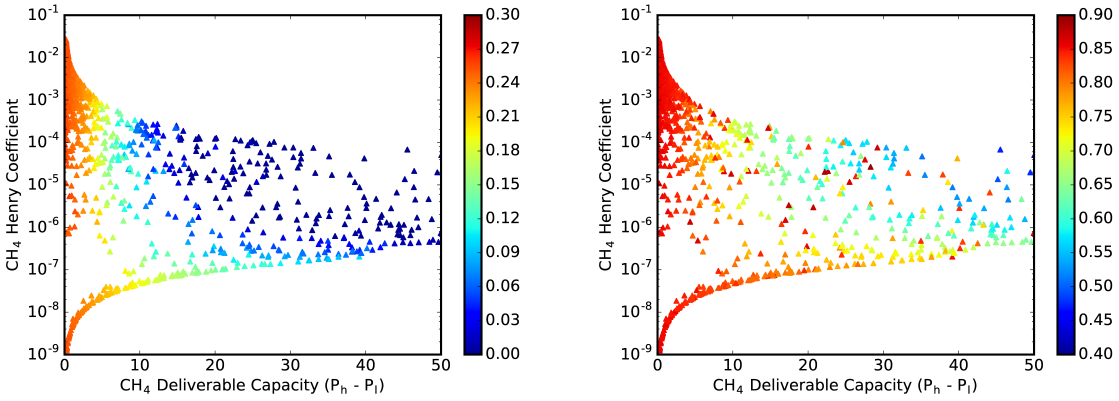

(a) Loss Fraction Constraint Violation

(b) Mole fraction of CH_4 in the gas phase

Figure 3.20: Constraint violation map corresponding to CH_4 Henry coefficient and CH_4 capacity difference between the optimal pressure P_h chosen and the initial pressure P_l = 5.8 bar for the loss constraint. It loosely follows the pattern of variation in gas phase CH_4 mole fraction in the column just before the start of the combined separation and storage step.

of the column after the pressurization step and just before the start of the combined separation and storage step just before the outlet of the column is opened will influence the loss of CH_4 through the outlet during the process. This is evident from Fig. 3.20, where the pattern of the variation in the loss fraction constraint violation loosely follows that of mole fraction of CH_4 in the column in the gas phase $y_{CH_4}^{e,press}$, just before the start of the combined separation and storage step. The higher the CH_4 adsorbent loading capacity difference from the initial fixed pressure P_l and the optimal pressure of operation P_h, the higher is the capacity of the adsorbent to adsorb CH_4 from the gas phase and thereby reduce the mole fraction of CH_4 in the gas phase. This results in the lower value of CH_4 exiting through the column outlet when it is opened leading to lower values of loss. Since the overall feasibility over most of the material property range is primarily influenced by the loss

constraint violation, it can be concluded that the mole fraction of CH_4 in the gas phase before the outlet of the column is opened has a considerable effect on the process feasibility for this feed condition.

3.6.5 Existing and Hypothetical Zeolite Database Structures in the Feasibility Map

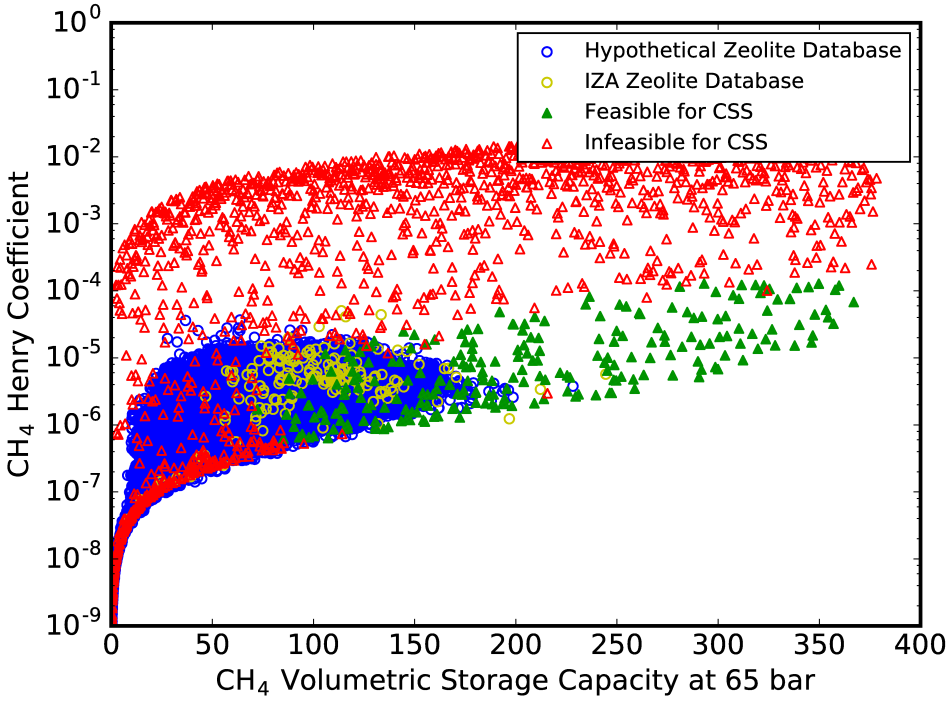

Figure 3.21: Existing and hypothetical zeolite frameworks in the feasibility map corresponding to the material property space spanned by CH_4 Henry coefficient and CH_4 volumetric storage capacity at 65 bar for feed of 85% CH_4 and 15% N_2. Red triangles denote the points in the material property space which are infeasible and the green triangles denote the points which are feasible with respect to the process constraints. The set of points shown in blue are obtained from the loading data for the hypothetical zeolite data set of zeolites made available by Simon *et al.* [46] and the yellow circles are the values obtained in this work for the existing IZA [78] zeolite structures.

The main advantage of utilizing the multi-scale process and material optimization framework is in obtaining target material properties which can maximize the process objectives subject to the constraint imposed on some of the process metrics. Feasibility maps discussed in the previous sub-

sections enable identifying material property ranges for maintaining feasibility with respect to the process constraints. Similarly the values of the process metrics can also be optimized and plotted as a function of the material property space. In Fig. 3.21, the CH_4 Henry coefficients and the CH_4 storage capacities obtained in this work for the considered 178 pure silica zeolitic frameworks in the International Database of Zeolite structures are plotted in the material property space as yellow circles. Furthermore, the 139,500 hypothetical computational zeolitic structures from the database of hypothetical structures [79] for which the CH_4 isotherm loading data and Henry coefficient data that has been laboriously obtained using molecular simulations and made publicly available by Simon *et al.* [46] at `http://nanoporousmaterials.org/methanestorage/` are plotted as blue circles. The geometric properties such as void fraction, crystal density, largest included diameter and accessible surface areas are also available. Depending on the desired target value of the material properties in terms of CH_4 storage capacity and CH_4 Henry coefficient required, appropriate range of geometric properties and/or sets of crystal structures can be identified from the database for further analysis and experimentation. Similarly, by superimposing the properties of these structures onto the constraint violation/optimal process metric maps of the material property space, the candidate material structures best suited for further investigation and the directions for material property improvement can be identified. Once the map is established for a given process design, data of multiple classes of materials such as metal-organic frameworks, zeolitic imidiazolate frameworks can be superimposed onto the maps to readily determine the best candidates.

3.7 Section Summary

A novel combined separation and storage (CSS) process technology for simultaneously separating and storing CH_4 from unconventional sources in a column filled with zeolite adsorbent was designed and optimized. The selective separation and storage capabilities of zeolite adsorbents were examined using optimization insights in order to develop a multi-functional intensified process. Material properties were obtained based on Monte Carlo simulations on pure silica zeolitic frameworks. The dynamic model describing the entire process was discretized to an algebraic form to be posed as a non-linear optimization problem which was optimized for every material. A

suitable initialization strategy was devised to aid convergence and reduce computation time. The key advantage with using such a completely discretized model is that the optimal conditions and materials can be recalculated for any changes in the process conditions (e.g. feed compositions) with ease. Material screening through process optimization was performed for feeds with varying CH_4 and N_2 compositions to obtain a combination of a zeolite and the corresponding process conditions which maximizes CH_4 storage subject to process constraints.

Among the zeolites considered, zeolites SBN, AFY, RHO, APD, DFT, EMT and STW are found to be most suitable for the CSS process for a variety of CH_4/N_2 feeds. The highest CH_4 storage obtained is 240.95 v (STP)/v for a feed of 85% CH_4/15% N_2 using zeolite SBN and operating the CSS mode of the process at a pressure of 64.82 bar. It is observed that the intensification of CH_4 separation and storage is primarily limited by the need to contain the loss of CH_4 through the column outlet. The top zeolites obtained and their corresponding optimal conditions vary with different feed compositions investigated. While these zeolites show promise for being applicable for CSS operation, zeolite selection decisions can be further influenced by the presence of impurities in the feed and the introduction of cations into the zeolites. From the process operation perspective, the relative ranking of materials can change with changes in the values of bounds imposed on the decision variables such as filling time t_f, feed velocity v_f. Similarly changes in the maximum CH_4 loss percentage allowed and minimum purity required constraints will also affect the optimal process decisions and material obtained. Increase in the percentage of impurity in the feed and especially, the presence of strongly adsorbing gases like CO_2 is found to reduce both the CH_4 storage capacity and the number of zeolites feasible for the CSS process operation.

Subsequently, the adsorption isotherm parameters for the zeolites themselves are set as decision variables in the complete algebraic optimization formulation of the model. The objective function for optimization is set as the total violation from the process performance constraints, such as CH_4 purity and CH_4 loss, imposed on the process. Based on the optimization results, a map of feasible operation of the process and the extent of its deviation from feasibility is presented as a function of material metrics. From this, the key constraints and variables which influence

process feasibility at different material property ranges is identified. The material properties of both existing and a large number of hypothetical structures available in public databases is plotted onto the material property space. This can enable identifying structures corresponding to desired target properties. Thus a multi-scale optimization based approach is useful to effectively determine process conditions, screen material candidates and determine target material properties during the design stage for novel intensified multi-functional processes such as CSS.

4. APPLICATION TO INTEGRATED CARBON CAPTURE AND CONVERSION (ICCC) PROCESS*

4.1 Key Contributions

In recent years, the concentration of carbon dioxide (CO_2) in the atmosphere has reached the highest level (>400 ppm) in recorded history [122]. CO_2 is a major greenhouse gas (GHG) and has been linked to global warming [123]. Adverse effects of global warming include climate change, extreme weather events, melting of polar ice caps, rise of sea levels and oceanic acidification [124]. The increased levels of CO_2 in the post-industrial period is attributed to the burning of fossil fuels [125, 126]. Emissions at the current rates would lead to increased global warming and the resulting adverse impacts in the future could be larger as compared to the last century [126]. World energy consumption will see a 48% increase from 2012 to 2040 and fossil fuel sources will still account for 78% of the world energy consumption in 2040 [127]. Reduction of CO_2 emissions by at least 50% is necessary to restrict the global temperature rise to 2°C by 2050 [128, 129]. Hence it is imperative to reduce CO_2 emissions from fossil fuel consumption.

While Carbon Capture and Sequestration (CCS) [14, 71, 123, 130–132] has the potential to reduce CO_2 emissions from energy sector by 20%14, high costs prevent the technology from being implemented on a large scale. For power plants, estimated cost for CCS ranges from \$60–\$114/ton of CO_2 avoided [133, 134]. The capture/separation step of CCS is the most energy intensive and hence accounts for a large share (60–70%) of the total cost. After the capture, there is cost associated with compression to high pressures (150 bar) for transportation via pipelines to storage sites [131, 135]. Additionally, limited geological storage capacity at certain locations, concerns over possible leaks, and costs associated with rigorous monitoring of injected CO_2 have raised concerns towards widespread implementation of CCS [129, 136].

*Reproduced in part with permission from Iyer, S. S., Bajaj, I., Balasubramanian, P. and Hasan, M. M. F., "Integrated Carbon Capture and Conversion to Produce Syngas: Novel Process Design, Intensification and Optimization" *Industrial & Engineering Chemistry Research*, 56(30), 8622-8648. Copyright 2017 American Chemical Society. Available at `https://pubs.acs.org/doi/abs/10.1021/acs.iecr.7b01688`

In the light of these issues with CCS, an alternative way to reduce CO_2 emissions is the capture and conversion of CO_2 to useful products which can be sold for profit [129]. CO_2 can be used as a source of carbon for chemicals such as syngas (a mixture of H_2 and CO), methanol, formic acid, carbonates, polymeric materials, fine chemicals, etc [123]. Specifically, CO_2 conversion to syngas has been widely studied in literature [137–139]. Syngas is a universal precursor that can be converted to various fuels and hydrocarbons [136] via Fischer-Tropsch synthesis which makes a potential case for large-scale CO_2 utilization to address the scale of global CO_2 emissions (around 35 Gt per year) [123, 140]. Different reforming approaches of natural gas using CO_2 (dry reforming [141, 142], mixed reforming [143], and tri-reforming [20]) have been studied as they can produce syngas with varying H_2/CO ratios. A recent study reports that CO_2 reforming has lower capital and operating cost compared to steam reforming, assuming CO_2 feed has negligible cost [144].

CO_2 capture and conversion also poses several technological challenges [145]. Firstly, due to high thermodynamic stability of CO_2, its conversion is energy-intensive [123, 129]. Secondly, existing utilization technologies use mostly high-purity CO_2 obtained from isolated capture plants. The cost of product syngas becomes high because of the additional expense ($35–$50 per ton) [67, 146] and high energy penalty (10–30% of power plant output) associated with CO_2 capture. Thirdly, the lack of proper integration between capture and conversion may lead to an overall negative utilization of CO_2 when auxiliary emissions from electricity consumption are considered.

To this end, process intensification [94–96] is paramount towards making carbon capture and conversion viable for large-scale deployment. Intensification can be achieved by combining the salient features of individual process technologies. Examples include multi-functional reactors [5, 147, 148], membrane reactors [149, 150], layered bed adsorption columns [9, 10, 151], sorption-enhanced reaction processes (SERP) [6, 7, 152, 153], combined separation and storage (CSS) [77], and multi-material simulated moving bed (MSMB) [12]. In the context of CO_2 utilization, an intensification method would have significant impact if it could combine post-combustion CO_2 capture and CO_2 reforming in a manner that would break the current barrier of high cost and high

energy penalty while ensuring a net positive CO_2 utilization.

This work is an attempt to combine and further intensify the post-combustion capture of CO_2 from flue gas (a mixture of predominantly N_2 and CO_2) with CO_2 conversion to produce syngas towards "direct" utilization of CO_2 at the source. In pursuit of this goal, an integrated carbon capture-conversion (ICCC) process [109] is designed and its technical and economic feasibility is evaluated. The key contributions are described as follows:

1. *Process Design and Intensification:* A conceptual design of a modular and multi-functional cyclic process is put forward to simultaneously capture CO_2 from flue gas, release CO_2 using methane/natural gas/fuel gas/biogas/landfill gas to provide a mixture of methane and CO_2 for dry reforming, and convert the mixture into syngas. Unlike independently operated/standalone capture and conversion processes, our integrated carbon capture and conversion (ICCC) process eliminates energy intensive temperature and /or pressure swings in the regeneration step of CO_2 capture by combining the CO_2 desorption with the reactor feed premixing step, which significantly reduces the overall energy penalty and cost of CO_2 utilization.

2. *High-Fidelity Model-based Process Simulation:* To establish the techno-economic feasibility and to predict the performance of our technology, rigorous simulation is performed using a detailed process model. The model describes the dynamics and interaction of the adsorption-purge-reaction system and is implemented to perform rigorous process simulations elucidating the key variables affecting the process.

3. *Process Optimization:* Though the conceptual design is innovative, it is imperative to optimize the process under physical, operational and regulatory constraints while meeting the product quality specifications. A simulation-based, data-driven and constrained grey-box optimization framework is developed to obtain feasible and optimal process configurations and operating conditions. The objectives of process optimization include (i) maximizing net utilization of CO_2, (ii) minimizing energy penalty and operating cost of the process, and

(iii) minimizing total cost of syngas production via "direct" CO_2 utilization. The objectives are met while operating within specified conditions for CH_4 and CO_2 losses, operational constraints, and bounded syngas ratios.

4. *Robustness and Techno-economic Analyses*: A simulation-based constrained optimization method is applied to find feasible operating windows, CO_2 utilization and total costs for a range of feed conditions to computationally show the robustness of the proposed technology.

In the subsections that follow, the description of the proposed ICCC process and its potential for utilizing greenhouse gases for both centralized and distributed chemicals manufacturing is provided. Next, the high-fidelity process model that is used for process simulation is described. Through rigorous simulations at different conditions, the complex dynamics and interactions between the capture and conversion sections and the effects of key design variables on the process performance are elucidated. This is followed by a discussion on the grey-box constrained optimization framework and optimization results for different methane-based feedstocks. Finally, remarks summarizing this section are provided.

4.2 Integrated Carbon Capture and Conversion (ICCC) Process

The key idea and the grand scope of the proposed process and the description of the detailed configuration of the process is provided as follows.

4.2.1 Key Concept

In this work, process intensification is defined as the merging of isolated processes with different core objectives e.g. CO_2 capture, syngas production into a process which can achieve integration of both objectives e.g. direct utilization of CO_2 from flue gas to syngas, in an attempt to reduce the cost and/or energy consumption. The proposed integrated carbon capture and conversion (ICCC) process uses flue gas as a source of CO_2, and natural gas/biogas/landfill gas/fuel gas as a source of CH_4. Since the feeds (especially flue gas) contain significant amount of N_2, the process has been designed to achieve four major tasks – (i) preferential adsorption of CO_2 over N_2 from flue gas using an adsorbent, (ii) CO_2 desorption, (iii) mixing of CO_2 and methane at a

ratio appropriate for dry reforming, and (iv) dry reforming of the CO_2/methane mixture to produce syngas over a catalyst. The novelty of this work is the simultaneous desorption (purging) of CO_2 and mixing of CO_2 and CH_4 through the use of methane (CH_4) rich feed. The introduction of the methane rich feed into a column saturated with adsorbed CO_2 reduces the partial pressure of CO_2 in the gaseous phase, thereby creating a concentration driving force for CO_2 desorption and a working capacity for adsorption-based CO_2 capture. This allows to partially regenerating the process at the same pressure and temperature of CO_2 adsorption without consuming energy as in the case of pressure and temperature swing adsorption (PSA and TSA) processes. A schematic of the effect of changing the concentration of CO_2 in a multi-component mixture on the equilibrium adsorbent loading and the working capacity is depicted in Figure 4.1. CH_4 rich feed is chosen to desorb the CO_2 via dilution, since the final goal is to convert the desorbed CO_2 to syngas using CH_4. Hence, the mixing of CO_2 and CH_4 would not be an issue. The mixing of CH_4 with CO_2 within the adsorption column also facilitates the feed preparation for subsequent dry reforming. Therefore, we have essentially combined the CO_2 desorption or regeneration step of the capture part with the reactor feed premixing while eliminating the need for any temperature and/or pressure swings. While concentration swing-based gas desorption and enrichment has been suggested in the past48,49, our proposed dilution of CO_2 using CH_4 is unique in a sense that it integrates both the regeneration and reactor feed pre-mixing for process intensification.

4.2.2 Process Configuration

The ICCC process shown in Figure 4.2 implements the intensification concept discussed above. Specifically, it involves separation of CO_2 from flue gas by selective adsorption in a column filled with a microporous material such as zeolite 13X followed by subsequent desorption of the adsorbed CO_2 using a methane (CH_4) rich feed. The outlet gas is then sent to the reactor for conversion of CO_2 to syngas. This is achieved in two steps run in a cyclic manner. In the first step, flue gas (N_2/CO_2 = 86% / 14%) is fed to the adsorption column for a time t_1 while in the second step, CH_4 rich feed is fed to the column for rest of the cycle duration (t_c). The high concentration of CH_4 in the feed gas of the second step leads to desorption of the CO_2 adsorbed in the column.

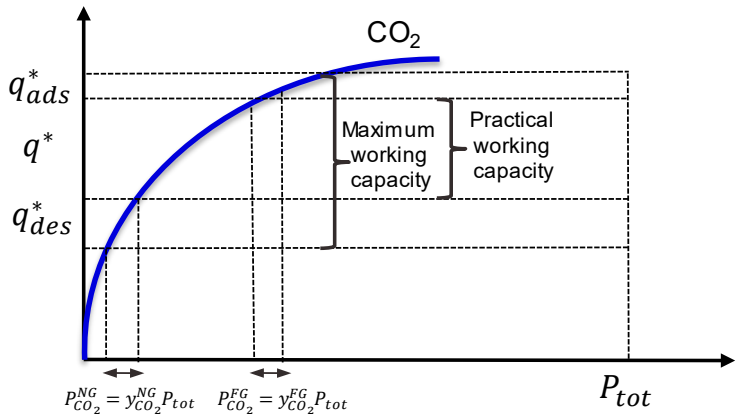

Figure 4.1: Schematic of the concentration driving force for adsorption and desorption of CO_2 from multi-component mixture using feed switching. Adsorbent capacity/loadings at equilibrium q^* is affected by the partial pressure of CO_2 in the multi-component mixture introduced i.e. flue gas or methane-rich feed e.g. natural gas. This leads to the possibility of a working capacity due to differences in equilibrium adsorbent loading of CO_2 in different feeds. Practical working capacity obtained will also depend on cycle times, feed step durations, kinetic factors and nature of isotherms of other gases relative to CO_2. The total pressure P_{tot} is kept constant (Iyer *et al.* [109]).

The CO_2 desorption is achieved by a change in concentration, rather than a change in pressure (PSA process) or temperature (TSA process) thus reducing the energy costs. The outlet gas from the column contains a mixture of CO_2, N_2 and CH_4. Since the final aim is to convert CO_2 to syngas which is usually achieved through reactions using CH_4, the outlet gas from the adsorption column can be directly sent to the reactor. The reactor section is filled with a suitable catalyst, where CO_2 reforming takes place leading to the formation of syngas. Since N_2 does not participate in the reforming reactions, the outlet gas from the adsorption column is vented out between two chosen times to remove N_2 without a considerable loss of CO_2 and CH_4. The adsorption column outlet gas from the non-venting period of each cycle is mixed and fed to the reactor throughout the duration of the cycle at a constant rate and composition. This makes the overall process continuous without interruptions. In practice, this can be achieved by collecting the outlet gas in a large well-mixed tank and setting the reactor feed withdrawal flow rate appropriately. This also enables us to study and optimize the process without dealing with the increased complexities associated with

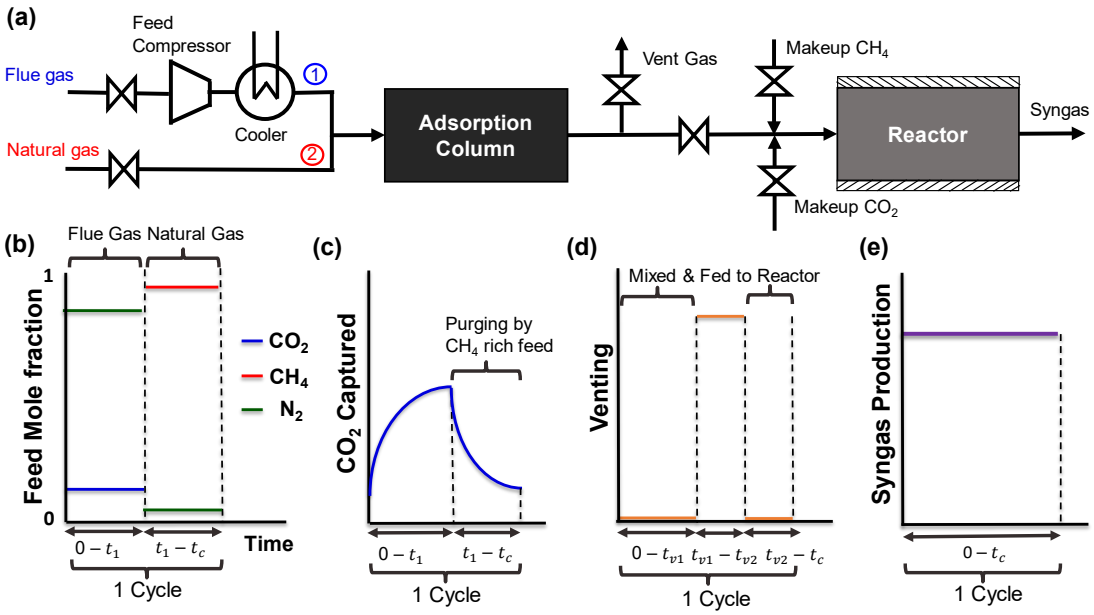

Figure 4.2: Process schematic for integrated carbon capture and conversion (ICCC) process. (a) The process is operated in a cyclic manner, where each cycle consists of two steps 1 and 2. t_1 is the duration of step 1, and t_c is the total cycle time. In step 1, flue gas is fed to the adsorption column, while in the second step, CH_4-rich feed e.g. Natural gas is fed to the column to desorb CO_2. The outlet gas from the adsorption column during the period when it is rich in N_2 is vented out and outlet gas from the rest of the cycle when it is rich in CH_4 and CO_2 becomes reactor feed. It is further mixed with makeup feed and fed to the reactor for continuous operation (b) Schematic of feed mole fraction variation with time. Flue gas feed of composition 14% CO_2 and 86% N_2 while Natural gas of composition 95% CH_4 and 5% N_2 is used. (c) Schematic of CO_2 captured/adsorbed and desorbed in the column at cyclic steady state. (d) Times of the cycle during which outlet gas from adsorption column is vented or mixed and fed to the reactor. t_{v1} is the venting start time and t_{v2} is the venting end time. (e) Schematic of syngas produced at the outlet of the overall process (Iyer *et al.* [109]).

operating the reactor at time-varying feed conditions. Makeup or extra CO_2 and CH_4 may be added to the reactor feed to ensure flexibility to meet the product specifications at the reactor outlet for a variety of operating conditions and feeds (flue gas, biogas, natural gas, etc.). The process thus demonstrates a potential to leverage the dynamic nature of the adsorption process while integrating it with conventional fixed bed reactor systems for CO_2 conversion to syngas.

4.2.3 Scope of Implementation

At least two scenarios for the implementation of the proposed technology are envisioned. One is a modular implementation for a grass root design for the utilization of small, stranded, unutilized and unconventional methane. An example of such unconventional methane is the excess fuel gas available in a refinery or a chemical plant. The lack of pressure and temperature changes further adds to the benefit of employing our technology on a modular level, thereby enhancing its applicability for stranded sources. The other possible implementation is within an integrated power and chemical complex (Figure 4.3) that co-produce fuels, power and chemicals. A part of the flue gas from the power generation section can be "directly" sent to the ICCC plant, while the rest can be processed via standalone CO_2 capture plant. The pure CO_2 obtained from the capture plant can then be either used for conversion or sent for external utilization or sequestration purposes. In this way, a balance can be struck between emission, utilization and storage for decarbonization at reduced overall cost of CO_2 avoidance.

4.3 Process Modeling and Simulation

The performance of the process needs to be predicted well to warrant selection of appropriate conditions and to evaluate different tradeoffs. To identify key decision variables which influence the feasibility of the process, it is important to model the overall process and study its behavior. The process is divided into two major sections, namely the adsorption and reaction sections, which are modeled as described below.

The process model for the adsorption section is similar to the one used for describing the combined separation and storage process in the previous section and hence is described in Appendix B.1.

4.3.1 Configuration of the Process Cycle

Since the process involves two feed steps repeated in a cyclic manner, variables are defined to denote different instances of time in the cycle, namely, the total cycle time (t_c) and the step-1 duration (t_1), both in seconds. t_{min} is the lower bound for the duration of any step while t_{max} is

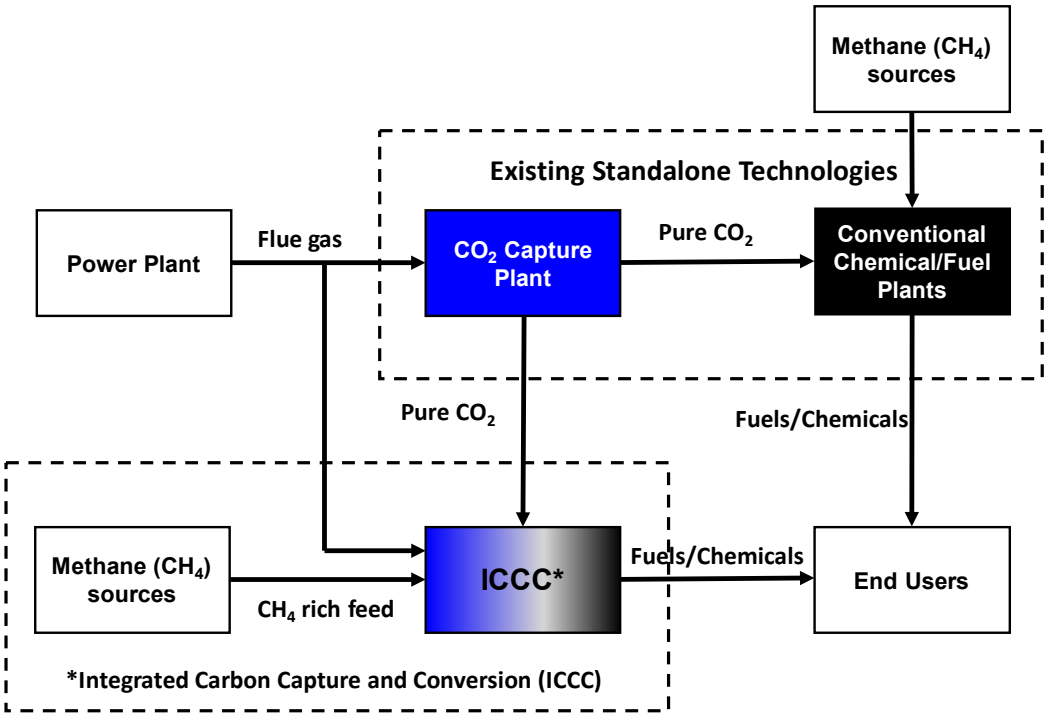

Figure 4.3: Integrated power and chemical production complex employing ICCC technology. Integration of the proposed process (ICCC) with existing CO_2 capture and utilization plants as shown can reduce the overall costs of CO_2 capture and utilization. Our process would utilize both low-cost flue gas and small, stranded and unconventional methane sources to produce syngas, a precursor to many fuels and chemicals (Iyer *et al.* [109]).

the upper bound for the total cycle duration. The configuration of the cycle, i.e., the chronology and duration of the two feed steps and the bounds on the cycle time are specified in eq. 4.1–4.3.

$$t_{min} \leq t_1 \leq t_c \tag{4.1}$$

$$t_{min} \leq t_c - t_1 \leq t_c \tag{4.2}$$

$$t_{min} \leq t_c \leq t_{max} \tag{4.3}$$

For the venting cycle, t_{v1} is defined as the time in seconds from start of cycle to the time at which venting starts, while t_{v2} is the time (s) at which venting ends. Therefore, the period at which venting is active is between $t_{v1} - t_{v2}$. Constraints which describe the times at which venting of the

outlet gas from the adsorption is performed are described in Eq. 4.4–4.6.

$$0 \leq t_{v1} \leq t_c \tag{4.4}$$

$$0 \leq t_{v2} \leq t_c \tag{4.5}$$

$$t_{min} \leq t_{v2} - t_{v1} \leq t_c \tag{4.6}$$

The gases at the outlet of the adsorption section during the non-venting period (between 0–t_{v1} and t_{v2}–t_c) is collected, mixed and sent to the reactor section.

4.3.2 Modeling Reaction Section

The outlet gas from the adsorption column pertaining to the non-venting period of each cycle is assumed to be mixed (in a tank) and withdrawn at a constant flow rate as reactor feed. The flow rate is set such that the moles of gas entering the tank from the adsorption column during each cycle are completely withdrawn before the end of that cycle. The withdrawn gas is mixed with appropriate amounts of makeup CO_2 and CH_4, and then fed to the reactor. The inlet feed flow rate and composition for the reactor are calculated as follows:

$$F^R_{0,i} = \frac{n^{NV}_i}{t_c} + \sum_{j \in J_M} y^{mk}_{i,j} F^{mk}_j \qquad \forall\, i \in I_A \tag{4.7}$$

$$n^{NV}_i = \int_0^{t_{v1}} y^{A,out}_i F^{A,out}_i dt + \int_{t_{v2}}^{t_c} y^{A,out}_i F^{A,out}_i dt \qquad \forall\, i \in I_A \tag{4.8}$$

$$F^{A,out}_i = \frac{\varepsilon A_{c,a}\, v|_{z=L_a}\, y_i|_{z=L_a}\, P|_{z=L_a}}{RT|_{z=L_a}} \qquad \forall\, i \in I_A \tag{4.9}$$

where $F^R_{0,i}$ is the molar feed flow rate of species $i \in I_A$ fed to the reactor section in mol/s, n^{NV}_i is the moles of species i collected during the non-venting period, F^{mk}_j is the molar flow rate of makeup feed $j \in J_M = \{CO_2, CH_4\}$ in mol/s, $y^{mk}_{i,j}$ is the composition of species i in makeup feed $j \in J_M$. Note that $y^{A,out}_i \left(= y_i|_{z=L_a}\right)$ and $F^{A,out}_i$ are the mole fraction and the corresponding molar flow rate in mol/s of species i, respectively at the outlet of the adsorption column at any given time t, while $A_{c,a}$ is the cross-sectional area of the adsorption column in m^2. The superscripts "A, out" and "mk" pertain to the adsorber outlet and makeup feeds, respectively.

The reaction considered for conversion of CO_2 to syngas uses CH_4 and is known as CO_2-reforming or dry reforming. While dry reforming may suffer from coke formation [154], it is not considered it in this work. The reactions involved in dry reforming are as follows:

$$CH_4 + CO_2 \rightleftharpoons 2\,CO + 2\,H_2 \quad \Delta H_{298\ K} = +247.0\ \text{kJ/mol} \quad \text{(R1)}$$

$$CO_2 + H_2 \rightleftharpoons CO + H_2O \quad \Delta H_{298\ K} = +41.7\ \text{kJ/mol} \quad \text{(R2)}$$

The CO_2-reforming of methane (R1) is a reversible and highly endothermic reaction and results in an increase in the number of moles. Hence, the production of syngas is thermodynamically favored at low pressures and high temperatures. The high endothermicity of the reaction makes this reaction energy intensive. The reverse water gas shift reaction (R2) is also an endothermic reaction.

The reactor feed thus obtained is heated to the reactor temperature (T_R) in the furnace of the reformer. The heat duty required in W is given by eq. 4.10.

$$Q_f = \frac{\sum_i n_i^{NV}}{t_c} \int_{T^{A,out}}^{T_R} C_{pm} dT + \sum_{j\ \in\ J_M} \left(F_j^{mk} \int_{T_f^{mk}}^{T_R} C_{pm,\ j} dT \right) \tag{4.10}$$

where $T^{A,out}\left(= T|_{z=L_a}\right)$ is the outlet temperature at the adsorption section in K, T_f^{mk} is the feed temperature of the makeup feeds in K, C_{pm} is the specific heat capacity of the appropriate gas mixture in J/mol/K calculated using Eq. 4.11. The variation of specific heat capacity with temperature is considered as per the Shomate equation as follows:

$$C_{pm} = \sum_{i\in I_m} y_i A_i + \sum_{i\in I_m} y_i B_i \left(\frac{T}{1000}\right) + \sum_{i\in I_m} y_i C_i \left(\frac{T}{1000}\right)^2 + \sum_{i\in I_m} y_i D_i \left(\frac{T}{1000}\right)^3 + \sum_{i\in I_m} y_i E_i / \left(\frac{T}{1000}\right)^2 \tag{4.11}$$

where I_m is the set of species present in the gas mixture considered. The values of the constants are taken from the NIST website [155].

A pseudo-homogenous model is used for modeling the reactor and its assumptions are listed as follows:

- Ideal gas behavior
- Steady state operation

- Isothermal operation
- One dimensional plug flow behavior
- Concentration, temperature and pressure gradients in radial direction are neglected
- Axial dispersion is neglected
- The thermal and chemical equilibrium between the bulk and the catalyst surface are achieved instantly, i.e. the gas and the catalyst have the same temperature and concentration.
- The catalyst effectiveness factor is assumed to be unity.

The component balance for all the species in the reaction mixture is given in eq. 4.12. The set of species considered in the reaction section are I_R = {CO_2, CH_4, N_2, CO, H_2, H_2O}.

$$\frac{dF_i^R}{dz_R} = \rho_b A_{c,r} r_i \qquad \forall\, i \in I_R \quad (4.12)$$

where F_i^R is the molar flow rate in mol/s of each species i inside the reactor bed at any z_R , r_i is the rate of generation of species i per unit mass of catalyst in mol/kg/s, ρ_b is the reactor bed density in kg/m^3, $A_{c,r}$ is the cross-sectional area of the reactor in m^2 and z_R is the spatial co-ordinate along the length (L_R) of the reactor bed in meters ($0 \leq z_R \leq L_R$). The inlet flow rates ($F_{0,i}^R$) for $i \in I_A$ are given in eq. 4.7 and is set to 0 for $i \notin I_A$.

$$r_i = \sum_k \vartheta_{i,k} R_k \qquad \forall\, i \in I_R \quad (4.13)$$

where $\vartheta_{i,k}$ is the stoichiometric coefficient of species i in reaction R_k . For example, $\vartheta_{H_2,1}$ is +2 and $\vartheta_{H_2,2}$ is -1 since two moles of H_2 are formed in reaction R1 while one mole of H_2 is consumed in reaction R2. The reaction kinetics and the parameters are taken from Richardson and Paripatyadar [156, 157] and are given in Table 4.1 and are incorporated in the process model.

$$R_1 = \frac{k_1 K_{CO_2,\,1} K_{CH_4,\,1}\, p_{CO_2} p_{CH_4}}{\left(1 + K_{CO_2,\,1}\, p_{CO_2} + \ K_{CH_4,\,1}\, p_{CH_4}\right)^2} \left(1 - \frac{\left(p_{CO} p_{H_2}\right)^2}{K_{eq,1}\, p_{CO_2} p_{CH_4}}\right) \quad (4.14)$$

$$R_2 = \frac{k_2 K_{CO_2,\,2} K_{H_2,\,2}\, p_{CO_2} p_{H_2}}{\left(1 + K_{CO_2,\,2}\, p_{CO_2} + \ K_{H_2,\,2}\, p_{H_2}\right)^2} \left(1 - \frac{p_{CO} p_{H_2O}}{K_{eq,2}\, p_{CO_2} p_{H_2}}\right) \quad (4.15)$$

Table 4.1: Reaction rate coefficients and parameters for dry reforming of methane (Iyer *et al.* [109]).

Parameter	Value
k_1 [mol/kg cat/s]	$1.29 \times 10^6\ e^{-102065/RT_R}$
k_2 [mol/kg cat/s]	$3.5 \times 10^5\ e^{-81030/RT_R}$
$K_{CH_{4,\ 1}}$ [/atm]	$2.60 \times 10^{-2}\ e^{40684/RT_R}$
$K_{CO_{2,\ 1}}$ [/atm]	$2.61 \times 10^{-2}\ e^{37641/RT_R}$
$K_{CO_{2,\ 2}}$ [/atm]	$0.5771\ e^{9262/RT_R}$
$K_{H_{2,\ 2}}$ [/atm]	$1.494\ e^{6025/RT_R}$
$K_{eq,1}$ [atm^2]	$6.781 \times 10^{14}\ e^{-259660/RT_R}$
$K_{eq,2}$	$56.4971\ e^{-36580/RT_R}$

where p_i is the partial pressure of species $i \in I_R$ in bar given by:

$$p_i = \frac{F_i^R}{\sum_{i \in I_R} F_i^R} \frac{P_R}{10^5} \qquad \forall\ i \in I_R \quad (4.16)$$

where P_R is the pressure in the reactor bed in Pa. The reactor operation is assumed to be isothermal, i.e., the reactor temperature T_R is kept constant. However, heat needs to be supplied to the reactor section to ensure isothermal operation to compensate for the heat consumed by the endothermic reaction. This heat can be provided by appropriate placement of natural gas fired burners along the reactor section. The following equation (eq. 4.17) describes the heat consumed by the reactions taking place in the reactor. Integrating over the length of the reactor bed (z_R), gives the cumulative heat duty (Q_R) in Watt needed to maintain an isothermal operation.

$$\frac{dQ_R}{dz_R} = \rho_b A_{c,r} \sum_k (-\Delta H_k) R_k \quad (4.17)$$

Ergun equation is used to describe the pressure drop in the axial direction in packed beds [158,159].

$$\frac{dP_R}{dz_R} = -\frac{\rho_f u_s^2 (1 - \varepsilon_R)}{d_{p,e} {\varepsilon_R}^3} f \quad (4.18)$$

$$f = \frac{150}{Re^*} + 1.75 \quad (4.19)$$

$$Re^* = \frac{\rho_f u_s d_{p,e}}{\mu_R (1 - \varepsilon_R)} \quad (4.20)$$

where ρ_f and μ_R are the density and viscosity of the fluid (gas) phase in the reactor in kg/m^3 and

Pa s respectively, u_s is the superficial velocity in m/s, ε_R is the void fraction of the reactor bed, f is the packed bed friction factor, Re^* is the modified Reynolds number for packed beds, $d_{p,e}(= \frac{6V_p}{S_p})$ is the effective particle diameter in m of the cylindrical catalyst particle with 10 hole rings. The viscosity of the gas is taken to be the mole fraction average of individual species viscosities which are provided in Table 4.2

Table 4.2: The individual species viscosity values in Pa s used for calculating the overall gas viscosity for the reactor section (Iyer *et al.* [109]).

Species	Viscosity [Pa s]
CO	3.62 E -05
CO_2	3.51 E -05
CH_4	2.4 E -05
H_2O	3.2 E -05
H_2	1.5 E -05
N_2	3.5 E -05

Inlet conditions at the $z_R = 0$ end are given as:

$$F_i^R\big|_{z_R=0} = F_{0,i}^R \tag{4.21}$$

$$P_R\big|_{z_R=0} = P_h \tag{4.22}$$

$$Q_R\big|_{z_R=0} = 0 \tag{4.23}$$

4.3.3 Calculating Process Performance Metrics

To evaluate the performance of the ICCC process for a given set of design and operating conditions, we can use several metrics. These include the overall (net) CO_2 utilization (%), losses or emissions of greenhouse gases (CO_2 and CH_4), and syngas quality (H_2/CO ratio). We also consider various economic costs, which are discussed in the next section.

4.3.3.1 Overall CO_2 Utilization at Cyclic Steady State Condition

The percent overall CO_2 utilization (POCU) over each cycle at cyclic steady state condition accounts for the net CO_2 utilized by the process via various feeds while discounting unreacted CO_2, the lost CO_2 which is vented and the auxiliary CO_2 produced by using heating utilities and electrical power.

Overall CO_2 utilization over one cycle, $$POCU = \frac{CO_{2,\ util}}{CO_{2,\ fed}} \times\ 100 \tag{4.24}$$

$$CO_{2,\ fed} = \int_0^{t_c} F_{CO_2}^{A,in}\, dt + t_c \sum_{j\ \in\ J_M} y_{CO_2,j}^{mk} F_j^{mk} \tag{4.25}$$

$$CO_{2,\ util} = CO_{2,\ fed} - \int_{t_{v1}}^{t_{v2}} F_{CO_2}^{A,out} dt - F_{CO_2}^{R}\big|_{z_R=L_R} t_c - \varphi_h Q_{HU} t_c - \varphi_e E_u \tag{4.26}$$

$$F_i^{A,in} = \frac{\varepsilon A_{c,a}\, v|_{z=0}\, y_i|_{z=0}\, P|_{z=0}}{RT|_{z=0}} \qquad \forall\ i \in I_A \tag{4.27}$$

where $F_{CO_2}^{A,in}$ is the molar flow rate in mol/s of CO_2 entering the adsorption column through either of the feeds, Q_{HU} is the total heating duty requirement in Watt of the process during each cycle, and E_u is "unclean" electricity in kWh contributing to auxiliary CO_2 emissions. If the total electricity requirement (E_t) of the process during a cycle is lesser than the clean electricity available, then the auxiliary CO_2 emission factor φ_e is set to be zero. However, if the electricity requirement is greater than the clean electricity available, then the unclean electricity E_u will contribute to auxiliary CO_2 emissions and an appropriate value for the auxiliary emission factor φ_e is used (e.g., 0.939 ton CO_2 per MWh, if the electricity comes from a coal-fired power plant, as listed in Table 4.3).

The heating requirement (Q_{HU}) is provided by burning natural gas and includes both the reactor feed heating duty (Q_f) and the heat duty (Q_R) necessary to maintain an isothermal operation of the reactor. Therefore, $Q_{HU} = (Q_f + Q_R)/\eta_h$ where η_h is the efficiency of the natural gas-fired furnace. The auxiliary CO_2 emissions by natural gas burnt for heating is calculated by applying the appropriate emission factor φ_h i.e. φ_{NG}. The auxiliary CO_2 emission parameters are obtained from the U. S. Energy Information Administration website [160, 161] and are listed in Table 4.3.

Table 4.3: Raw material pricing and auxiliary CO_2 emission parameters (Iyer *et al.* [109]).

Description	Value
Dehydrated Flue gas price (CO_2/N_2: 14/86 %) ($/ton)	1.87
Natural Gas price (CH_4/N_2: 95/5 %) ($/MMBTU) (Oct 2016)	2.98
Pure CO_2 price ($/ton)	38.5
Methane price ($/MMBTU)	2.98
Electricity price ($/kWh)	0.07
Cooling water ($/ton)	1
φ_{NG} (lb. CO_2/ MMBTU NG burnt)	117
φ_e (ton CO_2/ MWh from coal fired plant)	0.939
Compressor efficiency	0.75
Furnace efficiency	0.8

We assume that the CH_4 rich feeds and the makeup feeds are available at the required pressure of the process. A feed compressor is, however, necessary to compress the flue gas which is usually available at around 1 atm. Electricity is required by the process to run the feed compressor. All electricity is assumed to be sourced from a coal-fired power plant without carbon capture. Use of such electricity results in auxiliary CO_2 emissions. However, since our process utilizes CO_2, the amount of electricity corresponding to the CO_2 processed by the technology from flue gas and the CH_4 rich feed is considered as clean electricity i.e. free from auxiliary emissions and discount it from the total auxiliary CO_2 emitted due to electricity usage.

The total power consumed in kW by the feed compressor is given by:

$$W_{com} = \frac{0.001}{\eta_m \eta_c} F_{FG} R T_f \left(\frac{\gamma}{\gamma - 1}\right) \left(\left(\frac{P_h}{P_0}\right)^{\frac{\gamma-1}{\gamma}} - 1\right) \tag{4.28}$$

here η_m is the electric motor efficiency which is taken as 0.95, η_c is the compressor efficiency which is taken as 0.75, F_{FG} is the inlet flow rate of flue gas in mol/s, T_f is the temperature of flue gas in and is taken to be 298.15 K, and γ for flue gas is taken to be 1.4. F_{FG} is calculated as follows.

$$F_{FG} = \frac{\varepsilon A_{c,a} v_f P_h}{R T_f} \tag{4.29}$$

Since the feed compressor is used only during the flue gas step, the total electricity requirement E_t

in kWh can be calculated as follows,

$$E_t = W_{com} t_1 / 3600 \tag{4.30}$$

Since the use of a compressor results in temperature increase which is calculated as follows [162], a cooler is required which results in cooling utility costs. $T_{o,com}$ is the temperature of gas at the outlet of the compressor in K.

$$T_{o,com} = T_{i,com} + \frac{T_{i,com}}{\eta_c} \left(\left(\frac{P_h}{P_0} \right)^{\frac{\gamma-1}{\gamma}} - 1 \right) \tag{4.31}$$

The cooling duty (Q_C) in kW required to cool the compressed flue gas back to the inlet temperature T_f for the adsorption section is given below:

$$Q_C = F_{FG} \int_{T_{o,com}}^{T_f} C_{pm,\ FG} dT \tag{4.32}$$

The mass of cooling water in kg required in one cycle (M_{CW}) is given by the following equation assuming a ΔT =10 K change in temperature of cooling water. The specific heat capacity of water ($C_{p,\ CW}$) is taken to be 4200 J/kg/K.

$$M_{CW} = t_1 |Q_C| / (C_{p,\ CW} \Delta T) \tag{4.33}$$

The electricity needed for the cooling water system used is around 2 kWh per 1000 gal (0.528 kW per ton of cooling water) [163]. This is deducted from the clean electricity available from processing flue gas and the resulting "unclean" electricity (E_u) is given by the following equation.

$$E_u = E_t - \frac{MW_{CO_2} \int_0^{t_c} F_{CO_2}^{A,in}\, dt}{\varphi_e} - 2\frac{0.528 M_{CW}}{1000} \tag{4.34}$$

where MW_{CO_2} is taken as 44.01$\times 10^{-3}$ kg/ mol.

4.3.3.2 CO_2 and CH_4 Losses

Let $loss_i^t$ denote the fractional loss of a greenhouse gas $i \in \{CO_2, CH_4\}$ from the process either via the vent or as unreacted component in the product syngas. $loss_i^t$ is calculated using the following expressions:

$$loss_i^t = loss_i^V + loss_i^p \qquad \forall\, i \in \{CO_2, CH_4\} \tag{4.35}$$

$$loss^{V}_{CO_2} = \frac{\int_{t_{v1}}^{t_{v2}} F^{A,out}_{CO_2} dt}{CO_{2,\ fed}} \tag{4.36}$$

$$loss^{V}_{CH_4} = \frac{\int_{t_{v1}}^{t_{v2}} F^{A,out}_{CH_4} dt}{CH_{4,\ fed}} \tag{4.37}$$

$$loss^{p}_{CO_2} = \frac{t_c F^{R}_{CO_2}\big|_{z_R=L_R}}{CO_{2,\ in}} \tag{4.38}$$

$$loss^{p}_{CH_4} = \frac{t_c F^{R}_{CH_4}\big|_{z_R=L_R}}{CH_{4,\ fed}} \tag{4.39}$$

4.3.3.3 Syngas Quality Specifications

Though the CO_2 reforming reaction (R1) produces a 1:1 ratio of H_2 and CO, the extent of progress of the reverse water gas shift reaction (R2) which consumes H_2 to produce CO can affect the overall H_2/CO ratio in the product ($y^p_{H_2}/y^p_{CO}$). Product compositions, especially $y^p_{CH_4}$, $y^p_{CO_2}$, $y^p_{N_2}$, are key metrics since they should be within certain limits to ensure the quality of syngas. The product composition for a species y^p_i is calculated as follows:

$$y^p_i = \frac{F^R_i\big|_{z_R=L_R}}{\sum_{i\in I_R} F^R_i|_{z_R=L_R}} \qquad \forall\ i \in I_R \tag{4.40}$$

4.3.4 Economic Assessment

4.3.4.1 Operating Cost per kg of Syngas Produced

The operating costs involves cost of raw materials (C_{RM}), the cost of heating utilities (C_{HU}), cooling utilities (C_{CU}) and electricity (C_E) required by this process. The cost of raw materials used over one cycle is calculated using the following expressions:

$$C_{RM} = c_{FG} F_{FG} t_1 + \int_0^{t_c} \frac{c_{MF} F^{A,in}_{CH_4}}{y_{CH_4,\ MF}}\, dt + \sum_{j\ \in\ J_M} C_j F^{mk}_j t_c \tag{4.41}$$

The raw material cost parameters (such as c_{FG}, c_{FG}) are obtained from various literature sources [1, 67, 164], which are listed in Table 4.3. The cost of the electricity (C_E) required by the process is given by $c_e E_t$ where c_e is the unit cost of electricity and E_t is the electricity requirement of the process. Cost of cooling utility (C_{CU}) required is given by $c_{CW} M_{CW}$ where c_{CW} is the cooling

water price and M_{CW} is the amount of cooling water needed per cycle. Similarly, the cost of heating utilities (C_{HU}) is calculated by $c_{NG}Q_{HU}$ where c_{NG} is the price of natural gas.

The syngas produced is the sum of the moles of CO and H_2 in product. The operating cost per ton of syngas (OC) produced is given by the following equation, where MW_{SG} is the molecular weight of the product syngas in kg/mol.

$$OC = \frac{1000\ (C_{RM} + C_{HU} + C_{CU} + C_E)}{MW_{SG} t_c \left(F^R_{CO}|_{z_R=L_R} + F^R_{H_2}|_{z_R=L_R} \right)} \tag{4.42}$$

4.3.4.2 Total Production Cost per kg of Syngas

To calculate the overall production cost of syngas from the process, it is important to account for both investment and operating costs. These costs are annualized and then converted to cost per ton of syngas produced to evaluate whether the price is competitive. The breakdown of the different costs involved is taken from Hasan *et al.* [165] and is described in Appendix B.2

4.3.5 Process Simulation

To obtain the process metrics which are of interest, the overall process model described above needs to be solved. The model for the adsorption section comprises non-linear algebraic partial differential equations (NAPDE). The partial differential equations (PDE) are spatially discretized into a set of coupled ordinary differential equations (ODEs) by implementing an upwind differencing scheme. Although the accuracy of the model increases with increase in the number of spatial discretizations (N), it also increases the size of the discretized model leading to longer computation times. It is thus important to choose an acceptable value of N for performing the simulation and optimization studies. The set of ODEs along with the initial conditions constitute an ODE initial value problem (ODE-IVP) which is solved using a stiff ode time stepper ode23s in MATLAB®. Based on the solution, the concentration and temperature profiles along the adsorption column are obtained for the first step i.e. flue gas feed. For the second step of the cycle, when the feed is changed to a CH_4 rich feed, the final condition of the column at the end of the first step becomes the initial condition for the second step. The simulations are run for multiple such cycles of steps, until

the concentration and temperature profiles do not show significant change with further increase in the number of cycles, i.e. a cyclic steady state (CSS) is reached. Based on the solution obtained at CSS, the inlet conditions for the reactor section are calculated. The reactor model equations which constitute another ODE-IVP problem is then solved using ode23s. The process and product metrics are then calculated for the overall process.

Table 4.4: Simulation parameters and operating conditions for the reference case simulations (Iyer *et al.* [109]).

Adsorption section conditions	Value
Pressure P_h [bar]	5
Column inner radius r_{in} [m]	0.1445
Adsorption Column Length L_a [m]	1.5
Feed Temperature T_f [K]	298.15
Interstitial feed velocity v_f [m/s]	1
Ambient Temperature T_a [K]	298.15
Step 1 duration t_1 [s]	100
Total Cycle time t_c [s]	200
Venting start time t_{v1} [s]	25
Venting end time t_{v2} [s]	125
Number of spatial discretizations N	30
No of cycles run C	100
Reactor section conditions	**Value**
Makeup CO_2 $F^{mk}_{CO_2}$ [mol/s]	2.5
Makeup CH_4 $F^{mk}_{CO_2}$ [mol/s]	2.5
Makeup Feed Temperature T^{mk}_f [K]	298.15
Reactor Temperature T_R [K]	1000
Reactor Length L_R [m]	5
Superficial velocity in reactor v_f [m/s]	1

To study the effect of simulation parameters, such as the number of spatial discretization (N) and the number of cycles (C) to reach CSS, several simulations are performed at fixed conditions (given in Table 4.4). The relevant parameters are tabulated in Table 4.5.

Zeolite 13X is used as an adsorbent, the adsorption isotherm parameters for which are obtained by fitting a pure component dual site Langmuir isotherm to the experimental data provided in

Table 4.5: Values of constants and parameters used in the model (Iyer *et al.* [109]).

Constants	Value
Universal gas constant R [J/mol/K]	8.314
Adsorption section model parameters	**Value**
Specific heat capacity of adsorbent $C_{p,s}$ [J/kg/K]	1070
Specific heat capacity of column wall $C_{p,w}$ [J/kg/K]	502
Specific heat capacity of CO_2 [J/mol/K]	37.14
Specific heat capacity of N_2 [J/mol/K]	29.13
Specific heat capacity of CH_4 [J/mol/K]	35.61
Adsorbent density ρ_s [kg/m^3]	1130
Adsorption column wall density ρ_w [kg/m^3]	7800
Inside heat transfer coefficient h_{in} [J/m^2/K/s]	8.6
Outside heat transfer coefficient h_{in} [J/m^2/K/s]	2.5
Viscosity of gas in adsorption column μ [kg/m/s]	1.72 E -05
Molecular diffusivity D_m [m^2/s]	1.6 E -05
Thermal conductivity of column wall K_w [J/m/K/s]	16
Effective gas thermal conductivity K_z [J/m/K/s]	0.09
Adsorbent column void fraction ε	0.37
Adsorbent particle porosity ε_p	0.54
Adsorbent particle radius r_p [m]	1.6 E -03
Adsorbent tortuosity $\tau^{'}$	3
Reactor section model parameters	**Value**
Reactor bed density ρ_b [kg/m^3]	900
Catalyst particle diameter d_p [m]	0.019
Catalyst particle length d_l [m]	0.016
Number of hole rings in the catalyst particle n_h	10
Diameter of the hole rings r_h [m]	0.0023
Void fraction of reactor bed ε_R	0.4

Cavenati *et al.* [166]. These parameters are listed in Table 4.6 while the fitted isotherm model is shown in Figure 4.4. It is observed from Figure 4.5 that the steepness of CO_2 composition and temperature profiles increases with increase in N due to greater accuracy of the model at higher discretizations. The computation time needed for performing the simulation also increases with higher value of N.

Figure 4.6 shows the effect of the number of cycles (C) on the composition and temperature profiles with time obtained at the outlet of the adsorption column. Based on the profiles, it is necessary to simulate at least a few cycles (C $>$ 10) before the process reaches cyclic steady state.

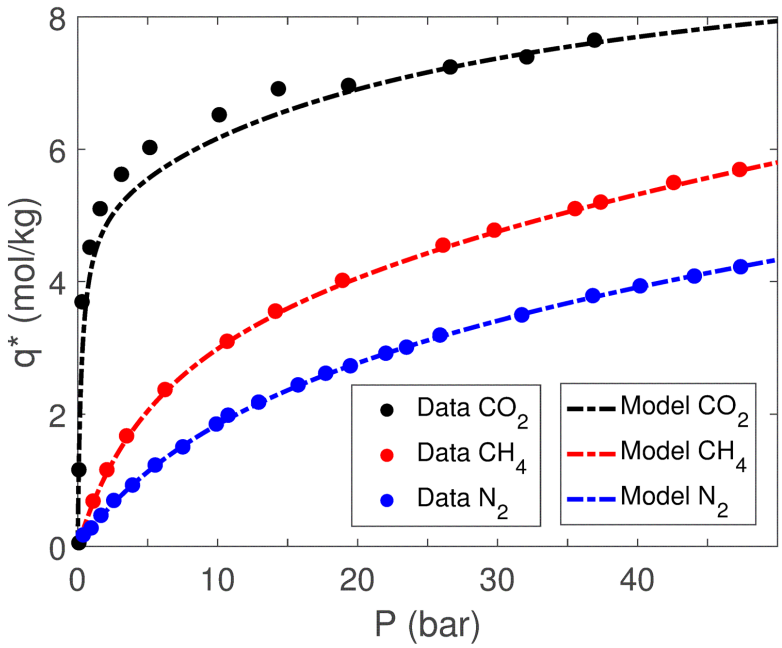

Figure 4.4: Dual site Langmuir adsorption isotherm model predictions of gas loading on the adsorbent at 298 K for zeolite 13X. The parameters are obtained by performing a least-square fit on the experimental data obtained from Cavenati *et al.* [166] (Iyer *et al.* [109]).

Table 4.6: Dual site Langmuir isotherm parameters for zeolite 13X fitted to experimental data from literature (Iyer *et al.* [109]).

Parameter	Value	Parameter	Value	Parameter	Value
$b^0_{CO_2}$ [m^3/mol]	1 E -09	$b^0_{N_2}$ [m^3/mol]	4.32 E -06	$b^0_{CH_4}$ [m^3/mol]	6.29 E -06
$d^0_{CO_2}$ [m^3/mol]	2.63 E -07	$d^0_{N_2}$ [m^3/mol]	2.65 E -06	$d^0_{CH_4}$ [m^3/mol]	1.84 E -06
$q^s_{b,\ CO_2}$ [mol/m^3]	4997.764	$q^s_{b,\ N_2}$[mol/m^3]	10557.477	$q^s_{b,\ CH_4}$[mol/m^3]	4616.276
$q^s_{d,\ CO_2}$ [mol/m^3]	5800.516	$q^s_{d,\ N_2}$[mol/m^3]	3674.76	$q^s_{d,\ CH_4}$[mol/m^3]	16950.00
$\Delta U_{b,CO_2}$ [J/mol]	-33917.46	$\Delta U_{b,N_2}$ [J/mol]	-8089.09	$\Delta U_{b,CH_4}$ [J/mol]	-15922.30
$\Delta U_{d,CO_2}$ [J/mol]	-31731.06	$\Delta U_{d,N_2}$ [J/mol]	-16361.22	$\Delta U_{d,CH_4}$ [J/mol]	-9465.77

The entire chemical process, as shown in Figure 4.2, is simulated using N=100 and C=30 for a reference case where the design variables are fixed to certain values listed in Table 4.7. The key results for the reference case simulation of the cyclic process after 30 cycles are provided in Table 4.7. The loss percentages CH_4 and CO_2 are 62.6% and 24.3%, respectively. These are significant at this reference case leading to an overall CO_2 utilization of 75.6%. The total loss

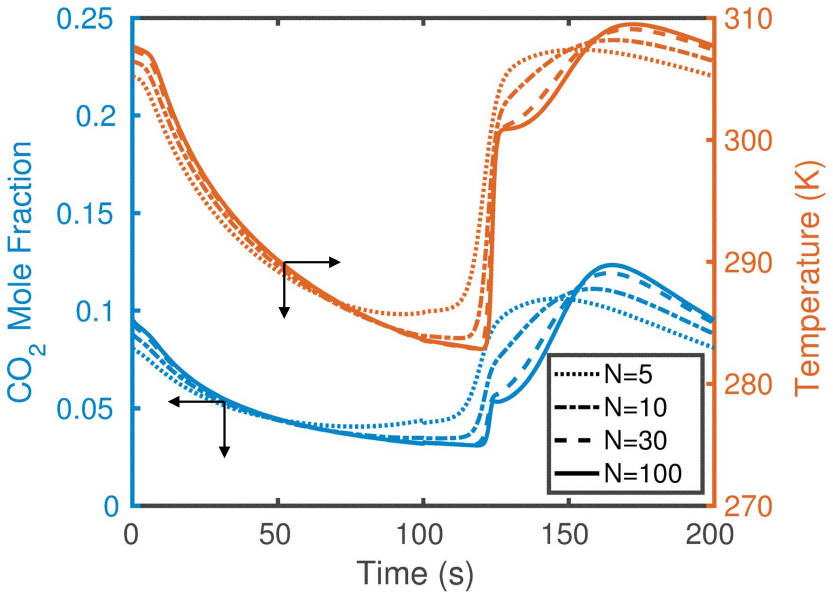

Figure 4.5: Comparison of process performance metrics obtained from short (N=5, C=5) simulations and long (N =30, C =100) simulations for the reference case. The absolute value of the percentage deviation of the short simulations from the longer simulations is also reported (Iyer *et al.* [109]).

includes both the losses through the vent and the presence in the product syngas. Reducing the loss of CO_2 will also lead to the overall increase in CO_2 utilization.

Table 4.7: Key process performance metrics for the reference case simulation calculated for the 30^{th} cycle (Iyer *et al.* [109]).

Process Metric	Value	Process Metric	Value
% CO_2 Utilization	75.63	Unreacted % CO_2	21.16
Total Cost ($/ton SG)	218.06	Syngas ratio (H_2/CO)	0.83
Operating Cost ($/ton SG)	175.33	CH_4 % in product	0.25
Total loss % CH_4	62.62	CO_2 % in product	0.05
Total loss % CO_2	24.29	N_2 % in product	0.03
Vent loss % CH_4	4.26	H_2 % in product	0.29
Vent loss % CO_2	3.14	CO % in product	0.35
Unreacted % CH_4	58.36	H_2O % in product	0.03

To better understand the reasons behind the high losses at the reference case, the gas compo-

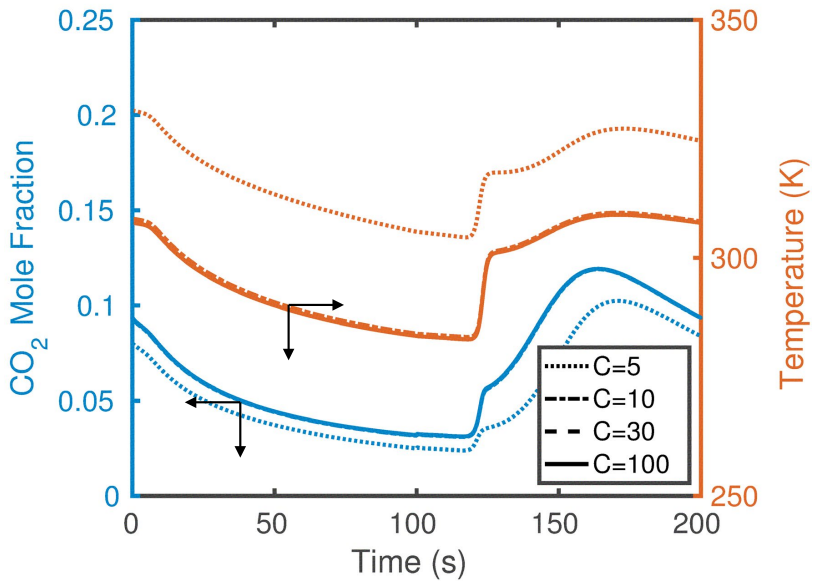

Figure 4.6: Temperature and CO_2 mole fraction profile at the outlet of the adsorption column vs the number of cycles for the reference case. Cyclic steady state is attained after 10 cycles (C) for this case, as seen from the co-incident profiles (Iyer *et al.* [109]).

sitions both at the adsorption column and reactor outlets are examined. The composition profiles at the outlet of the adsorption section for the reference case are shown in Figure 4.7. It is evident from the profiles that the outlet compositions show significant variation over the duration of a cycle. This is expected since the type of feed sent to the adsorption column is switched from flue gas to a CH_4 rich feed at each cycle. Two distinct periods are observed, a N_2-rich period and a CH_4-rich period, which correspond to the flue gas feed step and CH_4-rich feed step, respectively.

The outlet (product) compositions after the reaction section are shown in Figure 4.8. It shows high compositions of CH_4 and CO_2 in the product. This is because complete conversions of CO_2 and CH_4 have not been achieved in the reactor at the reference condition. It is important that the product compositions be further improved to meet the requisite product specifications of syngas and to improve the overall CO_2 utilization. It is also important to reduce losses of greenhouse gases (CH_4 and CO_2) and reduce costs at the same time.

To this end, a preliminary sensitivity analysis around the reference case is first performed by varying a chosen variable within $\pm 30\%$ of the reference case value while other variables are kept

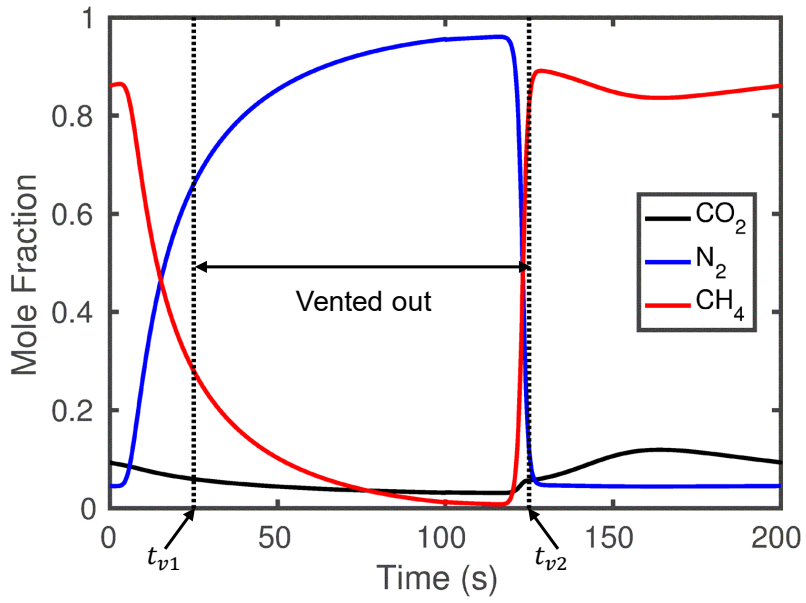

Figure 4.7: CO_2 mole fraction vs time obtained at the outlet of the adsorption column for the reference case for the 30^{th} cycle. Flue gas feed step (t_1) of 100 s is followed by Natural gas feed step of 100 s for a total cycle time (t_c) of 200 s. Venting start time (t_{v1}) considered is 25 s and venting end time (t_{v2}) is 125 s (Iyer *et al.* [109]).

constant to understand the effect of each variable. The feed velocity and the temperature of the adsorption column are held constant, while the column pressure, length, feed step durations and the venting times are varied. The reactor temperature and the reactor length are also varied. The reactor inlet flow rate is indirectly varied since it is influenced by the venting times and the makeup flow rates. The superficial velocity in the reactor is fixed at 1 m/s while the radius of the reactor is varied as a design decision based on the total flow rate entering the reactor. Since this study is in the design and conceptualization stage, the decisions on final reactor diameter or the number of tubes can be taken once the flow rate at optimal conditions is determined. During the sensitivity analysis, both the flue gas and the natural gas feed to the adsorption column are set to the same pressure and temperature. The adsorption column and the reactor pressures are also kept to be equal.

The effects of design variables (pressure, adsorption column length, duration of step-1 and step-2, total cycle duration, venting start and end times, reactor temperature, reactor length, makeup

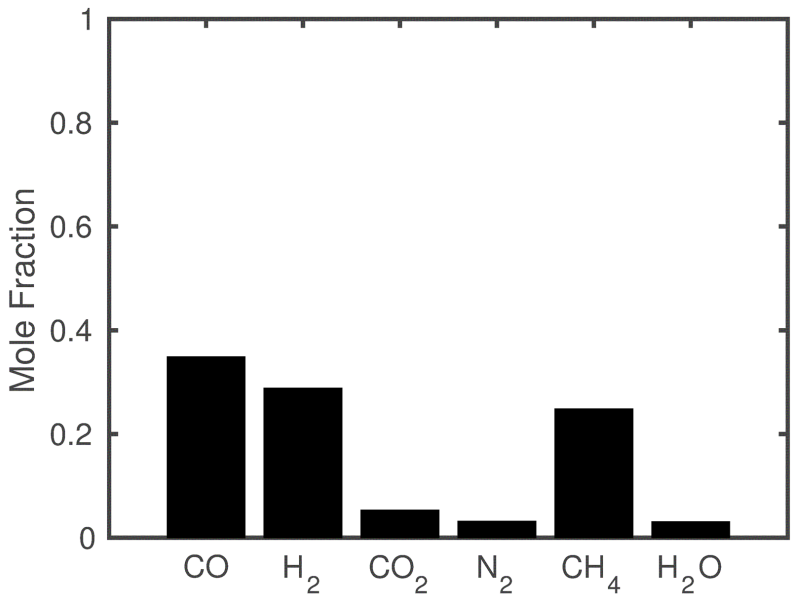

Figure 4.8: Compositions of different species in syngas (product) obtained at the reactor outlet for the reference case. The outlet gas from the adsorption column during the non-venting period (0–25 s) and (125–200 s) of the 30^{th} cycle is mixed with makeup CO_2 ($F^{mk}_{CO_2}$ = 2.5 mol/s) and makeup CH_4 ($F^{mk}_{CH_4}$ = 2.5 mol/s) and is fed to the reactor. Reactor temperature (T_R) considered is 1000 K and reactor bed length (L_R) is 5 m. CO_2 (dry) reforming of CH_4 takes place in the reactor (Iyer *et al.* [109]).

CO_2 flow rate and the makeup CH_4 flow rate) on the process performance metrics such as the overall CO_2 utilization, total cost, and the loss percentages are shown in Figures 4.9–4.11. These values are obtained by varying the variables within $\pm 30\%$ around the reference case (Table 4.4) while keeping the other variables constant. As shown in Figure 4.9, significant CO_2 utilization (almost 97%) can be achieved by changing the process conditions from the reference case. It is observed that the reactor temperature (T_R) has a significant effect on the process metrics (Figure 4.9). At low T_R, reaction kinetics are slow resulting in little CO_2 being consumed to form syngas. Hence, the CO_2 utilization is low at lower values of T_R. Moreover, the reactions are endothermic and hence are not thermodynamically favored at low temperatures. Increase in T_R results in significantly higher reaction rate leading to high conversion of CO_2 to syngas and thereby increasing the CO_2 utilization.

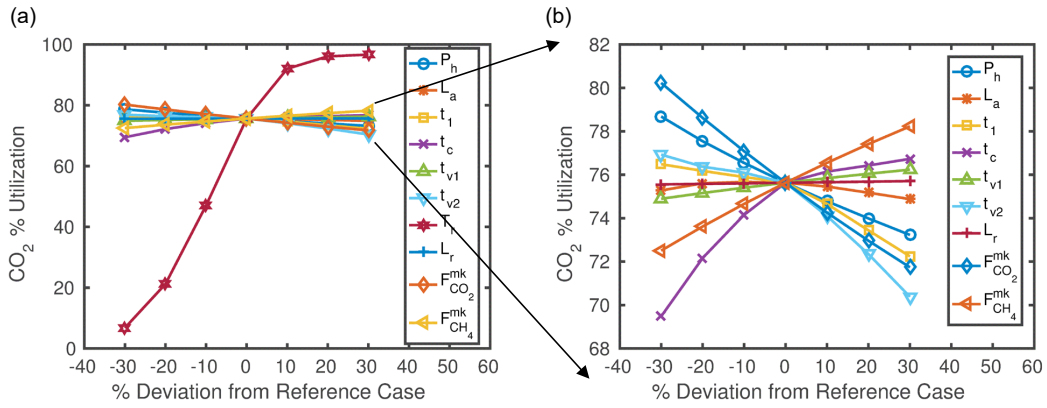

Figure 4.9: (a) Sensitivity analysis of overall CO_2 utilization performed for 10%, 20% and 30% above and below the values of the decision variables in the reference case. These include pressure (P_h), adsorption column length (L_a), feed step 1 duration (t_1), total cycle time (t_c), venting start time (t_{v1}), venting end time (t_{v2}), reactor temperature (T_R), reactor bed length (L_R), makeup CO_2 ($F^{mk}_{CO_2}$) and makeup CH_4 ($F^{mk}_{CH_4}$). (b) Zoomed in view of the effect of variables other than reactor temperature on % CO_2 utilization. The % CO_2 utilization is calculated over a representative cycle (Iyer *et al.* [109]).

Figures 4.10a-b show the effects of changing the reactor temperature T_R on the total cost per ton of syngas and the losses of CO_2 and CH_4 from the process. An increase in the reactor temperature (T_R), especially at the 700–1100 K range, results in a significant increase in the CO_2 utilization from 7% to 92%. This significant increase in CO_2 utilization results in higher amounts of syngas produced in each cycle, an almost 18-fold increase at T_R>1100 K compared to 700 K case. This in turn, leads to a drastic reduction in total cost ($/ton) of syngas produced. This correlation between the CO_2 utilization and total cost per ton of syngas is apparent from Figure 4.10a. Similarly, the losses of CO_2 and CH_4 also go down with increase in T_R, as observed in Figure 4.10b. This is due to increased conversion of CO_2 and CH_4 to syngas at higher temperatures. This thereby results in a decrease in the amount of unreacted CO_2 and CH_4 present in the product. Therefore, the losses decrease with increase in CO_2 utilization.

Other variables show a milder effect around the reference case as compared to T_R. It can be seen from Figure 4.9 that an increase in some of them such as cycle time and makeup CH_4 results in an increase in CO_2 utilization. Increasing other design variables, such as the pressure, step duration

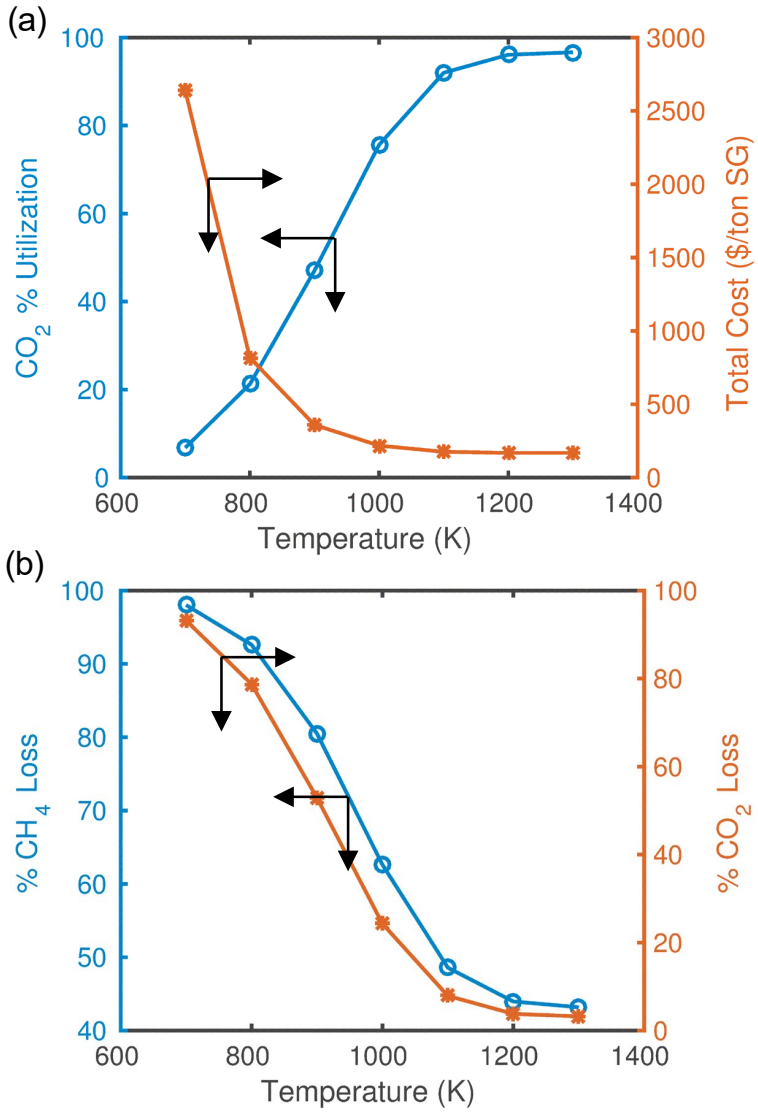

Figure 4.10: Effect of changing temperature (T_R) of reactor operating at isothermal conditions on key process metrics. (a) Overall % CO_2 utilization and total cost of the process per ton of syngas (SG) produced (b) % CO_2 loss and % CH_4 loss. CO_2 (dry) reforming of methane which is an endothermic reaction takes place in the reactor to convert CO_2 and CH_4 to syngas. Loss % (for CO_2 and CH_4) accounts for both loss through the venting step and the presence in the final product syngas. The process metrics are calculated over a representative cycle at cyclic steady state (Iyer *et al.* [109]).

of feed step 1, makeup CO_2 and venting end time, decreases the CO_2 utilization. Variables such as the lengths of the adsorption and the reactor sections do not have significant influence on CO_2 utilization. It can be observed from Figure 4.9 and 4.11c that the trends in CO_2 utilization are

opposite to that of CO_2 loss. This is because decrease in CO_2 utilization is mainly due to unreacted CO_2 and CO_2 loss through the vents. Increasing the pressure, step duration of feed step-1, makeup CO_2, and venting end-time increases the CO_2 loss, which then reduces the CO_2 utilization. An increase in the venting end-time increases the loss of CO_2 through the vent.

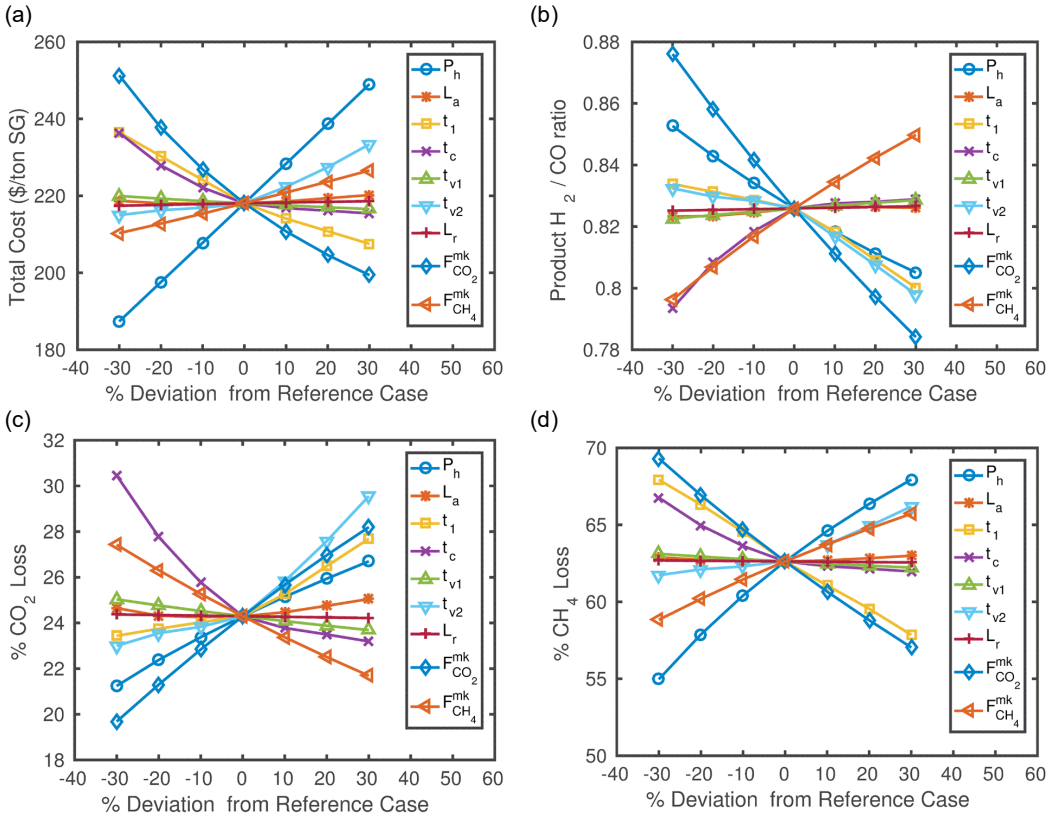

Figure 4.11: Sensitivity analysis for different performance metrics. (a) total cost of the process per ton of syngas (SG) produced, (b) H_2/CO ratio in the product syngas, (c) % CO_2 loss, and (d) % CH_4 loss performed at 10%, 20% and 30% above and below the values of the design variables from the reference case. Loss percentages for CO_2 and CH_4 account for both the loss through the venting step and the loss due to the presence in the final product syngas. The process metrics are calculated over a representative cycle at cyclic steady state (Iyer *et al.* [109]).

The total cost per ton of syngas (Figure 4.11a) increases significantly on increasing the pressure due to the operation of feed compressor. It also increases on increasing the venting end time and the makeup CH_4 but to a lesser degree. Although an increase in the makeup CO_2 adds an additional

cost of raw materials, this reduces the total cost per ton of syngas. This may be due to more syngas produced due to the added makeup CO_2 which offsets the increased cost of makeup CO_2 and lowers the unit cost per ton of syngas.

Moreover, from Figure 4.11a, the H_2/CO ratio in the product syngas is much lower than the desired ratio of 1 for the conditions at which this sensitivity analyses are performed. It is observed that makeup CH_4 is the only variable which when increased improves the H_2/CO ratio. For the H_2/CO ratio to be close to 1, the dry reforming reaction (R1), which consumes CH_4 and CO_2 to produce stoichiometric amounts of CO and H_2, should dominate the reverse water gas shift reaction (R2) which consumes CO_2 and H_2 to produce CO and H_2O. According to the Le Chatelier's principle, increase in CH_4 favors the dry reforming reaction (R1), while increase in CO_2 favors both the reactions. Hence increase in makeup CH_4 results in improving the H_2/CO ratio closer to 1.

For the values of variables considered in this sensitivity analysis, the loss percentages of both CH_4 and CO_2 are still high, as seen from Figure 4.11c–d. It is important to bring down the loss of CH_4 and CO_2 for the process to be viable. It is observed that the effect of some of the variables e.g. makeup feeds, duration of feed step 1 on the CH_4 and CO_2 loss are opposite to each other. This highlights the importance of balancing different tradeoffs while reducing losses of CH_4 and CO_2.

The compositions at the exit of the reactor are influenced by the reactor feed composition, pressure, temperature, reactor dimensions and mode of operation (isothermal or adiabatic). The reactor feed composition and flow rate are determined by the makeup feed amount and the composition and flow rate of the outlet gas from the adsorption column. These are in turn influenced by the start and end times of the venting step, duration of the feed steps, adsorption column pressure, temperature and dimensions.

The pressure at which the column is operated strongly affects the equilibrium saturation capacity of the adsorbent. Higher the pressure, the larger is the amount of gas that can be adsorbed at equilibrium. This then affects the kinetics of adsorption which is proportional to the difference

from the equilibrium amount. As observed from Figure 4.12a, as pressure increases, the steepness of the concentration fronts at the outlet of the adsorption column also increases. There is also a reduction in CH_4 mole fraction in the N_2-rich period of the profile and an increase in the CO_2 mole fraction over a major part of the CH_4-rich period. Thus, a change in pressure influences the venting times chosen and the composition of feed entering the reactor section.

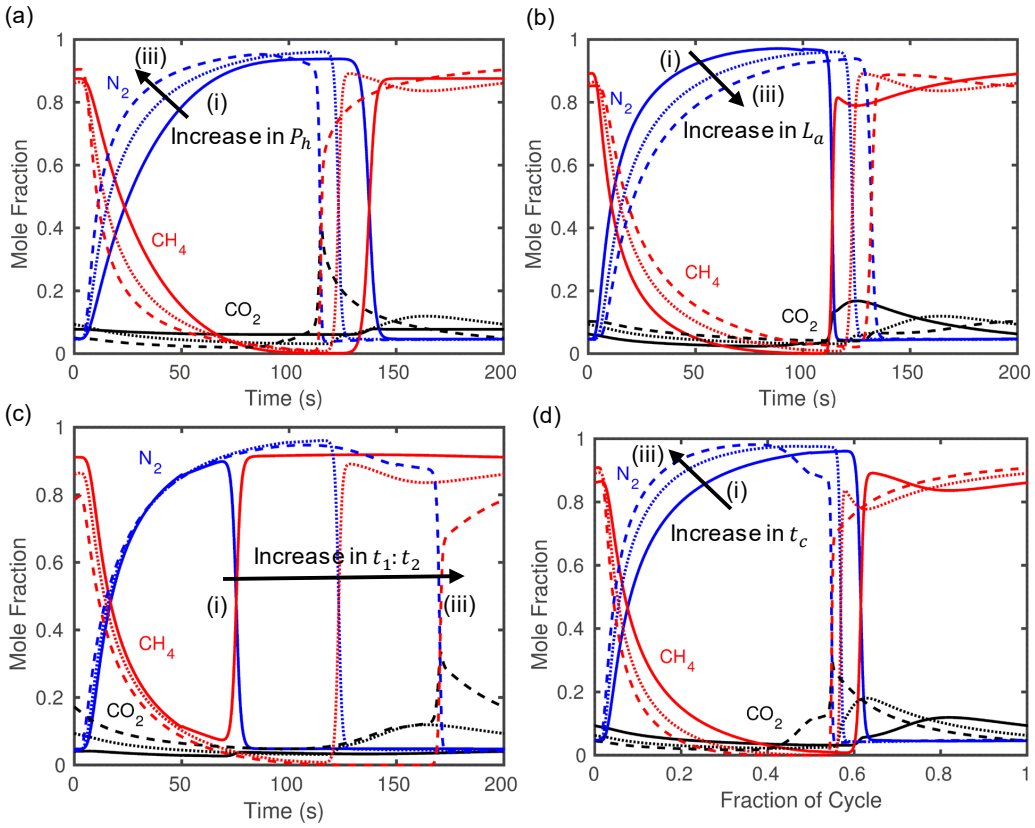

Figure 4.12: Effect of different design variables on the mole fractions at the outlet of the adsorption section. (a) Effect of three different values of pressure namely, (i) 1 bar (ii) 5 bar and (iii) 10 bar on the adsorption column outlet profiles; (b) Effect of three different values of adsorption column length L_a namely, (i) 1 m (ii) 1.5 m (iii) 2 m on the adsorption column outlet profiles; (c) Effect of different relative duration (i) 1:2 (ii) 1:1 (iii) 2:1 values of feed step 1 and 2 on adsorption column outlet profiles. Total cycle time = 200 s. (d) Effect of different values of total cycle time t_c (i) 200 s (ii) 300 s (iii) 400 s on the adsorption outlet profiles. The profiles are obtained for each case by changing the appropriate value of the variable, while setting the values of other variables same as the reference case (Iyer *et al.* [109]).

Figure 4.12b compares the effect of the adsorption column length on the adsorption outlet compositions. Increasing the adsorption column length increases the amount of adsorbent available for adsorption, thus raising the overall capacity of gas that can be adsorbed inside the column. This affects the compositions of the gas at the outlet of the column. An increase in the length of the column reduces the steepness of the concentration fronts, as observed in Figure 4.12b. An increase in CH_4 mole fraction is observed in the N_2-rich period of the composition profiles, while a reduction in CO_2 mole fraction is observed over the CH_4-rich period.

As discussed earlier, the process involves cyclic switching of input feeds to the adsorption column. With the total cycle time held constant, changing the relative durations of the individual steps at each cycle has an effect on the gas compositions at the outlet of the adsorption section, as shown in Figure 4.12c. Increasing the duration of the first step at the expense of the duration of the second step changes the N_2 and CH_4 contents in the adsorber outlet. The longer the duration of the first step, the longer the N_2-rich period, and vice versa. This is because the step-1 feed is flue gas which has a high percentage of N_2. This then influences the choice of the venting times and the composition and flow rate of feed entering the reactor.

Figure 4.12d compares the effect of total cycle time (t_c), which is the sum of the durations of step-1 and step-2, on the adsorption outlet gas compositions. Although the ratio of the durations of the first and second feed steps is the same, the overall cycle time affects the steepness and nature of the concentration fronts observed in the composition profiles. Different cycle times result in different durations of the individual steps leading to different amounts of gas adsorbed in the adsorption section. Increase in cycle time decreases the CH_4 mole fraction in the N_2 rich region, while the CO_2 mole fraction increases in the first half of the CH_4 rich region and then decreases.

The studies above show a variety of factors that affect the shapes and durations of the N_2-rich and CH_4-rich fronts at the outlet of the adsorption section. Therefore, the appropriate values of the downstream design variables (e.g., the venting times, makeup feed amounts) depend on the adsorption outlet. It is essential to choose the venting times appropriately to vent out enough N_2-rich gas while ensuring that the losses of CO_2 and CH_4 through the vents do not exceed maximum

limits. Since the venting times depend on the adsorption outlet profiles, they can only be chosen after the adsorption model is solved. Table 4.8 demonstrates how the loss percentages of CO_2 and CH_4 and the amount of N_2 gas vented out change with the choice of the venting times. As the venting period is increased to occupy more of the N_2 rich period, the amount of N_2 gas vented out increases but so does the losses of greenhouse gases CO_2 and CH_4. The venting duration will need to be restricted to meet the constraints on the loss percentages of the greenhouse gases.

Table 4.8: Effect of changing venting start time, with the venting end time is fixed, on loss percentages through the vents for the reference case. Total cycle time is fixed at 200 s (Iyer *et al.* [109]).

Venting start time t_{v1}	Venting end time t_{v2}	N_2 Vent Loss (%)	CO_2 Vent Loss (%)	CH_4 Vent Loss (%)
0	125	95.93	5.29	14.16
25	125	83.96	3.14	4.26
50	125	61.51	1.97	1.91
75	125	37.32	1.12	1.07
100	125	12.55	0.42	0.78

The gas compositions and flow rates from the adsorption section corresponding to the non-venting period is time averaged to calculate the inlet feed flow rates and compositions for the reactor section. The composition of the feed entering the reactor is determined by the adsorption inlet conditions and the venting times. Since the compositions of the feed gas are kept fixed and the venting times are primarily influenced by the loss constraints, this may restrict the range of compositions in the feed sent to the reactor. For example, there can be a high concentration of CH_4 and low concentration of CO_2 in the reactor feed. This might result in high amount of unreacted CH_4. A sensitivity analysis over various reactor feed compositions performed using the Gibbs free energy minimization module in Aspen Plus (RGIBBS) reveals that the outlet compositions are influenced significantly by the feed ratios (refer Table 4.9). Therefore, it is important that the CH_4/CO_2 ratio in the feed entering the reactor is adjusted. To provide the process with this flexibility, makeup CO_2 and CH_4 are added to the reactor feed to improve the feed ratios (See Figure 4.2a). Although adding makeup CO_2 and CH_4 increases the operating cost of the process,

Table 4.9: Mole fractions in reactor outlet (product) corresponding to feed mole fractions of CO_2 and CH_4 in a binary mixture at equilibrium conditions at 1 bar and 1000 K (Iyer *et al.* [109]).

CO_2 in Feed	CH_4 in Feed	CO_2 in Product	CH_4 in Product
0.095	0.86	5.52 E-05	0.64
0.27	0.69	0.003	0.28
0.39	0.57	0.013	0.13
0.48	0.49	0.032	0.06
0.54	0.43	0.06	0.03

it makes the process robust to handle different feed compositions of flue gas and CH_4-rich feeds and enable meeting the product specifications of syngas product. All the variables pertaining to the adsorption section and the makeup feeds discussed till now affect the compositions and flow rates of feed entering the reactor. The reactor cross-sectional area and the number of tubes need to be adjusted accordingly to handle variation in the feed flow rate. To address this, the superficial velocity to the reactor is kept fixed at 1 m/s, while the reactor diameter is made variable. In addition to the reactor feed compositions, the mode of operation of the reactor and the temperature can affect the final product compositions. The mode of reactor operation considered in this work is isothermal, i.e., the temperature is held constant throughout the reactor. CO_2 reforming is endothermic and is favored at high temperatures. At higher temperatures, the reaction rates are high. It is thus beneficial to operate the reactor section at the highest temperature allowable. However, to reduce coke formation and sintering of the catalyst, the upper limit of reactor temperature is set at 1223 K. The length of the reactor also needs to be sufficient for enough residence time for the reaction mixture to reach equilibrium before exiting. Due to these interplays between different design variables and process performance metrics, it is necessary to obtain a window of operation which reduces the loss of the greenhouse gases and meets the product quality specifications. A set of limits or constraints, as listed in Table 4.10, are imposed on the process performance metrics to characterize the feasible window of operation. The bounds on the design variables used in this work are summarized in Table 4.11.

To this end, a Latin Hypercube Design (LHD)-based space-filling sampling of the process

Table 4.10: Specifications of upper and /or lower bounds on key process metrics (Iyer *et al.* [109]).

Parameter	Value
Max. allowable CH_4 loss from process, $loss^{lim}_{CH_4}$ (%)	10
Min. allowable overall % CO_2 utilization	90
Min. allowable H_2/CO ratio in syngas, SG_L	0.9
Max. allowable H_2/CO ratio in syngas, SG_U	1.1
Max. allowable CH_4 mole fraction in syngas, $y^{spec}_{CH_4}$	0.03
Max. allowable CO_2 mole fraction in syngas, $y^{spec}_{CO_2}$	0.03
Max. allowable N_2 mole fraction in syngas, $y^{spec}_{N_2}$	0.1
Min. allowable step duration, t_{min}	10
Max. allowable cycle duration, t_{max}	200

Table 4.11: Lower and upper bounds of the decision variables chosen in the study (Iyer *et al.* [109]).

Decision variables	Lower Bound	Upper Bound
Pressure (P_h) [bar]	1	10
Adsorption bed length (L_a) [m]	0.5	2.5
Reactor temperature (T_r) [K]	373	1223
Reactor bed length (L_r) [m]	0.5	10
Step 1 duration (t_1) [s]	10 (t_{min})	t_c
Total cycle time (t_c) [s]	10 (t_{min})	200 (t_{max})
Start of venting (t_{v1}) [s]	0	t_c
End of venting (t_{v2}) [s]	0	t_c
Makeup CO_2 ($F^{mk}_{CO_2}$) [mol/s]	0	5
Makeup CH_4 ($F^{mk}_{CH_4}$) [mol/s]	0	5

performance at discrete points over the whole ranges of design variables is performed. A $1000K$ sampling is performed where K is the number of decision variables which in this case is 10. This leads to a total of 10,000 samples. However, not all sampling points satisfy the cycle configuration constraints (Eq. 4.1–4.6). These constraints are known *a priori* and they need to be satisfied for any valid operating condition for the process. Hence, a screen-and-replace algorithm is implemented to switch the incompatible values of design variables with values randomly chosen while satisfying the relevant constraints. The simulations are then run at the samples which have compatible values of decision variables to obtain the process performance metrics. To quickly identify the feasible operating window over the entire sample space, the simulations are run for N=5 and cycles C=5

(hereafter referred to as short simulations). The computation time is significantly reduced for short simulations. The resulting reduction in accuracy is not considerable as the values of the process metrics obtained from the short simulations and the longer simulations are close (refer Table 4.16). For these space-filling short simulations, flue gas (14% CO_2 and 86% N_2) is used as the feed for step-1, and natural gas (95% CH_4 and 5% N_2) is used as the feed for step-2 at each cycle.

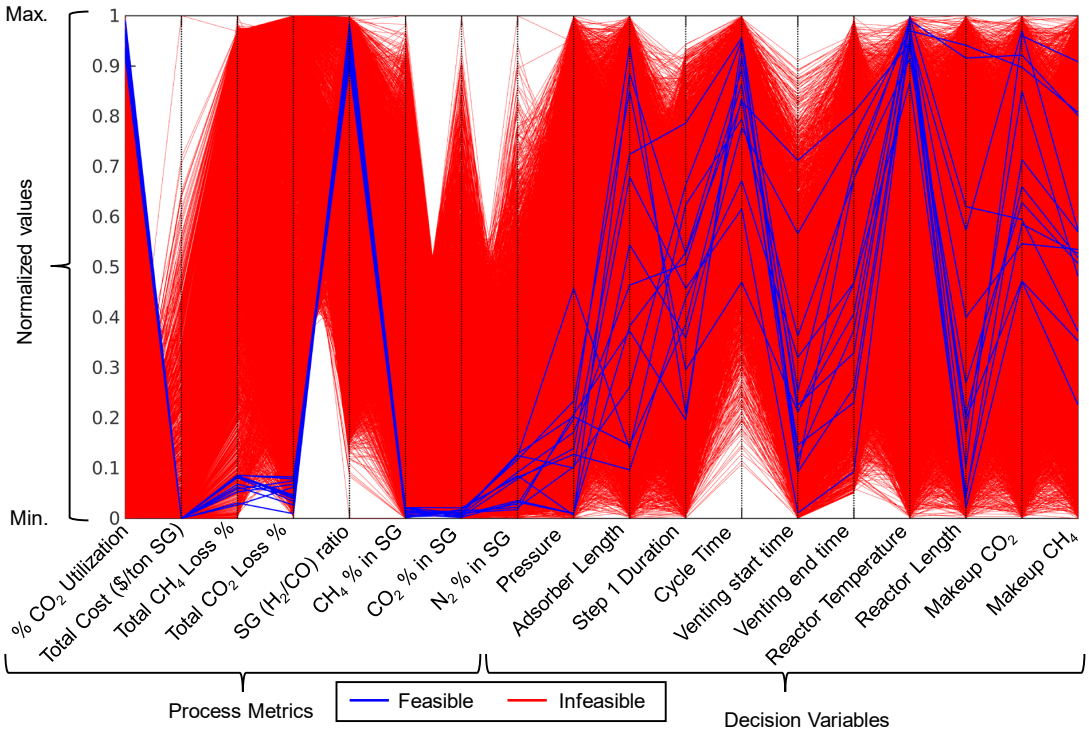

Figure 4.13: Large-scale simulations over the input decision space for 10,000 points. Feasible window of operation of the process for flue gas and natural gas as feeds while meeting overall % CO_2 utilization above 90% and other constraints in Table 4.10. Normalized decision variable values (inputs) and process metric values (outputs) obtained from simulations are plotted on the vertical axis. Input variable values for simulations are obtained by randomly sampling the compatible decision variable space. All the 10000 simulations run are plotted in the figure. Each simulation is represented by a line joining the normalized values of process metric obtained and the decision variable value used. The red region is composed of lines i.e. simulations which are infeasible, while the blue lines correspond to feasible region of operation. The simulations are run for number of spatial discretizations N=5 and cycles C=5 and the process metric values are calculated over a cycle (Iyer *et al.* [109]).

The process performance metrics obtained from the 10,000 simulations/samples are plotted in the Figure 4.13. Each simulation corresponds to a horizontal line joining the values of all the respective process metrics and the decision variable values which are normalized between the maximum and minimum values [167]. All the lines corresponding to the 10,000 simulations are shown in Figure 4.13, where each line represents a single simulation. The blue lines represent the simulations with feasible design for which all the performance metrics are feasible, i.e., they are within specified limits as outlined in Table 4.10. These simulations are hence forward referred to as feasible samples. The red lines represent the infeasible samples. It is interesting to note that the feasible region is very narrow as compared to the decision variable space. For the case considered, only 13 samples out of the 10,000 samples are found to be feasible.

Hence, finding a feasible point of operation by just performing parametric studies or sensitivity analyses requires a lot of simulations. It is important to resort to a systematic technique to obtain feasible operating conditions and optimize best operating conditions. In the following section, a novel simulation-based constrained grey-box optimization method to find feasible and optimal designs and operating conditions for the proposed ICCC process is described.

4.4 Process Optimization

To operate the ICCC process so that it meets the desired process and product specifications it may be necessary to run many simulations to narrow down the range of the input decision variables as observed in the previous section. This approach may become cumbersome and prohibitive with the increase in number of decision variables. Optimization helps in finding feasible conditions in less number of simulations compared to random sampling.

Several variables affect the CO_2 utilization, the cost of the process and other process metrics. Optimization techniques are necessary to balance different trade-offs while achieving a desired objective. For example, a set of conditions which result in the maximum CO_2 utilization might have high costs, while another set of conditions might minimize the costs at the expense of CO_2 utilization. An approach to balance both these objectives can be minimizing costs while maintaining CO_2 utilization above a certain threshold using appropriate constraints. Additional constraints may also

be needed for ensuring product purity, safety limits, containing losses, reducing dependence on makeup feed etc. This can be achieved by formulating and solving an optimization problem with an appropriate objective function, such as maximizing CO_2 utilization or minimizing operating cost, while incorporating all the relevant constraints.

4.4.1 Problem Formulation

The ICCC process optimization problem is formulated as follows:

$$\text{Maximize } POCU \text{ (Overall } CO_2 \text{ Utilization) or Minimize } TC \text{ (total cost)} \tag{4.43a}$$

s.t.

$$loss^{t}_{CH_4} \leq loss^{lim}_{CH_4} \tag{4.43b}$$

$$y^{p}_{CH_4} \leq y^{spec}_{CH_4} \tag{4.43c}$$

$$y^{p}_{CO_2} \leq y^{spec}_{CO_2} \tag{4.43d}$$

$$y^{p}_{N_2} \leq y^{spec}_{N_2} \tag{4.43e}$$

$$SG_l \leq y^{p}_{H_2}/y^{p}_{CO} \leq SG_u \tag{4.43f}$$

$$POCU \geq POCU^{min} \tag{4.43g}$$

$$\text{Cycle configuration constraints (Eq. 4.1–4.6)} \tag{4.43h}$$

$$\text{Decision variable bounds (Table 4.11)} \tag{4.43i}$$

$$\text{Complete process model (Eq. B.2–B.32)} \tag{4.43j}$$

where, Eq. 4.43a is the objective function, and Eqs. 4.43b-j are the constraints which must be satisfied. These include the constraints defining the process specifications (Eqs. 4.43b-g), cycle assignment (Eqs. 4.1–4.6), and the detailed description of the ICCC process (Eqs. B.2–B.32). When the objective is to minimize the total cost, $POCU^{min}$ is set to be 90%, which ensured that the cost is minimized while achieving at least 90% overall CO_2 utilization. The specifications (e.g., $loss^{lim}_{CH_4}$, $y^{spec}_{CH_4}$, $y^{spec}_{CO_2}$, $y^{spec}_{N_2}$, SG_l, SG_U) are tabulated in Table 4.10, and the bounds on the design variables are summarized in Table 4.11.

While there exists methods for the optimization of adsorption-based cyclic processes [17, 19, 25–27, 67, 81, 146, 168–173], it is not trivial to solve the optimization problem for the ICCC process, which is a highly nonlinear, non-convex NAPDE model with many algebraic and partial differential equations (PDEs). Furthermore, the objective function and the performance metrics ($POCU$, TC, $y^p_{CH_4}$, $y^p_{CO_2}$, $y^p_{N_2}$, and $y^p_{H_2}/y^p_{CO}$) within the NAPDE model are not expressed explicitly as functions of the design/decision variables ($P_h, L_a, t_1, t_c, t_{v1}, t_{v2}, T_R, L_R, F^{mk}_{CO_2}, F^{mk}_{CH_4}$). The metrics are obtained only after solving Eqs. B.2–B.32. Since they are not explicitly expressed in terms of design variables, we will refer to them as black-box. To this end, the NAPDE model can be viewed as a large grey-box model, which is a combination of both explicit and black-box/hidden models.

For performing optimization using gradient based solvers, the original NAPDE model needs to be completely discretized in both space and time resulting in a large number of nonlinear, non-convex equations whose size increases with the level of discretization. Optimizing the resultant model using standard nonlinear solvers is computationally expensive. An alternative and promising approach is to use data obtained from simulations and develop surrogate models to guide optimization. Replacing a large and complex discretized model by a surrogate model aids in performing optimization with less computational overhead. Similar black-box/grey-box optimization problems have been previously studied for process flowsheet optimization [174], pressure swing adsorption [175, 176], and superstructure optimization [22]. Several approaches motivated from classical nonlinear programming methods involving known functional forms are being applied to black-box/grey-box optimization [177–179]. Using a penalty-based trust-region approach [176], a constrained problem is converted to an unconstrained one by including the constraint violation within the objective function. Augmented Lagrangian based methods [180] have also been applied for constrained derivative-free optimization. A filter based technique [181] was recently proposed to solve general glass-box/black-box problems and was applied to chemical engineering based process optimization case studies. The filter approach [182] treats a constrained problem as a bi-objective problem where minimizing the objective function and the constraint violation are considered as separate goals.

In this work, a trust-region based optimization framework is proposed to solve the NAPDE problem in two phases: (i) finding feasible points (restoration phase), and (ii) reducing the objective function while maintaining feasibility (optimization phase). This approach is specifically useful for applications such as this one, where identifying the feasible set of operating conditions is not trivial. The overall optimization framework is described below.

4.4.2 Grey-box Optimization Methodology

The NAPDE optimization problem can be generalized as follows:

$$\min_{\mathbf{x}} \quad f(\mathbf{x}, \mathbf{Y}) \qquad \text{(Objective)} \tag{4.44a}$$

s.t.

$$h_p(\mathbf{x}, \mathbf{Y}) = 0 \qquad \forall p \in \{\text{Eq. B.2–B.32}\} \qquad \text{(process model)} \tag{4.44b}$$

$$g_k(\mathbf{x}) \leq 0 \qquad \forall k \in \text{Eq. 4.1–4.6} \qquad \text{(cycle assignment)} \tag{4.44c}$$

$$g_u(\mathbf{x}, \mathbf{Y}) \leq 0 \qquad \forall u \in \text{Eq. 4.43b–g} \qquad \text{(process specifications)} \tag{4.44d}$$

$$x_i^L \leq x_i \leq x_i^U \quad \forall i \in \{P_h, L_a, t_1, t_c, t_{v1}, t_{v2}, T_R, L_R, F_{CO_2}^{mk}, F_{CH_4}^{mk}\} \qquad \text{(decision variable bounds)} \tag{4.44e}$$

$$Y_j^L \leq Y_j \leq Y_j^U \quad \forall j \in \{POCU, TC, y_{CH_4}^p, y_{CO_2}^p, y_{N_2}^p, y_{H_2}^p/y_{CO}^p\} \qquad \text{(specification bounds)} \tag{4.44f}$$

where $\mathbf{x}$ is a vector of all design variables x_i, and $\mathbf{Y}$ is a vector of all process performance metrics Y_j. For the ICCC process, $\mathbf{x} = (P_h, L_a, t_1, t_c, t_{v1}, t_{v2}, T_R, L_R, F_{CO_2}^{mk}, F_{CH_4}^{mk})$, and $\mathbf{Y}$ = {*POCU*, *TC*, $y_{CH_4}^p$, $y_{CO_2}^p$, $y_{N_2}^p$, $y_{H_2}^p/y_{CO}^p$}. Furthermore, $f(x)$ is the black-box objective function, $g_k(x)$ a known function from the set of explicit equations describing the cycle assignment (Eqs. 4.1–4.6), $g_u(\mathbf{x}, \mathbf{Y})$ is a black-box function from the set of the equations describing the limits on the process

performance metrics (Eqs. 4.43b-g), and $h_p(\mathbf{x}, \mathbf{Y}) = 0$ represents the process model described by Eqs. B.2–B.32. We refer $g_u(\mathbf{x}, \mathbf{Y})$ to be black-box, since it relates the design variables $\mathbf{x}$ with the process performance metrics $\mathbf{Y}$ through implicit expressions. Furthermore, we refer to a simulation when all x_i will fixed such that their values satisfy $g_q(x) \leq 0$. Designing of simulations to find set of $\mathbf{x}$-values that satisfy the know constraints $g_q(x) \leq 0$ is a challenge. However, a simulation-based optimization framework, requires many simulations as the algorithm proceeds. Therefore, design of simulations is of significant importance. In this work, the method proposed by Bajaj and Hasan [84] is applied to design a set of feasible samples that satisfies known constraints. Further details are provided in Appendix B.3.

We use the surrogate model-based trust-region approach for both the restoration and optimization phases. The basic steps involved in this approach are: (1) Space filling samples are obtained such that they are feasible with respect to the known constraints; (2) After the simulations are performed on the design points, the black-box function is approximated by a fully-linear surrogate model; (3) A non-linear programming problem involving minimization of the surrogate model subject to the constraints is solved using GAMS/ANTIGONE [91] in a trust-region and the procedure is repeated in an iterative manner using a trust-region framework until a convergence criteria is satisfied. Based on a set of simulation samples, simpler models (surrogates) for both $f(\mathbf{x})$ are developed. At each iteration, a set of $5k$ samples are used to develop the surrogate model. All the samples are made sure to lie within the current trust-region. At the next iteration, previous samples lying within the new trust-region are reused. In case the number of samples is less than 5k, the remaining samples are obtained using an optimization model given in Appendix B.3. Let $f^r(\mathbf{x})$ represents the surrogate model of $f(\mathbf{x})$. The surrogate model used in this work is a cubic radial basis function and satisfies the fully-linear property [183]. A model is said to be fully-linear if for all $\mathbf{x} \in \Delta$, $||\nabla f(\mathbf{x}) - \nabla f^r(\mathbf{x})|| \leq \kappa_g \Delta$ and $||f(\mathbf{x}) - f^r(\mathbf{x})|| \leq \kappa_f \Delta^2$, where $\kappa_{\mathrm{g}}, \kappa_{\mathrm{f}} > 0$. Note that parameters of the cubic radial basis function representing $f^r(\mathbf{x})$ is obtained, whenever needed, based on a maximum-likelihood parameter estimation with cross-validation using a set of NAPDE simulation data (refer Appendix B.4).

4.4.2.1 Finding Feasible Solutions (Restoration Phase)

The restoration phase is an iterative approach which proposes new designs of simulations towards finding a feasible simulation point or sample. At each iteration of the restoration phase, an optimization problem is solved where all the unknown constraints are grouped into a single smooth constraint violation function (θ) defined as follows:

$$\theta = \sum_{u} \left(\max(0, g_u)\right)^2 \tag{4.45}$$

The constraint violation function is zero when the current simulation considered is feasible. It is positive whenever it is infeasible with respect to the unknown constraints. The following nonlinear model is solved at each iteration of the restoration phase:

$$\begin{aligned} &\min_{x} \quad \theta^r(x) \\ s.t. \quad &g_k(x) \leq 0 \\ &x \in \Delta_{k'} \end{aligned} \tag{4.46}$$

θ^r denotes an approximation of θ within a trust region $\Delta_{k'}$. Similar to f^r, θ^r is approximated using a cubic radial basis function which is fitted based on simulations of the NAPDE model, as described in Appendix B.4. The new point $\overline{x}_{k'}$ is acceptable as a new iterate if a decrease in the objective function (constraint violation in this case) is observed and the trust region is increased. It may also be possible that a given problem is infeasible. To check this, the criticality measure φ_r^{θ} is calculated by solving the following linear program.

$$\begin{aligned} &\varphi_r^{\theta} = \min_{d} \nabla\theta^r(\overline{x}_{k'})^T d \\ s.t. \quad &g_k(\overline{x}_{k'}) + \nabla g_k(\overline{x}_{k'})^T d \leq 0 \\ &||d||_1 \leq 1 \end{aligned} \tag{4.47}$$

where d is a vector of size n i.e. the number of design variables. Criticality measure evaluates if further decrease in infeasibility/violation of the unknown constraints is possible. For nonlinear programs with known smooth objective function and constraints, if the solution of the above problem is within a pre-specified tolerance, the problem is deemed to have converged. However, in the paradigm of black-box optimization, an additional condition on accuracy of the surrogate model is also needed. In this work, the accuracy of the surrogate model is tested by validating on an independent set of testing sample points (denoted by ST) by evaluating the root mean squared error (ε_θ). So, if the criticality measure (φ_r^θ) and root mean squared error (ε_θ) is below threshold values of φ^{tol} and ε^{tol}, the algorithm is terminated.

An alternative certificate of convergence could be the trust region being smaller than a pre-specified tolerance. In the algorithm, trust region is increased when a decrease in infeasibility (objective function of constraint violation in this case) is obtained in the current iteration and the trust region is decreased if a decrease in infeasibility is not observed. If the trust region size keeps on decreasing to a very small value, this implies that no better point is possible and hence the method has converged to the local minima. This argument is based on the assumption that the original function is sufficiently smooth. The above criterion is also employed as convergence criteria for the optimization phase as will be described in the next subsection. The restoration phase described above is illustrated in Figure 4.14. If the restoration phase does not yield a feasible point, a different initial guess is provided and the algorithm is run again.

4.4.2.2 Finding Optimal Solutions (Optimization Phase)

Once a feasible point is obtained, the focus is shifted towards decreasing the objective function while maintaining feasibility at all subsequent iterations. To achieve this, surrogate models for both the objective function and the constraint violation are developed. An optimization subproblem (Eq. 4.50) is also solved to find a point that decreases the objective function while ensuring feasibility with respect to both known and unknown constraints. The basis for considering surrogate model for the constraint violation, as well as for the objective, is to exclude the infeasible search space from consideration. A new iterate obtained by solving Eq. 4.50 is only acceptable if

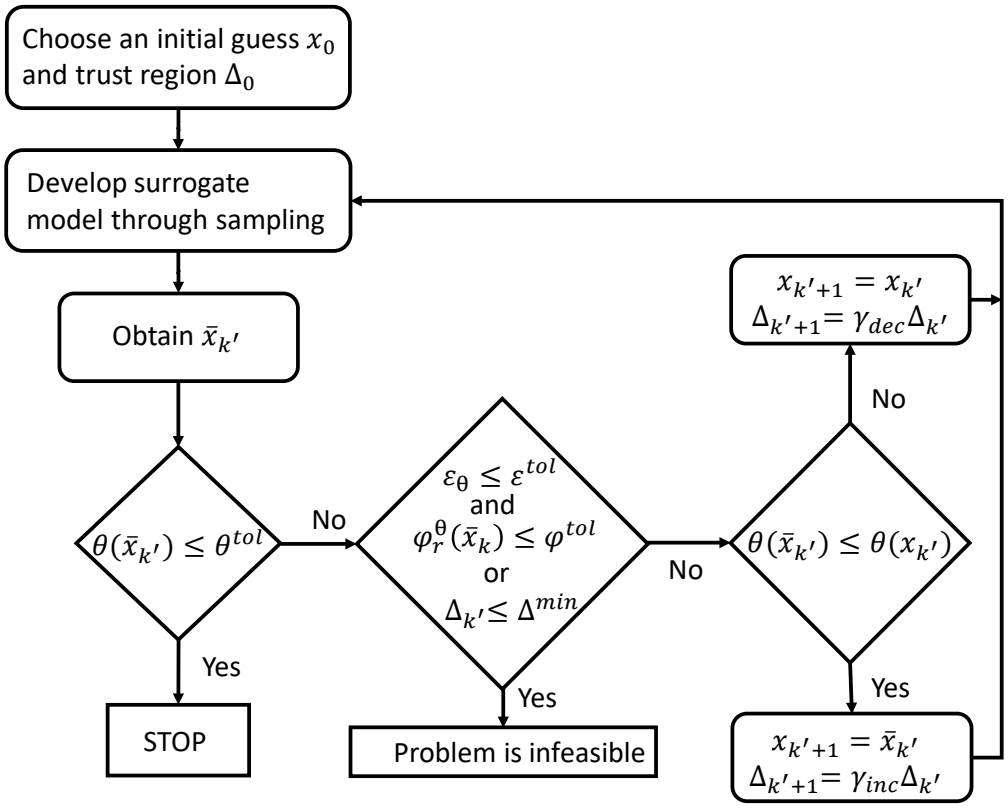

Figure 4.14: Restoration phase of the optimization algorithm used to obtain feasible point. It is a trust-region based algorithm which starts from an infeasible point, performs iterations to find a feasible point. The algorithm terminates if a feasible point is obtained or if the problem is infeasible (Iyer *et al.* [109]).

the new point is feasible and the objective function is reduced. In other words,

$$\theta\left(\overline{x}_k\right) \leq \theta^{tol} \quad \text{and} \quad f\left(\overline{x}_k\right) \leq f(x_k) \tag{4.48}$$

If the reduction obtained in the objective function is appreciable compared to the predicted reduction in objective function, the trust region, Δ_{k+1} can potentially be increased. The ratio relating the observed reduction with predicted reduction is given by:

$$\rho_k = \frac{f\left(x_k\right) - f(\overline{x}_k)}{f^r\left(x_k\right) - f^r(\overline{x}_k)} \tag{4.49}$$

The algorithm for minimizing the objective function is illustrated in Figure 4.15. The following

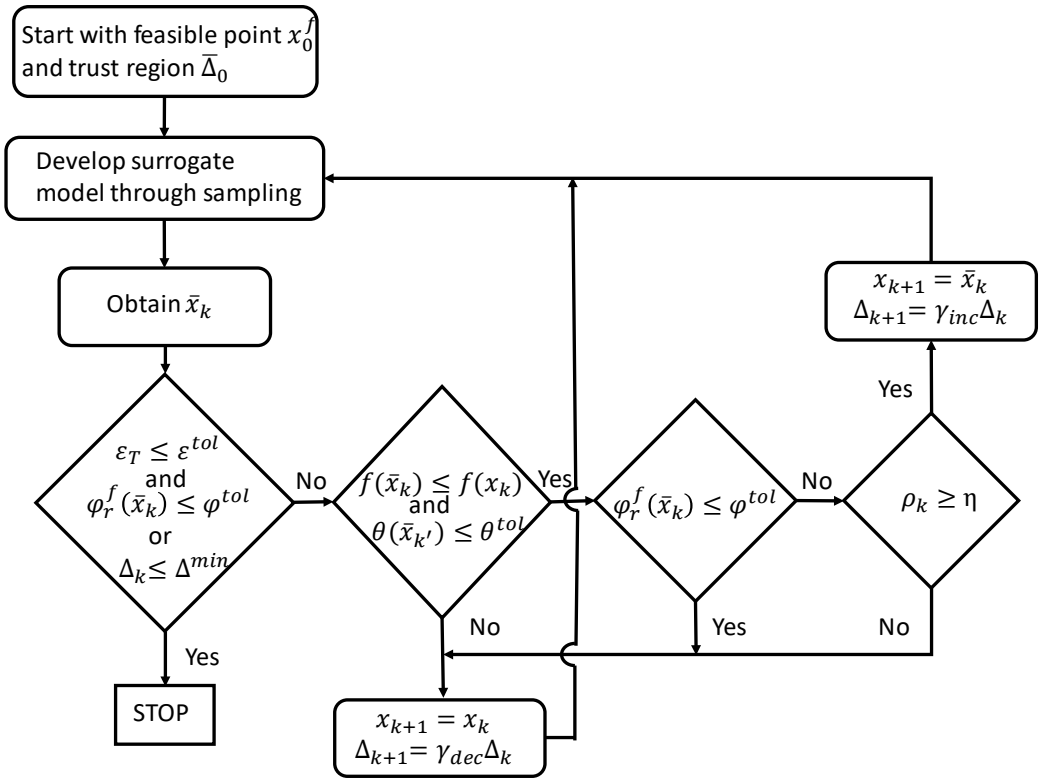

Figure 4.15: Algorithm used in the optimization phase. The algorithm aims to improve objective function after the restoration phase has terminated. In the optimization phase, an iterate is only acceptable when it improves the objective function while maintaining feasibility (Iyer *et al.* [109]).

sub-problem is solved at each iteration in the trust region to obtain candidate optimum point $\overline{x}_k$:

$$\min_{x} \quad f^r(x) \tag{4.50}$$

$$s.t. \quad \theta^r(x) \leq \theta^m$$

$$g_k(x) \leq 0$$

$$x \in \Delta_{k'}$$

where θ^m denotes the minimum constraint violation encountered among the samples. To check whether a candidate point is a first order critical point, criticality measure φ_r^f is calculated by

solving the following linear program.

$$\varphi_r^f = \min_d \quad \nabla f^r\left(\overline{x}_k\right)^T d \tag{4.51}$$

$$\begin{aligned} s.t. \quad & g_u^r\left(\overline{x}_k\right) + \nabla g_u^r(\overline{x}_k)^T d \leq 0 \\ & g_k\left(\overline{x}_k\right) + \nabla g_k\left(\overline{x}_k\right)^T d \leq 0 \\ & ||d||_1 \leq 1 \end{aligned} \tag{4.52}$$

This problem gives an indication as to whether the objective function can be decreased further while maintaining feasibility. The core of the algorithm relies on performing sampling and developing surrogate model. The strategy to obtain feasible samples with respect to the known constraints and the strategy for developing surrogate model are both provided in Appendix B.3 and B.4, respectively. The optimization algorithm parameters are listed in Table 4.12.

Table 4.12: Algorithm parameters used in the optimization runs performed. L_1 norm is used for defining trust region size (Iyer *et al.* [109]).

Algorithm Parameters	Values
Constraint violation tolerance (θ^{tol})	0
Root mean squared error tolerance (ε^{tol})	10^{-3}
Threshold value for criticality measure (φ^{tol})	10^{-3}
Minimum trust region size (Δ^{min})	10^{-5}
Trust region decrease factor (γ_{dec})	0.5
Trust region increase factor (γ_{inc})	3
Ratio of actual decrease and predicted decrease in objective function (η)	0.25

4.4.3 Optimization Results

We have applied the grey-box constrained optimization strategy to solve the NAPDE model for the optimization of the integrated carbon capture and conversion process presented in this work. In what follows, three case studies are described. In the first case study, the capture and conversion of CO_2 from dry flue gas (14% CO_2 and 86% N_2) from a coal-fired power plant using typical

natural gas containing 95% CH_4 and 5% N_2 as step-2 feed is considered. For case study 2, biogas is unconsidered, which is an unconventional and highly contaminated source of CH_4 with about 60% CH_4 and 40% CO_2, as the feed for step-2. In case study 3, the robustness of the proposed ICCC process under varying feed compositions is studied. Specifically, several optimization runs are performed, each of which considers a fixed flue gas but different CH_4-rich feed. The CO_2 contents in the CH_4-rich feed are varied over a range from 0–60% to cover the compositions of a wide range of unconventional, stranded and distributed sources of methane, such as shale gas, biogas, landfill gas, refinery off-gas, fuel gas, etc. All feeds are considered to be available at 1 atm. and 298 K for all case studies.

Table 4.13: Process and product specifications at optimum for natural gas (NG) and biogas (BG) as CH_4-rich feed used in the second feed step. Process metrics calculated over 1 cycle. Value of the objective shown in bold typeface (Iyer *et al.* [109]).

Process metric	Case (a)		Case (b)		Case (c)	
	Optimum Overall CO_2 % Utilization		Optimum Total Cost ($/ton Syngas)		Optimum "Direct" Utilization of CO_2 from Flue Gas	
Step 1 Feed	Flue Gas	Flue Gas	Flue Gas	Flue Gas	Flue Gas	Flue Gas
Step 2 Feed	Natural Gas	Biogas	Natural Gas	Biogas	Natural Gas	Biogas
Overall CO_2 % Utilization	**99.67**	**99.67**	97.14	97.35	92.00	90.76
Total cost ($/ton SG)	120.89	117.44	**109.42**	**110.08**	129.01	128.52
% CO_2 fed via FG over total CO_2 utilized	1.16	3.10	2.59	2.70	**11.69**	**16.14**
Total loss % CH_4	10.00	9.97	1.20	1.14	7.64	6.42
Total loss % CO_2	0.23	0.22	2.76	2.56	7.91	9.24
Vent loss % CH_4	9.79	0.01	0.01	0.00	1.38	0.00
Vent loss % CO_2	0.08	0.08	0.72	0.07	1.69	7.64
Unreacted % CH_4	0.20	9.96	1.19	1.14	6.26	6.42
Unreacted % CO_2	0.15	0.14	2.04	2.49	6.22	1.59
Syngas (SG) ratio (H_2/CO)	1.00	1.0	0.97	0.96	0.9	0.97
CH_4 % in product	2.61	2.57	0.29	0.27	1.44	1.5
CO_2 % in product	0.03	0.03	0.52	0.63	1.61	0.4
N_2 % in product	1.43	4.4	2.56	3.99	9.94	10.00
H_2 % in product	47.88	46.42	47.21	46.27	40.16	43.15
CO % in product	47.99	46.52	48.68	47.98	44.62	44.35
H_2O % in product	0.05	0.05	0.73	0.85	2.23	0.59

4.4.3.1 Case Study 1: Conversion of Flue gas and Natural gas to Syngas

For this case study, flue gas is used as the feed for the step-1, and natural gas (95 % CH_4 and 5 % N_2) is used as the methane rich feed for step-2 of each cycle. We perform the optimization with different objectives: (i) maximizing the overall CO_2 utilization (case a), (ii) minimizing the total cost per ton of syngas produced (case b), and (iii) maximizing "direct" utilization of CO_2 from flue gas with respect to the total utilization (case c). These cases are discussed below.

Case (a): Maximize Overall utilization of CO_2: Here, the overall % CO_2 utilization is maximized and the results are presented in Tables 4.13–4.15. It can be observed from Table 4.13 that the

product specifications, syngas ratio and the losses are within the limits set by the constraints. The overall CO_2 utilization is high around 99.7% while the corresponding cost per ton of syngas is \$120.9 which is within the range of costs described in Pei *et* al.98 The syngas is mostly composed of 47.88% H_2 and 47.99% CO, which confirms that the specified ratio of H_2/CO is met. The optimal design variables are listed in Table 4.15. The optimum is attained at 1 atm. pressure and at the highest reactor temperature allowed (1223 K) to maximize the CO_2 conversion to syngas. The process requires additional CO_2 and CH_4 to adjust the input feed ratios to the reactor to obtain higher CO_2 conversion while meeting all the constraints. The total loss of CH_4 is at its upper bound (10%) but the total loss of CO_2 is only 0.23%. CH_4 is mostly lost through the vent. However, the venting is important to eliminate N_2 from the reactor feed. This is apparent, as the N_2 content of the product syngas is found to be only 1.43%. The product syngas also contains 0.03% CO_2.

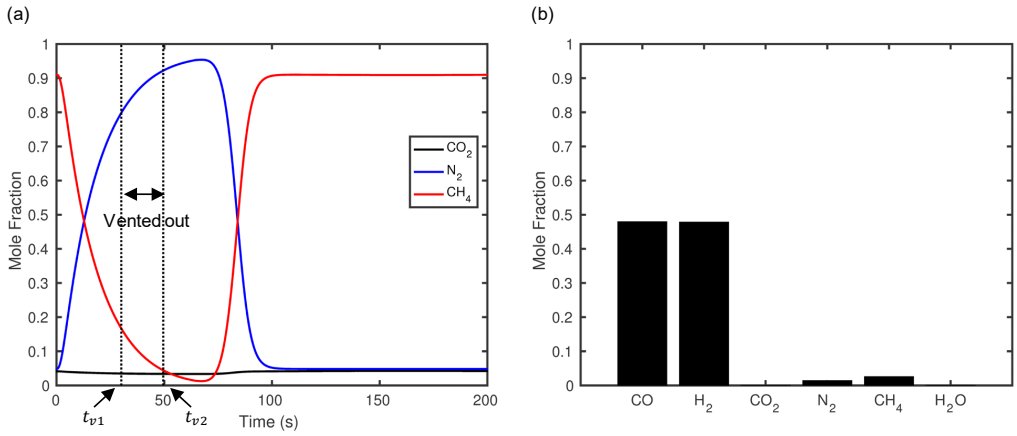

Figure 4.16: Gas compositions at the adsorption and reactor section outlets for case study 1. (a) Mole fraction profiles at the adsorption column outlet for optimal overall CO_2 utilization for flue gas as feed in step 1 and natural gas as feed in step 2. (b) Product (Syngas) composition at reactor outlet at optimum overall CO_2 utilization for flue gas and natural gas feeds. Maximum overall CO_2 utilization obtained at optimum is 99.7% at a cost \$120.9/ton syngas (Iyer *et al.* [109]).

Table 4.14: CO_2 consumption and utilization mole balance at optimum for natural gas (NG) and biogas (BG) feeds calculated over one cycle (Iyer *et al.* [109]).

Process metric	Case (a)		Case (b)		Case (c)	
	Optimum Overall CO_2 % Utilization		Optimum Total Cost ($/ton Syngas)		Optimum "Direct" Utilization of CO_2 from Flue Gas	
Step 1 Feed	Flue Gas	Flue Gas	Flue Gas	Flue Gas	Flue Gas	Flue Gas
Step 2 Feed	Natural Gas	Biogas	Natural Gas	Biogas	Natural Gas	Biogas
CO_2 from FG feed [moles]	9.03	22.16	25.78	21.83	117.64	72.34
CO_2 from NG/BG feed [moles]	0	10.52	0	3.97	0	11.82
Total CO_2 from both feeds [moles]	9.03	32.69	25.78	25.80	117.64	84.16
Makeup CO_2 [moles]	770.21	683.07	996.37	804.01	975.12	409.78
Total CO_2 input [moles]	779.24	715.76	1022.15	829.81	1092.76	493.94
CO_2 lost vent [moles]	0.64	0.57	7.35	0.55	18.44	37.77
Unreacted CO_2 [moles]	1.13	1.02	20.89	20.68	68.00	7.88
Total CO_2 utilized [moles]	777.47	714.17	993.91	808.58	1006.32	448.29
% CO_2 from FG over total CO_2 utilized	1.16	3.10	2.59	2.7	11.69	16.14

The adsorption outlet composition and the reactor outlet compositions for this case are shown in Figure 4.16. Looking at the adsorption outlet profiles, at first it would seem surprising that the venting period is not shifted further towards the later part of the cycle where there is high N_2 content and low CH_4 content. However, the optimization has obtained a balance between different trade-offs to maintain feasibility while maximizing the overall CO_2 utilization. It is also observed that although N_2 does not participate in the reaction, its presence can reduce the partial pressure of the reacting species to adjust the final conversion. The complex interplay of different variables and their influence on decision making for optimum results is thus well brought out in this case.

Table 4.15: Decision variables at optimum for natural gas (NG) and biogas (BG) feeds for different optimization objectives (Iyer *et al.* [109]).

Process metric	Case (a)		Case (b)		Case (c)	
	Optimum Overall CO_2 % Utilization		Optimum Total Cost ($/ton Syngas)		Optimum "Direct" Utilization of CO_2 from Flue Gas	
Step 1 Feed	Flue Gas	Flue Gas	Flue Gas	Flue Gas	Flue Gas	Flue Gas
Step 2 Feed	Natural Gas	Biogas	Natural Gas	Biogas	Natural Gas	Biogas
Pressure (P_h) [bar]	1.01	1.01	1.01	1.01	6.24	2.84
Adsorption bed length (L_a) [m]	0.9	1.45	0.57	1.205	1.66	0.97
Reactor Temperature (T_r) [K]	1223	1223	1203	1193.97	1221.76	1217.33
Reactor bed length (L_r) [m]	9.15	1.40	0.5	0.5	0.52	0.53
Step 1 duration (t_1) [s]	65.02	159.57	185.6	157.18	137.62	185.62
Total Cycle time (t_c) [s]	199.92	186.08	199.27	167.18	196.49	196.23
Start of venting (t_{v1}) [s]	30.07	172.59	35.12	156.96	48.49	84.95
End of venting (t_{v2}) [s]	49.54	182.59	101.48	167.18	108.29	194.44
Makeup CO_2 ($F_{CO_2}^{makeup}$) [mol/s]	3.85	3.67	5	4.81	4.96	2.09
Makeup CH_4 ($F_{CH_4}^{makeup}$) [mol/s]	3.67	4.15	4.83	4.67	3.22	2.24

Case (b): Minimize total cost per ton of syngas: For minimizing the total cost of the process per unit amount of syngas produced, an additional constraint is introduced which restricts the overall CO_2 utilization from going below 90%. A cost of $109.4 per ton syngas is achieved while maintaining around 97% overall CO_2 utilization. None of the process and product quality constraints are at their bounds, while the amount of makeup CO_2 needed is at its upper bound. The optimal step-1 duration is about 12 times larger than the duration of step-2. Although the makeup CO_2 is expensive, the optimization sets it at the maximum value to meet other process constraints. The reactor bed length is at its minimum and the pressure of the process is at 1 atm. The reactor temperature is 1203 K which is about 20 K less than the upper bound.

Case (c): Maximize "direct" utilization of CO_2 from flue gas over total CO_2 utilization: It can be observed from Tables 4.14 and 4.15 that the process is heavily dependent on makeup CO_2 and CH_4 supplied to the process to attain feasibility and optimality. For the previous optimal points

obtained, the CO_2 input via flue gas compared to the total amount of CO_2 utilized is around 1–2%. This means that from an overall process standpoint the contribution of flue gas to the total CO_2 utilized is quite low. Hence, to maximize the amount of flue gas processed while still maintaining the feasible nature of the process, we now set a new objective of maximizing the CO_2 from flue gas consumed over the total CO_2 utilized. The constraint of overall CO_2 utilization to be greater than 90% is also set. In this case, we see that 11.69% of "direct" CO_2 utilization from flue gas is achieved (see Figure 4.17). The distribution of CO_2 input from the flue gas and the makeup CO_2 is shown in Figure 4.17. This means almost 0.835 moles of flue gas can be processed with low costs for each mole of CO_2 utilized in the process. This result is achieved at increased pressure.

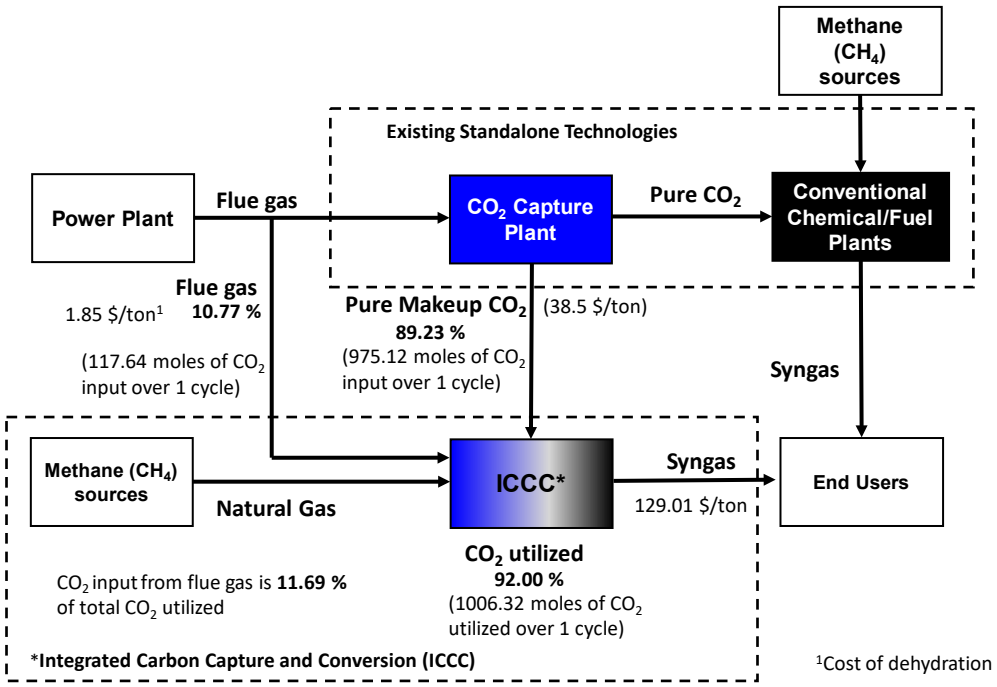

Figure 4.17: "Direct" utilization of CO_2 results for case study 1. The objective maximized herein is the relative percentage of CO_2 fed to the process via flue gas compared to the total CO_2 utilized by the process (Iyer *et al.* [109]).

Since changing the pressure controls the amount of flue gas and natural gas sent to the process,

the optimal pressure has increased to maximize the amount of CO_2 from flue gas processed. This however comes at a decrease in overall CO_2 utilization to 92% and an increase in the total cost to \$129/ton of syngas. Other results are presented in Table 4.14 (case b).

In 2016, about 1,241 million metric tons of CO_2 were emitted from coal-fired power plants in the USA [160]. The direct utilization of 11.69% of CO_2 indicates that as much as 130 million metric tons of CO_2 from the coal power plants in the USA can be directly utilized to produce syngas, assuming 90% utilization, without expending additional energy and cost for CO_2 capture. If we consider a typical cost of post-combustion CO_2 capture of \$40/ton, then we save more than \$5.2 billion per year.

4.4.3.2 Case Study 2: Conversion of Flue gas and Biogas to Syngas

For this case, we again have flue gas in feed step-1, but in step-2 we use biogas feed with 60% CH_4 and 40% CO_2 as the CH_4-rich purge feed. Similar optimizations are performed and the results are tabulated in Tables 4.13–4.15.

Case (a): Maximize Overall utilization of CO_2: The maximum overall CO_2 utilization obtained is 99.67% and it is observed that apart from temperature and pressure, there is a significant difference in the optimal value of the design variables between the natural gas and biogas cases. The adsorption outlet and reactor outlet profiles for this case are shown in Figure 4.18. The optimal step-1 duration is almost 6 times as large as the step-2 duration. Although the optimal value is close to that obtained in the natural gas case, the operating conditions are different. It is difficult to exactly predict the choice of the venting period in this scenario, which has been chosen by the optimization to balance all the tradeoffs. At this maximum overall CO_2 utilization, the cost is \$117.5 per ton of syngas, which is lower than the cost for the natural gas case.

Case (b): Minimize total cost per ton of syngas: The total cost of the process per ton of syngas is minimized while restricting the overall CO_2 utilization above 90% and meeting all other constraints. The minimum total cost per ton of syngas obtained for this case is \$110.1 per ton of syngas. All loss and product specifications are met. The pressure and reactor length hit the lower bound to reduce the cost while the reactor temperature is 1194 K. However, since biogas has 40%

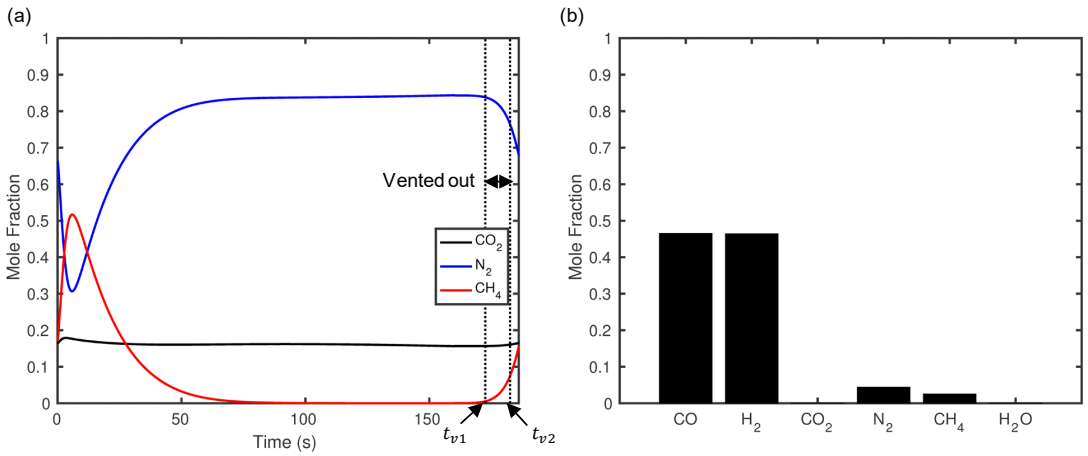

Figure 4.18: Gas compositions at the adsorption and reactor section outlets for case study 2. (a) Mole fraction profiles at the adsorption column outlet for maximum overall % CO_2 utilization for flue gas as feed in step 1 and biogas as feed in step 2. (b) Product (Syngas) composition at reactor outlet at maximum overall % CO_2 utilization for flue gas and natural gas feeds. Maximum overall % CO_2 utilization obtained at optimum is 99.67% at a cost \$117.44/ton syngas. Process metrics and decision variable values at optimum are listed in Table 4.13 and Table 4.15 respectively (Iyer *et al.* [109]).

CO_2 the makeup CO_2 required at optimum has not reached the upper bound. The step-1 duration is much longer than the step-2 duration. From Table 4.15, we see that the use of biogas which is rich in CO_2 reduces the need for makeup CO_2 as compared to the natural gas case. However, a higher makeup CH_4 is used.

Case (c): Maximize "direct" utilization of CO_2 from flue gas over total CO_2 utilization: The reduction in makeup CO_2 requirement results in an increase in the percentage of direct CO_2 input via flue gas as compared to the natural gas case. To further maximize the percentage of CO_2 utilized via flue gas, an optimization is run to maximize the same. It is ensured that the overall CO_2 utilization in the process does not drop below 90%. The optimization results suggest that it is possible to operate the process such that the CO_2 from flue gas accounts for 16.14% of the total CO_2 utilized and 14.6% of the total CO_2 input to the process (see Table 4.14 and Figure 4.19). This means that about 1.15 moles of flue gas can be processed without pressure or temperature swings for each mole of CO_2 utilized. This is achieved by reducing the makeup CO_2 required by the process while

increasing the overall amount of flue gas sent to the process. The overall CO_2 utilization and the cost at this condition are 90.7% and \$128.5/ton, respectively.

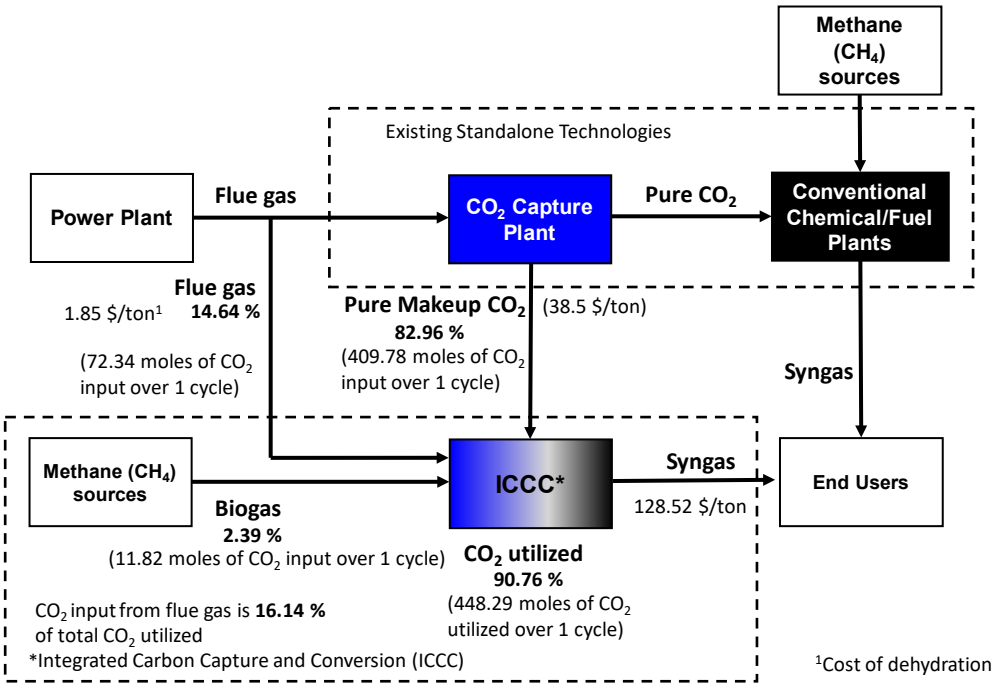

Figure 4.19: "Direct" utilization of CO_2 results for case study 2. CO_2 input contribution from various sources for optimal % of CO_2 input from flue gas over total CO_2 utilized in the process for the case of flue gas and biogas as feeds. The objective maximized herein is the relative percentage of CO_2 fed to the process via flue gas compared to the total CO_2 utilized by the process (Iyer *et al.* [109]).

4.4.3.3 Case Study 3: Technology Robustness in the Presence of Variable Feed Compositions

To examine the applicability of the process when there is varying CO_2 content in the CH_4-rich feed, optimizations are performed for CO_2 percentage composition in CH_4-rich feed varying from 0–60 %, considering different objectives of overall CO_2 utilization, total cost per ton of syngas, and direct utilization CO_2 from flue gas. The optimization results are shown in Figure 4.20. We have used different warm starts and variable bounds for the optimization algorithm to obtain these results. It can be observed that for a wide variety of CO_2 compositions in the methane rich feed

it is possible to operate the process feasibly with costs of around \$110/ton of syngas, maximum overall CO_2 utilization of around 99.5%, and direct flue gas based CO_2 utilization of around 16%. It is possible to maintain a certain desired objective value and operate the process at different compositions of CH_4-rich purge feed. This shows that our proposed technology could be robust under different feed conditions. It is important to note that the best results presented above are

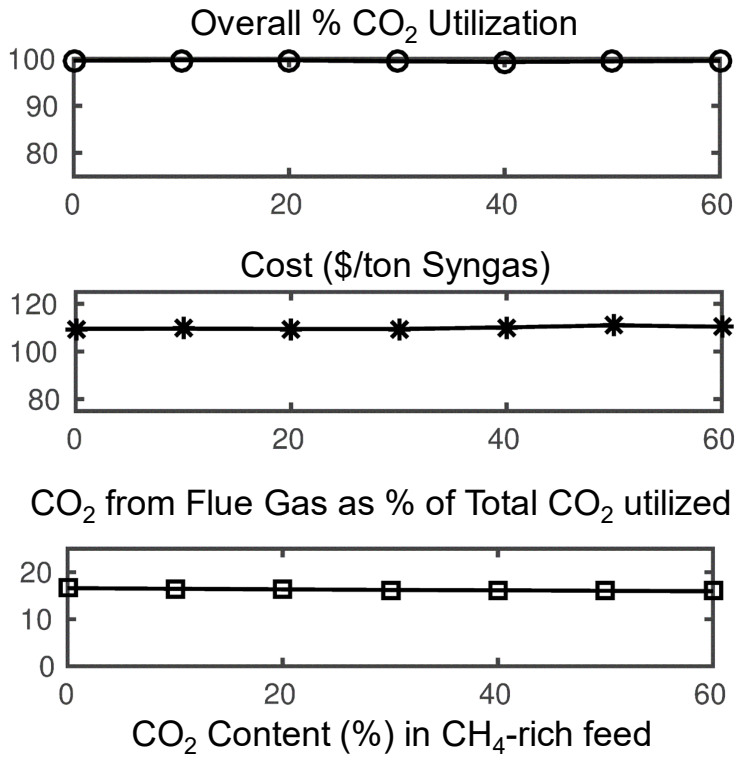

Figure 4.20: Results showing the robustness in the performance metrics for a range of feed conditions. Optimal objective values are obtained for different CO_2 content ranging from 0–60 % in methane-rich feed used in the second step. The objectives are optimized separately by changing the objective function accordingly to maximizing overall % CO_2 utilization, minimizing the total cost of the process per ton of syngas produced and maximizing the % of CO_2 input from flue gas over total CO_2 utilized (Iyer *et al.* [109]).

dependent on the bounds on the design variables and the limits on the process performance metrics. Since conservative values of these parameters are employed, relaxing some of these specifications

depending on the downstream needs may improve the results and applicability of the process even further.

The optimization case studies discussed above are performed with N=5 and C=5 along with the constraints and decision variable bounds already specified. The optimization algorithm requires function evaluations (simulations run at samples) to move towards feasibility and later towards the optimal point. Since the process model is dynamic involving partial differential equations and is operated cyclically, a highly accurate simulation performed with high N over many cycles is computationally expensive. The time required per simulation can be greatly reduced by performing the simulations for a fewer number of discretizations and cycles, hereafter referred to as short simulations. Though the accuracy might be reduced to an extent, the feasible and optimal points for short simulations are obtained within a shorter time. The values of the process metrics obtained for a sample point after the short simulation can be compared with a longer simulation (N=30 and C=100) to check if it is acceptable. The differences in the value of the process metrics obtained from short and long simulations are small as observed from Table 4.16. The results can be further refined using longer simulations.

4.4.3.4 Progress of the Algorithm

It is also important to look at the performance of the proposed optimization algorithm in terms of the number of simulations that it takes to reach an optimal solution. To this end, the progress of the optimization algorithm from an infeasible initial point to the optimal point is shown in Figure 4.21. This result is representative of a typical case and the numbers would change for different case studies. The optimization problem run in this case is the minimization of total cost when flue gas and natural gas are used as feeds. The initial point from which the optimization algorithm is started is same as the reference case listed in Table 4.4. The algorithm first decreases the cumulative constraint violation of all the constraints to reach the feasible operating point. After that the algorithm decreases the desired objective function till it reaches optimality. The optimization algorithm ends once the criticality measure is satisfied or the trust region size becomes sufficiently small. Feasible points obtained in this manner could be then provided as starting points to other

Table 4.16: Comparison of process performance metrics obtained from short N=5, C=5) simulations and long (N=30, C =100) simulations for the reference case. The absolute value of the percentage deviation of the short simulations from the longer simulations is also reported (Iyer *et al.* [109]).

Process Metric	N =30, C=100	N=5, C=5	% Deviation
% CO_2 Utilization	75.63	76.44	1.07
Total Cost ($/ton SG)	218.06	221.27	1.47
Operating Cost ($/ton SG)	175.33	178.03	1.54
Total loss % CH_4	62.62	62.86	0.38
Total loss % CO_2	24.29	23.49	3.29
Vent loss % CH_4	4.26	5.05	18.54
Vent loss % CO_2	3.14	3.00	4.46
Unreacted % CH_4	58.36	57.82	0.93
Unreacted % CO_2	21.16	20.49	3.17
Syngas ratio (H_2/CO)	0.83	0.83	0
CH_4 % in product	0.25	0.25	0
CO_2 % in product	0.05	0.05	0
N_2 % in product	0.03	0.03	0
H_2 % in product	0.29	0.29	0
CO % in product	0.35	0.35	0
H_2O % in product	0.03	0.03	0

optimization runs with different objectives. It is observed that the restoration phase of the algorithm needs 620 simulation/samples of the NAPDE model to reach a feasible solution with all the constraints satisfied. Afterwards, the algorithm switches to the optimization phase, which performs additional 2885 simulations to reach the final solution within a stipulated time.

4.5 Section Summary

An integrated cyclic process which captures CO_2 from flue gas using a CH_4-rich feed to perform regeneration without expending significant energy is designed, intensified and optimized. The choice of using CH_4-rich feed was motivated by the overarching goal which is to ultimately produce syngas by CO_2 reforming of methane. The cyclic operation required the use of a dynamic model to examine the effect of variables such as pressure, column lengths, and durations of individual feed steps. As the choice of some variables such as venting times and makeup feeds are based on the upstream adsorption outlet profiles, applying just a parametric simulation study for

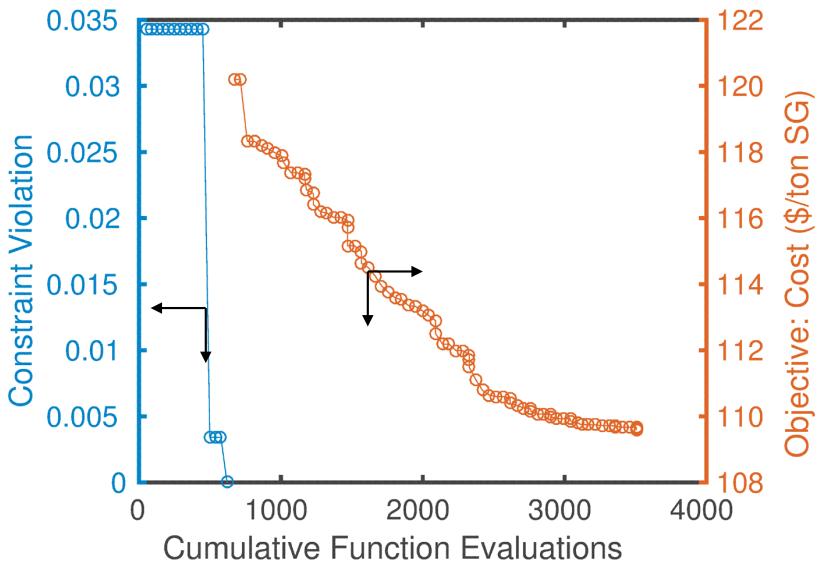

Figure 4.21: Progress of the optimization algorithm from infeasible operating point towards optimality. The restoration phase of the algorithm is used to reduce the constraint violation and converge to a feasible point, after which the optimization phase of the algorithm reduces the objective of cost of the process while maintaining feasibility. For the particular case of minimizing the total cost when flue gas and natural gas are used as the feed, the restoration phase needs 620 simulations to find a feasible solution where the constraint violation is zero. The algorithm then switches to the optimization phase to perform additional simulations toward finding better objective values (Iyer *et al.* [109]).

the whole process may not be the best approach. Even for finding conditions for feasible operation while meeting process constraints, an optimization framework is necessary for complex process configurations such as this one. A novel simulation-based, data-driven optimization strategy was used to obtain optimal operating conditions for maximum CO_2 utilization and minimum cost. An overall CO_2 utilization of 99.67% was obtained. The cost of syngas production is also reasonable \$109–110 per ton. As much as 14.6% of the total CO_2 input to the process can be also captured with low cost "directly" from flue gas while still maintaining more than 90% overall CO_2 utilization. This is possible due to the novel intensification of the separation and reaction steps and the optimization approach presented in this work. The process is found to be robust to operate efficiently under different feed conditions. Though the technology discussed is dependent on external reinforcement of CO_2 and CH_4 to meet the requisite syngas product specifications, an argument

can be made for the low-cost utilization of CO_2 and CH_4 from off-spec sources by employing this process in a grid or network along with existing technologies.

5. SUMMARY AND CONCLUSIONS

5.1 Key Conclusions

The key conclusions identified in this dissertation are summarized as follows:

- A multi-scale framework for integrated process and material design and intensification is developed where the process design problem is posed as an optimization formulation. Considerations on both the process and materials level is enables through the incorporation of process models, material models and models bridging material and process scales in the framework. The design of a technology for achieving process goals is not separated into process design and material design rather thought of as an integrated composite design.

- The framework is applied to exploit the storage and separation capabilities of zeolites in order to combine the separation and storage of CH_4 from a CH_4/N_2 feed mixture. 178 pure silica zeolitic frameworks are considered and corresponding optimal process conditions are obtained for each zeolite. These are then ranked based on the value of the objective maximized, which is the moles of CH_4 stored in the column at the end of the process. Among these, zeolite framework SBN which also has a high storage capacity from a pure feed of CH_4, is most suitable for combined separation and storage of CH_4 from a variety of feed compositions. However, the loss of CH_4 through the column outlet limits the effectiveness of combined natural gas separation and storage process.

- The feasibility of the combined separation and storage process with respect to satisfying imposed constraints on CH_4 loss and CH_4 purity is mapped over the material property space of adsorption isotherm parameters. Rather than just testing the feasibility, a map of total constraint violation of the process along with the individual constraint violation is plotted to identify key constraints and variables affecting the process feasibility. The loss constraint is found to affect overall process feasibility over most of the material property space for feed with 85% CH_4 and 15% N_2. It is observed that for satisfying the constraint on CH_4 loss,

there needs to be an appreciable capacity difference from the optimal operating pressure P_h and the initial pressure of the column. The properties of zeolites available in both existing and hypothetical material database is super-imposed over the generated feasibility maps to determine appropriate candidate material structures and directions for further improvement.

- A process to integrate the carbon capture from flue gas and subsequent conversion to syngas using methane rich feedstocks is designed and optimized. Different objectives such as overall CO_2 utilization, production cost, percentage of CO_2 in flue gas utilized without capture costs are optimized. About 14.6% of the total CO_2 input from flue gas can be utilized without additional capture cost while maintaining about 91% overall CO_2 utilization. The design is also found to be robust for natural gas feeds with different levels of CO_2 contamination.

5.2 Recommendations for Future Work

As mentioned above, there are clear advantages of using the multi-scale framework for designing novel intensified process which meet imposed constraints and for studying the variation in optimal process performance over the material property space. Such an analysis, even for well studied process systems can provide insights into further experimental design of materials. The analysis can be extended to other process systems involving nanoporous materials such as membrane processes, reaction processes and combinations of such processes. A determination can be made whether the limitation in performance is due to process operation or in material properties.

Since the design problem is posed as an optimization formulation, appropriate algebraic formulations of process models are necessary to solve the resulting optimization formulations to optimality using model-based optimization solvers. For processes which involve variation of state variables in multiple dimensions, have complex equipment geometries and/or have cyclical operations in space (e.g. recycle feeds) and time, the process model can be rigorous and complex with multiple differential terms. Discretization of such processes into an algebraic formulation can lead to a large scale nonlinear non convex formulation with a large number of variables and equations. Such models can be difficult and computationally expensive to solve to local optimality and might

require additional initialization, linearization and decomposition strategies to converge. An alternate approach is to use data-driven surrogate models and other approaches of model reduction in order to replicate the rigorous process models if adequate data is available to construct such models with acceptable accuracy. However, for high fidelity complex process models, even generating data for a single set of operating conditions can be time consuming.

It is difficult to obtain closed form analytical expressions relating material structures such as crystal structure, type of atoms, pore size distributions with key properties for many process applications such as diffusivity, heat of adsorption, equilibrium adsorption loadings. For some of the widely used structures, this data is available through past experimentation. For other potential materials where adequate experimental data is unavailable, computational molecular simulation methods can be used to obtain the values of these key properties for a given material structure. However, even these are computationally expensive especially for molecules with multiple atoms and at high pressures where the number of molecules under consideration per unit volume is high. Hence it might be difficult to incorporate these simulations directly in the multi-scale framework. Moreover, there is a large number of candidate material structures possible through introduction of different number of cations such as Al^{3+}, Na^{+} by replacing some of the Si^{4+}, changing crystal structures and topologies. There do exist a few databases [46, 79] incorporating both adsorbent structures, geometric and pore descriptors and their corresponding properties such as adsorption loading, Henry coefficients for select gases which can be useful in identifying structure-property relationships and rules through machine learning based approaches. However, more such generalized expressions with a few tunable parameters relating structures and structure modifications to changes in material properties can be useful for further analysis using the optimization approaches discussed in this dissertation. Vlachos *et al.* [70] highlights similar concerns that in transitioning to a multi-scale design and development approach, complexity in interactions, combinatorial explosion in parameters when considering multiple alternatives, need for more computational power and computationally efficient algorithms will be important challenges to overcome.

REFERENCES

[1] E. L. First, M. M. F. Hasan, and C. A. Floudas, "Discovery of novel zeolites for natural gas purification through combined material screening and process optimization," *AIChE J.*, vol. 60, no. 5, pp. 1767–1785, 2014.

[2] D. S. Sholl and R. P. Lively, "Seven chemical separations to change the world," *Nature*, vol. 532, pp. 435–437, 2016.

[3] T. Van Gerven and A. Stankiewicz, "Structure, energy, synergy, time — the fundamentals of process intensification," *Ind. Eng. Chem. Res.*, vol. 48, no. 5, pp. 2465–2474, 2009.

[4] J.-F. Portha, L. Falk, and J.-M. Commenge, "Local and global process intensification," *Chem. Eng. Process. Process Intensif.*, vol. 84, pp. 1 – 13, 2014. EPIC 2013.

[5] X. Wu, C. Wu, and S. Wu, "Dual-enhanced steam methane reforming by membrane separation of H_2 and reactive sorption of CO_2," *Chem. Eng. Res. Des.*, vol. 96, pp. 150–157, 2015.

[6] E. L. Lugo and B. A. Wilhite, "A theoretical comparison of multifunctional catalyst for sorption-enhanced reforming process," *Chem. Eng. Sci.*, vol. 150, pp. 1–15, 2016.

[7] B. T. Carvill, J. R. Hufton, M. Anand, and S. Sircar, "Sorption-enhanced reaction process," *AIChE J.*, vol. 42, no. 10, pp. 2765–2772, 1996.

[8] M. R. Rahimpour, "A dual-catalyst bed concept for industrial methanol synthesis," *Chem. Eng. Commun.*, vol. 194, no. 12, pp. 1638–1653, 2007.

[9] A. M. Ribeiro, C. A. Grande, F. V. S. Lopes, J. M. Loureiro, and A. E. Rodrigues, "A parametric study of layered bed PSA for hydrogen purification," *Chem. Eng. Sci.*, vol. 63, no. 21, pp. 5258–5273, 2008.

[10] M. Chlendi and D. Tondeur, "Dynamic behaviour of layered columns in pressure swing adsorption," *Gas Sep. Purif.*, vol. 9, no. 4, pp. 231–242, 1995.

[11] I. D. Lee and R. H. Kadlec, "Effects of adsorbent and catalyst distributions in pressure swing reactors.," in *AIChE Symposium Series*, no. 7-176, 1988.

[12] M. M. F. Hasan, E. L. First, and C. A. Floudas, "Discovery of novel zeolites and multi-zeolite processes for p-xylene separation using simulated moving bed (SMB) chromatography," *Chem. Eng. Sci.*, vol. 159, pp. 3–17, 2017.

[13] O. Onel, A. M. Niziolek, H. Butcher, B. A. Wilhite, and C. A. Floudas, "Multi-scale approaches for gas-to-liquids process intensification: CFD modeling, process synthesis, and global optimization," *Comput. Chem. Eng.*, vol. 105, pp. 276 – 296, 2017. Process Intensification.

[14] M. M. F. Hasan, F. Boukouvala, E. L. First, and C. A. Floudas, "Nationwide, regional, and statewide CO_2 capture, utilization, and sequestration supply chain network optimization," *Ind. Eng. Chem. Res.*, vol. 53, no. 18, pp. 7489–7506, 2014.

[15] L. T. Biegler, "Advanced optimization strategies for integrated dynamic process operations," *Comput. Chem. Eng.*, 2017.

[16] S. Effendy, C. Xu, and S. Farooq, "Optimization of a pressure swing adsorption process for nitrogen rejection from natural gas," *Ind. Eng. Chem. Res.*, vol. 56, no. 18, pp. 5417–5431, 2017.

[17] P. Shahkarami and S. Fatemi, "Mathematical modeling and optimization of combined steam and dry reforming of methane process in catalytic fluidized bed membrane reactor," *Chem. Eng. Commun.*, vol. 202, no. 6, pp. 774–786, 2015.

[18] L. Chen, Q. Jiang, Z. Song, and D. Posarac, "Optimization of methanol yield from a Lurgi reactor," *Chem. Eng. Technol.*, vol. 34, no. 5, pp. 817–822, 2011.

[19] S. Nilchan and C. C. Pantelides, "On the optimisation of periodic adsorption processes," *Adsorption*, vol. 4, no. 2, pp. 113–147, 1998.

[20] Z. A. Aboosadi, A. H. Jahanmiri, and M. R. Rahimpour, "Optimization of tri-reformer reactor to produce synthesis gas for methanol production using differential evolution (DE) method," *Appl. Energy*, vol. 88, no. 8, pp. 2691–2701, 2011.

[21] C. S. Bîldea, R. Győrgy, C. C. Brunchi, and A. A. Kiss, "Optimal design of intensified processes for DME synthesis," *Comput. Chem. Eng.*, vol. 105, pp. 142 – 151, 2017. Process Intensification.

[22] C. A. Henao and C. T. Maravelias, "Surrogate-based superstructure optimization framework," *AIChE J.*, vol. 57, no. 5, pp. 1216–1232, 2011.

[23] S. R. Ismail, E. Pistikopoulos, and K. Papalexandri, "Synthesis of reactive and combined reactor/separation systems utilizing a mass/heat exchange transfer module," *Chem. Eng. Sci.*, vol. 54, no. 13, pp. 2721 – 2729, 1999.

[24] S. Recker, M. Skiborowski, C. Redepenning, and W. Marquardt, "A unifying framework for optimization-based design of integrated reaction-separation processes," *Comput. Chem. Eng.*, vol. 81, no. Supplement C, pp. 260 – 271, 2015. Special Issue: Selected papers from the 8th International Symposium on the Foundations of Computer-Aided Process Design (FOCAPD 2014), July 13-17, 2014, Cle Elum, Washington, USA.

[25] D. Nikolić, E. S. Kikkinides, and M. C. Georgiadis, "Optimization of multibed pressure swing adsorption processes," *Ind. Eng. Chem. Res.*, vol. 48, no. 11, pp. 5388–5398, 2009.

[26] A. Agarwal, L. T. Biegler, and S. E. Zitney, "A superstructure-based optimal synthesis of PSA cycles for post-combustion CO_2 capture," *AIChE J.*, vol. 56, no. 7, pp. 1813–1828, 2010.

[27] A. Agarwal, L. T. Biegler, and S. E. Zitney, "Superstructure-based optimal synthesis of pressure swing adsorption cycles for precombustion CO_2 capture," *Ind. Eng. Chem. Res.*, vol. 49, no. 11, pp. 5066–5079, 2010.

[28] R. E. Swaney and I. E. Grossmann, "An index for operational flexibility in chemical process design. Part I: Formulation and theory," *AIChE J.*, vol. 31, no. 4, pp. 621–630, 1985.

[29] E. N. Pistikopoulos and T. A. Mazzuchi, "A novel flexibility analysis approach for processes with stochastic parameters," *Comput. Chem. Eng.*, vol. 14, no. 9, pp. 991–1000, 1990.

[30] G. Desmet, J. De Greef, H. Verelst, and G. V. Baron, "Performance limits of isothermal packed bed and perforated monolithic bed reactors operated under laminar flow conditions. I. General optimization analysis," *Chem. Eng. Sci.*, vol. 58, no. 14, pp. 3187–3202, 2003.

[31] V. Dua and E. Pistikopoulos, "Optimization techniques for process synthesis and material design under uncertainty," *Chem. Eng. Res. Des.*, vol. 76, no. 3, pp. 408 – 416, 1998. Techno-Economic Analysis.

[32] F. E. da Cruz and V. I. Manousiouthakis, "Process intensification of reactive separator networks through the ideas conceptual framework," *Comput. Chem. Eng.*, vol. 105, pp. 39 – 55, 2017. Process Intensification.

[33] J. C. Carrasco and F. V. Lima, "An optimization-based operability framework for process design and intensification of modular natural gas utilization systems," *Comput. Chem. Eng.*, vol. 105, pp. 246 – 258, 2017.

[34] D. J. Earl and M. W. Deem, "Toward a database of hypothetical zeolite structures," *Ind. Eng. Chem. Res.*, vol. 45, no. 16, pp. 5449–5454, 2006.

[35] P. Bai, M. Y. Jeon, L. Ren, C. Knight, M. W. Deem, M. Tsapatsis, and J. I. Siepmann, "Discovery of optimal zeolites for challenging separations and chemical transformations using predictive materials modeling," *Nat. Commun.*, vol. 6, p. 5912, 2015.

[36] C. M. Simon, J. Kim, D. A. Gomez-Gualdron, J. S. Camp, Y. G. Chung, R. L. Martin, R. Mercado, M. W. Deem, D. Gunter, M. Haranczyk, D. S. Sholl, R. Q. Snurr, and B. Smit, "The materials genome in action: identifying the performance limits for methane storage," *Energy Environ. Sci.*, vol. 8, pp. 1190–1199, 2015.

[37] J. Kim, L.-C. Lin, R. L. Martin, J. A. Swisher, M. Haranczyk, and B. Smit, "Large-scale computational screening of zeolites for ethane/ethene separation," *Langmuir*, vol. 28, no. 32, pp. 11914–11919, 2012. PMID: 22784373.

[38] J. Kim, M. Abouelnasr, L.-C. Lin, and B. Smit, "Large-scale screening of zeolite structures for CO_2 membrane separations," *J. Am. Chem. Soc.*, vol. 135, no. 20, pp. 7545–7552, 2013. PMID: 23654217.

[39] L.-C. Lin, A. H. Berger, R. L. Martin, J. Kim, J. A. Swisher, K. Jariwala, C. H. Rycroft, A. S. Bhown, M. W. Deem, M. Haranczyk, and B. Smit, "In silico screening of carbon-capture materials," *Nat. Mater.*, vol. 11, no. 7, pp. 633–641, 2012.

[40] C. E. Wilmer, M. Leaf, C. Y. Lee, O. K. Farha, B. G. Hauser, J. T. Hupp, and R. Q. Snurr, "Large-scale screening of hypothetical metal-organic frameworks," *Nat. Chem.*, vol. 4, p. 83, 2011.

[41] S. Li, Y. G. Chung, and R. Q. Snurr, "High-throughput screening of metal-organic frameworks for CO_2 capture in the presence of water," *Langmuir*, vol. 32, no. 40, pp. 10368–10376, 2016.

[42] Y. J. Colon and R. Q. Snurr, "High-throughput computational screening of metal-organic frameworks," *Chem. Soc. Rev.*, vol. 43, no. 16, pp. 5735–5749, 2014.

[43] D. Wu, C. Wang, B. Liu, D. Liu, Q. Yang, and C. Zhong, "Large-scale computational screening of metal-organic frameworks for CH_4/H_2 separation," *AIChE J.*, vol. 58, no. 7, pp. 2078–2084, 2012.

[44] R. Krishna and J. M. van Baten, "In silico screening of metal-organic frameworks in separation applications," *Phys. Chem. Chem. Phys.*, vol. 13, no. 22, pp. 10593–10616, 2011.

[45] D. A. Gomez-Gualdron, C. E. Wilmer, O. K. Farha, J. T. Hupp, and R. Q. Snurr, "Exploring the limits of methane storage and delivery in nanoporous materials," *J. Phys. Chem. C*, vol. 118, no. 13, pp. 6941–6951, 2014.

[46] C. M. Simon, J. Kim, L.-C. Lin, R. L. Martin, M. Haranczyk, and B. Smit, "Optimizing nanoporous materials for gas storage," *Phys. Chem. Chem. Phys.*, vol. 16, pp. 5499–5513, 2014.

[47] M. Pardakhti, E. Moharreri, D. Wanik, S. L. Suib, and R. Srivastava, "Machine learning using combined structural and chemical descriptors for prediction of methane adsorption performance of metal organic frameworks (MOFs)," *ACS Comb. Sci.*, vol. 19, no. 10, pp. 640–645, 2017.

[48] H. Ohno and Y. Mukae, "Machine learning approach for prediction and search: Application to methane storage in a metal-organic framework," *J. Phys. Chem. C*, vol. 120, no. 42, pp. 23963–23968, 2016.

[49] M. Fernandez, P. G. Boyd, T. D. Daff, M. Z. Aghaji, and T. K. Woo, "Rapid and accurate machine learning recognition of high performing metal organic frameworks for CO_2 capture," *J. Phys. Chem. Lett.*, vol. 5, no. 17, pp. 3056–3060, 2014.

[50] G. Anderson, B. Schweitzer, R. Anderson, and D. A. Gómez-Gualdrón, "Attainable volumetric targets for adsorption-based hydrogen storage in porous crystals: Molecular simulation and machine learning," *J. Phys. Chem. C*, vol. 123, no. 1, pp. 120–130, 2019.

[51] R. Anderson, J. Rodgers, E. Argueta, A. Biong, and D. A. Gómez-Gualdrón, "Role of pore chemistry and topology in the CO_2 capture capabilities of mofs: From molecular simulation to machine learning," *Chem. Mater.*, vol. 30, no. 18, pp. 6325–6337, 2018.

[52] M. Fernandez, T. K. Woo, C. E. Wilmer, and R. Q. Snurr, "Large-scale quantitative structure-property relationship (QSPR) analysis of methane storage in metal-organic frameworks," *J. Phys. Chem. C*, vol. 117, no. 15, pp. 7681–7689, 2013.

[53] O. Odele and S. Macchietto, "Computer aided molecular design: a novel method for optimal solvent selection," *Fluid Phase Equilib.*, vol. 82, no. Supplement C, pp. 47 – 54, 1993.

[54] R. Gani, B. Nielsen, and A. Fredenslund, "A group contribution approach to computer-aided molecular design," *AIChE J.*, vol. 37, no. 9, pp. 1318–1332, 1991.

[55] C. D. Maranas, "Optimal computer-aided molecular design: A polymer design case study," *Ind. Eng. Chem. Res.*, vol. 35, no. 10, pp. 3403–3414, 1996.

[56] A. T. Karunanithi, L. E. K. Achenie, and R. Gani, "A new decomposition-based computer-aided molecular/mixture design methodology for the design of optimal solvents and solvent mixtures," *Ind. Eng. Chem. Res.*, vol. 44, no. 13, pp. 4785–4797, 2005.

[57] E. Pistikopoulos and S. Stefanis, "Optimal solvent design for environmental impact minimization," *Comput. Chem. Eng.*, vol. 22, no. 6, pp. 717 – 733, 1998. Design of chemical compounds.

[58] A. Hamad and M. El-Halwagi, "Simultaneous synthesis of mass separating agents and interception networks," *Chem. Eng. Res. Des.*, vol. 76, no. 3, pp. 376 – 388, 1998. Techno-Economic Analysis.

[59] P. T. Benavides and U. Diwekar, "Optimal design of adsorbents for NORM removal from produced water in natural gas fracking. Part 1: Group contribution method for adsorption," *Chem. Eng. Sci.*, vol. 137, pp. 964–976, 2015.

[60] A. D. Wiersum, J.-S. Chang, C. Serre, and P. L. Llewellyn, "An adsorbent performance indicator as a first step evaluation of novel sorbents for gas separations: Application to metal-organic frameworks," *Langmuir*, vol. 29, no. 10, pp. 3301–3309, 2013. PMID: 23383594.

[61] A. K. Rajagopalan, A. M. Avila, and A. Rajendran, "Do adsorbent screening metrics predict process performance? a process optimisation based study for post-combustion capture of CO_2," *Int. J. Greenhouse Gas Control*, vol. 46, pp. 76–85, 2016.

[62] S. Ga, H. Jang, and J. H. Lee, "New performance indicators for adsorbent evaluation derived from a reduced order model of an idealized psa process for CO_2 capture," *Comput. Chem. Eng.*, vol. 102, pp. 188–212, 2017. Sustainability & Energy Systems.

[63] S. Guo, P. Vengsarkar, J. Bentley, M. Weber, G. Agrawal, C. Dorsi, and Y. Kawajiri, "A concurrent approach for process design and multicomponent adsorption modeling with local isotherms," *Chem. Eng. Sci.*, vol. 171, pp. 426 – 439, 2017.

[64] Y. Belmabkhout, V. Guillerm, and M. Eddaoudi, "Low concentration CO_2 capture using physical adsorbents: Are metal-organic frameworks becoming the new benchmark materials?," *Chem. Eng. J.*, vol. 296, pp. 386–397, 2016.

[65] A. H. Berger and A. S. Bhown, "Selection of optimal solid sorbents for CO_2 capture based on gas phase CO_2 composition," *Energy Procedia*, vol. 63, pp. 2092–2099, 2014.

[66] A. H. Berger and A. S. Bhown, "Optimizing solid sorbents for CO_2 capture," *Energy Procedia*, vol. 37, pp. 25–32, 2013.

[67] M. M. F. Hasan, E. L. First, and C. A. Floudas, "Cost-effective CO_2 capture based on in silico screening of zeolites and process optimization," *Phys. Chem. Chem. Phys.*, vol. 15, no. 40, pp. 17601–17618, 2013.

[68] T. Liu, E. L. First, M. M. F. Hasan, and C. A. Floudas, "A multi-scale approach for the discovery of zeolites for hydrogen sulfide removal," *Comput. Chem. Eng.*, vol. 91, pp. 206–218, 2016.

[69] L. T. Biegler, Y.-d. Lang, and W. Lin, "Multi-scale optimization for process systems engineering," *Comput. Chem. Eng.*, vol. 60, pp. 17–30, 2014.

[70] D. G. Vlachos, "Multiscale modeling for emergent behavior, complexity, and combinatorial explosion," *AIChE J.*, vol. 58, no. 5, pp. 1314–1325, 2012.

[71] M. F. Hasan, E. L. First, F. Boukouvala, and C. A. Floudas, "A multi-scale framework for CO_2 capture, utilization, and sequestration: CCUS and CCU," *Comput. Chem. Eng.*, vol. 81, pp. 2–21, 2015.

[72] M. Sen, A. Chaudhury, R. Singh, J. John, and R. Ramachandran, "Multi-scale flowsheet simulation of an integrated continuous purification-downstream pharmaceutical manufacturing process," *Int. J. Pharm.*, vol. 445, no. 1, pp. 29 – 38, 2013.

[73] Q. Wang, J. Bai, Z. Lu, Y. Pan, and X. You, "Finely tuning MOFs towards high-performance post-combustion CO_2 capture materials," *Chem. Commun.*, vol. 52, no. 3, pp. 443–452, 2016.

[74] J. Yu, L.-H. Xie, J.-R. Li, Y. Ma, J. M. Seminario, and P. B. Balbuena, "CO_2 capture and separations using MOFs: Computational and experimental studies," *Chem. Rev.*, vol. 117, no. 14, pp. 9674–9754, 2017.

[75] H. Jasuja, J. Zang, D. S. Sholl, and K. S. Walton, "Rational tuning of water vapor and CO_2 adsorption in highly stable Zr-based MOFs," *J. Phys. Chem. C*, vol. 116, no. 44, pp. 23526–23532, 2012.

[76] R. S. Thakur, N. Kaistha, and D. P. Rao, "Novel single-bed and twin-bed pressure swing adsorption systems," *Chem. Eng. Process. Process Intensif.*, vol. 95, pp. 165 – 174, 2015.

[77] S. S. Iyer, S. E. Demirel, and M. M. F. Hasan, "Combined natural gas separation and storage based on in silico material screening and process optimization," *Ind. Eng. Chem. Res.*, vol. 57, no. 49, pp. 16727–16750, 2018.

[78] C. Baerlocher and L. McCusker, "Database of zeolite structures." `http://www.iza-structure.org/databases/` Accessed Aug 10, 2017.

[79] M. W. Deem, R. Pophale, P. A. Cheeseman, and D. J. Earl, "Computational discovery of new zeolite-like materials," *J. Phys. Chem. C*, vol. 113, no. 51, pp. 21353–21360, 2009.

[80] A. Arora, S. S. Iyer, and M. F. Hasan, "GRAMS: A general framework describing adsorption, reaction and sorption-enhanced reaction processes," *Chem. Eng. Sci.*, vol. 192, pp. 335 – 358, 2018.

[81] R. Haghpanah, A. Majumder, R. Nilam, A. Rajendran, S. Farooq, I. A. Karimi, and M. Amanullah, "Multiobjective optimization of a four-step adsorption process for postcombustion CO_2 capture via finite volume simulation," *Ind. Eng. Chem. Res.*, vol. 52, no. 11, pp. 4249–4265, 2013.

[82] P. Cruz, J. Santos, F. Magalhães, and A. Mendes, "Simulation of separation processes using finite volume method," *Comput. Chem. Eng.*, vol. 30, no. 1, pp. 83 – 98, 2005.

[83] A. Cozad, N. V. Sahinidis, and D. C. Miller, "Learning surrogate models for simulation-based optimization," *AIChE J.*, vol. 60, no. 6, pp. 2211–2227, 2014.

[84] I. Bajaj and M. F. Hasan, "Effective sampling, modeling and optimization of constrained black-box problems," in *Proceedings of 26th European Symposium on Computer Aided Process Engineering*, pp. 553–558, 2016.

[85] C. Sangwichien, G. L. Aranovich, and M. D. Donohue, "Density functional theory predictions of adsorption isotherms with hysteresis loops," *Colloids Surf., A*, vol. 206, no. 1, pp. 313–320, 2002.

[86] D. Dubbeldam, S. Calero, D. E. Ellis, and R. Q. Snurr, "RASPA: molecular simulation software for adsorption and diffusion in flexible nanoporous materials," *Mol. Simul.*, vol. 42, no. 2, pp. 81–101, 2016.

[87] D. Frenkel and B. Smit, eds., *In Understanding Molecular Simulation*. San Diego, CA, USA: Academic Press, 2002.

[88] H. Van Koningsveld, H. Van Bekkum, and J. C. Jansen, "On the location and disorder of the tetrapropylammonium (TPA) ion in zeolite ZSM-5 with improved framework accuracy," *Acta Cryst.*, vol. B43, no. 2, pp. 127–132.

[89] W. Zhu, P. Hrabanek, L. Gora, F. Kapteijn, and J. A. Moulijn, "Role of adsorption in the permeation of CH_4 and CO_2 through a silicalite-1 membrane," *Ind. Eng. Chem. Res.*, vol. 45, no. 2, pp. 767–776, 2006.

[90] K. Watanabe, N. Austin, and M. R. Stapleton, "Investigation of the air separation properties of zeolites types A, X and Y by monte carlo simulations," *Mol. Simul.*, vol. 15, no. 4, pp. 197–221, 1995.

[91] R. Misener and C. A. Floudas, "ANTIGONE: Algorithms for coNTinuous / Integer Global Optimization of Nonlinear Equations," *J. Glob. Optim.*, vol. 59, no. 2, pp. 503–526, 2014.

[92] J. A. Ritter, S. J. Bhadra, and A. D. Ebner, "On the use of the dual-process Langmuir model for correlating unary equilibria and predicting mixed-gas adsorption equilibria," *Langmuir*, vol. 27, no. 8, pp. 4700–4712, 2011.

[93] BP, "Energy Outlook 2017," tech. rep., British Petroleum, 2017.

[94] A. I. Stankiewicz and J. A. Moulijn, "Process intensification: Transforming chemical engineering," *Chem. Eng. Prog.*, vol. 1, pp. 22–34, 2000.

[95] D. Reay, C. Ramshaw, and A. Harvey, *Process Intensification: Engineering for Efficiency, Sustainability and Flexibility*. Oxford: Butterworth-Heinemann, 2nd ed., 2013.

[96] S. E. Demirel, J. Li, and M. M. F. Hasan, "Systematic process intensification using building blocks," *Comput. Chem. Eng.*, vol. 105, pp. 2–38, 2017.

[97] V. Chowanietz, C. Pasel, M. Luckas, T. Eckardt, and D. Bathen, "Desorption of mercaptans and water from a silica-alumina gel," *Ind. Eng. Chem. Res.*, vol. 56, no. 2, pp. 614–621, 2017.

[98] B. Steuten, C. Pasel, M. Luckas, and D. Bathen, "Trace level adsorption of toxic sulfur compounds, carbon dioxide, and water from methane," *J. Chem. Eng. Data*, vol. 58, no. 9, pp. 2465–2473, 2013.

[99] J. Kuo, K. Wang, and C. Chen, "Pros and cons of different nitrogen removal unit (NRU) technology," *J. Nat. Gas Sci. Eng.*, vol. 7, pp. 52–59, 2012.

[100] EPA, "Optimizing nitrogen rejection units: Lessons learned from natural gas STAR," Apr. 2005. `https://www.epa.gov/sites/production/files/2017-09/documents/rejection_units.pdf` Processors Technology Transfer Workshop. Last accessed March 22, 2018.

[101] Y. Luo, "Adsorptive nitrogen rejection from natural gas," Apr. 2017. `https://www.aiche.org/rapid/projects/adsorptive-nitrogen-rejection-natural-gas#update-pane` Last accessed March 22, 2018.

[102] S. Sircar, "Separation of methane and carbon dioxide gas mixtures by pressure swing adsorption," *Sep. Sci. Technol.*, vol. 23, no. 6-7, pp. 519–529, 1988.

[103] M. Tagliabue, D. Farrusseng, S. Valencia, S. Aguado, U. Ravon, C. Rizzo, A. Corma, and C. Mirodatos, "Natural gas treating by selective adsorption: Material science and chemical engineering interplay," *Chem. Eng. J.*, vol. 155, no. 3, pp. 553–566, 2009.

[104] M. Fakhroleslam and S. Fatemi, "Comparative simulation study of PSA, VSA, and TSA processes for purification of methane from CO_2 via SAPO-34 core-shell adsorbent," *Sep. Sci. Technol.*, vol. 51, no. 14, pp. 2326–2338, 2016.

[105] J. Wegrzyn and M. Gurevich, "Adsorbent storage of natural gas," *Appl. Energy*, vol. 55, no. 2, pp. 71–83, 1996.

[106] K. V. Kumar, K. Preuss, M.-M. Titirici, and F. Rodríguez-Reinoso, "Nanoporous materials for the onboard storage of natural gas," *Chem. Rev.*, vol. 117, no. 3, pp. 1796–1825, 2017. PMID: 28094515.

[107] J. Kim, A. Maiti, L.-C. Lin, J. K. Stolaroff, B. Smit, and R. D. Aines, "New materials for methane capture from dilute and medium-concentration sources," *Nat. Commun.*, vol. 4, p. 1694, 2013.

[108] A. G. Slater and A. I. Cooper, "Function-led design of new porous materials," *Science*, vol. 348, no. 6238, 2015.

[109] S. S. Iyer, I. Bajaj, P. Balasubramanian, and M. M. F. Hasan, "Integrated carbon capture and conversion to produce syngas: Novel process design, intensification, and optimization," *Ind. Eng. Chem. Res.*, vol. 56, no. 30, pp. 8622–8648, 2017.

[110] A. Arora, I. Bajaj, S. S. Iyer, and M. F. Hasan, "Optimal synthesis of periodic sorption enhanced reaction processes with application to hydrogen production," *Comput. Chem. Eng.*, vol. 115, pp. 89 – 111, 2018.

[111] S. Sircar and J. Hufton, "Why does the linear driving force model for adsorption kinetics work?," *Adsorption*, vol. 6, no. 2, pp. 137–147, 2000.

[112] P. V. Danckwerts, "Continuous flow systems," *Chem. Eng. Sci.*, vol. 2, no. 1, pp. 1–13, 1953.

[113] T. J. H. Vlugt, E. García-Pérez, D. Dubbeldam, S. Ban, and S. Calero, "Computing the heat of adsorption using molecular simulations: The effect of strong coulombic interactions," *J. Chem. Theory Comput.*, vol. 4, no. 7, pp. 1107–1118, 2008.

[114] P. M. Mathias, R. Kumar, J. D. Moyer, J. M. Schork, S. R. Srinivasan, S. R. Auvil, and O. Talu, "Correlation of multicomponent gas adsorption by the dual-site langmuir model. application to nitrogen/oxygen adsorption on 5A-zeolite," *Ind. Eng. Chem. Res.*, vol. 35, no. 7, pp. 2477–2483, 1996.

[115] D. Siderius, V. Shen, R. Johnson III, and R. van Zee, eds., *NIST/ARPA-E Database of Novel and Emerging Adsorbent Materials, NIST Standard Reference Database Number 205*. Gaithersburg MD, 20899: National Institute of Standards and Technology. `http://adsorbents.nist.gov` Accessed Feb 15, 2106.

[116] E. García-Pérez, J. B. Parra, C. O. Ania, A. García-Sánchez, J. M. van Baten, R. Krishna, D. Dubbeldam, and S. Calero, "A computational study of CO_2, N_2, and CH_4 adsorption in zeolites," *Adsorption*, vol. 13, no. 5, pp. 469–476, 2007.

[117] D. A. Gomez-Gualdron, C. M. Simon, W. Lassman, D. Chen, R. L. Martin, M. Haranczyk, O. K. Farha, B. Smit, and R. Q. Snurr, "Impact of the strength and spatial distribution of adsorption sites on methane deliverable capacity in nanoporous materials," *Chem. Eng. Sci.*, vol. 159, pp. 18 – 30, 2017.

[118] R. Babarao, Z. Hu, J. Jiang, S. Chempath, and S. I. Sandler, "Storage and separation of CO_2 and CH_4 in silicalite, C168 schwarzite, and IRMOF-1: A comparative study from Monte Carlo simulation," *Langmuir*, vol. 23, no. 2, pp. 659–666, 2007.

[119] E. L. First, C. E. Gounaris, J. Wei, and C. A. Floudas, "Computational characterization of zeolite porous networks: an automated approach," *Phys. Chem. Chem. Phys.*, vol. 13, pp. 17339–17358, 2011.

[120] A. Drud, "CONOPT: A GRG code for large sparse dynamic nonlinear optimization problems," *Math. Program.*, vol. 31, no. 2, pp. 153–191, 1985.

[121] E. L. First, C. E. Gounaris, J. Wei, and C. A. Floudas, "Zeomics: Zeolites and microporous structures characterization." http://helios.princeton.edu/zeomics/. Last accessed April 28, 2018.

[122] "The relentless rise of carbon dioxide." http://climate.nasa.gov/climate_resources/24/ (accessed Dec 12, 2016).

[123] K. M. K. Yu, I. Curcic, J. Gabriel, and S. C. E. Tsang, "Recent advances in CO_2 capture and utilization," *Chem. Sus. Chem.*, vol. 1, no. 11, pp. 893–899, 2008.

[124] "Climate change: How do we know?." http://climate.nasa.gov/evidence/ Accessed Dec 12, 2016.

[125] IPCC, "IPCC special report on carbon dioxide capture and storage: Prepared by working group III of the intergovernmental panel on climate change," tech. rep., Cambridge, United Kingdom and New York, NY, USA, 2005.

[126] IPCC, "Climate change 2007: The physical science basis. contribution of working group I to the fourth assessment report of the intergovernmental panel on climate change," tech. rep., IPCC, Cambridge, United Kingdom and New York, NY, USA, 2007.

[127] EIA, "International Energy Outlook," tech. rep., U.S. Energy Information Administration, 2016.

[128] IPCC, "Climate change 2013: The physical science basis. contribution of working group I to the fifth assessment report of the intergovernmental panel on climate change," tech. rep., IPCC, Cambridge, United Kingdom and New York, NY, USA, 2013.

[129] R. M. Cuéllar-Franca and A. Azapagic, "Carbon capture, storage and utilisation technologies: A critical analysis and comparison of their life cycle environmental impacts," *J. CO2 Util.*, vol. 9, pp. 82–102, 2015.

[130] S. Chu, "Carbon Capture and Sequestration," *Science*, vol. 325, no. 5948, p. 1599, 2009.

[131] R. S. Haszeldine, "Carbon Capture and Storage: How Green Can Black Be?," *Science*, vol. 325, no. 5948, pp. 1647–1652, 2009.

[132] M. Kanniche, R. Gros-Bonnivard, P. Jaud, J. Valle-Marcos, J.-M. Amann, and C. Bouallou, "Pre-combustion, post-combustion and oxy-combustion in thermal power plant for CO_2 capture," *Appl. Therm. Eng.*, vol. 30, no. 1, pp. 53–62, 2010.

[133] DOE, "Report of the interagency task force on carbon capture and storage," tech. rep., U.S. Department of Energy, Washington, D.C., 2010.

[134] "Cost and performance baseline for fossil energy plants. volume 1: Bituminous coal and natural gas to electricity," tech. rep., U.S. Department of Energy and National Energy Technology Laboratory, 2010.

[135] A. S. Bhown and B. C. Freeman, "Analysis and status of post-combustion carbon dioxide capture technologies," *Environ. Sci. Technol.*, vol. 45, no. 20, pp. 8624–8632, 2011.

[136] Z. Yuan, M. R. Eden, and R. Gani, "Toward the development and deployment of large-scale carbon dioxide capture and conversion processes," *Ind. Eng. Chem. Res.*, vol. 55, no. 12, pp. 3383–3419, 2016.

[137] M. K. Nikoo and N. Amin, "Thermodynamic analysis of carbon dioxide reforming of methane in view of solid carbon formation," *Fuel Process. Technol.*, vol. 92, no. 3, pp. 678–691, 2011.

[138] H. Y. Wang and C. T. Au, "Carbon dioxide reforming of methane to syngas over SiO_2-supported rhodium catalysts," *Appl. Catal., A*, vol. 155, no. 2, pp. 239–252, 1997.

[139] A. L. Larentis, N. S. de Resende, V. M. M. Salim, and J. C. Pinto, "Modeling and optimization of the combined carbon dioxide reforming and partial oxidation of natural gas," *Appl. Catal., A*, vol. 215, no. 1-2, pp. 211–224, 2001.

[140] J. G. Olivier, G. Janssens-Maenhout, M. Muntean, and J. A. Peters, "Trends in global co_2 emissions: 2015 report," tech. rep., PBL Netherlands Environmental Assessment Agency, The Hague, 2015.

[141] D. Pakhare and J. Spivey, "A review of dry (CO_2) reforming of methane over noble metal catalysts," *Chem. Soc. Rev.*, vol. 43, no. 22, pp. 7813–7837, 2014.

[142] A. M. Gadalla and B. Bower, "The role of catalyst support on the activity of nickel for reforming methane with CO_2," *Chem. Eng. Sci.*, vol. 43, no. 11, pp. 3049–3062, 1988.

[143] N. Park, M.-J. Park, S.-C. Baek, K.-S. Ha, Y.-J. Lee, G. Kwak, H.-G. Park, and K.-W. Jun, "Modeling and optimization of the mixed reforming of methane: Maximizing CO_2 utilization for non-equilibrated reaction," *Fuel*, vol. 115, pp. 357–365, 2014.

[144] K. Mondal, S. Sasmal, S. Badgandi, D. R. Chowdhury, and V. Nair, "Dry reforming of methane to syngas: a potential alternative process for value added chemicals - A techno-economic perspective," *Environ. Sci. Pollut. Res.*, vol. 23, no. 22, pp. 22267–22273, 2016.

[145] A. Taheri Najafabadi, "CO_2 chemical conversion to useful products: An engineering insight to the latest advances toward sustainability," *Int. J. Energy Res.*, vol. 37, no. 6, pp. 485–499, 2013.

[146] M. M. F. Hasan, R. C. Baliban, J. A. Elia, and C. A. Floudas, "Modeling, simulation, and optimization of postcombustion CO_2 capture for variable feed concentration and flow rate. 2. pressure swing adsorption and vacuum swing adsorption processes," *Ind. Eng. Chem. Res.*, vol. 51, no. 48, pp. 15665–15682, 2012.

[147] T. P. Tiemersma, A. S. Chaudhari, F. Gallucci, J. A. M. Kuipers, and M. van Sint Annaland, "Integrated autothermal oxidative coupling and steam reforming of methane. Part 2: Development of a packed bed membrane reactor with a dual function catalyst," *Chem. Eng. Sci.*, vol. 82, pp. 232–245, 2012.

[148] M. A. Murmura, M. Diana, R. Spera, and M. C. Annesini, "Modeling of autothermal methane steam reforming: Comparison of reactor configurations," *Chem. Eng. Process. Process Intensif.*, vol. 109, pp. 125–135, 2016.

[149] E. Favre, "Carbon dioxide recovery from post-combustion processes: Can gas permeation membranes compete with absorption?," *J. Membr. Sci.*, vol. 294, no. 1, pp. 50–59, 2007.

[150] T. C. Merkel, H. Lin, X. Wei, and R. Baker, "Power plant post-combustion carbon dioxide capture: An opportunity for membranes," *J. Membr. Sci.*, vol. 359, no. 1-2, pp. 126–139, 2010.

[151] J. H. Park, J. N. Kim, S. H. Cho, J. D. Kim, and R. T. Yang, "Adsorber dynamics and optimal design of layered beds for multicomponent gas adsorption," *Chem. Eng. Sci.*, vol. 53, no. 23, pp. 3951–3963, 1998.

[152] P. S. Lawrence, M. Grünewald, W. Dietrich, and D. W. Agar, "Optimal distribution of catalyst and adsorbent in an adsorptive reactor at the reactor level," *Ind. Eng. Chem. Res.*, vol. 45, no. 14, pp. 4911–4917, 2006.

[153] G.-h. Xiu, J. L. Soares, P. Li, and A. E. Rodrigues, "Simulation of five-step one-bed sorption-enhanced reaction process," *AIChE J.*, vol. 48, no. 12, pp. 2817–2832, 2002.

[154] D. Qin and J. Lapszewicz, "Study of mixed steam and CO_2 reforming of CH_4 to syngas on MgO-supported metals," *Catal. Today*, vol. 21, no. 2, pp. 551–560, 1994.

[155] "NIST webbook." `http://webbook.nist.gov/chemistry/` Accessed Dec 12, 2016.

[156] Y. Benguerba, L. Dehimi, M. Virginie, C. Dumas, and B. Ernst, "Modelling of methane dry reforming over Ni/Al_2O_3 catalyst in a fixed-bed catalytic reactor," *React. Kinet. Mech. Cat.*, vol. 114, no. 1, pp. 109–119, 2015.

[157] J. T. Richardson and S. A. Paripatyadar, "Carbon dioxide reforming of methane with supported rhodium," *Appl. Catal.*, vol. 61, no. 1, pp. 293–309, 1990.

[158] S. Ergun and A. A. Orning, "Fluid flow through randomly packed columns and fluidized beds," *Ind. Eng. Chem.*, vol. 41, no. 6, pp. 1179–1184, 1949.

[159] L. D. Harrison, K. M. Brunner, and W. C. Hecker, "A combined packed-bed friction factor equation: Extension to higher reynolds number with wall effects," *AIChE J.*, vol. 59, no. 3, pp. 703–706, 2013.

[160] EIA, "How much carbon dioxide is produced per kilowatthour when generating electricity with fossil fuels?." https://www.eia.gov/tools/faqs/faq.cfm?id=74&t=11 Accessed Dec 12, 2016.

[161] EIA, "How much carbon dioxide is produced when different fuels are burned?." https://www.eia.gov/tools/faqs/faq.cfm?id=73&t=11 Accessed Dec 12, 2016.

[162] W. D. Seider, J. D. Seider, and D. R. Lewin, *Product and Process Design Principles: Synthesis, Analysis and Evaluation*. New York: Wiley, 2004.

[163] G. Towler and R. Sinnott, "Chapter 3 - Utilities and Energy Efficient Design," in *Chemical Engineering Design (Second Edition)* (G. Towler and R. Sinnott, eds.), pp. 103–160, Boston: Butterworth-Heinemann, second ed., 2013.

[164] EIA, "Henry Hub Natural Gas Spot Price." https://www.eia.gov/dnav/ng/hist/rngwhhdm.htm Accessed Dec 12, 2016.

[165] M. M. F. Hasan, R. C. Baliban, J. A. Elia, and C. A. Floudas, "Modeling, simulation, and optimization of postcombustion CO_2 capture for variable feed concentration and flow rate. 1. chemical absorption and membrane processes," *Ind. Eng. Chem. Res.*, vol. 51, no. 48, pp. 15642–15664, 2012.

[166] S. Cavenati, C. A. Grande, and A. E. Rodrigues, "Adsorption equilibrium of methane, carbon dioxide, and nitrogen on zeolite 13X at high pressures," *Journal of Chemical & Engineering Data*, vol. 49, no. 4, pp. 1095–1101, 2004.

[167] D. Woolf, J. Lehmann, and D. R. Lee, "Optimal bioenergy power generation for climate change mitigation with or without carbon sequestration," *Nat. Commun.*, vol. 7, p. 13160, oct 2016.

[168] M. T. Ho, G. W. Allinson, and D. E. Wiley, "Reducing the cost of CO_2 capture from flue gases using pressure swing adsorption," *Ind. Eng. Chem. Res.*, vol. 47, no. 14, pp. 4883–4890, 2008.

[169] L. T. Biegler, L. Jiang, and V. G. Fox, "Recent advances in simulation and optimal design of pressure swing adsorption systems," *Sep. Purif. Rev.*, vol. 33, no. 1, pp. 1–39, 2005.

[170] L. Jiang, V. G. Fox, and L. T. Biegler, "Simulation and optimal design of multiple-bed pressure swing adsorption systems," *AIChE J.*, vol. 50, no. 11, pp. 2904–2917, 2004.

[171] D. Nikolic, A. Giovanoglou, M. C. Georgiadis, and E. S. Kikkinides, "Generic modeling framework for gas separations using multibed pressure swing adsorption processes," *Ind. Eng. Chem. Res.*, vol. 47, no. 9, pp. 3156–3169, 2008.

[172] B. V. Ayodele and C. K. Cheng, "Modelling and optimization of syngas production from methane dry reforming over ceria-supported cobalt catalyst using artificial neural networks and Box-Behnken design," *J. Ind. Eng. Chem.*, vol. 32, pp. 246–258, 2015.

[173] M.-S. Fan, A. Z. Abdullah, and S. Bhatia, "Hydrogen production from carbon dioxide reforming of methane over Ni-Co/MgO-ZrO_2 catalyst: Process optimization," *Int. J. Hydrogen Energy*, vol. 36, no. 8, pp. 4875–4886, 2011.

[174] J. A. Caballero and I. E. Grossmann, "An algorithm for the use of surrogate models in modular flowsheet optimization," *AIChE J.*, vol. 54, no. 10, pp. 2633–2650, 2008.

[175] F. Boukouvala, M. M. F. Hasan, and C. A. Floudas, "Global optimization of general constrained grey-box models: new method and its application to constrained PDEs for pressure swing adsorption," *J. Glob. Optim.*, vol. 67, no. 1, pp. 3–42, 2017.

[176] A. Agarwal and L. T. Biegler, "A trust-region framework for constrained optimization using reduced order modeling," *Optim. Eng.*, vol. 14, no. 1, pp. 3–35, 2013.

[177] M. B. Arouxét, N. E. Echebest, and E. A. Pilotta, "Inexact restoration method for nonlinear optimization without derivatives," *J. Comput. Appl. Math.*, vol. 290, pp. 26–43, 2015.

[178] F. Augustin and Y. Marzouk, "NOWPAC: A provably convergent derivative-free nonlinear optimizer with path-augmented constraints," *arXiv preprint arXiv:1403.1931*, 2014.

[179] C. Audet, A. R. Conn, S. Le Digabel, and M. Peyrega, "A progressive barrier derivative free trust-region algorithm for constrained optimization," 2016.

[180] M. A. Diniz-Ehrhardt, J. M. Martinez, and L. G. Pedroso, "Derivative-free methods for nonlinear programming with general lower-level constraints," *Comput. Appl. Math.*, vol. 30, pp. 19–52, 2011.

[181] J. P. Eason and L. T. Biegler, "A trust region filter method for glass box/black box optimization," *AIChE J.*, vol. 62, no. 9, pp. 3124–3136, 2016.

[182] R. Fletcher, N. I. M. Gould, S. Leyffer, P. L. Toint, and A. Wächter, "Global convergence of a trust-region sqp-filter algorithm for general nonlinear programming," *SIAM J. Optim.*, vol. 13, no. 3, pp. 635–659, 2002.

[183] S. M. Wild, R. G. Regis, and C. A. Shoemaker, "ORBIT: Optimization by radial basis function interpolation in trust-regions," *SIAM J. Sci. Comput.*, vol. 30, no. 6, pp. 3197–3219, 2008.

[184] V. R. Rao, S. Farooq, and W. B. Krantz, "Design of a two-step pulsed pressure-swing adsorption-based oxygen concentrator," *AIChE J.*, vol. 56, no. 2, pp. 354–370, 2010.

[185] D. M. Ruthven, *Principles of Adsorption and Adsorption Processes*. New York: Wiley, 1984.

[186] H. V. Mott and Z. A. Green, "On Danckwerts' boundary conditions for the plug-flow with dispersion/reaction model," *Chem. Eng. Commun.*, vol. 202, no. 6, pp. 739–745, 2015.

[187] K. S. Fisher, K. Searcy, G. T. Rochelle, S. Ziaii, and C. Schubert, "Advanced amine solvent formulations and process integration for near-term CO_2 capture success," tech. rep., U.S. Department of Energy, 2007.

[188] S. M. Wild and C. Shoemaker, "Global convergence of radial basis function trust-region algorithms for derivative-free optimization," *SIAM Rev.*, vol. 55, no. 2, pp. 349–371, 2013.

APPENDIX A

MODELING DETAILS PERTAINING TO COMBINED NATURAL GAS SEPARATION AND STORAGE*

A.1 Approximation of Column Outlet Profiles Using a Simplified Equilibrium-based Model

To approximate the outlet gas composition profiles during the CSS mode, an equilibrium-based model described below is employed. The column at the start of the CSS mode is saturated with gas of mole fraction $y_i^{e,press}$ which is the equilibrium composition after the end of the pressurization mode. Thus the number of moles of gas species i present in the column at the start of the CSS mode can be calculated as given in eq. A.1–A.3.

$$AL\left(\frac{\varepsilon y_i^{e,press} P^h}{RT^{init}} + (1-\varepsilon)\rho_s q_i^{*\,e,press}\right) = n_i^{e,press} \qquad \forall i \in I \quad \text{(A.1)}$$

$$q_i^{*\,e,press} = \sum_{s\in S} \frac{q_{i,s}^s b_{i,s} c_i^{e,press}}{1+\sum_{i\in I} b_{i,s} c_i^{e,press}} \qquad \forall i \in I \quad \text{(A.2)}$$

$$c_i^{e,press} = y_i^{e,press} P_h/(RT^{init}) \qquad \forall i \in I \quad \text{(A.3)}$$

Similarly, after the column is completely saturated with gas at the feed composition y_i^f, the moles of gas species i present in the column is calculated using A.4–A.6.

$$AL\left(\frac{\varepsilon y_i^f P^h}{RT^{init}} + (1-\varepsilon)\rho_s q_i^{*\,f}\right) = n_i^f \qquad \forall i \in I \quad \text{(A.4)}$$

$$q_i^{*\,f} = \sum_{s\in S} \frac{q_{i,s}^s b_{i,s} c_i^f}{1+\sum_{i\in I} b_{i,s} c_i^f} \qquad \forall i \in I \quad \text{(A.5)}$$

$$c_i^f = y_i^f P_h/(RT^{init}) \qquad \forall i \in I \quad \text{(A.6)}$$

*Reproduced in part with permission from Iyer, S. S., Demirel, S. E. and Hasan, M. M. F., "Combined Natural Gas Separation and Storage Based on in Silico Material Screening and Process Optimization" *Industrial & Engineering Chemistry Research*, 57 (49), 16727-16750. Copyright 2018 American Chemical Society. Available at `https://pubs.acs.org/doi/10.1021/acs.iecr.8b02690`

After the outlet end of the column at $z = L$ is opened for CSS operation, the composition of the gas exiting the column will be the initial equilibrium mole fraction $y_i^{e,press}$ up to a certain time t_b when the adorbent in the column gets saturated with either of the gas species. After time t_b, there is a transition to mole fraction of y_i^f. The transition is sudden in case of an equilibrium-based model, where instantaneous equilibrium is assumed to be achieved between the gas and solid adsorbent This corresponds to the two zones in the column, one in equilibrium with the initial gas phase composition before start of CSS operation $y_i^{e,press}$ and the other in equilibrium with the composition of incoming feed gas with mole fraction y_i^f, being present at any time $0 \leq t \leq t_b$. The time $t_{b,i}$ taken for all the adsorbent to be completely saturated with gas species i at the feed composition is given by eq. A.7. The outlet feed mole fraction will be the initial mole fraction $y_i^{e,press}$, until the species with the smallest saturation time $t_{b,i}$ breaks through the column.

$$n_i^{e,press} + t_{b,i}\,\dot{n}_i^{in\,css} - t_{b,i}\,\dot{n}_i^{out\,css} = n_i^f \tag{A.7}$$

For the case of the simple equilibrium based model, the outlet velocity is assumed to be same as the inlet velocity v_f. Then the molar flow rate of gas species i exiting the column till $t_{b,i}$ are calculated as in eq. A.8 while the molar flow rate of gas species i fed to the column during CSS operation is given by eq. A.9.

$$\dot{n}_i^{out\,css} = \frac{\varepsilon A v_f\, y_i^{e,press} P_h}{RT^{init}} \qquad \forall i \in I \tag{A.8}$$

$$\dot{n}_i^{in\,css} = \frac{\varepsilon A v_f\, y_i^f P_h}{RT^{init}} \qquad \forall i \in I \tag{A.9}$$

Using equations A.1–A.9, the saturation time $t_{b,i}$ for species i can be expressed as in eq. A.10

$$t_{b,i} = \frac{L}{v_f}\left(1 + \frac{(1-\varepsilon)\rho_s RT^{init}}{\varepsilon P_h}\left(\frac{q_i^{*\,f} - q_i^{*\,e,press}}{y_i^f - y_i^{e,press}}\right)\right) \tag{A.10}$$

The smallest of the times $t_{b,i}$, will be the time until which the outlet gas mole fraction is same as the initial gas mole fraction $y_i^{e,press}$. After this time, the outlet mole fraction will be the mole fraction of the feed gas y_i^f under the instantaneous equilibrium assumption. The intermediate change in outlet mole fraction from $y_i^{e,press}$ to y_i^f between the time the adsorbent first get saturated with respect to one of the gas species and when the adsorbent is saturated with all the species is

neglected in case of the simplified model. For the case shown in Fig. 3.5, the smallest saturation time t_b is obtained for CH_4 with t_{b,CH_4} = 34.58 s. As seen in Fig. 3.5, there is a deviation in the profiles predicted using the simplified equilibrium-based model and the rigorous dynamic model which can lead to appreciable difference in the calculation of the loss of CH_4 through the column outlet.

A.2 Nonlinear Programming (NLP) Model Formulation for Combined Separation and Storage Process

The optimization problem to be solved is the maximization of CH_4 storage at the end of the CSS process for a given zeolite and it is formulated as follows:

Type:	*Index:*	*Set:*
Gas species	i	$i \in I = \{1, 2, .., N_I\}$
Adsorption sites	s	$s \in S = \{1, 2, .., N_S\}$
Spatial finite volumes	j	$j \in J = \{1, 2, .., N_J\}$
Temporal steps	k	$k \in K = \{1, 2, .., N_k\}$

where N_I is the total number of gas species, N_S is the total number of adsorption sites in the isotherm model, N_J and N_k are the total number of finite volumes and time steps employed for discretization, respectively.

State Variables: $\tilde{\boldsymbol{\alpha}}$

$x_{i,j,k}$ Dimensionless adsorbate loading of component i in finite volume j at time step k

$y_{i,j,k}$ Gas phase mole fraction of component i in finite volume j at time step k

$\overline{P}_{j,k}$ Dimensionless pressure inside the column at finite volume j at time step k

$\overline{T}_{j,k}$ Dimensionless temperature inside the column at finite volume j at time step k

$\overline{T}_{w\,j,k}$ Dimensionless column wall temperature at finite volume j at time step k

Decision Variables: $\mathbf{X}$

P_h Pressure set at outlet of the column during the CSS mode of the process

t_f Duration of operation of the CSS mode of the process

v_f Inlet feed velocity during the CSS mode of the process

A.2.1 Scaling Factors

The different scaling factors used for non-dimensionalizing the state variables are described below. Since the pressure and velocity are decision variables and vary over a large range, their scaling factors are set equal to their respective values (eq. A.11– A.12). In our experience, this aids in convergence because the resulting scaled terms involving pressure and velocity are close to 1. The value of scaling factors chosen for temperature (T_0) and adsorbate loading (q_0^s) are set to 298.15 K and 15 mol/kg respectively. The overbar on the state variables denotes that they are in their dimensionless form.

$$P_0 = P_h \tag{A.11}$$

$$v_0 = v_f \tag{A.12}$$

A.2.2 Discretization

The dimensionless length of each finite volume j along the column axial dimension (z) is given by eq. A.13 and the dimensionless duration of each time step k is given by eq. A.14.

$$\Delta Z = 1/N_J \tag{A.13}$$

$$\Delta\tau = t_f v_0/(L(N_K - 1)) \tag{A.14}$$

The upwind differencing scheme (UDS) employed for the discretization of the spatial derivative terms and the implicit backward Euler scheme employed for the discretization of the temporal terms are given below in eq. A.15–A.18 and eq. A.19–A.23

$$\overline{y}_{i,j+0.5,k} = \overline{y}_{i,j,k} \qquad \forall i \in I \setminus \{N_I\}, \forall j \in J \setminus \{N_J\}, \forall k \in K \tag{A.15}$$

$$\overline{P}_{j+0.5,k} = \overline{P}_{j,k} \qquad \forall j \in J \setminus \{N_J\}, \forall k \in K \tag{A.16}$$

$$\overline{T}_{j+0.5,k} = \overline{T}_{j,k} \qquad \forall j \in J \setminus \{N_J\}, \forall k \in K \quad \text{(A.17)}$$

$$\overline{T}_{w\,j+0.5,k} = \overline{T}_{w\,j,k} \qquad \forall j \in J \setminus \{N_J\}, \forall k \in K \quad \text{(A.18)}$$

$$\frac{\partial x_{i,j,k}}{\partial t}\,\Delta\tau = x_{i,j,k} - x_{i,j,k-1} \qquad \forall i \in I, \forall j \in J, \forall k \in K \setminus \{1\} \quad \text{(A.19)}$$

$$\frac{\partial y_{i,j,k}}{\partial t}\,\Delta\tau = y_{i,j,k} - y_{i,j,k-1} \qquad \forall i \in I, \forall j \in J, \forall k \in K \setminus \{1\} \quad \text{(A.20)}$$

$$\frac{\partial \overline{P}_{j,k}}{\partial t}\,\Delta\tau = \overline{P}_{j,k} - \overline{P}_{j,k-1} \qquad \forall j \in J, \forall k \in K \setminus \{1\} \quad \text{(A.21)}$$

$$\frac{\partial \overline{T}_{j,k}}{\partial t}\,\Delta\tau = \overline{T}_{j,k} - \overline{T}_{j,k-1} \qquad \forall j \in J, \forall k \in K \setminus \{1\} \quad \text{(A.22)}$$

$$\frac{\partial \overline{T}_{w\,j,k}}{\partial t}\,\Delta\tau = \overline{T}_{w\,j,k} - \overline{T}_{w\,j,k-1} \qquad \forall j \in J, \forall k \in K \setminus \{1\} \quad \text{(A.23)}$$

A.2.3 Conservation Equations

The discretized dimensionless form of the equations pertaining to mass and energy conservation and the corresponding auxiliary equations are listed in eq A.2.3–A.38 .

Component Mass Balance:

$$\frac{\partial y_{i,j,k}}{\partial t} = \frac{y_{i,j,k}}{\overline{T}_{j,k}}\left(\frac{\overline{T}_{j,k} - \overline{T}_{j,k-1}}{\Delta\tau}\right) - \frac{y_{i,j,k}}{\overline{P}_{j,k}}\left(\frac{\overline{P}_{j,k} - \overline{P}_{j,k-1}}{\Delta\tau}\right) \quad \text{(A.24)}$$

$$+ \frac{1}{Pe}\frac{\overline{T}_{j,k}}{\overline{P}_{j,k}}\frac{1}{\Delta Z}\left[\left.\frac{\overline{P}}{\overline{T}}\right|_{j+0.5,k}\left(\frac{y_{i,j+1,k} - y_{i,j,k}}{\Delta Z}\right) - \left.\frac{\overline{P}}{\overline{T}}\right|_{j-0.5,k}\left(\frac{y_{i,j,k} - y_{i,j-1,k}}{\Delta Z}\right)\right]$$

$$- \frac{\overline{T}_{j,k}}{\overline{P}_{j,k}}\frac{1}{\Delta Z}\left[\left.\frac{y_i\overline{P}\overline{v}}{\overline{T}}\right|_{j+0.5,k} - \left.\frac{y_i\overline{P}\overline{v}}{\overline{T}}\right|_{j-0.5,k}\right]$$

$$- \psi\frac{\overline{T}_{j,k}}{\overline{P}_{j,k}}\left(\frac{x_{i,j,k} - x_{i,j,k-1}}{\Delta\tau}\right) \qquad \forall i \in I \setminus \{N_I\}, j \in J, \forall k \in K \setminus \{1\}$$

Total Mass Balance:

$$\frac{\partial \overline{P}_{j,k}}{\partial t} = \frac{\overline{P}_{j,k}}{\overline{T}_{j,k}}\frac{\partial \overline{T}_{j,k}}{\partial \tau} - \frac{\overline{T}_{j,k}}{\Delta Z}\left[\left.\frac{\overline{P}\overline{v}}{\overline{T}}\right|_{j+0.5,k} - \left.\frac{\overline{P}\overline{v}}{\overline{T}}\right|_{j-0.5,k}\right]$$

$$- \overline{T}_{j,k}\psi \sum_{i \in I} \left(\frac{x_{i,j,k} - x_{i,j,k-1}}{\Delta\tau} \right) \qquad \forall j \in J, \forall k \in K \setminus \{1\} \quad \text{(A.25)}$$

Energy Balance inside the Column:

$$\frac{\partial \overline{T}_{j,k}}{\partial t} = \frac{\Omega_{1\,j,k}}{\Delta Z} \left[\left(\frac{\overline{T}_{j+1,k} - \overline{T}_{j,k}}{\Delta Z} \right) - \left(\frac{\overline{T}_{j,k} - \overline{T}_{j-1,k}}{\Delta Z} \right) \right] - \frac{\Omega_{2a\,j,k}}{\Delta Z} \left[\overline{v}\overline{P}\big|_{j+0.5,k} - \overline{v}\overline{P}\big|_{j-0.5,k} \right]$$

$$- \Omega_{2b\,j,k} \left(\frac{\overline{P}_{j,k} - \overline{P}_{j,k-1}}{\Delta\tau} \right) + \sum_{i \in I} \sigma_{i,j,k} \left(\frac{x_{i,j,k} - x_{i,j,k-1}}{\Delta\tau} \right) - \Omega_{3\,j,k} \overline{T}_j \sum_{i \in I} \left(\frac{x_{i,j,k} - x_{i,j,k-1}}{\Delta\tau} \right)$$

$$- \Omega_{4\,j,k} \left(\overline{T}_{j,k} - \overline{T}_{w\,j,k} \right) \qquad \forall j \in J, \forall k \in K \setminus \{1\} \quad \text{(A.26)}$$

Energy Balance across the Column Wall:

$$\frac{\partial \overline{T}_{w\,j,k}}{\partial t} = \frac{\pi_1}{\Delta Z} \left[\left(\frac{\overline{T}_{w\,j+1,k} - \overline{T}_{w\,j,k}}{\Delta Z} \right) - \left(\frac{\overline{T}_{w\,j,k} - \overline{T}_{w\,j-1,k}}{\Delta Z} \right) \right]$$

$$+ \pi_2 \left(\overline{T}_{j,k} - \overline{T}_{w\,j,k} \right) - \pi_3 \left(\overline{T}_{w\,j,k} - \overline{T}_{a\,j,k} \right) \qquad \forall j \in J, \forall k \in K \setminus \{1\} \quad \text{(A.27)}$$

$$L_{inv} = 1/L \qquad \text{(A.28)}$$

$$\Psi = RT_0 \rho_s q_0^s (1 - \varepsilon)/(P_0 \varepsilon) \qquad \text{(A.29)}$$

$$\Omega_{j,k} = \rho_s C_{p,s} + \rho_s q_0^s C_{p,a} \sum_{i \in I} x_{i,j,k} \qquad \forall j \in J, \forall k \in K \quad \text{(A.30)}$$

$$\Omega_{3\,j,k} \Omega_{j,k} = \rho_s C_{p,a} q_0^s \qquad \forall j \in J, \forall k \in K \quad \text{(A.31)}$$

$$\Omega_{1\,j,k} = \frac{K_z L_{inv}}{v_0 (1 - \varepsilon) C_{p,a} \rho_s q_0^s} \Omega_{3\,j,k} \qquad \forall j \in J, \forall k \in K \quad \text{(A.32)}$$

$$\Omega_{2\,j,k} = \frac{C_{p,g} P_0}{RT_0 C_{p,a} \rho_s q_0^s} \frac{\varepsilon}{1 - \varepsilon} \Omega_{3\,j,k} \qquad \forall j \in J, \forall k \in K \quad \text{(A.33)}$$

$$\Omega_{4\,j,k} = \frac{2 h_i L \Omega_{3\,j,k}}{r_i v_0 (1 - \varepsilon) C_{p,a} \rho_s q_0^s} \Omega_{3\,j,k} \qquad \forall j \in J, \forall k \in K \quad \text{(A.34)}$$

$$\pi_1 = \frac{K_w L_{inv}}{\rho_w C_{p,w} v_0} \tag{A.35}$$

$$\pi_2 = \frac{2 r_i h_i L}{(r_o^2 - r_i^2)\rho_w C_{p,w} v_0} \tag{A.36}$$

$$\pi_3 = \frac{2 r_o h_o L}{(r_o^2 - r_i^2)\rho_w C_{p,w} v_0} \tag{A.37}$$

$$\sigma_{i,j,k} = \frac{(-\Delta H_{i,j,k})\Omega_{3\,j,k}}{T_0 C_{p,a}} \qquad \forall i \in I, \forall j \in J, \forall k \in K \tag{A.38}$$

Other relations used to calculate some of the parameters appearing in the conservation equations are discussed below. The molar density of the gas is given by eq. A.39 considering ideal gas behavior.

$$\rho_g = P_h / R T_f \tag{A.39}$$

The Peclet number for mass transfer (Pe) is given by eq. A.40 where L is the length of the column and D_L is the axial dispersion co-efficient (D_L) given by eq. A.41. D_m is the molecular diffusivity of the gas mixture in m^2/s, r_p is the particle diameter in m and v_f is the feed velocity in m/s.

$$Pe = v_0 L / D_L \tag{A.40}$$

$$D_L = 0.7 D_m + v_f r_p \tag{A.41}$$

Similarly, the Peclet number for heat transfer Pe_h for heat transfer is given by eq. A.42 where ε is the void fraction of the column, $C_{p\,g}$ is the molar specific heat capacity of the gas in J/mol/K, K_z is the effective axial gas thermal conductivity.

$$Pe_h = \varepsilon v_0 L C_{p\,g} \rho_g / K_z \tag{A.42}$$

The concentration of each species in the gas phase is given by eq. A.43 and A.44. The mole fraction of the N_I component is calculated from the mole fractions of other components because the sum of mole fractions add up to 1.

$$c_{i,j,k} = \frac{y_{i,j,k} P_0 \overline{P}_{j,k}}{R T_0 \overline{T}_{j,k}} \qquad \forall i \in I \setminus \{N_I\}, \forall j \in J, \forall k \in K \tag{A.43}$$

$$c_{i,j,k} = \frac{(1 - \sum_{i=1}^{N_I - 1} y_{i,j,k}) P_0 \overline{P}_{j,k}}{R T_0 \overline{T}_{j,k}} \qquad i = N_I, \forall j \in J, \forall k \in K \quad \text{(A.44)}$$

The equations which describe the equilibrium adsorption of gas onto zeolites are given by eq. A.45 and A.46. The extended dual site Langmuir model is used to approximate gas adsorption from a multi-component mixture from the respective pure component dual site Langmuir parameters $(b^0, \Delta U, q^s)$.

$$q^{*'}_{i,j,k} = \sum_{s \in S} \frac{q^s_{i,s} b^0_{i,s} e^{\frac{-\Delta U_{i,s}}{R T_0 \overline{T}_{j,k}}}}{1 + \sum_{i \in I} b^0_{i,s} e^{\frac{-\Delta U_{i,s}}{R T_0 \overline{T}_{j,k}}} c_{i,j,k}} \qquad \forall i \in I, \forall j \in J, \forall k \in K \quad \text{(A.45)}$$

$$x^*_{i,j,k} = q^{*'}_{i,j,k}\, c_{i,j,k} / q^s_0 \qquad \forall i \in I, \forall j \in J, \forall k \in K \quad \text{(A.46)}$$

The kinetics of mass transfer into the adsorbent is described by a lumped linear driving force (LDF) model (eq. A.47) where $\alpha_{i,j,k}$ is the dimensionless mass transfer coefficient (eq. A.48), ε_p is the porosity of the material, D_p is the effective macropore diffusivity (eq. A.49), D_m is the molecular diffusivity, τ' is the tortuosity of the material. Macropore diffusion is considered to be the dominant mass transfer limitation. Though D_m can vary with the gas species and the temperature, we consider a constant value for D_m.

$$\frac{\partial x_{i,j,k}}{\partial \tau} = \alpha_{i,j,k} \left(x^*_{i,j,k} - x_{i,j,k} \right) \qquad \forall i \in I, \forall j \in J, \forall k \in K \setminus \{1\} \quad \text{(A.47)}$$

$$\alpha_{i,j,k}\, q^{*'}_{i,j,k} = \frac{15 \varepsilon_p D_p L}{v_0 r_p^2 \rho_s} \qquad \forall i \in I, \forall j \in J, \forall k \in K \quad \text{(A.48)}$$

$$D_p = D_m / \tau' \qquad \text{(A.49)}$$

The Darcy's law which describes the pressure drop due to flow through a packed column is then used to relate the velocity and pressure values.

$$\overline{v}_{j+0.5,k} = \frac{-4}{150\ \Delta Z} \frac{r_p^2 P_0}{\mu v_0 L} \left(\frac{\varepsilon}{1 - \varepsilon} \right)^2 \left(\overline{P}_{j+1,k} - \overline{P}_{j,k} \right) \qquad \forall j \in J \setminus \{N_J\}, \forall k \in K \quad \text{(A.50)}$$

A.2.4 Boundary Conditions

The dimensionless forms of the appropriate boundary conditions for the open-open column operation used in the CSS mode are given in eq. A.51–A.59. Here, the subscript 0.5 and $N_j + 0.5$ refers to the value of the variable at the inlet and outlet boundary of the column respectively.

At $Z = 0$ end of the column:

$$\overline{v}_{0.5} = v_f / v_0 \tag{A.51}$$

$$\overline{P}_{0.5,k} = \overline{P}_{1,k} + \frac{\overline{v}_{0.5} \frac{\Delta Z}{2}}{\frac{4}{150} \frac{r_p^2 P_0}{\mu v_0 L} \left(\frac{\varepsilon}{1-\varepsilon}\right)^2} \qquad \forall k \in K \tag{A.52}$$

$$\overline{y}_{i,0.5,k} = \overline{y}_{i,1,k} + \frac{y_{f,i} \overline{v}_{0.5} Pe \frac{\Delta Z}{2}}{1 + \overline{v}_{0.5} Pe \frac{\Delta Z}{2}} \qquad \forall i \in I \setminus \{N_I\}, \forall k \in K \tag{A.53}$$

$$\overline{T}_{0.5,k} = \overline{T}_{1,k} + \frac{\overline{T}_f \overline{v}_{0.5} Pe_h \frac{\Delta Z}{2}}{1 + \overline{v}_{0.5} Pe \frac{\Delta Z}{2}} \qquad \forall k \in K \tag{A.54}$$

$$T_{w\ 0,k} = T_a / T_0 \qquad \forall k \in K \tag{A.55}$$

At $Z = 1$ end of the column:

$$P_{N_J+0.5,k} = P_h / P_0 \qquad \forall k \in K \tag{A.56}$$

$$y_{i,N_J+0.5,k} = T_{i,N_j,k} \qquad \forall i \in I \setminus \{N_I\}, \forall k \in K \tag{A.57}$$

$$T_{N_J+0.5,k} = T_{N_j,k} \qquad \forall k \in K \tag{A.58}$$

$$T_{w\ N_J+1,k} = T_a / T_0 \qquad \forall k \in K \tag{A.59}$$

For the value of state variables at the dummy/imaginary finite volumes at inlet ($j = 0$) and outlet ($j = N_J + 1$) of the column, the approximations listed below in eq. A.60–A.65 are used.

$$\overline{P}_{0,k} = 2\overline{P}_{0.5,k} - \overline{P}_{1,k} \tag{A.60}$$

$$\overline{P}_{N_J+1,k} = 2\overline{P}_{N_J+0.5,k} - \overline{P}_{N_J,k} \qquad \forall k \in K \tag{A.61}$$

$$\overline{T}_{0,k} = 2\overline{T}_{0.5,k} - \overline{T}_{1,k} \qquad \forall k \in K \quad \text{(A.62)}$$

$$\overline{T}_{N_J+1,k} = 2\overline{T}_{N_J+0.5,k} - \overline{T}_{N_J,k} \qquad \forall k \in K \quad \text{(A.63)}$$

$$\overline{y}_{i,0,k} = 2\overline{y}_{i,0.5,k} - \overline{y}_{i,1,k} \qquad \forall i \in I \setminus \{N_I\}, \forall k \in K \quad \text{(A.64)}$$

$$\overline{y}_{i,N_J+1,k} = 2\overline{y}_{i,N_J+0.5,k} - \overline{y}_{i,N_J,k} \qquad \forall i \in I \setminus \{N_I\}, \forall k \in K \quad \text{(A.65)}$$

A.2.5 Initial Conditions

To determine the initial conditions at the start of the combined separation and storage mode, it is necessary to calculate the equilibrium conditions achieved after the pressurization mode.

Equilibrium Conditions after Pressurization: Let P^{init} and T^{init} represent the initial pressure and temperature of the column before processing. Since the column is assumed to come from the vehicular application, the initial pressure P^{init} is set as P_l = 5.8 bar [36, 45, 48, 52]. T^{init} is assumed to be same as the feed temperature T_f which is set to 298 K. This is the pressure of the column depleted of CH_4 received by the facility from the end-user. Let the initial composition of the gases in the depleted column be denoted by y_i^{init}. The column is assumed to be saturated at P_l, with the initial mole fractions of the CH_4 at 95% *i.e.* $y_{CH_4}^{init} = 0.95$ and N_2 at 5% $y_{N_2}^{init} = 0.05$.

The pressurization step is operated for a certain time duration to reach the desired filling pressure P_h. The equilibrium compositions some time after pressurization depend only on the total amount of moles of each component in the column and the ambient temperature. During pressurization, there can be significant variations in the velocity and pressure in the column. This would require solving a dynamic model of the column to determine the amount of gas fed to the column at any time instant. However, the total moles of gas fed to the column over time can be calculated by employing a simplifying assumption that the column is pressurized within a very short time to a dummy pressure P_d (bar). The gas fed during this short time is assumed to just go into the gas phase raising the pressure of the column till P_d and no gas adsorbing onto the adsorbent. The adsorption of this gas into the adsorbent and subsequent equilibration occurs afterwards to the desired filling pressure P_h. No changes in temperature is considered, as the column is assumed to

equilibrate to the ambient temperature. The use of the dummy pressure P_d serves as a place holder to evaluate the total moles fed to the column during the pressurization mode. The initial number of moles of the gas present in the column in the gas phase before the start of the pressurization is given by eq. A.66.

$$n_g^{init} = \frac{\varepsilon A L \, P^{init}}{R T^{init}} \tag{A.66}$$

where A is the cross-sectional area of the column given by eq. A.67.

$$A = \pi r_i^2 \tag{A.67}$$

The total number of moles of the gas in the gas phase at the dummy pressure is given by eq. A.68.

$$n_g^{press} = \frac{\varepsilon A L \, P_d \times 10^5}{R T^{init}} \tag{A.68}$$

The amount of gas fed to the column during the pressurization step is then equal to the difference between n_g^{init} and n_g^{press}. The relative number of moles of gas species i added during pressurization will be same as the feed composition of the gas species i in the mixture.

$$n_i^{in,press} = y_i^f (n_g^{press} - n_g^{init}) \qquad \forall i \in I \tag{A.69}$$

As the outlet of the column is kept closed during pressurization, the moles of component i exiting the column is zero.

$$n_i^{out,press} = 0 \qquad \forall i \in I \tag{A.70}$$

Now, the number of moles of each component i present in the column initially is denoted by n_i^{init} and is given by eq. A.71.

$$n_i^{init} = AL\left(\frac{\varepsilon y_i^{init} P^{init}}{R T^{init}} + (1-\varepsilon)\rho_s q_i^{*\,init}\right) \qquad \forall i \in I \tag{A.71}$$

where, A is the cross sectional area of the column of inner radius r_{in}, L is the length of the column and $q_i^{*\,init}$ is the initial adsorbed phase loading of species i on the adsorbent in column in equilibrium with the gas phase composition y_i^{init} at pressure P^{init} and temperature T^{init}. $q_i^{*\,init}$ is

obtained using the extended dual-site Langmuir isotherm model given by eq. A.72 and A.73.

$$q_i^{*\,init} = \sum_{s \in S} \frac{q_{i,s}^s b_{i,s} c_i^{init}}{1 + \sum_{i \in I} b_{i,s} c_i^{init}} \qquad \forall i \in I \quad \text{(A.72)}$$

$$b_{i,s} = b_{i,s}^0 e^{-\Delta U_{i,s}/RT^{init}} \qquad \forall i \in I, \forall s \in S \quad \text{(A.73)}$$

The concentration of the gas species in eq. A.72 is obtained by applying the ideal gas assumption and is given in eq. A.74 for the initial conditions at the start of the pressurization.

$$c_i^{init} = y_i^{init} P^{init} / (RT^{init}) \qquad \forall i \in I \quad \text{(A.74)}$$

The equilibrium composition of each species in the gas phase some time after pressurization can now be calculated by solving eq. A.75–A.77. P_h is the pressure in the column after equilibration.

$$AL\left(\frac{\varepsilon y_i^{e,press} P^h}{RT^{init}} + (1-\varepsilon)\rho_s q_i^{*\,e,press}\right) = n_i^{init} + n_i^{in,press} \qquad \forall i \in I \quad \text{(A.75)}$$

$$q_i^{*\,e,press} = \sum_{s \in S} \frac{q_{i,s}^s b_{i,s} c_i^{e,press}}{1 + \sum_{i \in I} b_{i,s} c_i^{e,press}} \qquad \forall i \in I \quad \text{(A.76)}$$

$$c_i^{e,press} = y_i^{e,press} P_h / (RT^{init}) \qquad \forall i \in I \quad \text{(A.77)}$$

Thus, the calculated equilibrium conditions of the column some time after pressurization *i.e.* $q_i^{*\,e,press}$, $y_i^{e,press}$, P_h will be the initial conditions for the combined separation and storage mode. The initial conditions of the column at every finite volume j are given in eq. A.78–A.82.

$$P_{j,k} = P_h / P_0 \qquad \forall j \in J, k = 1 \quad \text{(A.78)}$$

$$T_{j,k} = T_f / T_0 \qquad \forall j \in J, k = 1 \quad \text{(A.79)}$$

$$T_{w\,j,k} = T_a / T_0 \qquad \forall j \in J, k = 1 \quad \text{(A.80)}$$

$$x_{i,j,k} = x_i^{*\,e,press} \qquad \forall i \in I, \forall j \in J, k = 1 \quad \text{(A.81)}$$

$$y_{i,j,k} = y_i^{e,press} \qquad \forall i \in I \setminus \{N_I\}, \forall j \in J, k = 1 \quad \text{(A.82)}$$

where T_f is the feed temperature, T_a is the ambient temperature, $y_i^{e,press}$ is the gas phase compo-

sition of species i and $x_i^{*e,press}$ is the dimensionless equilibrium saturation capacity at the initial conditions.

A.2.6 Process Performance Metrics

CH_4 Storage and Purity: To calculate the purity of CH_4 stored in the column, it is necessary to calculate the moles of each gas component stored in the column at the end of the CSS mode n_{i,N_K} (eq. A.83). This includes both the gas present in the gas phase and adsorbed phase.

$$n_{i,k} = \sum_{j \in J} \left(\varepsilon c_{i,j,k} + \rho_s q_0^s (1-\varepsilon) x_{i,j,k} \right) AL\Delta Z \qquad \forall i \in I, k = N_K \quad \text{(A.83)}$$

The number of moles of gas species i stored Δn_i in the column during the operation of CSS mode is given by eq. A.84.

$$\Delta n_i = \sum_{j \in J} \left(\varepsilon c_{i,j,N_K} + \rho_s q_0^s (1-\varepsilon) x_{i,j,N_K} \right) AL\Delta Z \qquad \forall i \in I \quad \text{(A.84)}$$
$$- \sum_{j \in J} \left(\varepsilon c_{i,j,1} + \rho_s q_0^s (1-\varepsilon) x_{i,j,1} \right) AL\Delta Z$$

The total moles of all the gas components stored in the column at the end of the process is given by eq. A.85.

$$n_k^{tot} = \sum_{j \in J} \left(\varepsilon \frac{P_0}{RT_0} \frac{\overline{P}_{j,k}}{\overline{T}_{j,k}} + \rho_s q_0^s (1-\varepsilon) \sum_{i \in I} x_{i,j,N_k} \right) AL\Delta Z \qquad k = N_K \quad \text{(A.85)}$$

The purity of the gas stored in the column at the final time $pur_{i,k}$ is calculated as a ratio of the moles of CH_4 stored over the total moles of other gases stored and is described by eq. A.86. The inequality constraint limiting the minimum value of purity of stored methane (pur_{lim}) is described by eq. A.87.

$$pur_{i,k}\, n_k^{tot} = n_{i,k} \qquad i = CH_4, k = N_K \quad \text{(A.86)}$$

$$pur_{i,k} \geq pur_{lim} \qquad i = CH_4, k = N_K \quad \text{(A.87)}$$

CH_4 Loss: In order to calculate the loss of CH_4 due to gas exiting the column during the CSS mode of the process, the moles of gas entering and exiting the column are calculated using eq. A.88 and

A.89. Integration over time steps is approximated using a Riemann right hand sum.

$$n_i^{in,\,css} = \varepsilon A \overline{v}_{0.5} \sum_{k \in K} c_{0.5\;i,k} \Delta\tau \qquad \forall k \in K \setminus \{1\}, i = CH_4 \quad \text{(A.88)}$$

$$n_i^{out,\,css} = \varepsilon A \overline{v}_{N_J+0.5} \sum_{k \in K} c_{N_J+0.5\;i,k} \Delta\tau \qquad \forall k \in K \setminus \{1\}, i = CH_4 \quad \text{(A.89)}$$

The concentration at the inlet ($c_{0.5,k}$) and outlet ($c_{N_J+0.5,k}$) of the column at any time step k is given by eq. A.90–A.93.

$$c_{0.5\;i,k} = \frac{P_0}{RT_0} \frac{\overline{P}_{0.5,k}}{\overline{T}_{0.5,k}} \overline{y}_{0.5\;i,k} \qquad \forall i \in I \setminus \{N_I\}, \forall k \in K \quad \text{(A.90)}$$

$$c_{0.5\;N_I,k} = \frac{P_0}{RT_0} \frac{\overline{P}_{0.5,k}}{\overline{T}_{0.5,k}} (1 - \sum_{i=1}^{N_I-1} \overline{y}_{0.5\;i,k}) \qquad \forall k \in K \quad \text{(A.91)}$$

$$c_{N_j+0.5\;i,k} = \frac{P_0}{RT_0} \frac{\overline{P}_{N_j+0.5,k}}{\overline{T}_{N_j+0.5,k}} \overline{y}_{N_j+0.5 i,k} \qquad \forall i \in I \setminus \{N_I\}, \forall k \in K \quad \text{(A.92)}$$

$$c_{N_j+0.5\;N_I,k} = \frac{P_0}{RT_0} \frac{\overline{P}_{N_j+0.5,k}}{\overline{T}_{N_j+0.5,k}} (1 - \sum_{i=1}^{N_I-1} \overline{y}_{N_j+0.5\;i,k}) \qquad \forall k \in K \quad \text{(A.93)}$$

The CH_4 loss l_{CH_4} during the process is given by eq. A.94 and the corresponding constraint imposed on the maximum allowable loss is given by eq. A.95.

$$l_i \; (n_i^{in,\,press} + n_i^{in,\,css}) = n_i^{out} \qquad i = CH_4 \quad \text{(A.94)}$$

$$l_i \leq l_{max} \qquad i = CH_4 \quad \text{(A.95)}$$

A.2.7 Variable Bounds

Appropriate upper and lower bounds on some of the state variables (T,P,T_w and y) to aid the simulations are provided in eq. A.96–A.103 and Table A.1.

$$\overline{T}^L \leq \overline{T}_{j,k} \leq \overline{T}^U \qquad \forall j \in J, \forall k \in K \quad \text{(A.96)}$$

$$\overline{T}^L \leq \overline{T}_{0.5,k} \leq \overline{T}^U \qquad \forall k \in K \quad \text{(A.97)}$$

$$\overline{T}^L \leq \overline{T}_{N_J+0.5,k} \leq \overline{T}^U \qquad \forall k \in K \quad \text{(A.98)}$$

$$\overline{P}^L \leq \overline{P}_{j,k} \leq \overline{P}^U \qquad \forall j \in J, \forall k \in K \quad \text{(A.99)}$$

$$\overline{T}_w^L \leq \overline{T}_{w\,j,k} \leq \overline{T}_w^U \qquad \forall j \in J, \forall k \in K \quad \text{(A.100)}$$

$$y^L \leq y_{i,j,k} \leq y^U \qquad \forall i \in I \setminus \{N_I\}, \forall j \in J, \forall k \in K \quad \text{(A.101)}$$

$$\overline{T}^L \leq \overline{T}_{j+0.5,k} \qquad \forall j \in J, \forall k \in K \quad \text{(A.102)}$$

$$\overline{P}^L \leq \overline{P}_{j+0.5,k} \qquad \forall j \in J, \forall k \in K \quad \text{(A.103)}$$

The upper and lower bounds imposed on the decision variables of filling pressure, duration and feed velocity for the CSS mode in the optimization formulation are provided below.

Table A.1: Value of parameters denoting bounds on state variables defined in CSS model (Iyer *et al.* [77]).

Parameter	Value
$\overline{T}^L$	0.50
$\overline{T}^U$	1.50
$\overline{P}^L$	1.00
$\overline{P}^U$	1.30
$\overline{T}_w^L$	0.80
$\overline{T}_w^U$	1.20
y^L	0
y^U	1.00
P_d^L	5.8
P_d^U	350

$$t_f^L \leq t_f \leq t_f^U \qquad \text{(A.104)}$$

$$P_h^L \leq P_h \leq P_h^U \qquad \text{(A.105)}$$

$$v_f^L \leq v_f \leq v_f^U \qquad \text{(A.106)}$$

A.3 Pure Silica Zeolite Frameworks Considered in the CSS Process

Table A.2: List of pure silica zeolite frameworks from the IZA-SC database considered in the CSS process (Iyer *et al.* [77])

ABW	ACO	AEI	AEL	AEN	AET	AFG	AFI	AFN	AFO	AFR	AFS	AFT	AFX
AFY	AHT	ANA	APC	APD	AST	ASV	ATN	ATO	ATS	ATT	ATV	AWO	AWW
BEA	BEC	BIK	BOF	BOG	BPH	BRE	CAN	CAS	CDO	CFI	CGF	CGS	CHA
CON	CZP	DAC	DDR	DFT	DOH	DON	EAB	EDI	EMT	EON	EPI	ERI	ESV
ETR	EUO	EZT	FAR	FER	FRA	GIS	GIU	GME	GON	GOO	HEU	IFR	IHW
ISV	ITE	ITH	ITR	ITW	IWR	IWW	JBW	JOZ	JRY	JSN	JSW	KFI	LAU
LEV	LIO	LOS	LOV	LTA	LTJ	LTL	MAR	MAZ	MEI	MEL	MEP	MER	MFI
MFS	MON	MOR	MRE	MSE	MSO	MTF	MTN	MTT	MTW	MWW	NAB	NAT	NES
NON	NPO	NPT	NSI	OBW	OFF	OSI	OSO	OWE	PCR	PHI	PON	PUN	RHO
RRO	RSN	RTE	RTH	RUT	RWR	RWY	SAF	SAO	SAS	SAT	SAV	SBN	SBS
SFE	SFF	SFG	SFH	SFN	SFO	SFS	SGT	SIV	SOD	SOF	SOS	SSF	SSY
STF	STI	STO	STT	STW	SZR	TER	THO	TOL	TON	UEI	UFI	UOS	UOZ
USI	UTL	UWY	VET	VFI	VNI	VSV	WEI	YUG	ZON				

APPENDIX B

MODELING DETAILS PERTAINING TO THE INTEGRATED CARBON CAPTURE AND CONVERSION (ICCC) PROCESS*

B.1 Modeling the Adsorption Section of the ICCC Process

The dynamics of gas adsorption onto adsorbent inside the adsorption column is described by a 1-dimensional nonlinear algebraic partial differential equation (NAPDE) model [81] in time and space domains. This model includes total and component mass balances, energy balances, pressure drop correlations, a driving force model to calculate the adsorption loadings and other empirical relations. The major assumptions used in the model are listed as follows:

1. Ideal gas behavior
2. Plug flow model with axial dispersion
3. No gradients in the radial direction
4. Thermal equilibrium between gas and solid phase achieved instantly
5. Linear driving force (LDF) model to describe mass transfer in the adsorbent
6. Mass transfer into the adsorbent is controlled by molecular diffusion in the macropores.
7. The equilibrium loading of gas on the adsorbent at a temperature is described using a multi-component dual site Langmuir adsorption isotherm.
8. No reaction occurs in the adsorption section.

*Reproduced in part with permission from Iyer, S. S., Bajaj, I., Balasubramanian, P. and Hasan, M. M. F., "Integrated Carbon Capture and Conversion to Produce Syngas: Novel Process Design, Intensification and Optimization" *Industrial & Engineering Chemistry Research*, 56(30), 8622-8648. Copyright 2017 American Chemical Society. Available at `https://pubs.acs.org/doi/abs/10.1021/acs.iecr.7b01688`

Eq. 1 below describes the mass conservation for each species $i \in I_A$ entering and leaving the adsorption section. It accounts for contribution to the accumulation term from convection, axial dispersion and gas adsorption.

$$\frac{\partial c_i}{\partial t} = -\frac{\partial}{\partial z}\left(-cD_L\frac{\partial y_i}{\partial z} + c_i v\right) - \frac{(1-\varepsilon)}{\varepsilon}\frac{\partial q_i}{\partial t} \qquad \forall\, i \in I_A \quad \text{(B.1)}$$

where c_i and y_i are the gas phase bulk concentration in mol/m^3 and mole fraction respectively, q_i is the adsorbed phase loadings on the solid adsorbent in mol/m^3, D_L is the axial dispersion coefficient in m^2/s, v is the interstitial velocity in m/s and z is the spatial co-ordinate in m along the length (L_a) of the column, i.e., $0 \leq z \leq L_a$ and t is the temporal co-ordinate in seconds.

Applying the ideal gas assumption $c_i = \frac{y_i P}{RT}$ and using the chain rule for differentiation, eq. B.1 becomes

$$\frac{\partial y_i}{\partial t} + \frac{y_i}{P}\frac{\partial P}{\partial t} - \frac{y_i}{T}\frac{\partial T}{\partial t} = \frac{T}{P}D_L\frac{\partial}{\partial z}\left(\frac{P}{T}\frac{\partial y}{\partial z}\right) - \frac{T}{P}\frac{\partial}{\partial z}\left(\frac{y_i P v}{T}\right) - \frac{RT}{P}\frac{(1-\varepsilon)}{\varepsilon}\frac{\partial q_i}{\partial t} \qquad \forall\, i \in I_A \quad \text{(B.2)}$$

Here P is the adsorption column pressure in Pa which is considered to be the same for both the adsorption and reactor sections, T is the temperature inside the column in K and R is the universal gas constant in J/mol/K. Summing up the component balance equations for all the components results in the total mass balance equation shown in eq. B.3 (Since $\sum_{i\in I_A} y_i = 1$). The pressure (P) explicitly appears in this formulation.

$$\frac{\partial P}{\partial t} = \frac{P}{T}\frac{\partial T}{\partial t} - T\frac{\partial}{\partial z}\left(\frac{Pv}{T}\right) - RT\frac{(1-\varepsilon)}{\varepsilon}\sum_{i\in I_A}\frac{\partial q_i}{\partial t} \quad \text{(B.3)}$$

Only $|I_A| - 1$ component balance equations are considered along with the total mass balance equations so that the system of equations is independent.

Eq. B.4 describes the conservation of thermal energy of the gas stream entering and exiting the adsorption section. The gas and the adsorbent are assumed to be at the same temperature.

$$(1-\varepsilon)\left(\rho_s C_{p,s}\frac{\partial T}{\partial t} + C_{p,a}\frac{\partial\left(\sum_{i\in I_A} q_i T\right)}{\partial t}\right) + \varepsilon C_{p,g}\frac{\partial\left(\rho_g T\right)}{\partial t} = K_z\frac{\partial^2 T}{\partial z^2} - \frac{2h_{in}}{r_{in}}\left(T - T_w\right) \quad \text{(B.4)}$$

$$+ (1-\varepsilon) \sum_{i \in I_A} (-\Delta H_i) \frac{\partial q_i}{\partial t}$$

where ε is the void fraction of the adsorbent column, ρ_s is the density of the adsorbent in kg/m^3, ρ_g is the density of the gas in mol/m^3, $C_{p,s}$, $C_{p,a}$ and $C_{p,g}$ are the specific heat capacities of the solid adsorbent, the gas in the adsorbed phase and gaseous phase in J/mol/K respectively, K_z is the effective axial thermal conductivity of the gas in W/m/K, ΔH_i is the isoteric heat of adsorption of species i in J/mol, h_{in} is the inside heat transfer co-efficient in W/m^2/K, r_{in} is the inner radius of the column in m and T_w is the temperature of the column wall in K. $C_{p,g}$ is calculated by mole fraction average of the individual specific heat capacities of the species and $C_{p,a}$ is equal to $C_{p,g}$. Substituting $\rho_g = \frac{P}{RT}$ using the ideal gas assumption and expanding the terms, we obtain Eq. B.5

$$\left(\rho_s C_{p,s} + C_{p,a} \sum_{i \in I_A} q_i\right) \frac{\partial T}{\partial t} = -\frac{C_{p,g}\varepsilon}{R\,(1-\varepsilon)} \frac{\partial P}{\partial t} - C_{p,a} T \sum_i \frac{\partial q_i}{\partial t} + \sum_{i \in I_A} (-\Delta H_i) \frac{\partial q_i}{\partial t} + \frac{K_z}{(1-\varepsilon)} \frac{\partial^2 T}{\partial z^2} - \frac{C_{p,g}\varepsilon}{R\,(1-\varepsilon)} \frac{\partial}{\partial z}(vP) - \frac{2h_{in}}{r_{in}\,(1-\varepsilon)} (T - T_w) \tag{B.5}$$

Eq. B.6 describes the heat transfer across the column wall and the ambient.

$$\rho_w C_{p,w} \frac{\partial T_w}{\partial \tau} = K_{\mathrm{w}} \frac{\partial^2 T_w}{\partial z^2} + \frac{2 r_{in} h_{in}}{(r_{out}^2 - r_{in}^2)} (T_w - T_a) - \frac{2 r_{out} h_{out}}{(r_{out}^2 - r_{in}^2)} (T_w - T_a) \tag{B.6}$$

where ρ_w, $C_{p,w}$ and K_{w} are the density in kg/m^3, specific heat capacity in J/kg/K and thermal conductivity of the column wall in W/m/K respectively, h_{out} is the outside heat transfer co-efficient in W/m^2/K, r_{out} is the outer radius of the column in m, T_a is the ambient temperature outside the column in K.

Darcy's Law is used to describe the axial pressure drop across the packed bed.

$$v = \frac{-4}{150\mu} r_p^{\,2} \left(\frac{\varepsilon}{1-\varepsilon}\right)^2 \left(\frac{\partial P}{\partial z}\right) \tag{B.7}$$

where μ is the viscosity of the gas (fluid) phase in Pa s and r_p is the particle radius of the adsorbent in m.

The kinetics of gas adsorption into the adsorbent are described by a linear driving force relation

given in eq. B.8. Mass transfer is assumed to be limited by molecular diffusion in the macropores.

$$\frac{\partial q_i}{\partial t} = k_i \left(q_i^* - q_i\right) \qquad \forall\, i \in I_A \quad \text{(B.8)}$$

$$k_i = \frac{15 \varepsilon_p D_p c_i}{r_p^2 q_i^*} \qquad \forall\, i \in I_A \quad \text{(B.9)}$$

where k_i is a lumped mass transfer rate coefficient [184] in s^{-1}, ε_p is the particle porosity, $D_p (= \frac{D_m}{\tau'})$ is the effective macropore diffusivity in m^2/s, D_m is the molecular diffusivity in m^2/s and τ' is the tortuosity of the adsorbent.

The equilibrium loading (q_i^*) of gas on the adsorbent at given temperature, pressure and composition is given by a multi-component dual-site Langmuir adsorption isotherm, as follows:

$$q_i^* = \frac{q_{b,i}^s b_i c_i}{1 + \sum_{i \in I_A} b_i c_i} + \frac{q_{b,i}^s d_i c_i}{1 + \sum_{i \in I_A} d_i c_i} \qquad \forall\, i \in I_A \quad \text{(B.10)}$$

where $q_{b,i}^s$ and $q_{d,i}^s$ are the saturation loadings of the species i on the adsorbent in mol/m^3, b_i and d_i are parameters in an Arrhenius type relation for the two sites in m^3/mol, which are calculated as follows:

$$b_i = b_i^0 e^{-\Delta U_{b,i}/RT};\ d_i = d_i^0 e^{-\Delta U_{d,i}/RT} \quad \text{(B.11)}$$

where $\Delta U_{b,i}$ and $\Delta U_{d,i}$ relate to sites 1 and 2, respectively, in J/mol.

The axial dispersion coefficient [185] is calculated as follows:

$$D_L = 0.7 D_m + v_0 r_p \quad \text{(B.12)}$$

For the adsorption section, both ends of the column are open resulting in the following Danckwerts boundary conditions. The Danckwerts boundary conditions are used to account for continuity of flux at the inlet for dispersed plug flow system considered [81, 112, 186].

At $z = 0$ end of the adsorption section/column:

$$D_L \left.\frac{\partial y_i}{\partial z}\right|_{z=0} = -v|_{z=0} \left(y_{i,f} - y_i|_{z=0}\right) \quad \text{(B.13a)}$$

$$K_z \left.\frac{\partial T}{\partial z}\right|_{z=0} = -\varepsilon v|_{z=0} \rho_g C_{p,g} \left(T_f - T|_{z=0}\right) \quad \text{(B.13b)}$$

$$v|_{z=0} = v_f \tag{B.13c}$$

$$T_w|_{z=0} = T_a \tag{B.13d}$$

At $z = L_a$ end of the adsorption section/column:

$$\left.\frac{\partial y_i}{\partial z}\right|_{z=L_a} = 0 \tag{B.14a}$$

$$\left.\frac{\partial T}{\partial z}\right|_{z=L_a} = 0 \tag{B.14b}$$

$$P|_{z=L_a} = P_h \tag{B.14c}$$

$$T_w|_{z=L_a} = T_a \tag{B.14d}$$

where P_h is the pressure value set at the outlet end of the adsorption column in Pa, $y_{i,f}$ is the mole fraction of species $i \in I_A$ in the feed, while T_f is the feed inlet temperature in K.

The column is assumed to be initially saturated with pure N_2 prior to the introduction of the feeds. The initial conditions of the column at $t = 0$ is given by:

$$q_{N_2}|_{t=0} = q^*_{N_2}\ , \quad q_{CO_2}|_{t=0} = 0 \text{ and } \quad q_{CH_4}|_{t=0} = 0 \tag{B.15a}$$

$$y_{N_2}|_{t=0} = 1\ , \quad y_{CO_2}|_{t=0} = 0 \text{ and } \quad y_{CH_4}|_{t=0} = 0 \tag{B.15b}$$

$$P|_{t=0} = P_h \tag{B.15c}$$

$$T|_{t=0} = T_a \tag{B.15d}$$

$$T_w|_{t=0} = T_a \tag{B.15e}$$

B.2 Total Production Cost Calculation for ICCC Process

The total cost of syngas produced (TC) in \$/ton syngas is given by:

$$TC = \frac{AIC}{P_{SG}} + OC \tag{B.16}$$

where AIC and OC are the annualized investment cost in \$/year and operating cost in \$/ton syngas produced respectively and P_{SG} is the ton of syngas produced in a year. Total operating time in a year is assumed to be 8000 hours. AIC is related to the total plant cost (TPC) and annual maintenance cost (AMC) as shown below.

$$AIC = \emptyset\, TPC + AMC \tag{B.17}$$

where $\emptyset$ is the capital recovery factor which is set to be 0.154 in this work.67 Annual maintenance cost (AMC) is assumed to be about 5% of TPC. The total plant cost (TPC) can be further broken down into total installed cost (TIC), indirect cost (IDC) and balance of plant cost (BPC).

$$TPC = TIC + IDC + BPC \tag{B.18}$$

The indirect cost (IDC) and balance of plant cost (BPC) are assumed to be 32% and 20% of TIC.

$$TPC = TIC + 0.32\, TIC + 0.2\, TIC = 1.52\, TIC \tag{B.19}$$

The details of the total installed cost (TIC) calculation are provided below

The total installed cost is the sum of all individual equipment costs for compressors, columns and heat exchangers used. Our process includes an adsorption column, compressors and a reformer type of reactor. The total installed cost is given by

$$TIC = TIC_{ads} + TIC_{com} + \ TIC_{RR} \tag{B.20}$$

The cost calculated for a past base year (C_0) is converted to 2016 values (C) using the Chemical Engineering (CE) Plant Cost Index.

$$C = C_0 \frac{I_{2016}}{I_0} \tag{B.21}$$

where I_0= index value at the base year and $I_{2016}$is the CE index value for Sept. 2016 i.e. 542.8. The equipment installation cost for compressors is taken to be 80% of the purchased cost while for other equipment (heat exchangers and columns) it is taken to be 4% of the purchased cost based on a DOE report by Fisher *et al.* [187]. Hence $C_{com} = 1.8\ C_{p,com}$, $TIC_{cool} = 1.04\ C_{p,cool}$ and

$TIC_{ads} = 1.04\ C_{p,ads}$. The purchased costs for these are obtained from Seider *et al* [162] and are described below.

The adjusted purchase cost for the compressors and the subsequent cooler is given below [165]:

$$C_{com} = 3791.3\frac{I_{2016}}{I_0}\left(\frac{W_{com}}{0.7453}\right)^{0.82} \tag{B.22}$$

$$C_{cool} = 130\frac{I_{2016}}{I_0}|Q_C|^{0.78} \tag{B.23}$$

where I_0 for this case is CE value in 2004 i.e. 444.2, W_{com} is the consumed power of a compressor in kW and $|Q_C|$ is the cooling duty in kW.

The purchased cost for the adsorption column is given below [146, 162]:

$$C^0_{p,ads} = F_M C_{V,ads} + C_{PL,ads} + V_{P,ads}C_{PK} + C_{DR,\ ads} \tag{B.24}$$

where F_M is the materials of construction factor, $C_{V,ads}$ is the free on board purchase cost of empty vessel with weight W_{ads}, $C_{PL,ads}$ is cost of platforms and ladders, V_{ads} is the adsorber packing volume, C_{PL} is the installed cost of packing (adsorbent) per unit volume, $C_{DR,\ ads}$ is the installed cost of flow distributors. These are further calculated using the expressions below:

$$C_{V,ads} = \exp(7.0374 + 0.18255\ln W_{ads}\ + 0.02297(\ln W_{ads}\ )^2 \tag{B.25}$$

$$W_{ads} = \pi(39.37D_{ads} + t_s)(39.37\,(0.8D_{ads} + L_a)\,t_s\rho_w) \tag{B.26}$$

$$C_{PL,ads} = 237.1(3.281D_{ads})^{0.63316}(3.281L_a)^{0.80161} \tag{B.27}$$

$$V_{ads} = \frac{\pi}{4}(3.281D_a)^2(3.281L_a) \tag{B.28}$$

$$C_{DR,ads} = 100\frac{\pi}{4}(3.281D_a)^2 \tag{B.29}$$

where F_M=2.1, C_{PK}=60, ρ_w=0.2818 lb/in^3, t_s=0.688 in and D_a is the diameter of the column. The base index value (I_0) in this case was CE in mid-2000 and its then value was 394. The CE index in Oct. 2016 i.e. I_{2016}=543.3.

$$C_{p,ads} = C^0_{p,ads}\frac{I_{2016}}{I_0} \tag{B.30}$$

To estimate the total installed cost of isothermal dry reforming reactor (TIC_R) with feed heating in our process, we consider the cost of furnace and that of the reactor bed. A reformer usually consists

of a furnace section where natural gas is burnt. This heat is then supplied to the catalyst tubes in the convection section where the reaction takes place. There are different types of reformers with different configuration of burners to achieve the heat flux desired. This can help achieve both feed heating and isothermal operation which is needed in our process implementation. The purchased cost for the reactor bed ($C_{p,reac}$) is calculated in the same manner as for the adsorbent column.

The purchased cost for the furnace ($C_{p,furn}$) is given by

$$C_{p,furn} = 0.677 \frac{I_{2016}}{I_0} Q_h^{0.81} \tag{B.31}$$

where Q_h is the heat duty requirement in Btu/hr.

The total installed cost of the reforming reactor is given by

$$TIC_{RR} = 1.04\, C_{p,reac} + 1.04\, C_{p,furn} \tag{B.32}$$

B.3 Design of Simulations for Data-driven Optimization of ICCC Process

The desired number of feasible samples are obtained by solving the following optimization problem. This problem aims to find space filling samples within the known feasible region:

$$\min_{u} \quad \left(\frac{4}{3}\right)^n + \frac{1}{{N_s}^2} \sum_{i',j=1}^{N_s} \prod_{i=1}^{n} \left[\frac{3}{2} - |u_i^{(i')} - u_i^{(j)}| \left(1 - |u_i^{(i')} - u_i^{(j)}|\right)\right] \tag{B.33}$$

$$s.t. \quad g_{k,i}(u) \leq 0 \qquad \forall\, i \in \{1, \ldots, p\}$$

$$u_i \in [0,1] \qquad \forall\, i \in \{1, \ldots, n\}$$

where u represents the normalized decision variables. The decision variables are normalized such that their scaled bounds fall within the range [0,1].

B.4 Surrogate Models and Parameter Estimation

Cubic radial basis function with the following functional form is used as a surrogate model:

$$f^r = a + \sum_{i=1}^{n} b_i x_i + \sum_{j=1}^{|SMB|} \lambda_j \left(\left(\sum_{i=1}^{n} (x_i - x_{j,i})^2\right)\right)^{3/2} \tag{B.34}$$

The above function is nonlinear and interpolating in nature. It has also been shown that the

function satisfies the fully-linear property [188] assuming certain conditions on the geometry of sample set.

The samples obtained are divided into 3 sets: interpolating (denoted by *SMB*), cross-validation (denoted by *SCV*) and testing (denoted by *ST*). In this work, at each iteration, the total number of samples used are 5*n*. 20% of the samples are used for testing ($|ST| = n$), 30% of the samples are employed for cross-validation ($|SCV| = \lceil 1.5n \rceil$) and the remaining samples are utilized for interpolation. To estimate the parameters ($a,\ b_i,\ \lambda_j$), following linear program is solved, using GAMS/CPLEX:

$$\min_{a,b_i,\lambda_j} \sum_{i'=1}^{|SCV|} SP_{i'} + SN_{i'} \tag{B.35}$$

$$s.t. \quad y_{i'} + SP_{i'} - SN_{i'} = a + \sum_{i=1}^{n} b_i x_{i',i} + \sum_{j=1}^{|SMB|} \lambda_j \left(\left(\sum_{i=1}^{n} \left(x_{i',i} - x_{j,i} \right)^2 \right) \right)^{3/2} \qquad \forall i^{'} \in SCV$$

$$u_i \in [0,1] \qquad \forall\, i \in \{1, \ldots, n\}$$